MICROFLUIDIC ELECTROCHEMICAL SENSORS FOR THE SELECTIVE DETECTION OF TOXIC COMPOUNDS

BY

NICOLAS JAVIER LONDOÑO

DISSERTATION

Submitted in partial fulfillment of the requirements
for the degree of Doctor of Philosophy in Chemical Engineering
in the Graduate College of the
University of Illinois at Urbana-Champaign, 2011

Urbana, Illinois

Doctoral Committee:

Professor Paul J. A. Kenis, Chair
Professor Richard I. Masel, Director of Research
Professor Alexander Scheeline
Assistant Professor Christopher V. Rao

Abstract

This thesis details the use and optimization of several different analyte selective, liquid based detection chemistries, as well as the micro-fluidic device platforms which enable these sensors to be operated in a practical, effective manner. The majority of the work in this thesis involves an aqueous based chemistry utilizing an oxime reagent for the detection of acetylcholinesterase inhibitors. However, two other liquid chemistries based on the principles of chemical amplification were also studied in great detail.

Research first focused on improving the life time of the oxime reagent in solution. The oxime reagent decomposition in solution was studied electrochemically as well as by solid phase micro-extraction (SPME). Through these data, both an empirical degradation kinetic rate law and likely decomposition mechanisms were established. This information then allowed a degradation suppression scheme to be developed. By dissolving the oxime in an organic solvent, it could be prevented from dissociating, thereby greatly suppressing degradation. The concentrated organic oxime solution could then be combined with a basic aqueous buffer just prior to being used in the detection process, thus suppressing degradation without significantly affecting electrochemical performance. Ethanol was chosen as the optimal organic solvent as it was able to increase the oxime life time in solution 10 fold, while causing minimal decreases in sensor sensitivity and response speed. Finally, in order to mix the aqueous and organic solutions on chip, a serpentine channel micro-mixer was created with the same dimensions and material as the original micro-sensor to allow for seamless integration.

The micro-fluidic platform previously developed for this oxime based chemistry yielded a sensor able to rapidly and selectively detect acetylcholinesterase inhibitors. A large variety of

possible gaseous sensor interferent compounds were evaluated on this oxime based micro-sensor and none were found to produce any response from the device. Further characterization of this micro-sensor showed that although its response speed was fundamentally limited by the reaction rate of oxime with the analyte, this limitation had a negligibly affect on sensor performance if the device was coupled to a chromatography column. The rapid, selective nature of the oxime micro-sensor allowed for quick evaluation of individual compounds separated by the GC column; only responding to acetylcholinesterase inhibitors even if they are co-eluted with interferent compounds. Finally, this oxime micro-sensor was further miniaturized and created via a silicon micro-fabrication process. This allowed it to be integrated with 7 single walled carbon nano-tube (SWNT) based sensors on a single chip to form a complete micro-sensor array.

The other liquid chemistries studied in this thesis are classified as Non-Biological Inhibition Based Sensing (NIBS) mechanisms. These detection schemes utilize the inhibition of a catalyst with the target analyte to dramatically slow the rate of a main reaction, thus chemically amplifying the presence of a single molecule by reducing the production of hundreds or thousands of molecules. Two such examples of this NIBS mechanism have been previously developed; one for the detection of toxic sulfides and one for the detection of the riot control agent Adamsite. The final chapter in this thesis is a critical evaluation of these two NIBS mechanisms which includes a more detailed study of the chemistry involved, possible issues which hamper the detection of the target analytes and recommendations for future research using these types of sensing mechanisms.

Dedicated to my family and friends

Acknowledgments

First and foremost, I would like to thank my parents, Alejandro Londoño and Donna Carrick Londoño, and my brother Damian Londoño. You have always believed in me and encouraged me to pursue my interest to the fullest extent possible. I am forever grateful for all your love and support. I would also like to thank all my close friends who have never failed to brighten my day or put a smile on my face.

I would like to acknowledge all the support from my advisor Prof. Richard Masel, whose ideas and guidance have allowed me to succeed in my graduate research career. I would like to thank Prof. Paul Kenis for all the academic and professional advice he has given me. I would also like to thank Prof. Christopher Rao and Alexander Scheeline for taking the time to serve on my committee, as well as Prof. Mark Shannon for all this help in clean-room device fabrication.

Over my 5 years as a graduate student, I have had the pleasure of working with many wonderful people. I would like to thank Prof. Chelsea Monty for being a great collaborator on many of the micro-sensor projects. I would like to thank Dr. Kevin Lin and Dr. Christopher Field for all their assistance on the fabrication of the micro-sensor array. I am grateful for the friendship from my officemate Dr. Tianjiao Wu who I had many fascinating and bizarre conversations with over the years. I would also like to acknowledge all the other past and present members of the Masel research group: Dr. Zachary Dunbar, Dr. John Haan, Cody Jensen, Dr. Matthew Leubbers, Dr. Robert Morgan, Dr. Adarsh Radadia, Brian Rosen, Dr. Amin Salehi-Khojin, Maryam Sayyah and Lingjuan Shen, Dr. Wei Zhu.

Finally, I would like to thank the SCS Machine Shop and SCS Electronics Shop for all their expertise and hard work in creating many of the sensor components I used in my research.

Table of Contents

List of Figures ..... **ix**

List of Tables ..... **xv**

List of Symbols ..... **xvi**

List of Abbreviations ..... **xvii**

Chapter 1: Introduction to Chemical Sensor Technology **1**

1.1 Fundamentals of sensor operation 1
1.2 Overview of common gas sensor technology 2
1.2.1 Acoustic wave sensors *2*
1.2.2 Micro-cantilever beam sensors *3*
1.2.3 Metal oxide semiconductor sensors *5*
1.2.4 Conductive polymer sensors *6*
1.2.5 Carbon nano-tube sensors *7*
1.2.6 Ion mobility spectroscopy *8*
1.2.7 Optical sensors *9*
1.3 Conclusions 10
1.4 References 12

Chapter 2: Degradation of 1-phenyl-1,2,3-butanetrione 2-oxime in Toxic Organophosphate Sensor **15**

2.1 Introduction 15
2.1.1 Acetylcholinesterase and organophosphate poisoning *15*
2.1.2 Oxime based sensor chemistry *17*
2.2 Materials and experimental procedures 19
2.2.1 Chemical and materials *19*
2.2.2 Solid phase micro-extraction procedure *19*
2.2.3 Beaker-scale experimental procedure *21*
2.3 Results and discussion 21
2.3.1 Cyanide production kinetics *21*
2.3.2 Solid phase micro-extraction analysis *26*
2.3.3 Oxime degradation mechanism *33*
2.3.4 Oxime degradation suppression *37*
2.3.5 Oxime micro-sensor and integrated micro-mixer performance *41*
2.4 Conclusions and recommendations 45
2.5 References 49

Chapter 3: Characterization of Microfluidic Oxime Based Sensor **51**

3.1 Introduction 51
3.2 Materials and experimental procedures 54
3.2.1 Oxime micro-sensor fabrication *54*
3.2.2 Testing of oxime micro-sensor with interferent mixture *56*
3.2.3 Integration of micro-sensor with commercial gas chromatography system *57*

3.2.4 Fabrication of GC micro-column and integration with oxime micro-sensor *58*
3.2.5 Testing of oxime micro-sensor integrated in GC system *59*
3.3 Results and discussion 60
3.3.1 Interferent mixture tests *60*
3.3.2 Effects of temperature and gas flow rate on oxime micro-sensor performance *61*
3.3.3 Oxime micro-sensor integrated with commercial fused silica GC column *68*
3.3.4 Oxime micro-sensor integrated with silicon GC micro-column *72*
3.4 Conclusions and recommendations 74
3.5 References 79

Chapter 4: Oxime and Single-Walled Carbon Nanotube Based Sensors Integrated into a Micro-Machined Silicon Array 81

4.1 Introduction 81
4.1.1 Electronic noses *82*
4.1.2 Signal processing for sensor arrays *85*
4.1.3 Single walled carbon nano-tube (SWNT) based sensors *87*
4.2 Integrated micro-sensor array design 90
4.3 Array fabrication process 98
4.3.1 Layer 1 (SWNT-based sensor layer) *98*
4.3.2 Layer 2 (Gas micro-channel layer) *102*
4.3.3 Layer 3 (Oxime sensor and gas/liquid membrane layer) *104*
4.3.4 Layer 4 (Liquid micro-channel layer) *106*
4.3.5 Device assembly *108*
4.4 Preliminary sensor array performance 110
4.5 Conclusions and recommendations 113
4.6 References 117

Chapter 5: A Critical Review of Existing Non-Biological Inhibition Based Sensing (NIBS) Mechanisms 120

5.1 Introduction 120
5.1.1 Chemical amplification *120*
5.1.2 Non-Biological Inhibition Based Sensing (NIBS) mechanisms *124*
5.2 NIBS for the detection of toxic sulfide compounds 127
5.2.1 Chemicals and materials *128*
5.2.2 Experimental procedures *128*
5.2.3 Results and discussion *129*
5.3 NIBS for the detection of the riot control agent Adamsite 141
5.3.1 Chemicals and materials *142*
5.3.2 Experimental procedures *143*
5.3.3 Results and discussion *144*
5.4 Conclusions and recommendations 156
5.5 References 160

Chapter 6: Thesis Summary and Recommendations for Future Research 164

Appendix A: Fabrication Steps for Silicon Micro-Array 168

Appendix B: Photolithography Mask for Fabrication of Silicon Micro-Array 171

Appendix C: Experimental Procedures 184

Solid phase micro-extraction and analysis procedures 184
Spectroscopic experiments on NIBS mechanism for Adamsite detection 185
Beaker scale electrochemical studies 186
Cyanide production kinetics for oxime based chemistry 186
Organic solvent evaluation in oxime based chemistry 187
NIBS mechanism for toxic sulfide detection 189
NIBS mechanism for Adamsite detection 190
Oxime micro-sensor testing 191
Operation with gas chromatograph automatic injector assembly 191
Evaluation of organic solvents in micro-sensor 193
Operation with continuous gas sample delivery 193
Micro-mixer evaluation 194
Single walled carbon nano-tube (SWNT)-based sensor operation 196

Author's Biography 198

List of Figures

Figure 2.1: Normal operation of a cholinergic synapse. Acetylcholine is released by the axon terminal, triggers receptors on the dendritic spine, is hydrolyzed to choline and acetate, and then is re-absorbed. 16
Figure 2.2: Reaction mechanism of an organophosphate analyte with PBO to produce a cyanide anion. 18
Figure 2.3: Potential response decrease over 24 hour period, as measured by CN ISE. 5 mM PBO in pH 10 borate buffer. 22
Figure 2.4: Cyanide ion concentration versus time for various initial PBO concentrations at pH 10. 23
Figure 2.5: Cyanide formation rate versus pH for various initial PBO concentrations at pH 10. 24
Figure 2.6: Experimentally observed rate versus predicted rate of cyanide formation calculated with simple rate law. 25
Figure 2.7: Possible mechanism for the formation of acetophenone found in SPME analysis. 29
Figure 2.8: Expanded reaction mechanism of PBO with a typical reactive organophosphate. 30
Figure 2.9: Peak area trends over time for various compounds found through SPME. (A) Increasing peak area trends. (B) Decreasing peak area trends. Each curve is normalized to initial peak area. 31
Figure 2.10: PBO rearrangement via anionic attack of either carbonyl carbon and subsequent decomposition and hydrolysis to produce cyanide ions. 33
Figure 2.11: Increasing peak area trends from SPME performed on 5% ethanol aqueous PBO solution. Each curve is normalized to initial peak area. 35
Figure 2.12: PBO anion attack on an acyl cyanide molecule. 36
Figure 2.13: Typical potential response curves for each solvent tested. Curves normalized to baseline potential. All test at pH 10. 39
Figure 2.14: Comparison of beaker-scale potential response between freshly prepared and 8 day old oxime/ethanol solution. 40
Figure 2.15: Typical differentiated signal from micro-sensor when using ethanol, ethylene glycol or no organic solvent. 42

Figure 2.16: Performance of micro-sensor with integrated micro-mixer in comparison to micro-sensor with mixing performed externally. In both cases, the total liquid flow rate is 5.5 μL/min and the gas flow rate was 1 ml/min. The gas is 100 ppb acetic anhydride, and flow is turned on at t = 50 s and off at t = 200 s.....44
Figure 3.1: A cross sectional diagram of the micro-sensor (figure is not to scale). The gas microchannel and the liquid microchannel are aligned over each other and are separated by a nanoporous membrane with a sputtered layer of gold for electrodes. The liquid side of the nanoporous membrane is coated with a gold electrode material. (A) Profile along the microchannel. (B) Profile perpendicular to the microchannel. 55
Figure 3.2: Top view of liquid (A) and gas (B) polycarbonate micro-channels.....55
Figure 3.3: (A) SEM image of the 165 μm wide 60 μm deep cross section of the PBMC channel geometry. (B) Photograph of the 1.4 cm square PBMC showing the Nanoport® vapor connections.....58
Figure 3.4: Example of typical potential response of the oxime micro-sensor when exposed to a "pulse" of simulant in an inert carrier gas stream. Injection of 9.4×10^{10} molecules of acetic anhydride at a flow rate of 0.5 mL/min and an oven temperature of 50 °C. 62
Figure 3.5: Derivative of oxime micro-sensor potential response signal from figure 3.4. Injection of 9.4×10^{10} molecules of acetic anhydride at a flow rate of 0.5 mL/min and an oven temperature of 50 °C. 63
Figure 3.6: Effect of carrier gas flow rate on (A) peak height and (B) peak width at half height from the oxime micro-sensor and commercial GC FID. Performed at a constant oven temperature of 35 ºC.....65
Figure 3.7: Effect of oven temperature on (A) peak height and (B) width at half height from the oxime micro-sensor and commercial GC FID. Performed at carrier gas flow rates of 0.1 and 0.5 mL/min. 67
Figure 3.8: Oxime micro-sensor and normalized FID signal for separated sample. Gas flow rates of (A) 0.5 and (B) 1.0 mL/min, with a temperature of 50 °C. From left to right, the peaks in the FID signal are acetone, methyl pyruvate, acetic anhydride, ethyl oxoacetate and toluene. 70

Figure 3.9: (A) FID signal and (B) oxime micro-sensor signal to a separated mixture of MeSC, IPSC and C_7-C_{11} n-alkanes in n-pentane. This mixture was separated using the 34 cm PBMC at a carrier gas flow rate of 0.2 mL/min and a temperature of 50 °C. 73
Figure 4.1: Optical absorption based sensor array utilizing various metalloporphyrin compounds created by Rakow and Suslick [15]. Array undergoes color change when exposed to various compounds. 84
Figure 4.2: Typical SWNT-based sensor used in our silicon micro-sensor array. Not to scale. ..89
Figure 4.3: Simplified side profile of silicon micro-sensor array stack. Not to scale....93
Figure 4.4: Rendering of micro-sensor array design between layers 1 and 2. This diagram is to scale. 94
Figure 4.5: Rendering of micro-sensor array design between layers 2 and 3. This diagram is to scale. 96
Figure 4.6: Rendering of micro-sensor array design between layers 3 and 4. This diagram is to scale. 97
Figure 4.7: Cross-sectional diagram of layer 1 at various steps in the micro-fabrication process. Not to scale. 100
Figure 4.8: Photograph of the top and bottom of a completed layer 1. 102
Figure 4.9: Cross-sectional diagram of layer 2 at various steps in the micro-fabrication process. Not to scale. 103
Figure 4.10: Photograph of the top and bottom of a completed layer 2. 103
Figure 4.11: Cross-sectional diagram of layer 3 at various steps in the micro-fabrication process. Not to scale. 105
Figure 4.12: Photograph of the top and bottom of a completed layer 3. 106
Figure 4.13: Cross-sectional diagram of layer 4 at various steps in the micro-fabrication process. Not to scale. 107
Figure 4.14: Photograph of the top and bottom of a completed layer 4. 107
Figure 4.15: Photograph of the side and bottom of the final assembled micro-sensor array in its PGA package with all capillaries attached. 110
Figure 4.16: Response of a SWNT-based sensor in the silicon array to a “pulse” of 10 ppm DMMP at 1 mL/min. The sensor was operated at a drive current of 0.1 mA. 111

Figure 4.17: Response of the oxime based sensor in the silicon array to a "pulse" of acetic anhydride at 0.2 mL/min. The sensor was operated at a temperature of 30 ºC. 112
Figure 5.1: Schematic of the dual microchannel/membrane system. Vapor flows through the top microchannel and is separated from the liquid microchannel by a nanoporous membrane with 40-nm thick layer of sputtered gold on the liquid side. The gold layer is separated into a working and a counter electrode by using a shadow mask during sputtering. A thin film of AChE is immobilized inside the liquid microchannel in a cross-linked gel with glutaraldehyde [31]. 122
Figure 5.2: Chemical amplification mechanism using $NADP^+$ to active two enzymes which facilitates the production of 6-phosphogluconate [40].....123
Figure 5.3: General form of a Non-Biological Inhibition Based Sensing (NIBS) mechanism. Substrates are converted to produces by the catalyst. Addition of the analyte molecule inhibits the catalyst and prevents the substrate conversion from taking place.....125
Figure 5.4: Theorized NIBS mechanism for the detection of toxic sulfide compounds.....128
Figure 5.5: Open circuit potential response of the NIBS sulfide detection mechanism as measured by Monty [41]. 0.4 µM of formic hydrazide and 31.4 µM of copper (II) acetate in methanol, with and without the presence of CEMS.....130
Figure 5.6: Open circuit potential response of the NIBS mechanism. 0.4 µM of formic hydrazide and 31.4 µM of copper (II) acetate in methanol, with and without the presence of CEMS.....131
Figure 5.7: Open circuit potential response of the NIBS mechanism. 40 µM of formic hydrazide and 31.4 µM of copper (II) acetate in methanol, with and without the presence of 30 µM CEMS.....132
Figure 5.8: Open circuit potential response of the NIBS mechanism. 40 µM of formic hydrazide and 31.4 µM of copper (II) acetate in methanol, with and without the presence of 30 µM CEMS.....133
Figure 5.9: Effect of catalyst/substrate ratio on potential response of NIBS mechanism for both protic and aprotic solvents [41].....134
Figure 5.10: Lineweaver-Burke plot of inverse reaction rate versus inverse formic hydrazide concentration [41].....136

Figure 5.11: Open circuit potential response of the NIBS mechanism. 4 µM of formic hydrazide and 0.3 µM of copper (II) acetate in methanol, with and without the presence of 0.5 µM CEMS. 140
Figure 5.12: Theorized NIBS mechanism for the detection of Adamsite. 142
Figure 5.13: Effect of catalyst/substrate ratio on potential response of NIBS mechanism for both 100 mM and 1 mM phenylenediamine (250 mM and 2.5 mM acetone, respectively) [42]. 145
Figure 5.14: Open circuit potential response of the NIBS Adamsite detection mechanism as measured by Monty [XXX]. 1 mM phenylenediamine, 2.5 mM acetone, and 2 µM silver nitrate in water with and without the presence of 1.8 µM Adamsite [42] ... 146
Figure 5.15: Open circuit potential response of the NIBS Adamsite detection mechanism. 0.25 mM phenylenediamine, 2.5 mM acetone, and 23.5 µM silver nitrate in water with and without the presence of 3.6 µM Adamsite. 147
Figure 5.16: Absorbance at 417 nm of a 25 mM solution of phenylenediamine in water over a period of 48 hours. 148
Figure 5.17: Absorbance spectrum of the NIBS mechanism after 25 minutes. 8.33 mM phenylenediamine, 83.3 mM acetone, 783 µM silver nitrate and 120 µM Adamsite present depending on the experimental conditions. 150
Figure 5.18: Absorbance spectrum of the solutions containing 8.33 mM phenylenediamine, 83.3 mM acetone and 783 µM silver nitrate after 25 minutes. The concentration of methanol in the one experiment is 494 mM. No Adamsite is present in any of these experiments. 152
Figure 5.19: Absorbance spectrum of the solutions containing 8.33 mM phenylenediamine, and 783 µM silver nitrate after 25 minutes. Acetone concentration is either 0 mM or 83.3 mM, depending on the experiment. 153
Figure 5.20: Absorbance of the NIBS mechanism over time at both 434 nm and 650 nm. 0.25 mM phenylenediamine, 2.5 mM acetone, 20.5 µM silver nitrate and 1.8 µM Adamsite present depending on the experimental conditions. 155
Figure B.1: Mask 1a – Pattern for alignment marks on top of layer 1. 171
Figure B.2: Mask 1b – Pattern for integrated resistive heater element on top of layer 1. 172

Figure B.3: Mask 1c – Pattern for gold contact pads for resistive heater element on top of layer 1. 173
Figure B.4: Mask 1d – Pattern for gold electrodes/contact/leads for SWNT-based sensors on top of layer 1. 174
Figure B.5: Mask 1e – Optimal mask for SWNT film deposition alignment on top of layer 1. .175
Figure B.6: Mask 1f – Pattern for through-holes, thermal break and die edges on bottom of layer 1. 176
Figure B.7: Mask 2a – Pattern for through-holes, thermal break and die edges on top of layer 2. 177
Figure B.8: Mask 2b – Pattern for gas micro-channel on bottom of layer 2. 178
Figure B.9: Mask 3a – Pattern for gold electrode/leads/contacts for oxime sensor on top of layer 3. 179
Figure B.10: Mask 3b – Pattern for membrane as well as through-holes, thermal break and die edges on top of layer 3. 180
Figure B.11: Mask 3c – Pattern for gas micro-channel as well as through-holes, thermal break and die edges on bottom of layer 3. 181
Figure B.12: Mask 4a – Pattern for thermal break and die edges on top of layer 4. 182
Figure B.13: Mask 4b – Pattern for liquid micro-channel on bottom of layer 4. 183

List of Tables

Table 2.1: Kinetic rate law parameters for Equation 1 25
Table 2.2: Identifiable peaks (ignoring known contaminants) from SPME of a 5 mM solution of oxime in aqueous buffer (pH 10) performed 1 hour after solution preparation. 28
Table 2.3: Effects of various solvents on beaker cell potential response (ΔE).....39
Table 3.1: Components in TO-15 interferent mixture at 100 ppb in nitrogen. 60
Table 3.2: Width at half height of the acetic anhydride peak from both the oxime micro-sensor and FID signals shown in figure 3.8. 71

List of Symbols

a	reaction order of PBO
b	reaction order of hydroxide ions
$[CN^-]$	concentration of cyanide ions in solution, M
ΔE	magnitude of potential change of solution, mV
k	rate constant for PBO degradation rate law
K_a	acidity constant
$[OH^-]$	concentration of hydroxide ions in solution, M
[PBO]	concentration of PBO in solution, M
r_{cn}	rate of cyanide production, M/s

List of Abbreviations

AC	alternating current
ANN	artificial neural network
APTES	3-aminopropyl triethoxysilane
BAW	bulk acoustic wave
BOE	buffered oxide etch
BOX	buried oxide
CEMS	2-chloroethyl methyl sulfide
CN ISE	cyanide ion selective electrode
CV	cyclic voltametry
CVD	chemical vapor deposition
DMA	differential mobility analyzers
DMS	differential mobility spectrometers
DMMP	dimethyl methyl phosphonate
DMSO	dimethyl sulfoxide
DNA	deoxyribonucleic acid
DRIE	deep reactive ion etching
DSP	double side polished
ESI	electro-spray ionization
FID	flame ionization detection
FTIR	Fourier transform infrared spectroscopy
G6PDH	glucose-6-phosphate dehydrogenase
GC	gas chromatograph
GDH	glutamate dehydrogenase
IC	integrated circuit
ICP	inductively coupled plasma
IMS	ion mobility spectroscopy
IPA	isopropyl alcohol
IPSC	isopropyl sulfonyl chloride

LC	liquid chromatography
LD50	median lethal dosage
LED	light emitting diode
MCE	mixed cellulose ester
MeSC	methyl sulfonyl chloride
MOS	metal oxide semiconductor
MS	mass spectrometer
MW	molecular weight
NIBS	non-biological inhibition based sensing
OP	organophosphate
PA	polyacrylate
PAO	*anti*-pyruvic aldehyde 1-oxime
PARC	pattern recognition
PBMC	“partially buried” micro-column
PBO	1-phenyl-1,2,3,-butanetrione 2-oxime
PCA	principle component analysis
PDMS	polydimethylsiloxane
PGA	pin grid array
PR	photo-resist
PTFE	polytetrafluoroethylene
QCM	quartz crystal micro-balance
TCD	thermal conductivity detectors
TEA	triethanolamine
RIE	reactive ion etch
SAM	self assembled monolayer
SAW	surface acoustic wave
SDS	sodium dodecyl sulfate
SOI	silicon on insulator
SPME	solid phase micro-extraction
SSP	single side polished
SWNT	single wall carbon nanotube

VOC	volatile organic compound

Chapter 1:

Introduction to Chemical Sensor Technology

1.1 Fundamentals of sensor operation

Chemical sensors for the detection of gaseous species are composed of two major elements; a chemical-sensitive element which interacts in some manner with the compound(s) of interest and a transducer element which converts this chemical interaction into a qualitative and/or quantitative electrical signal which forms the raw response of the sensor. Additional elements of a gas sensor system could possibly include signal processing electronics, sensor operation and control electronics, a gas sample concentration or sample injection system, and even a chromatography or separation system. Together, these elements form the total analytical system required for detection of gaseous chemicals. Although there are a wide assortment of sensors available, each operating under fundamentally different principles, the general requirements of any gas sensor, especially one designed for the detection harmful chemicals, are the following[1, 2]:

- High sensitivity
- High selectivity
- Rapid detection
- Portable

The ideal gas sensor should be sensitive to its target analyte(s) in concentrations well below their toxic exposure level or other critical dangerous threshold. Detection speed, as measured from initial gas sampling to final processed sensor signal, should take place fast enough to allow for proactive instead of reactive use of the data. A rapid detection process also

enables multiple, successive measurements to be conducted within a short period of time and ensures the sensor can keep pace with changing environmental conditions. The ideal gas sensor should have a high selectivity towards its intended target compound(s) or have the ability to distinguish the chemical identity of a large variety of species. It is also important that the rate of false positives, as well as false negative results be very low, as to avoid any inaccuracies in detection. Finally, a gas sensor designed to detect toxic compounds should be portable. Ideally, sample gathering, processing and analysis should all be carried out in the same unit. Such a system should be small enough to be operated by a single person or integrated within another piece of equipment to streamline its use.

In the following section, several common miniature (or micro) gas sensor technologies will be examined. Their general operating process and method of signal transduction will be discussed, as well as their typical material construction and chemical selectivity.

1.2 Overview of common gas sensor technology

1.2.1 Acoustic wave sensors

Piezoelectric materials have the ability to accumulate charges when mechanically strained or deformed. These materials will also mechanically deform in response to an external applied charge. By attaching electrodes on the surface of these materials and applying an alternating current to them, they can be made to vibrate at their resonance frequency. Depending on the material crystal quality, this frequency can be fairly precise and is related to material type and geometry, crystal plane cut, as well as the electrode configuration and dimensions [3]. When an analyte molecule adsorbs onto the surface of an acoustic wave sensor, the overall mass of the

device is slightly increased, which alters its resonance frequency. This then changes the alternative current frequency used to drive the sensor.

The two major types of devices based on this operating principle are bulk and surface acoustic wave sensors. Quartz crystal micro-balances (QCM) are an example of a bulk acoustic wave (BAW) sensor. A QCM is typically comprised of a quartz crystal several millimeters thick sandwiched between two gold electrodes which are used to apply an alternating current with a frequency of a few MHz [3]. This produces a standing wave that spans the entire thickness of the quartz. Surface acoustic wave (SAW) sensors utilize inter-digitated electrodes to create a mechanical wave travelling only through the surface of the piezoelectric material. Two versions of SAW sensors currently exist: delay-line and resonator configurations. In delay-line SAW devices, one pair of electrodes creates the Rayleigh wave in the material, while a second pair of electrodes detects the wave after it has propagated across the surface some distance. In the resonator configuration, only a single pair of inter-digitated electrodes is used and the surface wave is simply reflected back towards it by ridges in the substrate. SAW sensors are typically fabricated with quartz, as well as lithium niobate or lithium tantalite, and they operate at frequencies of several hundred MHz or even a few GHz [3]. Because both BAW and SAW types sensors work via an adsorption process, they are fairly non-selective. However, their chemical specificity can be change and tuned with the use of various surface functionalizations; such as polymer coatings [4-6], self assembled monolayers [7, 8] or metalloporphyrins [9].

1.2.2 Micro-cantilever beam sensors

Micro-cantilever beams are a unique sensor technologies which have the ability to detect chemical interactions in a number of different ways. These devices are essentially thin beams of

material anchored on one end to a bulk substrate and will deflect when subjected to an applied force. The deflection physics are well understood and are dependent on material properties and beam geometry. These sensors are typically composed of silicon, silicon nitride or silicon oxide, and can be easily micro-fabricated in large arrays [10-12].

Micro-cantilever beam sensors can be operated in one of two modes: resonance frequency vibration or beam bending mode. In resonance frequency mode, the entire device can be mechanically vibrated by pairing it with a piezoelectric actuator, which causes the cantilever to oscillate at its resonance frequency. Similar to the operation of BAW and SAW sensors, additional mass on the micro-cantilever beam due to adsorbed analytes alters its resonance frequency. When the sensor operates in a beam bending mode, there are two manners in which a chemical can interact with the cantilever. By functionalizing a single side of the beam, specific analytes will preferentially adsorb to this surface. In doing so, they alter the surface tension forces on that side, which causes a mechanical stress in the material and results in beam deflection. Calorimetric effects of adsorbed analytes can also be measured if the micro-cantilever beam is constructed as a lamination of two materials with dissimilar thermal expansion coefficients. As the beam heats, the two materials expand at different rates and cause a deflection of the cantilever.

The measurement of beam deflection/vibration can also be accomplished in several different ways. The most common method involves measuring the angle of reflection of a light emitting diode (LED) laser beam focused at the cantilever tip [13]. Deflection can also be measured through laser beam interference, as a change in capacitance between a fixed electrode and the beam itself, or electrically as a change in resistance if the beam is constructed with a piezoresistive material [13]. Each method has its own drawbacks and usage depends on the

specific detection situation. Sensitivity of these sensors can be increased by lowering the beam stiffness; however this comes with an increase in signal noise and response speed [13-15]. Selectivity is again similar to that for BAW and SAW sensor technologies and can be improved through the use of surface modifications, although bending mode operation does have the advantage of introducing analyte surface tension or thermal effects to enhance detection specificity.

1.2.3 Metal oxide semiconductor sensors

Metal oxide semiconductor (MOS) devices are chemi-resistive type sensors. They are commonly constructed of a ceramic or silicon oxide substrate with a metal oxide film on the surface. Tin oxide, an n-type semiconductor, is typically used in these sensors, however other p-type metal oxides can be used such as zinc oxide, titanium oxide and iron (III) oxide. During operation, atmospheric oxygen adsorbs to the surface of the oxide, trapping free electrons from the conduction band of the material and thus increasing film resistance. When the sensor is subsequently exposed to a volatile organic compound (VOC) or other oxidizable material, a chemical reaction takes place which consumes the adsorbed oxygen. This releases electrons into the conduction band and temporarily decreases sensor resistance.

These sensors are usually operated at high temperatures ranging from 200 – 650 ºC to provide a sufficiently excited surface to ensure rapid, complete reaction of analytes, to promote reversible adsorption of surface species, and to prevent the formation of a chemisorbed water layer [16, 17]. As a result of these elevated operating temperatures, these sensors tend to consume a large amount of power. MOS sensors can be generally categorized into thin (nanometer) or thick (micrometer) film types. Thin MOS film sensors typically offer better sensitivity and response

rate, however they are more difficult to manufacture compared to thick film types. Because of the high operating temperature, typical chemical functionalization techniques cannot be used to tune the selectivity of these sensors. Instead, selectivity is altered by doping the MOS films with noble metal catalyst such as platinum or palladium, changing film crystal grain size or operating temperature [18, 19].

1.2.4 Conductive polymer sensors

Another example of chemi-resistive type detector technology is conductive polymer sensors. These sensors generally consist of an insulating substrate with two gold electrodes separated by a micrometer sized gap which is bridged with the conducting polymer film. These polymer films can either be intrinsically or extrinsically conductive. Intrinsic conductive polymers are usually formed by electropolymerization of a solution of an appropriate monomer compounds, such as pyrrole, indole, aniline and thiophene. The polymer film thickness can be precisely directed by controlling the applied voltage and current during the electrochemical deposition. Although the detection mechanism in these sensors is not clearly understood, detector selectivity is based on the type of monomer and counter ion used in solution for the electropolymerization process [16].

Extrinsic type conductive polymer sensors utilize an insulating polymer which has been doped with a conductive material, such as carbon black, graphite, or metal particles. A number of fabrication techniques can be used to deposit these doped polymer films, however they all operate via the same process. Analytes absorbed into the polymer matrix cause swelling which affects the connectivity of the conductive material network and changes the film resistance. For both types of sensors, film thickness and operating current or voltage also play an important role

by altering sensitivity or other aspects of device performance. Conductive polymer sensors have a fairly rapid and reversible detection process, and as a result are usually operated close to room temperature. However the low operating temperatures make them sensitive to humidity and the polymers can be aged by oxidative or other chemical degradation processes [3].

1.2.5 Carbon nano-tube sensors

Single wall carbon nanotubes (SWNTs) are unique fullerene materials with great mechanical strength, high thermal conductivity and tunable electronic properties. In applications for gas sensors, they can be utilized in a similar method to conducting polymers, by depositing a thin film of SWNTs which are bridge a small gap between two metal electrodes on an insulating surface. SWNT-based gas sensors are usually operated in a chemi-resistive manner [20-24], however chemi-capacitive SWNT-based gas sensors [23, 25], as well as three electrode chemi-transistive SWNT-based sensors have also been developed [26-28]. SWNT films can be deposited via solvent evaporation [21, 29], chemical vapor deposition (CVD) [22], alternating current (AC) dielectrophoresis [27], or through a vacuum filtration and transfer method [30, 31]. The general detection process for these sensors is thought to involve adsorbed analyte molecules interacting with defect sites on the nano-tubes, which changes their electronic properties and alters the conductivity [32-34]. As a result, they respond rapidly and the analyte adsorption on their surface is highly reversible if operated at sufficient driving currents. Chemical selectivity of these SWNTs-based sensors can be enhanced by the use of polymers. Polymers can be incorporated directly into the SWNT film [24, 35], grown over the film using electropolymerization [36, 37], or polymer molecules can be covalently bonded to the surface of the nano-tubes [38].

1.2.6 Ion mobility spectroscopy

Another technology commonly used in portable gas sensor applications is ion mobility spectroscopy (IMS). Differential mobility spectrometers (DMS) and differential mobility analyzers (DMA) are also commonly used variants of this detection technology. These devices work similarly to mass spectrometry (MS) detectors in that they sort or separate analyte ions. Ion mobility spectrometers however separate ions based on their movement speed in atmospheric pressure gases, while mass spectrometers measure mass-to-charge ratios and require a vacuum to operate. As a result, IMS is a much easier detection technology to miniaturize.

IMS sensors generally function by ionizing a sample of the gaseous analyte, either with a radioactive source such as Ni-63 or Am-241 [39, 40], by electrospray ionization (ESI) [41, 42], photoionization [43] or corona discharge [44]. The ionized sample is held in an intermediate chamber where it is released in pulses by an electrode gate into the drift tube. Within the drift tube, a uniform electric field is applied, which promotes the movement of ions through the tube towards the detector unit. The ion travel is impeded by molecular collisions with a drift gas stream flowing in the opposite direction. As a result, ions are separated based on their speed or mobility within this drift gas. Ion mobility is related to the collision cross section of the ion with the drift gas molecules, and is affected by ion charge, and as well as the shape and size of both the ion and molecule. Once the ions travel through the drift tube, they are collected by a Faraday plate. Individual compounds can be identified in this way by the characteristic ion travel time spectrum they produce in the IMS. Mixtures of gases can also be analyzed using this sensor technology, provided the device has sufficient separating power to resolve any ion species with similar mobility. The separation properties of IMS sensors can be tuned by changing electric field strength, device pressure or temperature, and drift gas flow rate, composition or concentration [45].

Altering these parameters provides a fair degree of flexibility in which to effectively analyze different sample mixtures.

1.2.7 Optical sensors

Optical detection methods encompass a wide array of sensor technologies and involve measurement of device-analyte interaction by fluorescence, absorbance or other emission-based spectroscopy. One of the most common of these detection methods employs optical fibers to focus and route light to and from the chemically sensitive area of the sensor. Optical fibers can be used in a number of ways. The surface of an unclad fiber can be coated with a dye or polymer which changes its optical properties when exposed to an analyte [16]. Light undergoing total internal reflection through the fiber interacts with these coatings through the evanescent waves produced at the outside surface. The resulting fluorescence from the coating can be measured as it exits the fiber. Total internal reflection fluorescence or infra-red attenuated total reflectance sensors are examples of this optical detection method. Optical fibers can be used in an alternative manner, either by directly coating the end or tip of the fiber with a fluorescent dye [46, 47], or by placing the end of the fiber is close proximity to a coated substrate which will exhibit the color change or fluorescence [48]. In general, fiber based optical sensors are semi-selective to various chemicals depending on the coating or dye used.

Another detection technology is bulk liquid based optical sensors. These devices use a reagent in a liquid medium which undergoes a reaction with its target analyte as it diffuses into solution. This reaction produces an optically active product which may be measured via an absorbance or fluorescence change of the liquid [49]. These detection methods typically have low sensitivities and slow response rates, but are highly selective to very specific types of compounds

due to the unique chemistry taking place. Optical sensors can even be created without the use of any chemically selective coatings or reagents, by utilizing plasma to ionize gaseous species and then measuring the resultant emission spectra [50].

1.3 Conclusions

The majority of the gas sensor technologies discussed in this chapter are non-selective or semi-selective, solid state based devices. Selectivity can be altered for most detectors by modifying or functionalizing the chemically sensitive portion of the device with metals atoms or particles, polymers, self assembling monolayers, and other organic molecules, however their chemical sensitivity will still remain fairly broad. BAW, SAW, micro-cantilever beam and other chemi-resistive type sensors can utilize biological components such as enzymes, antibodies or entire cells to make them selectivity to very specific types of analytes; however this generally comes at the expense of device life time and restricted operating conditions. IMS can identify a broad array of compounds, provided the spectrums for individual compounds are known and the device has sufficient power to separate all ions species present in the mixture. Liquid based detection methods frequently involve non-biological, chemically selective reactions which produce an absorbance or fluorescence change in solution. Unfortunately these detection techniques usually have a much slower response time and decreased sensitivity compared to solid state sensors.

Combining liquid reagent chemistries with electrochemical monitoring methods can yield sensors which are not only highly selective, but also have higher sensitivities similar to solid-state detectors. The majority of this thesis focuses on an electrochemical sensors which uses an aqueous based oxime reagent for the detection of acetylcholinesterase inhibitors. Research on

the lifetime issues of this detection chemistry will be detailed, along with characterization work of the micro-fluidic sensor platform which enables this chemistry to be operated effectively. Alternative liquid detection chemistries following Non-Biological Inhibition Based Sensing (NIBS) mechanisms will also examined in greater detail in the final chapter of this thesis.

1.4 References

1. Krausa, M. and A.A. Reznev. *Vapour and trace detection of explosives for anti-terrorism purposes*. 2004. Dordrecht ;: Kluwer Academic.
2. Pearce, T.C., et al., *Handbook of Machine Olfaction: Electronic Nose Technology*. 2003, Weinheim, Germany: Wiley-VCH.
3. Deisingh, A.K., D.C. Stone, and M. Thompson, *Applications of electronic noses and tongues in food analysis.* International Journal of Food Science and Technology, 2004. **39**(6): p. 587-604.
4. Grate, J.W., et al., *The Predominant Role of Swelling-Induced Modulus Changes of the Sorbent Phase in Determining the Responses of Polymer-Coated Surface Acoustic-Wave Vapor Sensors.* Analytical Chemistry, 1992. **64**(6): p. 610-624.
5. Park, J., W.A. Groves, and E.T. Zellers, *Vapor recognition with small arrays of polymer-coated microsensors. A comprehensive analysis.* Analytical Chemistry, 1999. **71**(17): p. 3877-3886.
6. Zellers, E.T., et al., *Optimal Coating Selection for the Analysis of Organic Vapor Mixtures with Polymer-Coated Surface-Acoustic-Wave Sensor Arrays.* Analytical Chemistry, 1995. **67**(6): p. 1092-1106.
7. Li, D.Q. and M. Ma, *Surface acoustic wave microsensors based on cyclodextrin coatings.* Sensors and Actuators B-Chemical, 2000. **69**(1-2): p. 75-84.
8. McGill, R.A., et al., *Performance optimization of surface acoustic wave chemical sensors.* Ieee Transactions on Ultrasonics Ferroelectrics and Frequency Control, 1998. **45**(5): p. 1370-1380.
9. Caliendo, C., et al., *Advances in SAW-based gas sensors.* Smart Materials & Structures, 1997. **6**(6): p. 689-699.
10. Betts, T.A., et al., *Selectivity of chemical sensors based on micro-cantilevers coated with thin polymer films.* Analytica Chimica Acta, 2000. **422**(1): p. 89-99.
11. Fagan, B.C., et al., *Modification of micro-cantilever sensors with sol-gels to enhance performance and immobilize chemically selective phases.* Talanta, 2000. **53**(3): p. 599-608.
12. Wang, Y.H., C.Y. Lee, and C.M. Chiang, *A MEMS-based air flow sensor with a free-standing micro-cantilever structure.* Sensors, 2007. **7**(10): p. 2389-2401.
13. Raiteri, R., et al., *Micromechanical cantilever-based biosensors.* Sensors and Actuators B-Chemical, 2001. **79**(2-3): p. 115-126.
14. Lavrik, N.V., M.J. Sepaniak, and P.G. Datskos, *Cantilever transducers as a platform for chemical and biological sensors.* Review of Scientific Instruments, 2004. **75**(7): p. 2229-2253.
15. Ziegler, C., *Cantilever-based biosensors.* Analytical and Bioanalytical Chemistry, 2004. **379**(7-8): p. 946-959.
16. James, D., et al., *Chemical sensors for electronic nose systems.* Microchimica Acta, 2005. **149**(1-2): p. 1-17.
17. Schaller, E., J.O. Bosset, and F. Escher, *'Electronic noses' and their application to food.* Food Science and Technology-Lebensmittel-Wissenschaft & Technologie, 1998. **31**(4): p. 305-316.

18. Azad, A.M., et al., *Solid-State Gas Sensors - a Review.* Journal of the Electrochemical Society, 1992. **139**(12): p. 3690-3704.
19. Comini, E., *Metal oxide nano-crystals for gas sensing.* Analytica Chimica Acta, 2006. **568**(1-2): p. 28-40.
20. Lee, C.Y., et al., *On-chip micro gas chromatograph enabled by a noncovalently functionalized single-walled carbon nanotube sensor array.* Angewandte Chemie-International Edition, 2008. **47**(27): p. 5018-5021.
21. Li, J., et al., *Carbon nanotube sensors for gas and organic vapor detection.* Nano Letters, 2003. **3**(7): p. 929-933.
22. Novak, J.P., et al., *Nerve agent detection using networks of single-walled carbon nanotubes.* Applied Physics Letters, 2003. **83**(19): p. 4026-4028.
23. Snow, E.S. and F.K. Perkins, *Capacitance and conductance of single-walled carbon nanotubes in the presence of chemical vapors.* Nano Letters, 2005. **5**(12): p. 2414-2417.
24. Wang, F., H.W. Gu, and T.M. Swager, *Carbon nanotube/polythiophene chemiresistive sensors for chemical warfare agents.* Journal of the American Chemical Society, 2008. **130**(16): p. 5392-+.
25. Snow, E.S., F.K. Perkins, and J.A. Robinson, *Chemical vapor detection using single-walled carbon nanotubes.* Chemical Society Reviews, 2006. **35**(9): p. 790-798.
26. Heller, I., et al., *Identifying the mechanism of biosensing with carbon nanotube transistors.* Nano Letters, 2008. **8**(2): p. 591-595.
27. Lee, C.Y., et al., *Charge transfer from metallic single-walled carbon nanotube sensor arrays.* Journal of Physical Chemistry B, 2006. **110**(23): p. 11055-11061.
28. Lee, C.Y. and M.S. Strano, *Amine basicity (pK(b)) controls the analyte blinding energy on single walled carbon nanotube electronic sensor Arrays.* Journal of the American Chemical Society, 2008. **130**(5): p. 1766-1773.
29. Valcarcel, M., S. Cardenas, and B.M. Simonet, *Role of carbon nanotubes in analytical science.* Analytical Chemistry, 2007. **79**(13): p. 4788-4797.
30. Wu, Z.C., et al., *Transparent, conductive carbon nanotube films.* Science, 2004. **305**(5688): p. 1273-1276.
31. Zhou, Y.X., L.B. Hu, and G. Gruner, *A method of printing carbon nanotube thin films.* Applied Physics Letters, 2006. **88**(12): p. 3.
32. Salehi-Khojin, A., et al., *Sensitivity of nanotube chemical sensors at the onset of Poole-Frenkel conduction.* Applied Physics Letters, 2010. **96**(16).
33. Salehi-Khojin, A., et al., *On the Sensing Mechanism in Carbon Nanotube Chemiresistors.* Acs Nano, 2011. **5**(1): p. 153-158.
34. Salehi-Khojin, A., et al., *Nonthermal Current-Stimulated Desorption of Gases from Carbon Nanotubes.* Science, 2010. **329**(5997): p. 1327-1330.
35. Wang, H.C., Y. Li, and M.J. Yang, *Sensors for organic vapor detection based on composites of carbon nonotubes functionalized with polymers.* Sensors and Actuators B-Chemical, 2007. **124**(2): p. 360-367.
36. Zhang, T., et al., *Electrochemically functionalized single-walled carbon nanotube gas sensor.* Electroanalysis, 2006. **18**(12): p. 1153-1158.
37. Zhang, X.T., J. Zhang, and Z.F. Liu, *Conducting polymer/carbon nanotube composite films made by in situ electropolymerization using an ionic surfactant as the supporting electrolyte.* Carbon, 2005. **43**(10): p. 2186-2191.

38. Zhang, T., et al., *Poly(m-aminobenzene sulfonic acid) functionalized single-walled carbon nanotubes based gas sensor.* Nanotechnology, 2007. **18**(16): p. 6.
39. Steiner, W.E., et al., *Detection of a chemical warfare agent simulant in various aerosol matrixes by ion mobility time-of-flight mass spectrometry.* Analytical Chemistry, 2005. **77**(15): p. 4792-4799.
40. Tuovinen, K., H. Paakkanen, and O. Hanninen, *Determination of soman and VX degradation products by an aspiration ion mobility spectrometry.* Analytica Chimica Acta, 2001. **440**(2): p. 151-159.
41. Wittmer, D., et al., *Electrospray-Ionization Ion Mobility Spectrometry.* Analytical Chemistry, 1994. **66**(14): p. 2348-2355.
42. Wu, C., et al., *Separation of isomeric peptides using electrospray ionization/high-resolution ion mobility spectrometry.* Analytical Chemistry, 2000. **72**(2): p. 391-395.
43. Baumbach, J.I., et al., *Detection of the gasoline components methyl tert-butyl ether, benzene, toluene, and m-xylene using ion mobility spectrometers with a radioactive and UV ionization source.* Analytical Chemistry, 2003. **75**(6): p. 1483-1490.
44. Ross, S.K. and A.J. Bell, *Reverse flow continuous corona discharge ionisation applied to ion mobility spectrometry.* International Journal of Mass Spectrometry, 2002. **218**(2): p. L1-L6.
45. Rock, F., N. Barsan, and U. Weimar, *Electronic nose: Current status and future trends.* Chemical Reviews, 2008. **108**(2): p. 705-725.
46. Walt, D.R., *Fiber optic imaging sensors.* Accounts of Chemical Research, 1998. **31**(5): p. 267-278.
47. Dickinson, T.A., et al., *A chemical-detecting system based on a cross-reactive optical sensor array.* Nature, 1996. **382**(6593): p. 697-700.
48. Dickinson, T.A., et al., *Convergent, self-encoded bead sensor arrays in the design of an artificial nose.* Analytical Chemistry, 1999. **71**(11): p. 2192-2198.
49. Toda, K., et al., *Micro-gas analysis system for measurement of nitric oxide and nitrogen dioxide: Respiratory treatment and environmental mobile monitoring.* Analytica Chimica Acta, 2007. **603**(1): p. 60-66.
50. Bessoth, F.G., et al., *Towards an on-chip gas chromatograph: the development of a gas injector and a dc plasma emission detector.* Journal of Analytical Atomic Spectrometry, 2002. **17**(8): p. 794-799.

Chapter 2:

Degradation of 1-phenyl-1,2,3-butanetrione 2-oxime in Toxic Organophosphate Sensor

2.1 Introduction

2.1.1 Acetylcholinesterase and organophosphate poisoning

Of particular importance for detecting are acetylcholinesterase inhibitors, specifically toxic organophosphates (OP). For example, nerve agents such as Tabun, Sarin, Soman, VM, VG and VX are all examples of organophosphates which function as highly effective human acetylcholinesterase inhibitors. Organophosphate pesticides such as Malathion, Parathion and Dichlorvos, as well as carbamate pesticides such as Carbaryl and Pirimicarb also function as acetylcholinesterase inhibitors. These pesticides are generally designed to inhibit the enzymes of insects and other small pest and interact to a far smaller degree than the chemical weapon nerve agents previously mentioned.

Acetylcholine is a neurotransmitter produced at chemical synapses and is commonly found in neuromuscular and interneuronal transmission. Acetylcholinesterase is a crucial component in these synaptic transmission processes. Synapses are the nanometer-sized gaps which serve as communication junctions between neurons as well as from neurons to other non-neuronal cells. Electrical signals travelling through an individual neuron are transmitted across the synaptic cleft when acetylcholine contained in synaptic vesicles is released by the axon terminal of the transmitting cell. Acetylcholine then diffuses towards the dendritic spine at the opposite end of the gap, where it stimulates the acetylcholine receptors on the receiving cell, thus

continuing the electrical signal or changing the activity of the receiving cell. Finally, acetylcholine is rapidly hydrolyzed by acetylcholinesterase to remove it from the synaptic cleft and reset the junction for future transmissions [1]. Figure 2.1 depicts the acetylcholine neurotransmission process.

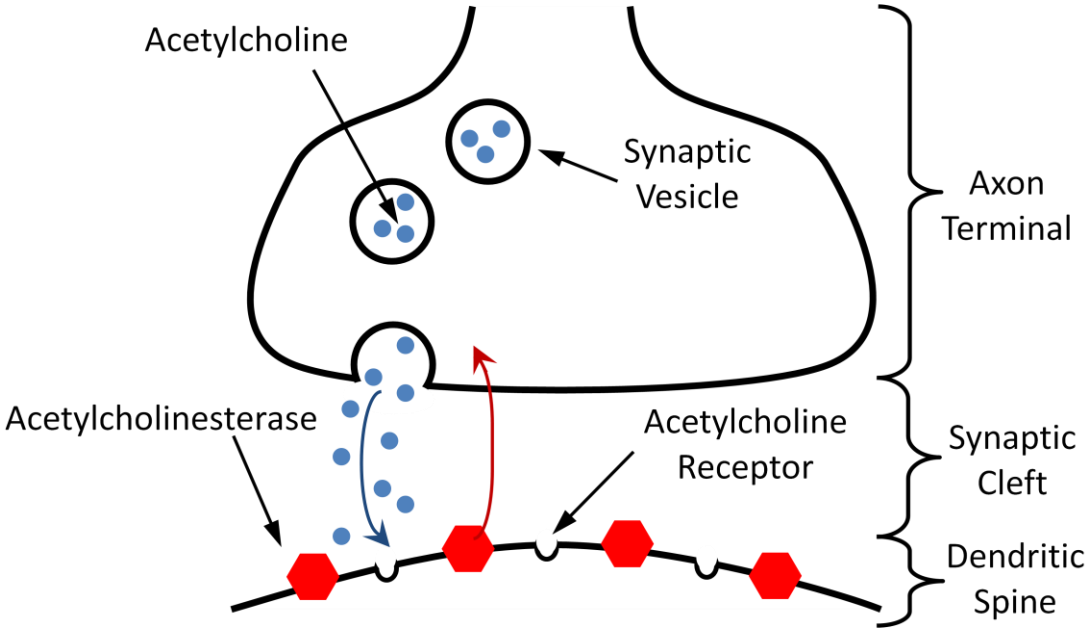

Figure 2.1: Normal operation of a cholinergic synapse. Acetylcholine is released by the axon terminal, triggers receptors on the dendritic spine, is hydrolyzed to choline and acetate, and then is re-absorbed.

It is this swift destruction of acetylcholine that allows for rapid intercellular communication. Acetylcholinesterase inhibitors derive their toxicity from their ability to bind to the enzymes' active site, thus preventing acetylcholine from being hydrolyzed. This in turn causes a buildup of acetylcholine in the synapse, which over stimulates receptors, and could eventually lead to a major disruption in normal nervous system activity. Poisoning from these inhibitor compounds predominately results in an over-stimulation of the parasympathetic nervous system as well as skeletal muscles causing spasms.

Acetylcholinesterase inhibition by organophosphates, especially nerve agents, is usually irreverible; however such poisoning can be reversed by introduction of a number of compounds based on the oxime functional group ($R_1R_2C=NOH$) [2]. Oxime-based antidotes compete with the acetylcholinesterase inhibitor to bind with the enzyme. Once the oxime compound is bound to the active site of the enzyme it can react with the inhibitor, rendering it harmless. This reactivates the enzyme and allows it to continue functioning normally. Many therapeutic oxime compounds such as Pralidoxime, Obidoxime, Methoxime, HI-6 and HLö-7 have been developed for the treatment of organophosphate poisoning based on this reaction mechanism [3].

2.1.2 Oxime based sensor chemistry

It has been known for quite some time of the selective reaction between toxic organo-phosphates and compounds containing oxime functional groups [4-6]. In 1968, the U.S. Army developed the M8 Portable Automatic Chemical Agent Alarm based on this selective oxime chemistry [7-10]. The device consisted of two major parts; the M43 detector unit where the reaction takes place and the M42 alarm unit which provided audible and visual signals for the operator, and combined the system weighed roughly 10 pounds. Detection took place by passing air through a basic aqueous solution containing the oxime compound, and measuring the resulting potential change with a silver working and platinum reference electrode [7]. A major limitation of this device lay in the stability of the oxime solution, which would have to be replaced every 12 hours to maintain sensor performance [11]. The additional maintenance this created, as well as the system weight, its semi-portable nature, inadequate battery capacity and its poor reliability eventually led it to being retired in 1996[7], having been replaced by the M43A1 ionization type sensor [8].

Transitioning this oxime detection method to a micro-fluidic environment allowed our research group to solve the problems of weight, reliability and poor battery life that limited the original device, while also creating a smaller, more portable system [12]. Within this micro-sensor, the vapor phase species to be detected diffuses from the high flow rate gas stream through a nanoporous polycarbonate membrane to the low flow rate (or static) aqueous phase. Once in the aqueous phase, the analyte reacts with 1-phenyl-1,2,3,-butanetrione 2-oxime (PBO). This reaction is highly selective towards reactive organophosphates and acid anhydrides due to the good leaving groups (X group) these compounds possess. An oxime-analyte complex is formed, and then quickly decomposes into several small molecules, including cyanide ions. It is these cyanide ions which are detected electrochemically by the change in solution potential. This reaction mechanism is shown in figure 2.2.

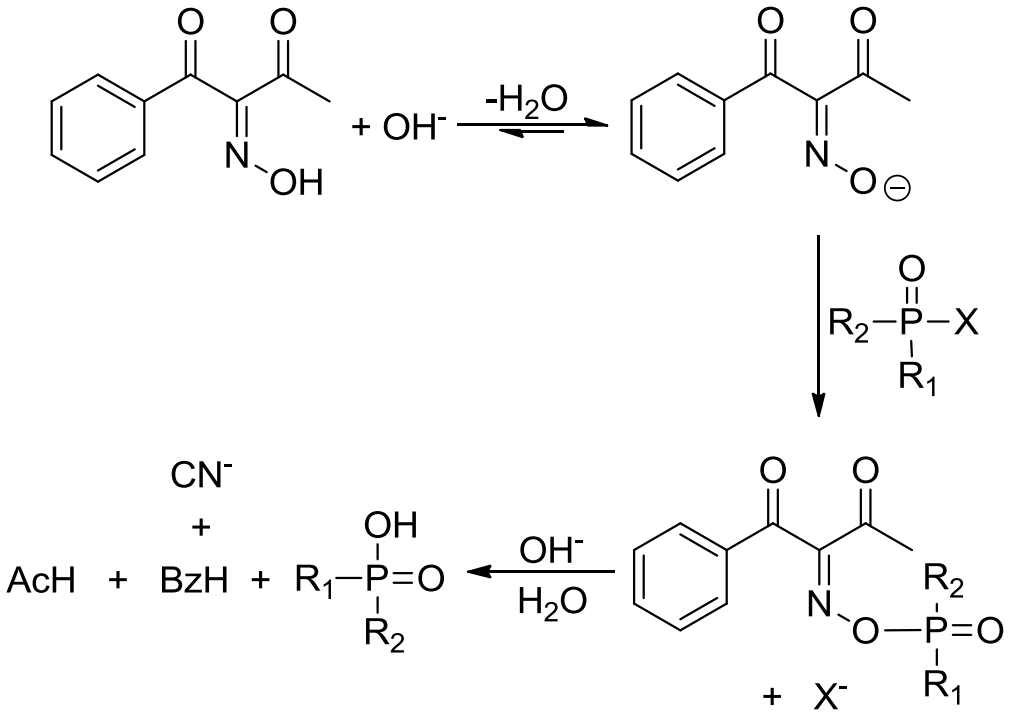

Figure 2.2: Reaction mechanism of an organophosphate analyte with PBO to produce a cyanide anion.

Although this microfluidic sensor eliminated most of the problems that plagued the M8 sensor, oxime solution stability remains an issue. Within the first 24 hours, the sensors' potential response to a fixed amount of analyte exposure decreases by approximately 50%. Under these conditions, the poor long term stability of the oxime solution severely limits the practical use of this type of detection mechanism. By studying the kinetics and mechanism of this degradation reaction, we can determine how to suppress this process.

2.2 Materials and experimental procedures

2.2.1 Chemical and materials

1-phenyl-1,2,3,-butanetrione 2-oxime (PBO, Sigma-Aldrich), acetic anhydride (99.5%, Sigma-Aldrich), acetonitrile (≥99.9%, Fisher), aqueous sodium hydroxide (5.0 N, Alfa Aeser), sodium chloride (>99.0%, Sigma-Aldrich). Solid phase micro-extraction (SPME) Fiber Assembly 85μm Polyacrylate Coating for Manual Holder (No. 57304, SUPELCO), SPME Fiber Holder for Manual Use (No. 57330-U, SUPELCO). The cyanide ion selective electrode (CN ISE) was purchased from Thermo Electron Co. and has a combined liquid-junction reference electrode. The surface of the CN ISE is periodically polished to remove any residue on the surface. In order to make borate buffer, $NaB_4O_7 \cdot 10H_2O$ (Fisher) is used to create a 25 mM solution, and the solution pH is then adjusted by adding highly concentrated NaOH (5.0 N, Alfa Aeser).

2.2.2 Solid phase micro-extraction procedure

Disposable 10ml glass vials were used for when performing the extraction. A gas chromatograph (GC) inlet septum is fitted into the top of the vial to provide a gas tight seal

which can be punctured by the solid phase micro-extraction (SPME) needle. At the appropriate time, 4 mL of solution is sampled into the 10ml vial and 1.25 g of NaCl (~23.8 wt%) is added to decrease the solubility of organics in solution. A small stir bar is also included in the vial to facilitate mixing. Once completely mixed, the vial is then allowed to equilibrate in a water bath at 40 °C for 15 minutes and a stir rate of 450 rpm. The polyacrylate fiber is cleaned by inserting it 3 cm into the GC injector port for 15 minutes. The GC injector is set to 280 °C, and the oven temperature is set at 250 °C to prevent contaminates from the cleaning from collecting in the column. Once the fiber has been cleaned, it is quickly removed, the needle depth readjusted to 2.8 cm, and then inserted into the sample vial. At this depth, the fiber is completely submerged in the solution. The extraction is takes place at 40°C for 50 minutes and a stir rate of 450 rpm. The SPME analysis was conducted on an Agilent 6890N gas chromatograph with a Restek RTX-OPPesticide column (30 m x 250 µm x 0.40 µm), coupled with an Agilent 5973N mass spectrometer. The SPME fiber is manually inserted 3 cm into the GC injector left for 4 minutes, then removed. Ultra-pure helium is used as the carrier gas at a constant flow rate of 1 mL/min. The GC is set for a splitless injection for 1 minute, after which the injector is purged with helium at 50 ml/min for the rest of the run. The injector assembly is set to 200 °C. The column temperature is slowly increased over the course of the run with the following programmed ramp up: The column oven is set to 35 °C for 5 minutes, then increased by 5 °C/min to 170 °C, then by 20 °C/min to 250 °C, and finally remaining at this temperature for 10 minutes. The mass spectrometer (MS) is set with a positive electrode bias. To avoid noise produced by atmospheric oxygen, nitrogen and carbon dioxide, the minimum m/z ratio was set at 45. The maximum m/z for the MS scan was set at 195; slightly higher than the molecular weight of the oxime at 191.

2.2.3 Beaker-scale experimental procedure

Macro-scale beaker cell experiments were performed by immersing the end of the CN ISE in at least 10 ml of the solution to be tested (in 60ml beaker). Unless specifically noted, the test solution will contain the oxime PBO at a 5mM concentration. An initial or baseline potential is measured for this solution. To evaluate the potential response performance of the test solution, 50 μL of a 21 mM solution of acetic anhydride (analyte) in acetone is injected into 10 mL of the test solution, resulting in a final acetic anhydride concentration in solution of 50 μM. Potential measurements are made once the solution has reached a steady-state (constant potential reading). During all beaker cell tests, the solution is continuously stirred at a constant rate to maintain uniform species concentrations throughout. The inner portion of this combined electrode is filled daily with a reference solution pre-made by the same company. The surface of the CN ISE is periodically polished with DI water and an abrasive strip to remove any residue on the surface of the outer (working) electrode. The analyte solution is freshly prepared each day to minimize the amount of acetic anhydride lost due to hydrolysis.

2.3 Results and discussion

2.3.1 Cyanide production kinetics

The apparent degradation of the oxime in the aqueous buffer solution manifest itself as an increase in both the initial (before analyte exposure) and final (after analyte exposure) potential of the system (figure 2.3). Both changes are a result of increased cyanide ion concentration in the solution caused by the breakdown of PBO. However, due to the logarithmic nature of the concentration versus potential relationship, the increase in cyanide ion concentration raises the

initial potential substantially more than the final potential, thus having the end effect of decreasing the overall magnitude of the sensor's potential response to an analyte.

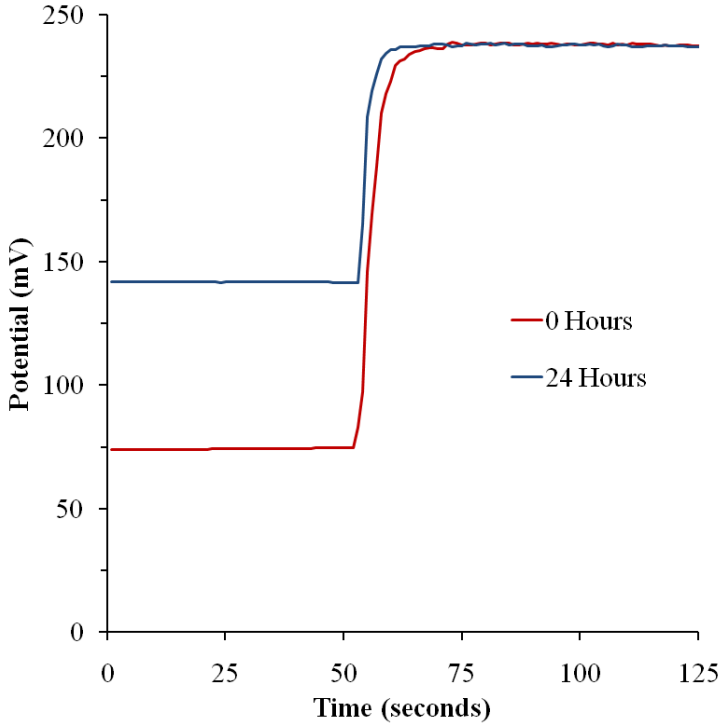

Figure 2.3: Potential response decrease over 24 hour period, as measured by CN ISE. 5 mM PBO in pH 10 borate buffer.

Potential measurements made with a cyanide ion selective electrode can be converted to cyanide ion concentration via a logarithmic relationship (The Nerst equation). This relationship can be affected by PBO concentration and solution pH, and was determined through additions of standardized amounts of aqueous cyanide solution. From this calibration data, we find that under most pH and oxime concentrations, the amount of cyanide produced over 120 hours is less than 100 μM, indicating that the change in PBO concentration caused by degradation is fairly negligible (<2%). Unless degradation is occurring more rapidly by other unknown mechanisms which do not produce cyanide ions, both hydroxide and PBO concentrations can be assumed to

be constant over the course of several days of degradation, and the rate of cyanide ion production can be determined by applying a linear fit to the cyanide ion concentration versus time data in an initial rate measurement type study (figure 2.4) [13].

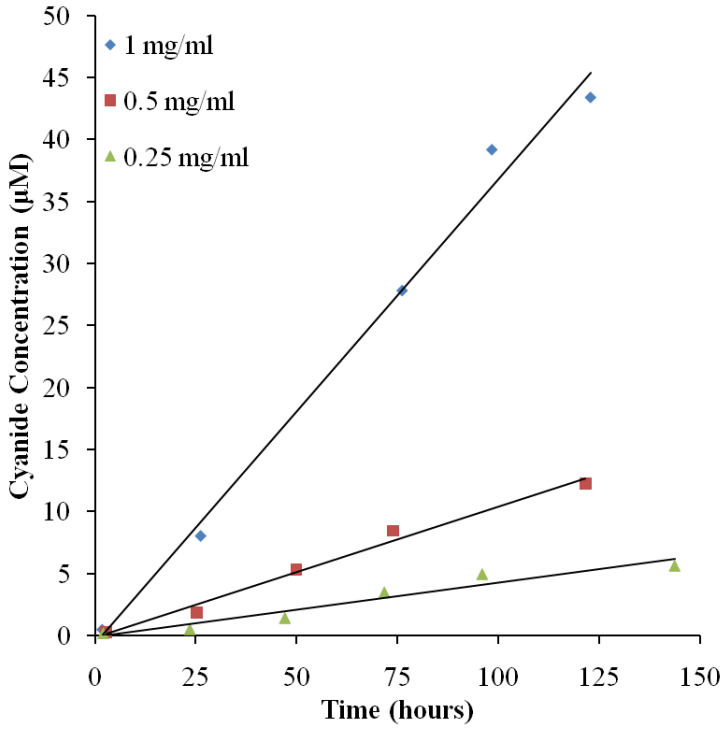

Figure 2.4: Cyanide ion concentration versus time for various initial PBO concentrations at pH 10.

Previous work on this oxime electrochemistry indicated that the optimal buffer pH for the aqueous solution was approximately 10 [14]. At this pH, the potential change, or response, of the detector to a fixed amount of analyte was maximized. Therefore, cyanide ion production was studied at pH values from 9 to 12 at PBO concentrations of 1, 0.5 and 0.25 mg/ml (5, 2.5 and 1.25 mM PBO). Plotting the rate of cyanide production over this range of pH values shows a clear increase in the degradation rate for increased hydroxide as well as PBO concentrations (figure 2.5).

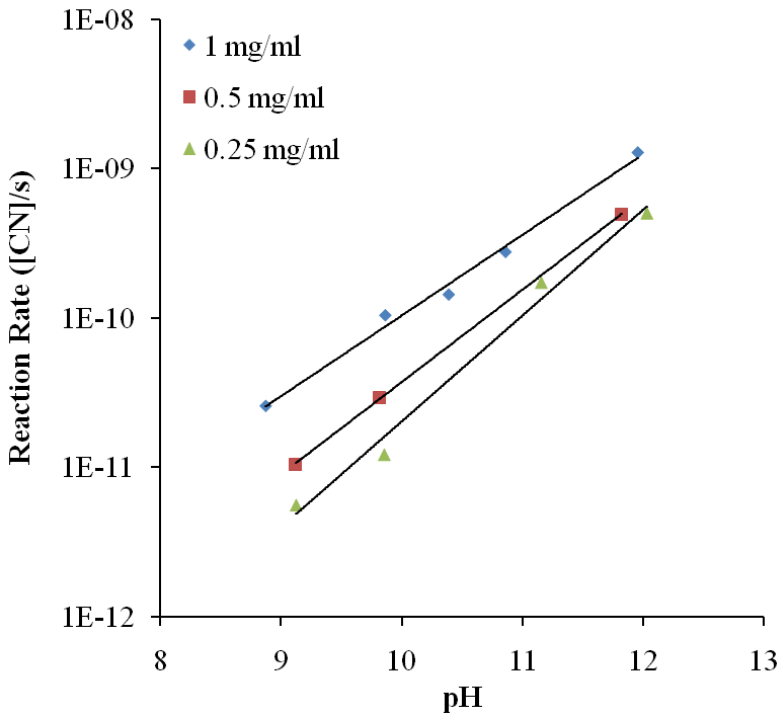

Figure 2.5: Cyanide formation rate versus pH for various initial PBO concentrations at pH 10.

A simple rate law governing the degradation process can then be created from this reaction rate data. Such a rate law would be of the form:

$$r_{CN^-} = k[\text{PBO}]^a[\text{OH}^-]^b \qquad 2.1$$

where r_{cn} is the rate of cyanide production in M/s, k is the rate constant, a is the reaction order of PBO, b is the reaction order of hydroxide, and [PBO] and [OH^-] are the concentrations of PBO and hydroxide in M, respectively. As the logarithmic form of equation 2.1 is a plane, by plotting ln[PBO] and ln[OH^-] versus ln(r_{cn}) and applying a planar fit to this data, the parameters a, b and k were determined and are given in table 2.1. A graphical depiction of the discrepancy between

measured and predicted cyanide production rate based on this planar fit reaction rate model is shown in figure 2.6.

Parameter	Value	Standard Error
k	7.52×10^{-6}	$18.2\times10^{-6} - 3.1\times10^{-6}$
a	0.62	±0.03
b	1.06	±0.14

Table 2.1: Kinetic rate law parameters for Equation 1

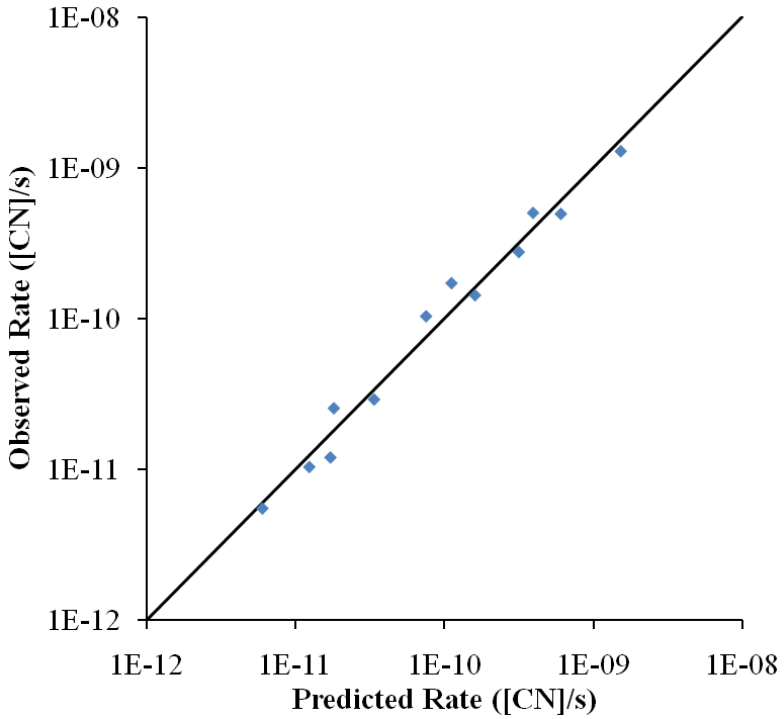

Figure 2.6: Experimentally observed rate versus predicted rate of cyanide formation calculated with simple rate law.

Figure 2.6 shows that the experimental data conforms well to the rate law model that was developed, with no individual outliers present. PBO concentration appears to be roughly 1st order, which would suggest that the degradation reaction involves only a single oxime molecule

or ion. However, the unusual sub-1st order for hydroxide ion concentration may indicate that the rate law used is too simplistic to model its contribution to the degradation reaction appropriately. Further understanding of the mechanism of PBO degradation requires identifying and monitoring of any other decomposition products in solution.

2.3.2 Solid phase micro-extraction analysis

To understand this decomposition mechanism better, solid phase micro-extraction was performed on the basic aqueous buffer solution to determine what other compounds were being formed. A polyacrylate (PA) coated fiber was used for all the extractions because its polar nature is ideal for capturing any organic acids or other polar compounds which may be produced during the degradation process. Unfortunately, the vapor pressure of hydrogen cyanide is too high for it to be significantly absorbed by the fiber. The small amount of cyanide that is absorbed by the fiber will not be retained by the GC column due to its low molecular weight (MW). As a result, hydrogen cyanide would not be separated from any other low MW compounds present and this makes it impossible to track the production of cyanide ions with this method.

To serve as a comparison to the SPME results for the aqueous oxime solution, PBO dissolved in an organic solvent was directly injected into the GC, thus avoiding any degradation most likely caused by the formation of the oxime anion. Acetonitrile was found to be the ideal organic solvent for dissolving the oxime, as it gave the "cleanest" spectrum with the fewest extraneous peaks. The first thing to note about this spectrum is that PBO is eluted in 2 peaks, possibly due to some sort of oxime dimer being formed, although MS results do not show any fragments of PBO dimer present. It is also important to note that benzoic acid, benzoyl cyanide

and acetic acid also appeared in this spectrum. These compounds may have been originally present in the solid PBO powder; however it is also possible that they were created by the oxime spontaneously decomposing in the high temperature environment of the GC injector assembly. Other compounds of note are a large peak most likely corresponding to toluene as well as several small nitrile peaks, most likely related to the solvent used. Because this was a direct injection of solution, the MS could not be turned on until 3 minutes into the run, to avoid exposing the filament to the large initial solvent peak. Therefore, compounds eluted within the first 3 minutes of the run were not monitored.

To create a background spectrum, SPME was first performed on the basic aqueous borate buffer (pH 10) without PBO present to determine what contaminants may be present. Several compounds identified as 1,2-benzenedicarboxylic acid esters were found, as well as benzophenone, diphenylamine and diphenylether. Several peaks identified as benzene and one as toluene were also found. These compounds will be ignored when analyzing the SPME results, unless their elution times differ significantly from the background spectrum. Additionally, these contaminant peaks are also substantially smaller when oxime is present in the aqueous solution due to competitive absorption to the SPME fiber, and it is highly unlikely that these contaminants will mask or interfere with any degradation products.

When SPME was performed on the basic aqueous buffer with oxime, the following major identifiable peaks excluding contaminants were found (table 2.2).

Compound	Elution Time (min)	Peak Area(×105)
acetic acid	4.09	14
toluene	5.44	540
acetophenone	19.25	12
benzoic acid	20.38	150
benzoyl cyanide	20.54	275
1-phenyl 1,3-butadione	27.92	92
2-isonitrosoacetophenone	28.35	6
PBO minus oxygen	29.30	4
PBO (1st peak)	34.57	1665
PBO (2nd peak)	35.05	566

Table 2.2: Identifiable peaks (ignoring known contaminants) from SPME of a 5 mM solution of oxime in aqueous buffer (pH 10) performed 1 hour after solution preparation.

Similar to the spectrum from the direct injection of oxime, we find acetic acid, benzoic acid, benzoyl cyanide, and two PBO peaks. We also find acetophenone, 1-phenyl 1,3-butadione, 2-isonitrosoacetophenone, and a compound whose weight of 175 corresponds to that of oxime minus an oxygen atom. It is reasonable to believe that the compound with a weight 175 is the oxime in which the hydroxyl group is replaced by a hydrogen group, which would be 1-phenyl 1,3-butadione 2-imine. If this is the case, 1-phenyl 1,3-butadione, 2-isonitrosoacetophenone and 1-phenyl 1,3-butadione 2-imine are all PBO fragments where a portion of the molecule is replaced with one or more hydrogen atoms. It is unknown whether these compounds were all present in the aqueous solution or whether they were created from an intermediate degradation product that decomposed in the GC.

Acetophenone on the other hand is not likely to have formed due to a simple substitution reaction. The most probable route of formation for this compound is shown in figure 2.7.

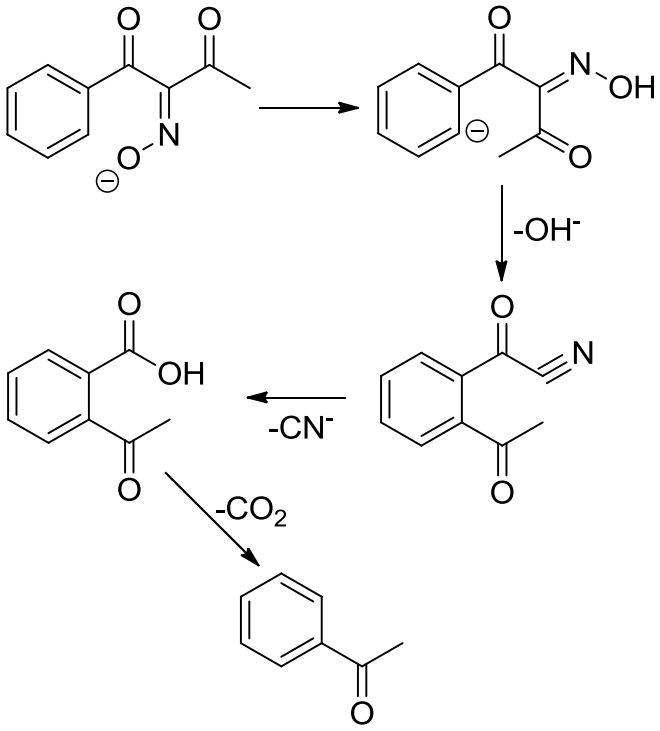

Figure 2.7: Possible mechanism for the formation of acetophenone found in SPME analysis.

In the aqueous solution, the oxime anion removes a proton from the ortho position of the benzene ring. This type of rearrangement has been postulated before for similar phenyl containing oximes [15, 16]. The negatively charged carbon on the benzene ring then attacks the carbonyl carbon transferring the acetyl group over to this location. The final step which occurs in the aqueous solution is the release of cyanide through hydrolysis to form the carboxylic acid. This compound is then absorbed via SPME and upon injection into the GC, is decarboxylated by pyrolysis to form acetophenone.

Ford and Watts performed a detailed investigation of the reaction mechanisms of PBO with the organophosphate isopropyl methylphosphonofluoridate, otherwise known as the nerve

agent Sarin. They found that in addition to the type of reaction shown in figure 2.2, a secondary reaction was also taking place [17]. This secondary mechanism was proposed in order to account for the larger than 1:1 ratio of oxime to organophosphate consumed in the reaction at pH values roughly less than 8. The overall mechanism given in their paper is shown in figure 2.8.

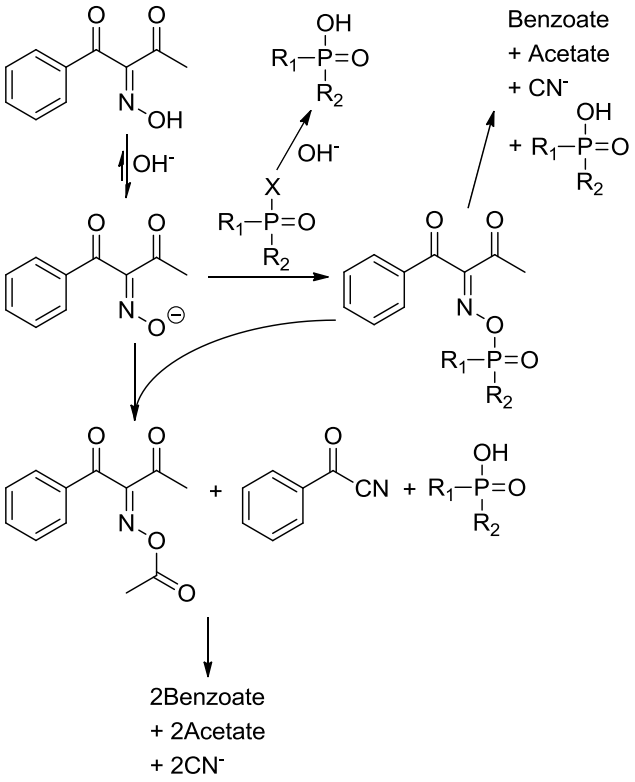

Figure 2.8: Expanded reaction mechanism of PBO with a typical reactive organophosphate.

In this secondary reaction, the oxime-phosphate intermediate complex is attacked not by a hydroxide ion but instead by another oxime anion. This attack takes place on the carbonyl carbon of the acetyl group, yielding an acetyl-oxime complex and benzoyl cyanide, as well as the organophosphate acid. Both the acetyl-oxime complex and benzoyl cyanide hydrolyze further to produce the same products as the main reaction mechanism.

Acetic acid, benzoic acid, and benzoyl cyanide are products or intermediates in the reaction mechanism seen in figure 2.8, and could all possibly be involved in a similar mechanism for the degradation of PBO. However, benzoyl cyanide present in the solid oxime or created during the degradation would be quickly hydrolyzed to form benzoic acid; therefore most of the benzoyl cyanide eluted most likely originated from the spontaneous decomposition of the oxime in the GC injector inlet. The data from the direct injection of oxime would indicate that this spontaneous decomposition is also responsible for some of the acetic acid and benzoic acid seen, as well as most of the toluene.

Monitoring the oxime degradation over a period of several days we see the following increasing (Figure 2.9a) and decreasing (Figure 2.9b) trends in the peak area of the compounds detected via SPME GC-MS.

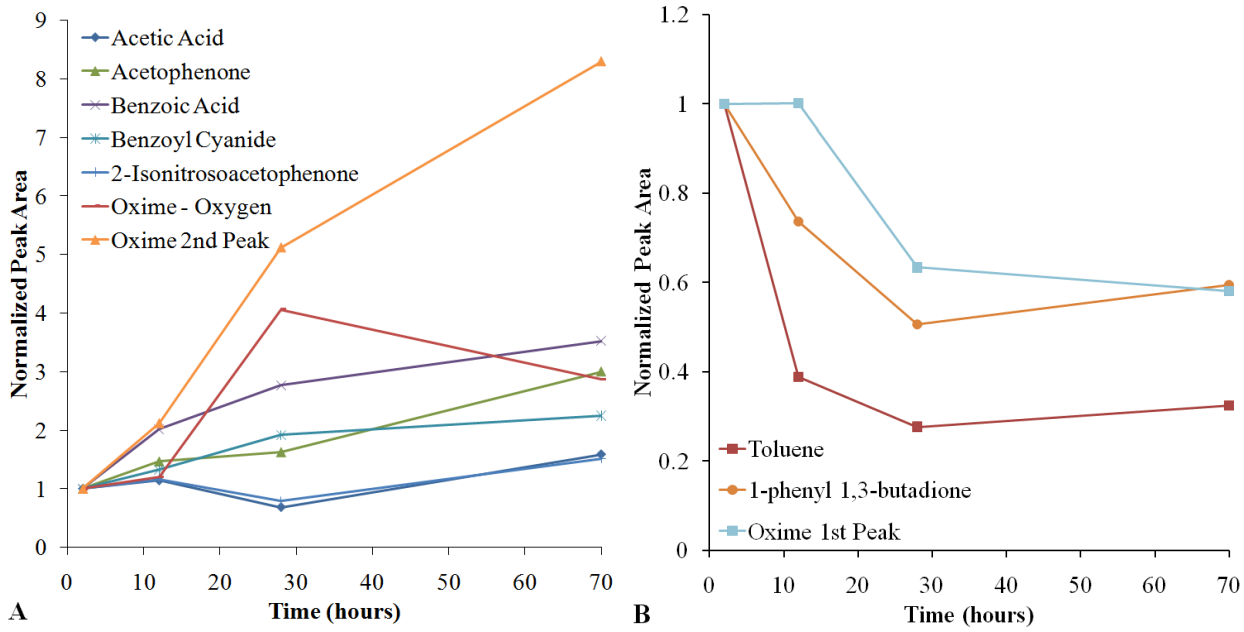

Figure 2.9: Peak area trends over time for various compounds found through SPME. (A) Increasing peak area trends. (B) Decreasing peak area trends. Each curve is normalized to initial peak area.

As expected, the first oxime peak decreases over time, however the second oxime peak increases dramatically. It is possible this is due to further oxime dimerization while in the aqueous solution. The roughly 40% decrease in the oxime peak area is much larger however than the 0.1% decrease predicted by the electrochemical measurements of cyanide production. Such a large reduction in the amount of PBO present in solution would be visibly noticeable as a decrease in the intensity of the yellow color of the solution. However, this color change in the solution was not observed, even at the highest pH conditions. Therefore this peak area decrease is most likely due to matrix effects in the polyacrylate fiber. The remaining compounds, with the exception of 1-phenyl 1,3-butadione, increase over time, indicating that they could possibly be degradation products of PBO. In the case of acetic acid, because of its low molecular weight, the column does not retain this compound very well. This leads to the acetic acid peak being extremely susceptible to variability in the manual injection process of the SPME fiber, with elution times varying by up to a second. This could explain the lack of a strong increasing trend in the acetic acid peak area seen. In general though, peak area cannot be easily correlated with aqueous solution concentration, and therefore only an overall increasing or decreasing trend can be noted.

Liquid-chromatograph coupled with mass spectrometry (LC-MS) was used to confirm the presence of some of the PBO degradation products. Using standard solutions of these two compounds, this analytical technique was able to detect both benzoic acid and 2-isonitroso acetophenone, confirming the SPME GC-MS results with respect to the presence of these compounds. Identification of additional degradation products would require standard solutions which were not available at the time this analysis was performed.

2.3.3 Oxime degradation mechanism

The rearrangements of α-oximino ketones have been studied in great deal. It has been found that in the aqueous phase, these compounds are known to undergo Beckmann rearrangements or fragmentations [18, 19]. However, these reactions usually occur in acidic conditions or with the help of chlorinating agents such as phosphorus pentachloride, which replace the hydroxyl group of the oxime with chlorine to act as a better leaving group. Studies of the gas phase rearrangements of α-oximino ketone anions in mass spectrometers have shown that these compound breakdown predominantly by the oxime anion attacking its own ketone carbon [15]. With a diketo-oxime such as PBO, this mechanism is even more likely to occur, and in an aqueous environment, would likely take place via a mechanism similar to that in figure 2.10.

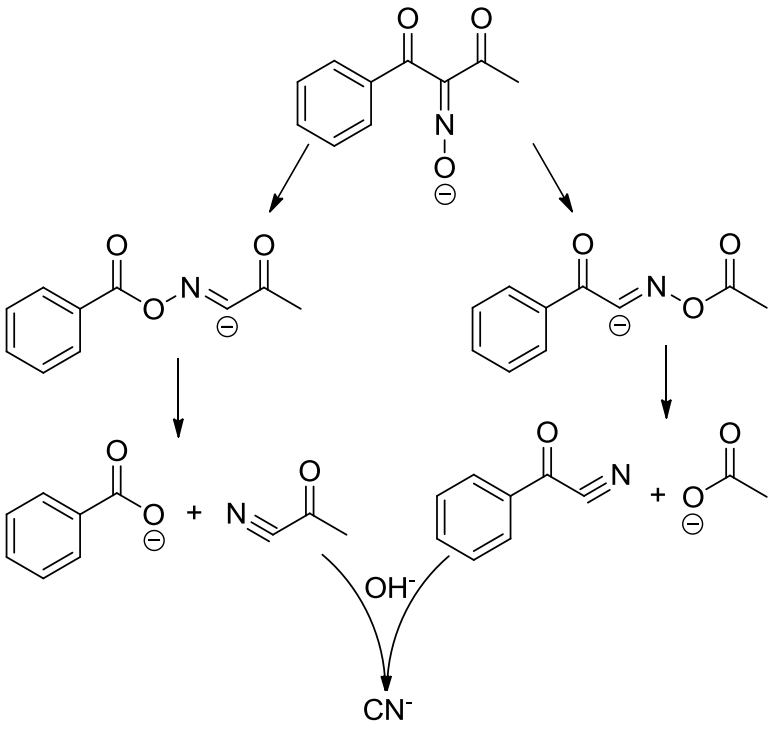

Figure 2.10: PBO rearrangement via anionic attack of either carbonyl carbon and subsequent decomposition and hydrolysis to produce cyanide ions.

The oxime undergoes rearrangement to form a charged intermediate which then breaks up to form a carboxylic acid and a nitrile. These nitriles will be quickly hydrolyzed to form their corresponding acid and a cyanide ion. The pathway which results in the formation of benzoyl cyanide is most likely the preferential one, as the acetyl carbon is more reactive than the benzoyl carbon. This is confirmed by the preferential hydrolysis of acetic benzoic anhydride [20], as well as in beaker scale work used to develop the PBO based detection chemistry [14]. Of the oximes tested in these beaker scale studies, it can also be seen that when comparing acyl groups in keto oximes, the benzoyl group results in a lower reaction rate with the analyte compared to the equivalent oxime with an acetyl group. Additionally, the two diketo-oximes provided a lower initial potential than the monoketo-oximes, which allows for a larger potential change to an analyte. The diketo-oximes provide a larger conjugated structure with which to distribute negative charges in, leading to a more stable anion [20]. This can be seen by comparing the K_a values of mono and diketo-oximes. The K_a for PBO is more than an order of magnitude lower than that of a comparable mono-keto oxime such as *anti*-pyruvic aldehyde 1-oxime (PAO), indicating the anion PBO has a lower affinity for protons than PAO [14]. It is clear that resonance within the benzyl group delocalizes the partial positive charge on the adjacent carbonyl carbon, lowering its reactivity towards nucleophiles. It is also this charge delocalization that results in the reaction in figure 2.7, which must also be a contributing degradation mechanism.

The affect of the addition of ethanol to the aqueous PBO solution was also studied briefly. Ethanol has been previously used by some researchers to aid in the preparation of aqueous oxime solutions by increasing oxime solubility. For example, Ford and Watts used a 5% ethanol aqueous solution to dissolve PBO for their kinetic studies [17]. They found that although ethanol did not initially react with the PBO anion, it was involved in subsequent

reaction steps. Studies conducted with the cyanide ion selective electrode found no noticeable change in the rate of cyanide production for ethanol concentrations from 5 – 20% (by volume). However, SPME studies of an aqueous PBO solution containing 5% ethanol by volume show a significant production ethyl benzoate which is proof of the preferential hydrolysis mentioned previously (figure 2.11).

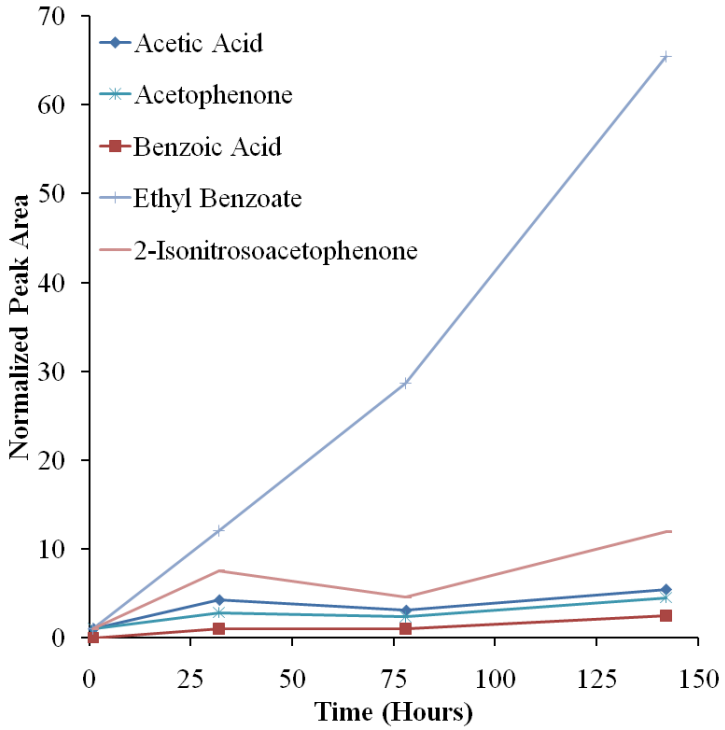

Figure 2.11: Increasing peak area trends from SPME performed on 5% ethanol aqueous PBO solution. Each curve is normalized to initial peak area.

Due to the addition of an organic solvent, 0.5 g of NaCl were added during the preparation of the sample instead of 1.25g in order to prevent the formation of a secondary liquid phase composed of ethanol. Consequently, these SPME results cannot be quantitatively compared to the SPME results in figure 2.9. However it can clearly be seen from figure 2.11 that ethyl benzoate is a major product of the degradation reaction, while ethyl acetate was not

detected at all. Benzoyl cyanide and benzoic acid were detected in diminished quantities, most likely a result of the nitrile preferentially reacting to form the ester versus the acid.

Finally, it is reasonable to believe that even though the hydrolysis of the acyl cyanides produced in figure 2.10 occurs rapidly [21], there is still a possibility that some of these molecules will react with PBO anions (figure 2.12).

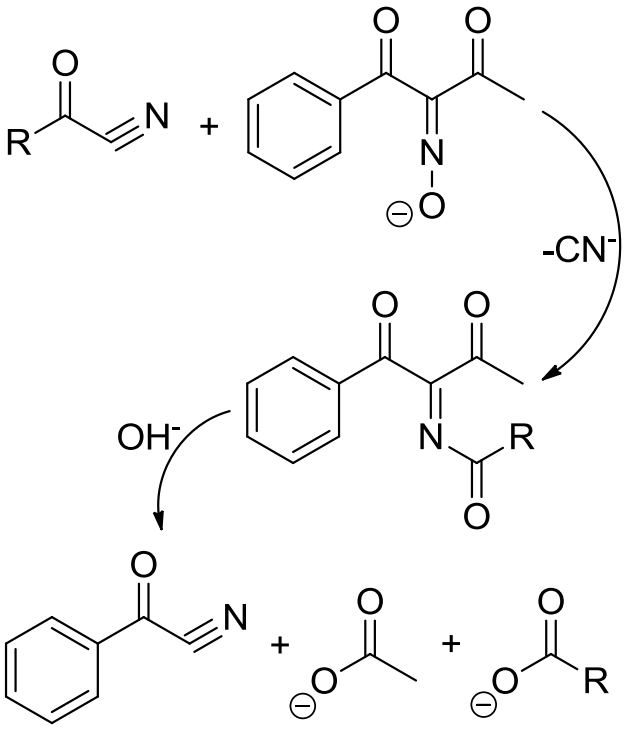

Figure 2.12: PBO anion attack on an acyl cyanide molecule.

In the figure above, R is either a phenyl or methyl group. The oxime anion attacks the carbonyl carbon of the nitrile and forms an acyl-oxime complex. This complex then decomposes with the help of hydroxide ions to form benzoyl cyanide, acetic acid and either a benzoic or acetic acid molecule, depending on the initial acyl cyanide in the reaction. Benzoyl cyanide is produced due to the reactivity of the acetyl group leading it to be preferentially attacked by the hydroxide ion.

2.3.4 Oxime degradation suppression

Although the PBO degradation mechanisms postulated in the previous section have not been fully confirmed, they all suggest that the decomposition process originates with the oxime anion. To prevent this degradation from occurring, it is obvious that the oxime must not be allowed to dissociate until the moment it is needed in the sensor. This will be accomplished by initially dissolving PBO in an organic solvent, then combining this organic oxime solution with the basic aqueous buffer solution just prior to use in the sensor. The oxime anion will then be formed at this point and would be available for subsequent reaction with any organophosphate analytes. An effective organic solvent should prevent dissociation of the oxime, be miscible in the aqueous buffer, have a minimal affect on sensor performance and be able to significantly concentrate the oxime to prevent drastically increasing the total volume of solution needed.

Rough test indicated that in general, PBO is approximately 400 – 500 times more soluble in organic solvents then in the basic aqueous buffer solution currently used, with the exception of ethylene glycol. A concentrated organic PBO solution not only minimizes the increase in total solution needed, it also reduces the organic solvent to aqueous solvent ratio needed to reach the standard PBO concentration of 5 mM needed in the final mixed solution used for detection. This is helpful in minimizing the interference of the organic solvent on the electrochemical performance of the system.

Each organic solvent was first tested in beaker scale experiments to effectively screen a variety of compounds before use in the actual microfluidic sensor. The organic solvents were first evaluated on their ability to suppress the degradation of PBO. They were also assessed for the degree to which they interfere with the cyanide selective electrode or the oxime/analyte reaction chemistry. PBO was initially dissolved in the organic solvent at a 50 mM concentration.

These organic oxime solutions were then mixed with the basic aqueous buffer at t = 0 or 24 hours after being prepared. The mixing is done at a 9:1 ratio of aqueous buffer to organic oxime solution, respectively. This results in a final PBO concentration of 5 mM for all test solutions. The 9:1 ratio is chosen rather arbitrarily for convenience; at higher ratios, the effects of the organic solvent on the electrochemistry decrease; however if these two solutions are to be mixed on-chip, it becomes increasingly difficult for a microfluidic device to control liquid flowrates at more extreme ratios.

Once the organic oxime solution has been mixed with the basic aqueous buffer solution, the potential (as measured with the CN ISE) is allowed to equilibrate. At this point, the analyte is injected into the beaker cell and the potential is again allowed to equilibrate. The difference in measurements is the potential response (ΔE) of the system to the analyte and is a critical parameter in judging sensor performance. Table 2.3 shows the effects of the various solvents on ΔE measured in the beaker cell experiments. In the "no organic solvent" case, PBO is directly dissolved in the buffer at t = 0 hours at a concentration of 5 mM. Analyte is then injected into the solution at t = 0 or 24 hours and the resulting ΔE is measured as usual. As mentioned previously, degradation manifests itself as a decrease in ΔE over time. Compared to the "no organic solvent" case, all organic solvents tested greatly suppressed PBO degradation. Electrochemical interference manifests itself as a decrease in ΔE compared the "no organic solvent" case at t = 0 hours. Most solvents tested do interfere with the electrochemistry to varying degrees, except for ethylene glycol, which may have a slight enhancing effect on ΔE. It is clear from this data that the best solvents for use in further experiments are ethylene glycol and ethanol. The differences in ΔE for each solvent can be clearly seen in figure 2.13, with ethylene glycol and ethanol closest to the original "no organic solvent" system.

Organic Solvents	0 Hour ΔE (mV)	24 Hour ΔE (mV)	Decrease in ΔE (mV)
No Organic Solvent	154	92	62 ± 9
Ethylene Glycol	157	145	11 ± 8
Ethanol	150	149	1 ± 10
Acetone	145	141	5 ± 10
Acetonitrile	113	113	0 ± 5
DMSO	74	66	9 ± 14

Table 2.3: Effects of various solvents on beaker cell potential response (ΔE).

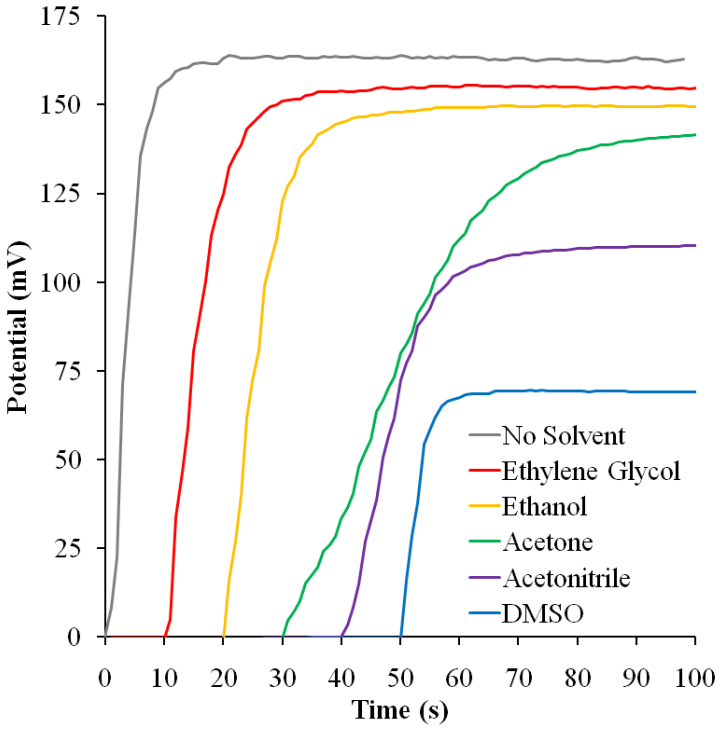

Figure 2.13: Typical potential response curves for each solvent tested. Curves normalized to baseline potential. All test at pH 10.

Sample response curves of each solvent tested at t = 0 hours (as well as t = 24 hours) show a decrease in the slope of the potential response curve during the reaction in comparison to

the “no organic solvent” case (figure 2.13). Acetone in particular has a quite a detrimental effect on the rate of potential increase, indicating that either acetone interferes greatly in the oxime-analyte reaction or the subsequent mass transport of CN^- to the electrode. Although ethylene glycol and ethanol do not decrease the rate of cyanide formation as much as acetone, this aspect of solvent – electrochemistry interaction was investigated further during the micro-sensor tests. Additionally acetone was not considered as a possible solvent due to its incompatibility with the polycarbonate sensor material.

Long term degradation studies were conducted using ethanol as the organic solvent to suppress PBO degradation. These experiments showed that the beaker scale potential response using ethanol dropped roughly 35 mV during the course of 8 days (figure 2.14). For comparison, the decrease in potential response when using the aqueous PBO solution (without organic solvent) was 62 mV after only 1 day since being prepared.

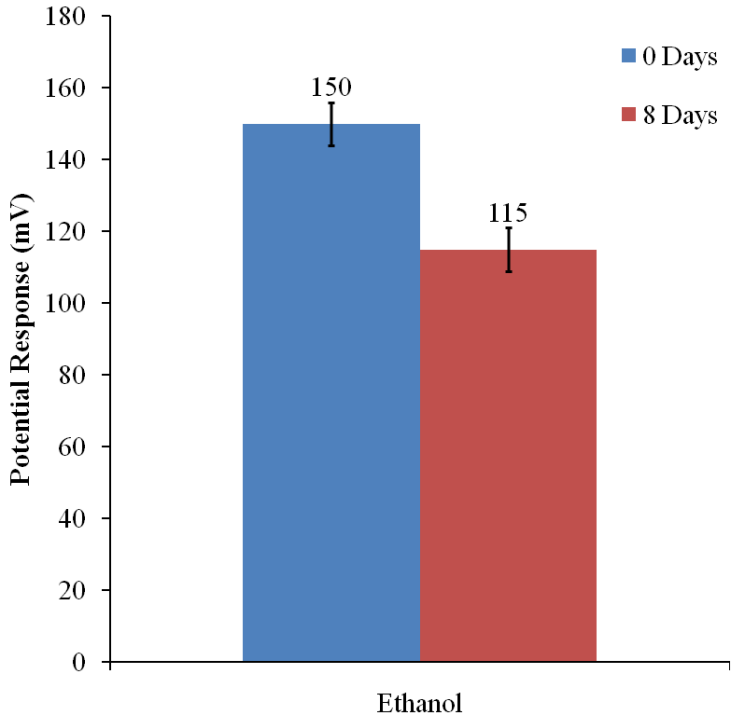

Figure 2.14: Comparison of beaker-scale potential response between freshly prepared and 8 day old oxime/ethanol solution.

2.3.5 Oxime micro-sensor and integrated micro-mixer performance

The final step in evaluating these organic solvents is to test their impact on the electrochemical performance of the actual micro-fluidic sensor platform for this organophosphate detection chemistry. Based on the results from the previous section, only ethanol and ethylene glycol were chosen for further study in the oxime micro-sensor. This micro-sensor is constructed entirely from polycarbonate, and consists of a gas and liquid channel separated by a nano-porous membrane. Gold sputtered on the liquid side of this membrane serves as electrodes. Detailed micro-sensor fabrication and testing procedures will be given in the subsequent chapter. The micro-sensor can then be connected to the auto-injector of a GC system to accurately and reproducibly expose the device to "pulse" of analyte in an inert carrier gas stream. This system allows for more precise assessment of the effects of the organic solvents on the sensors electrochemical performance.

Micro-sensor performance was evaluated by manually mixing freshly prepared organic oxime solution with the basic aqueous buffer in a 9:1 ratio. This mixture was then introduced to the micro-sensor with a syringe and allowed to remain static in the device during testing to maximize detection performance. The micro-sensor was exposed to a "pulse" on acetic anhydride and the resulting potential change was measured. This signal was then averaged and then differentiated to produce the data shown in figure 2.15.

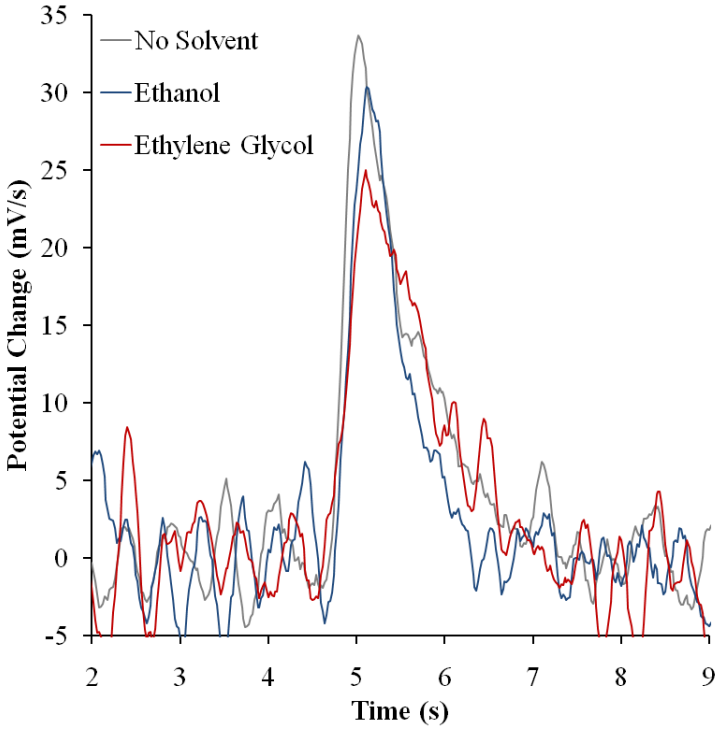

Figure 2.15: Typical differentiated signal from micro-sensor when using ethanol, ethylene glycol or no organic solvent.

These results represent the rate at which cyanide ions are being produced at the gold electrode near the gas-liquid interface. As one can see, the presence of an organic solvent lowers the maximum rate of cyanide production. On average, both ethylene glycol and ethanol decrease the rate of cyanide formation compared to the "no organic solvent" case by roughly 30% and 20%, respectively. The use of ethylene glycol also significantly increases the total detection time, which is seen when comparing the average peak width (at half maximum height) of the differentiated signals. Peak width is 0.86 s for ethylene glycol, compared to 0.54 s for ethanol, and 0.61 s for the "no organic solvent" case. It is clear from these studies that ethanol is the optimal solvent for use with this oxime based micro-sensor, as it will have minimal impact on performance while sufficiently suppressing PBO degradation.

All previous tests relied on the organic oxime solution being mixed with the basic aqueous buffer on the macro scale. This assured that the solutions were well mixed before being exposed to an analyte sample and ensured reproducible results. Mixing in the current micro-sensor design is rather poor, due to the laminar nature of the fluid flow. In order for the final micro-fluidic system to effectively mix these two solutions, a micro-mixer unit was design which would easily integrate with the existing micro-sensor device.

Micro-mixers can be divided into two major categories: passive mixing devices which rely solely on the energy provided by the flow pressure, and active devices which utilize an external energy input to operate [22]. However, design constraints of our micro-fluidic system require a simple, passive mixer unit. Examples of passive mixers include simple T-type contact designs [23], cross type fluid focusing [24], multiple parallel lamination [25, 26], repeated stream folding and flattening [27], forced fluid contact (Tesla structures) [28], ridged channel walls [29, 30], and Dean vortices in spiral mixers [31]. For the sake of simplicity and ease of fabrication, a serpentine channel type mixer was chosen. Such a design takes advantage of diffusive mixing by substantially increasing mixer length, which increases the contact time of the two solutions and give sufficient time for complete diffusive mixing to occur.

All previous micro-sensor test were conducted at zero (or static) liquid flow rate to maximize cyanide ion accumulation and potential response. Since the mixer and sensor both benefit from lower liquid flow rates, the integrated mixer - sensor system should have a maximum operational liquid flow rate, above which the performance of the device decreases considerably. To evaluate the effectiveness of the micro-mixer it is only necessary to compare the sensor performance of the integrated device to the original device with the two solutions pre-mixed externally. A syringe pump is used to dispense the solutions, at a 10:1, basic aqueous

buffer to organic oxime solution flow rate, respectively. For the integrated mixer test, a flow rate ratio of 10:1 gives flow rates of 5.0 μL/min and 0.5 μL/min for the aqueous solution and organic solution, respectively. Due to equipment size constraints, the syringe pump cannot be run in conjunction with the automatic injector of the GC. Therefore a second syringe pump will be used to supply the analyte vapor to the sensor. The results of this comparison test show that the integrated micro-mixer was effective in completely mixing the two solutions (figure 2.16).

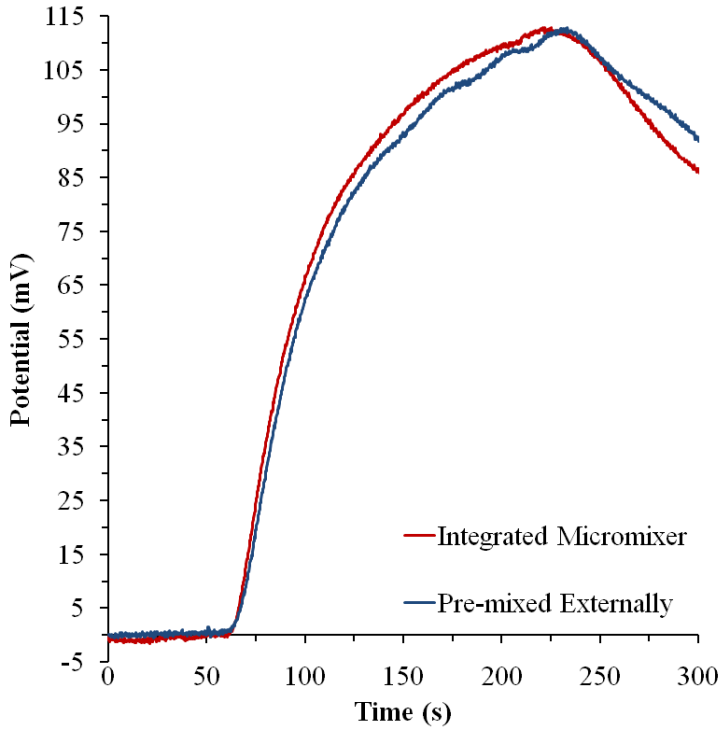

Figure 2.16: Performance of micro-sensor with integrated micro-mixer in comparison to micro-sensor with mixing performed externally. In both cases, the total liquid flow rate is 5.5 μL/min and the gas flow rate was 1 ml/min. The gas is 100 ppb acetic anhydride, and flow is turned on at t = 50 s and off at t = 200 s.

In practice the mixer will not be used in this manner. When the micro-sensor is exposed to a vapor sample, the liquid will remain static, ensuring the maximum possible potential

response. While this takes place, stationary fluid in the serpentine micro-mixer should have more than enough time to mix completely via diffusion. Between exposures, when the sensor must be flushed out to remove cyanide build up, the fully mixed fluid is transferred to the micro-sensor. The fluid in the mixer is replaced with the organic and aqueous solutions which will again mix (at static flow rate) while the sensor operates.

2.4 Conclusions and recommendations

The oxime based micro-sensor our group has developed to selectively detect toxic organophosphates and other reactive acid anhydrides suffers from a long term stability issue. In the basic, aqueous buffer solution, the dissolved oxime PBO slowly decomposes over a period of several days. This decomposition process releases cyanide ions, for which a rate law of $r_{cn} = 5\times10^{-7}[PBO]^{0.6}[OH^-]^{0.6}$ was determined. However this rate law is too simplistic to fully model the degradation kinetics and better understanding of the reaction mechanism is required to generate a more accurate rate law. Solid phase micro-extraction performed on the aqueous oxime solution shows several other possible degradation products, including acetic acid, acetophenone, benzoic acid, benzoyl cyanide, 1-phenyl 1,3-butadione, 2-isonitrosoacetophenone and 1-phenyl 1,3-butadione 2-imine. These SPME studies also show general increasing concentration trends over time for all compounds except for oxime, toluene and 1-phenyl 1,3-butadione. Judging from the compounds found through SPME, degradation most likely occurs via a rearrangement reaction where the PBO anion attacks itself. The negative oxygen of the oxime group either attacks one of the two carbonyl carbons, or the ortho position of the benzene ring, and in the process eventually produces a cyanide ion.

Dissolving the PBO in an organic solvent proved to slow the degradation process significantly. The use of the organic solvent prevents the oxime anion from forming and stops hydroxide ions from attacking it. This organic solution could be added, when needed, to the aqueous buffer for use in the sensor. The aqueous to organic solutions were mixed in a 9:1 ratio which minimized the amount of organic solvent while maintaining the original 5 mM concentration of oxime. From the beaker scale test performed, it was determined that ethanol and ethylene glycol were the best solvents based on their ability to prevent degradation as well as their compatibility with the electrochemical detection method. Examining the solution potential and the rate of change in solution potential in response to a pulse of analyte we find that both ethanol and ethylene glycol lower the rate of formation of cyanide ions. Total response time is also slightly increased when using ethylene glycol, most likely due to mass transport effects. These results indicate that ethanol is the optimal solvent for use with the existing oxime microsensor.

For the micro-sensor to be used in a real world application, it is necessary for the organic and aqueous solutions mixing to be done automatically and with the whole process occurring on the micro-scale. A serpentine channel mixer was designed to seamlessly integrate with the current micro-sensor using the same polycarbonate material and fabrication techniques. Such a mixer works by increasing contact time between the two solutions for diffusion, and operates effectively at very low flow rates. The response from integrated micro-sensor/mixer system was shown to be identical to the case where mixing is done externally when operated at a total liquid flow rate (10:1 aqueous to organic ratio) of less than 5.5 μL/min.

The oxime solution could be directly analyzed using GC-MS if the non-volatile borate buffer salt is replaced with a volatile buffer salt such as ammonium formate buffer. This would

not only allow the use of the automatic injector assembly of the GC, it may reveal compounds which could not be appreciably absorbed by SPME fibers. It may also be useful to evaluate other types of GC columns to ensure that species are not being co-eluted or reacting with the column stationary phase.

Optical analysis methods can be used to track the concentration of both oxime and cyanide in solution. The PBO anion, which is found in basic aqueous solutions, absorbs ultraviolent (UV) light at approximately ~260 nm, however this absorbance peak is broad and extends into the visible range, giving these solutions a characteristic yellow color. PBO dissolved in an organic solvent does not dissociate into ions and absorbs light in a more narrow range with a maximum at ~240 nm. The loss of oxime in either solution could be monitored via a UV-vis spectrometer, as long as the high UV absorbance of the solution does not overwhelm the detection mechanism. Cyanide ions absorb infrared light at a frequency of approximately 2640 cm^{-1} and thus their production can be monitored via Fourier transform infrared spectroscopy (FTIR). Preliminary work on this detection method revealed that in order to detect cyanide in the concentrations being produced, a multi-pass IR beam would be needed to achieve sufficient absorbance for a cyanide peak to be seen.

Oxime degradation could also be further suppressed by refrigeration of the organic oxime solutions as well as including desiccants in solution to remove traces of water. A possible improvement which could be made in the integrated micro-mixer and sensor device would be the addition of cyanide "filter". A small porous region of fine silver or gold particles can be placed in the liquid flow channel shortly before entering the actual sensor. Cyanide binds very strongly to these metals and any present due to degradation would be removed from the liquid, thus preventing it from interfering with cyanide produced in the detection process. The difficulty lies

in the creation of this cyanide “filter” within the flow channel in a way that is compatible with existing fabrication techniques and prevents metal particles from being flushed out of the system and contaminating the gold electrodes.

2.5 References

1. Soreq, H. and H. Zakut, *Human Cholinesterases and Anticholinesterases*. 1993, San Diego, CA: Academic Press.
2. Davies, D.R. and A.L. Green, *The Kinetics of Reactivation, by Oximes, of Cholinesterase Inhibited by Organophosphorus Compounds.* Biochemical Journal, 1956. **63(4)**: p. 529-535.
3. Kassa, J., *Review of oximes in the antidotal treatment of poisoning by organophosphorus nerve agents.* Journal of Toxicology-Clinical Toxicology, 2002. **40**(6): p. 803-816.
4. Green, A.L. and B. Saville, *The reaction of oximes with isopropyl methylphosphono-fluoridate (Sarin).* Journal of the Chemical Society, 1956(756): p. 3887 - 3892.
5. Saville, B., *A new approach to the determination of microgram quantities of phosphorylating or acylating agents.* Analyst, 1957. **82**: p. 269 - 274.
6. Moll, R.B., et al., *Atmosphere monitoring electrochemical cell*. 1976, The United States of America as represented by the Secretary of the Army: United States.
7. Smart, J.K., *History of Chemical and Biological Detectors, Alarms, and Warning Systems*. 2000, U. S. Army Soldier and Biological Chemical Command: Aberdeen Proving Ground, MD. p. 41.
8. Sun, Y. and K.Y. Ong, *Detection Technologies for Chemical Warfare Agents and Toxic Vapors*. 2005, Boca Raton, Fla: CRC Press. 272.
9. Taylor, E.R., *Lethal Mists: An Introduction to the Natural and Military Sciences of Chemical, Biological Warfare, and Terrorism*. 1999, Commack, N.Y.: Nova Science Publishers.
10. Mauroni, A.J., *America's Struggle with Chemical-Biological Warfare*. 2000, Westport, CT: Praeger.
11. *TM 3-6665-225-12. Operator's and Organizational Maintenance Manual: Chemical Agent, Automatic*. 1975, Headquarters Department of the Army: Washington, D.C.
12. Oh, I., C.N. Monty, and R.I. Masel, *Electrochemical multiphase microreactor as fast, selective, and portable chemical sensor of trace toxic vapors.* IEEE Sensors Journal, 2008. **8**(5): p. 522-526.
13. Masel, R.I., *Chemical kinetics and catalysis*. 2001, New York: Wiley-Interscience.
14. Oh, I. and R.I. Masel, *Electrochemical organophosphate sensor based on oxime chemistry.* Electrochemical and Solid State Letters, 2007. **10**(2): p. J19-J22.
15. Adams, G.W., J.H. Bowie, and R.N. Hayes, *The Complex Anionic Rearrangements of Deprotonated Alpha-Oximino Carbonyl Derivatives in the Gas-Phase.* Journal of the Chemical Society-Perkin Transactions 2, 1991(11): p. 1809-1818.
16. Bowie, J.H. and S. Janposri, *Electron-Impact Studies .107. Negative-Ion Mass-Spectra of Oxime Group - Monoximes Derived from Alpha-Dicarbonyl Systems.* Organic Mass Spectrometry, 1976. **11**(12): p. 1290-1296.
17. Ford, B.W. and P. Watts, *Reaction of Isopropyl Methylphosphonofluoridate with 1-Phenylbutane-1,2,3-Trione 2-Oxime.* Journal of the Chemical Society-Perkin Transactions 2, 1974(9): p. 1009-1013.
18. Ferris, A.F., *α-Oximino Ketones. I. The "Normal" and "Abnormal" Beckmann Rearrangements.* Journal of Organic Chemistry, 1959. **24**(4): p. 580-581.

19. Ferris, A.F., *α-Oximino Ketones. IV. The "Normal" and "Abnormal" Beckmann Rearrangements.* Journal of Organic Chemistry, 1960. **25**(1): p. 12-18.
20. Bailey, P.S. and Y.G. Chang, *Rearrangements of Certain Alpha-Alkoxy-Alpha-Hydroperoxyacophenones - Alcoholysis of Acetic Benzoic Anhydride.* Journal of Organic Chemistry, 1962. **27**(4): p. 1192-1197.
21. Hunig, S. and R. Schaller, *The Chemistry of Acyl Cyanides.* Angewandte Chemie-International Edition in English, 1982. **21**(1): p. 36-49.
22. Hessel, V., H. Lowe, and F. Schonfeld, *Micromixers - a review on passive and active mixing principles.* Chemical Engineering Science, 2005. **60**(8-9): p. 2479-2501.
23. Wong, S.H., M.C.L. Ward, and C.W. Wharton, *Micro T-mixer as a rapid mixing micromixer.* Sensors and Actuators B-Chemical, 2004. **100**(3): p. 359-379.
24. Knight, J.B., et al., *Hydrodynamic focusing on a silicon chip: Mixing nanoliters in microseconds.* Physical Review Letters, 1998. **80**(17): p. 3863-3866.
25. Koch, M., et al. *Two simple micromixers based on silicon*. 1998: Iop Publishing Ltd.
26. Wu, Z.G. and N.T. Nguyen, *Convective-diffusive transport in parallel lamination micromixers.* Microfluidics and Nanofluidics, 2005. **1**(3): p. 208-217.
27. Lee, N.Y., M. Yamada, and M. Seki, *Development of a passive micromixer based on repeated fluid twisting and flattening, and its application to DNA purification.* Analytical and Bioanalytical Chemistry, 2005. **383**(5): p. 776-782.
28. Hong, C.C., J.W. Choi, and C.H. Ahn, *A novel in-plane passive microfluidic mixer with modified Tesla structures.* Lab on a Chip, 2004. **4**(2): p. 109-113.
29. Stroock, A.D., et al., *Chaotic mixer for microchannels.* Science, 2002. **295**(5555): p. 647-651.
30. Fu, X., et al., *Research on staggered oriented ridges static micromixers.* Sensors and Actuators B-Chemical, 2006. **114**(2): p. 618-624.
31. Sudarsan, A.P. and V.M. Ugaz, *Fluid mixing in planar spiral microchannels.* Lab on a Chip, 2006. **6**(1): p. 74-82.

Chapter 3:

Characterization of Microfluidic Oxime Based Sensor

3.1 Introduction

Using the oxime based organophosphate detection chemistry described in the previous chapter, our research group has worked to transition this chemistry from the beaker scale to a micro-fluidic platform [1, 2]. There are many benefits from this transition to a micro-fluidic based oxime sensor, such as greatly decreased size and weight of the sensor package, reduced amount of oxime reagent and sample required, increased reliability and eliminating the need for any active mixing equipment (i.e. stir plate). The micro-sensor developed by our research group is a simple two phase device that is easily fabricated and cheap to produce. Compared to the beaker scale detection setup, this micro-sensor has proven to be more accurate and also allows for multiple tests to be conducted without having to replenish the oxime solution. Within this micro-sensor, the vapor phase species to be detected diffuses from the high flow rate gas stream through a nano-porous polycarbonate membrane to the static aqueous phase containing the oxime reagent (figure 3.1). Once in the aqueous phase, the analyte reacts with the 1-phenyl-1,2,3,-butanetrione 2-oxime (PBO) anion. This reaction is highly selective towards reactive organophosphates and acid anhydrides due to the good leaving groups (X group) these compounds possess [1]. An oxime-analyte complex is formed and then quickly decomposes into several small molecules, including a cyanide ion. The liquid micro-channel in the device is split into two parallel channels and each channel has an independent gold electrode over it (figure 3.2). The liquid in the channel exposed to the actual gas sample produces cyanide ions which are detected electrochemically by the "working" electrode as a change in the solution potential. The

liquid in the other channel is exposed to an inert gas and the electrode over that channel serves as a "reference". The response of the oxime sensor is measured as the difference in open circuit potential between these two electrodes. The use of a "reference" electrode improves the reliability of this micro-sensor by correcting for any variability in the oxime solution preparation, the effects of temperature on the sensor, as well as variability between sensors due to fabrication. Further work in our research group has focused on optimizing the design of this oxime micro-sensor by investigation the effect of membrane pore size and hydrophobicity, as well as liquid channel depth, width and length [3]. This has greatly increased the sensitivity of this sensor and has made it comparable with other commercial organophosphate sensors in terms of sensitivity and detection speed. Additionally, the selective nature of this oxime chemistry applies not only to organophosphates, but to all forms of acetylcholinesterase inhibitors. Using this micro-sensor as a platform for the tests, it was found by our research group that the oxime chemistry would selectively respond to over 40 different acetylcholinesterase inhibitors proportional to the toxicity of the compound. Highly toxic acetylcholinesterase inhibitors with low LD50 values produced large potential responses from the micro-sensor, while compounds with low toxicity (high LD50) produced much smaller responses.

In an effort to further increase the analytical power and portability of this oxime micro-sensor, it will be integrated with a micro-gas chromatography (GC) system. A total GC system is comprised of a sample pre-concentrator/injector unit, a chromatography column for separation of mixtures and finally one or more detectors for sample analysis. Many successful designs of micro-fabricated pre-concentrators/injectors units [4-7], as well as micro-fabricated gas chromatography columns have been reported in the literature[8-12]. A wide variety of micro-fabricated detectors have been shown in literature being successfully integrated with commercial

as well as experimental micro-fabricated GC units. Examples of micro-detectors coupled with commercial GC systems include arrays of polymer coated surface acoustic wave (SAW) sensors [13, 14], arrays of polymer based chemi-resistive sensors [15, 16], arrays of functionalized micro-cantilever beam sensors [17], and optical ring resonator detectors [18, 19]. In an effort to create a total miniaturized GC system, micro-GC columns and pre-concentrator/injector units have been integrated with various micro-fabricated detectors such as polymer coated carbon nano-tube resistor sensors [20], thermal conductivity detectors (TCD) [21, 22], metal oxide sensors [23, 24], arrays of polymer coated surface acoustic wave (SAW) sensors [25-27], differential mobility mass spectrometers [28], and arrays of polymer based chemi-resistive sensors [29]. These GC systems were often evaluated by their ability to separate and respond to mixtures of various hydrocarbons and other VOCs such as the TO-15 mixture studied in this chapter, however due to the relatively non-selective nature of these sensors, it was often necessary for them to be combined in functionalized arrays in order for them to effective identify compounds.

The detectors listed thus far have all been solid-state devices. Alternatively, liquid reagent based sensors have the benefit of being highly selective in the types of compounds they respond to. Micro-sensors based on selective liquid chemistries usually require a gas permeable membrane to separate the slow moving liquid phase from the rapidly moving gas phase. Ohira *et al*. developed a micro-sensor with a porous polypropylene membrane which detected SO_2 by conversion to H_2SO_4 in an acidic aqueous solution of H_2O_2 and IPA [30]. The H_2SO_4 formed was then measured by the change in electrical conductance of the solution [30]. Toda *et al*. created a liquid based micro-sensor to detect NOx compounds[31]. NO_2 was first selectively absorbed through a porous polytetrafluoroethylene (PTFE) membrane into an aqueous solution of 3% triethanolamine (TEA) and then subsequently reacted at elevated temperature with Griess–

Saltzman reagent. This results in a color change reaction that is measured by absorption spectroscopy. A similar liquid based micro-sensor was also created by Takabayashi *et al*. [32]. Timmer *et al*. created a multiphase micro-sensor for detection of ammonia [33]. Ammonia is first absorbed through a polypropylene membrane and converted to NH_4^+ in a solution of $NaHSO_4$. NaOH is added and the resulting solution flows past another membrane where NH_4^+ diffuses into a pure water stream. The concentration of NH_4^+ in this phase is then measured by electrical conductance. While these and other liquid based micro-sensors have excellent selectivity to their target compounds, the mass transport and kinetic processes in the sensor take place slowly, usually over the course of several minutes [34]. As a result, these sensors cannot be successfully integrated with a GC system that typically requires detection times of seconds or less.

The oxime based micro-sensor created by our research group can selectively detect its target molecules much more rapidly than other liquid based detectors. In this chapter, I will detail the development work performed to create the first liquid electrochemical sensor successfully integrated in a GC system.

3.2 Materials and experimental procedures

3.2.1 Oxime micro-sensor fabrication

The micro-sensor is fabricated by precision machining channels on the surface of small (1 x 1.5 x 0.5 cm) polycarbonate blocks. The liquid channels are 500 μm wide, the gas channels are 1000 μm wide, and all channels are machined to a depth of 100 μm into the polycarbonate surface. Through holes are cut at the ends of all channels to allow for external fluid hook-ups. Figures 3.1 and 3.2 show the design of both the liquid and gas micro-channels from various perspectives.

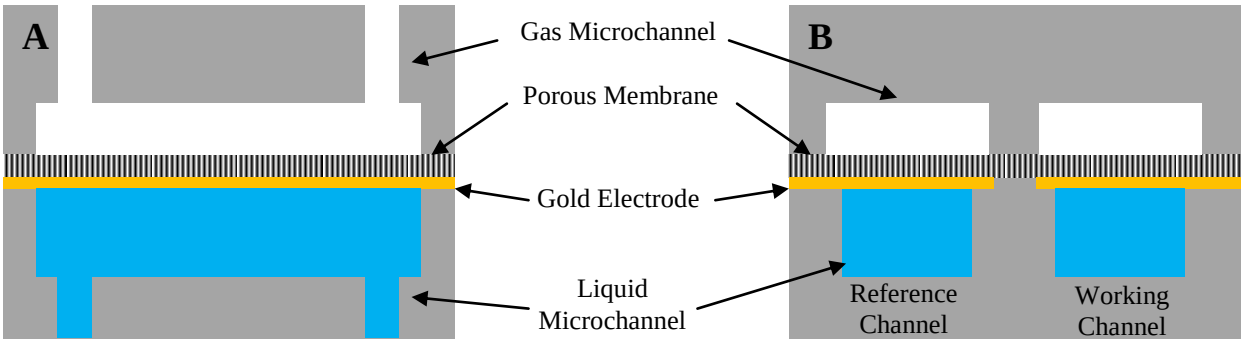

Figure 3.1: A cross sectional diagram of the micro-sensor (figure is not to scale). The gas microchannel and the liquid microchannel are aligned over each other and are separated by a nanoporous membrane with a sputtered layer of gold for electrodes. The liquid side of the nanoporous membrane is coated with a gold electrode material. (A) Profile along the microchannel. (B) Profile perpendicular to the microchannel.

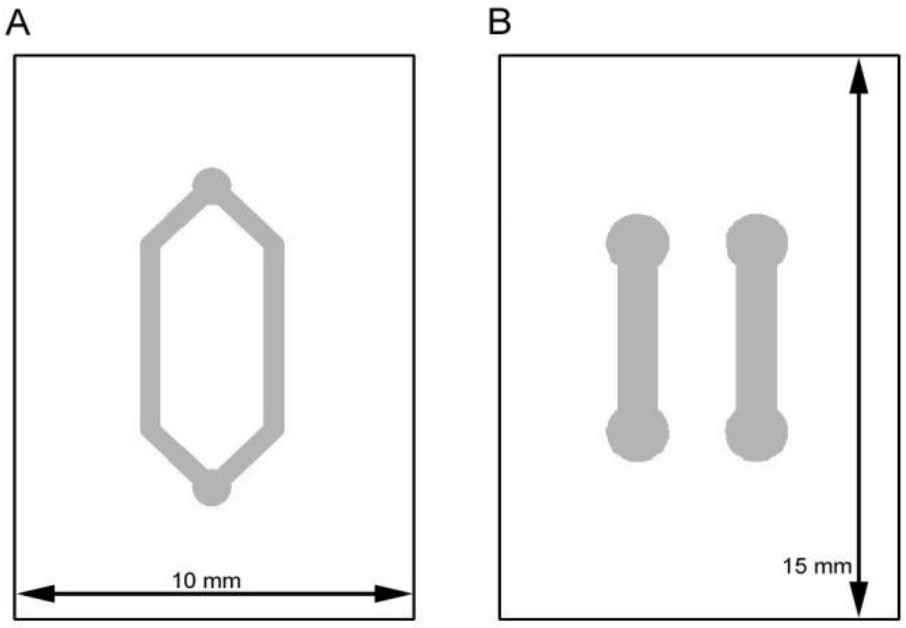

Figure 3.2: Top view of liquid (A) and gas (B) polycarbonate micro-channels.

As you can see from figure 3.1, the gas and liquid channels are designed to overlap when both pieces are aligned on top of each other (figure 3.2). Separating the two pieces is a 6 μm thick, track etched polycarbonate membrane with 50 nm pores (SPI-Pore™ Polycarbonate Membrane Filters, Non-Hydrophilic Pore Coating, SPI Supplies). A 40 nm layer of gold is sputtered on to the liquid side of the polycarbonate membrane. This layer is patterned by an aluminum foil shadow mask into two separate regions, one for each liquid/gas channel pair, which will function as a "working" and "reference" electrode. Bonding of all pieces is done via an epoxy (Loctite, 81120) transfer process from a flat polydimethylsiloxane (PDMS) puck to ensure a thin (~6 μm), even layer of adhesive which will create a gas tight seal. For the through holes on the liquid side of the device, 1/16 inch tubing is connected to the entrance and exit, and is affixed using epoxy. This tubing is then connected to an oxime delivery syringe and a waste reservoir.

3.2.2 Testing of oxime micro-sensor with interferent mixture

In order to test the effect of interferent mixture on the oxime chemistry, the gas inlet of the micro-sensor was connected to a cylinder containing the gaseous mixture. This cylinder contains a mixture called TO-15, which are 62 of the most common chemicals in ambient air as defined by the EPA. Each compound in the mixture was present at 100 ppb and the mixture was purchased from Scott Specialty Gases. A 4.75 mM oxime solution is prepared by dissolving 1mg of oxime per 1 ml of buffer solution (25 mM borate buffer solution, adjusted to pH 10 with concentrated NaOH). The solution is then loaded into a syringe and slowly introduced into the liquid channel of the sensor. Gas flow was controlled using a bubble flow meter set to 1 mL/min. Initially, there was no gas flow through the device. The electrochemical response of

the sensor is pre-processed by the 20× amplifier and low pass noise filter. The resulting signal is then measured by the external potentiostat unit. After a stable baseline signal was recorded, vapor flow from the cylinder containing the TO-15 mixture was introduced. The micro-sensor was exposed to a steady stream of interferent vapors for 5 seconds. This process was repeated several times to ensure the reliability of the results.

3.2.3 Integration of micro-sensor with commercial gas chromatography system

To connect to the gas inlet of the micro-sensor, capillary sleeves (Upchurch Scientific, F-239, 200 μm I.D., 1/16" O.D.) are used which serve as adaptors between the large diameter through holes and the small diameter fused silica capillaries (150 μm I.D., IP deactivated fused silica guard/retention gap columns, Restek) used in the GC system. These capillary sleeves are also bonded to the polycarbonate sensor using epoxy. When a single compound is being tested and no gas separation is necessary, the sensor can be connected directly to the injector assembly by a short length (1 or 2 meters) of passivated column (150 μm I.D., IP deactivated fused silica guard/retention gap columns, Restek). When testing a mixture of compounds, a commercial fused silica column or silicon micro-column fabricated in house can be used to separate the mixture prior to it reaching the oxime micro-sensor. The automatic injector assembly of the GC provides discrete "pulses' of the sample within an inert helium carrier gas flow. The automatic injector assembly is the outfitted with a 10μL syringe for sampling. An integrated low pass filter and 20 times amplifier is connected to the two electrodes of the sensor to remove high frequency noise and boost the sensor response. The output of this amp/filter is connected to the Voltmaster potentiostat, which is again set to measure an open circuit potential.

3.2.4 Fabrication of GC micro-column and integration with oxime micro-sensor

The "partially buried" micro-column (PBMC) was fabricated in silicon by the method previously reported by Radadia *et al.* [9]. The micro-column is 34 cm long with a cross-sectional shape that resembles that of a flattened circular tube (165 µm wide and 65 µm deep) (figure 3.3).

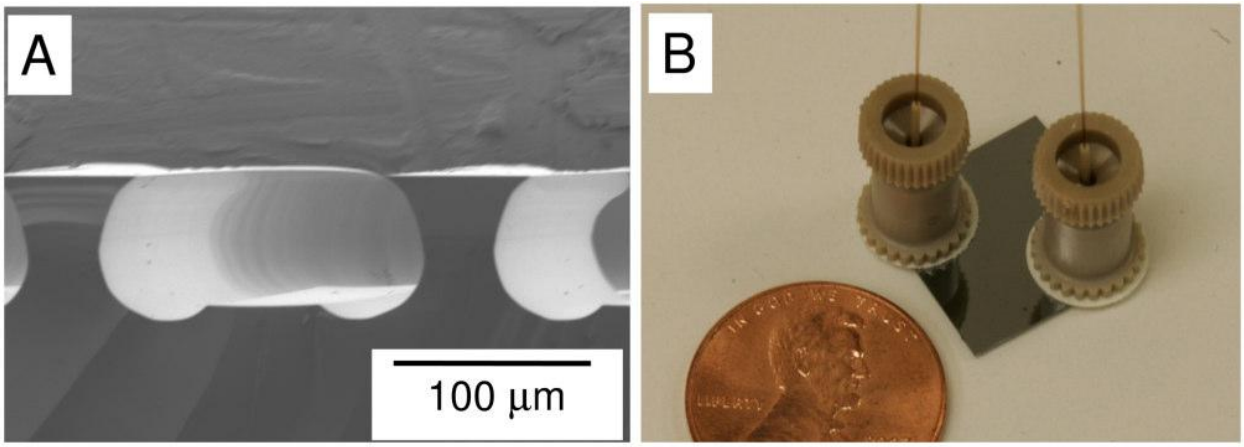

Figure 3.3: (A) SEM image of the 165 µm wide 60 µm deep cross section of the PBMC channel geometry. (B) Photograph of the 1.4 cm square PBMC showing the Nanoport® vapor connections.

The channels were made in two etching steps: the first step consists of an anisotropic deep reactive ion etching (DRIE) of silicon using the Bosch® process and the second step consisted of an isotropic SF_6 to round out the side walls. Vias were created using DRIE at each end of the micro-channel for capillary connections. After fabrication, organosilicon hydride passivation using phenyltris(dimethylsiloxy) silane (Ah3P) (Gelest, SIP6826) was performed and the column was coated with OV-5® stationary phase as previously reported by Radadia *et al.* [9]. Deactivated fused silica capillaries 25 cm in length (Restek, IP deactivated, 100 µm I.D., 200 µm I.D.) were attached to micro-column inlet and outlet using Nanoports® fittings. The micro-

column was then connected to the automatic injector assembly and either the FID or the oxime micro-sensor.

3.2.5 Testing of oxime micro-sensor integrated in GC system

All micro-sensor experiments with the exception of the interferent tests follow the general procedures outlined in this section. A 4.75 mM oxime solution is prepared by dissolving 1mg of oxime per 1 ml of buffer solution (25 mM borate buffer solution, adjusted to pH 10 with concentrated NaOH). The solution is then loaded into a syringe and slowly introduced into the liquid channel of the sensor. The micro-sensor, oxime containing syringe and the chromatography column (if present) are all loaded into the GC oven. The oven temperature is set and the sensor is then allowed equilibrate for 20 – 30 minutes before any analyte is introduced. The injection assembly temperature is set to 250 °C. Test mixtures were prepared using puriss-grade chemicals (GC standards) from Aldrich (Milwaukee, WI). When an injection is started, the sampling needle automatically draws in ambient air 6 times to "wash" the syringe. The vial containing the compound(s) to be tested is then sampled, injected, diluted by the split flow, and sent through the passivated capillary or GC column to the micro-sensor as a "pulse" in the inert helium carrier flow. The electrochemical response of the sensor is pre-processed by the 20x amplifier and low pass noise filter. The resulting signal is then measured by the external potentiostat unit. During the test, the oxime solution remains static to maximize the potential response. Once a set of tests have been finished, the oven is opened and fresh oxime solution is again slowly flowed through the sensor to remove reaction products and reset the device. After the oven is closed, the sensor again requires a short period of time to re-equilibrate before testing can resume.

3.3 Results and discussion

3.3.1 Interferent mixture tests

Previous work in our research group has shown that the oxime based chemistry is selective to organophosphate and other acetylcholinesterase inhibitors. To further evaluate its selectivity, the response of the micro-sensor to various common atmospheric chemicals was tested. A mixture of the 62 most common compounds found in ambient air was used to for this purpose. Table 3.1 shows the entire list of chemicals in the mixture. Each component was present at a concentration of 100 ppb in a nitrogen medium. The sensor was exposed to a steady stream of the interferent mixture at a flow rate of 1 mL/min for 5 seconds in order to ensure that the sensor had sufficient time to register a response. However, no potential response was detected from the oxime micro-sensor after repeated 5 second exposures to the interferent mixture. This combined with previous work in our research group shows that this oxime chemistry is highly selective and not effected by a large variety of chemical interferents.

Acetone	1,1-Dichloroethene	Methylene Chloride
Benzene	Cis-1,2-Dichloroethene	Methyl-Tert-Butylether (MTBE)
Benzyl Chloride	Trans-1,2-Dichloroethene	2-Propanol
Bromoform	1,2-Dichloropropane	Propylene
Bromomethane	Cis-1,3-Dichloropropene	Styrene
Bromodichloromethane	Trans-1,3-Dichloropropene	1,1,2,2-Tetrachloroethane
1,3-Butadiene	1,4-Dioxane	Tetrachloroethene
2-Butanone (MEK)	Ethanol	Tetrahydrofuran
Carbon Disulfide	Ethyl Acetate	Toluene
Carbon Tetrachloride	Ethyl Benzene	1,1,1-Trichloroethane
Chlorobenzene	Ethyl Dibromide	1,1,2-Trichloroethane
Chloroethane	4-Ethyltoluene	Trichloroethene
Chloroform	Freon 11 (Trichlorofluoromethane)	1,2,4-Trichlorobenzene
Cyclohexane	Freon 12 (Dichlorodifluoromethane)	1,2,4-Trimethylbenzene
Chloromethane	Freon 113 (1,1,2-Trichlorotrifluoroethane)	1,3,5-Trimethylbenzene
Dibromochloromethane	Freon 114 (1,2-Dichlorotetrafluoroethane)	Vinyl Acetate
1,2-Dichlorobenzene	Heptane	Vinyl Chloride
1,3-Dichlorobenzene	Hexachloro-1,3-butadiene	m-Xylene
1,4-Dichlorobenzene	Hexane	o-Xylene
1,1-Dichloroethane	2-Hexanone (MBK)	p-Xylene
1,2-Dichloroethane	4-Methyl-2-Pentanone (MIBK)	

Table 3.1: Components in TO-15 interferent mixture at 100 ppb in nitrogen.

3.3.2 Effects of temperature and gas flow rate on oxime micro-sensor performance

For the interferent test in the previous section, a constant stream of the sample gas was passed through the oxime micro-sensor was exposure to past the device. These types of experiments can be used to quickly and easily evaluate a large variety of possible sensor analytes or interferents. However, variability in testing conditions, such as gas flow rate, exposure time and analyte concentration make it difficult to accurately evaluate the sensors performance. By connecting the micro-sensor to the automatic injector assembly unit on a GC system, much more precise, repeatable analyte exposures are possible. The automatic injector of the GC system allows the sample to be routed to the sensors as a "pulse" in the inert helium carrier gas. Both the pulse height (concentration) and width (exposure duration) can be reliably controlled and reproduced using this GC equipment. For the experiments conducted in this section, no gas chromatography column was used. Instead the oxime micro-sensor is connected directly to the automatic injector assembly by way of a short (2.3 m) passivated fused silica capillary with no stationary phase. As a result, the "pulse" of analyte quickly reaches the sensor with minimal peak broadening from diffusion of the analyte in the carrier gas. Oven temperature and carrier gas flow rate still have an effect on the peak height and width, but in the range tested, the peak width at half maximum height is on average only 3.5 milliseconds. The changes in the peak width (and height) of the acetic anhydride "pulse" are taken into account by replacing the oxime micro-sensor with the normal flame ionization detector (FID) in the GC system. The FID is an extremely rapid, non-selective sensor whose behavior will remain constant despite flow rate and oven temperature changes, and will show a true representation of the acetic anhydride "pulse" shape.

All tests conducted in this section were performed by injecting 0.2 µL of saturated acetic anhydride vapor and diluting it with a split flow of 300:1. After dilution with helium, approximately 9.4×10^{10} molecules of acetic anhydride are routed to the oxime micro-sensor. Figure 3.4 is an example of the potential response of the micro-sensor to a "pulse" of acetic anhydride at a helium carrier flow rate of 0.5 mL/min and an oven temperature of 50 °C. As the acetic anhydride pulse passes through the micro-sensor at approximately t = 340 seconds, the open circuit potential very rapidly increases from 172 mV to 191 mV. This increase in open circuit potential is caused by the gold electrode interacting with the cyanide ions produced in the "working" liquid microchannel which is exposed to the acetic anhydride "pulse".

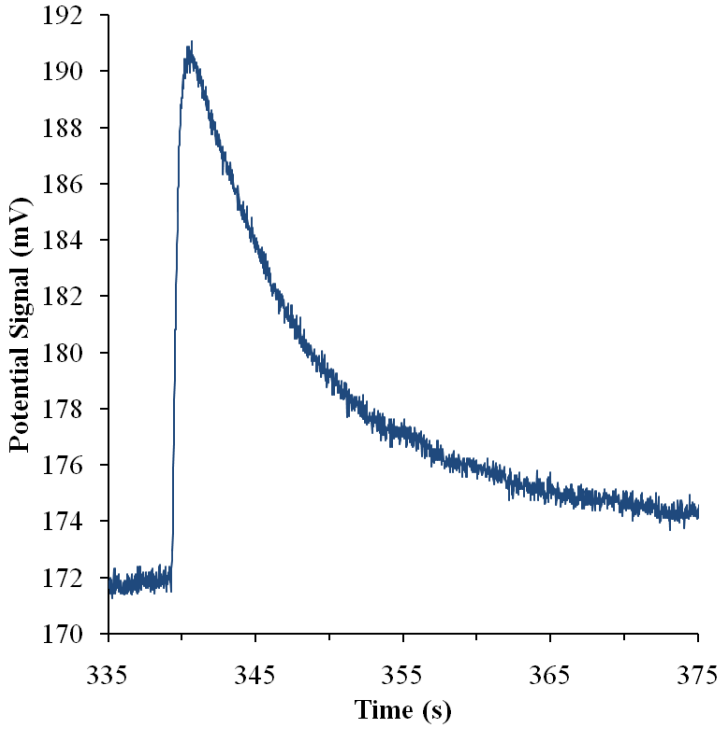

Figure 3.4: Example of typical potential response of the oxime micro-sensor when exposed to a "pulse" of simulant in an inert carrier gas stream. Injection of 9.4×10^{10} molecules of acetic anhydride at a flow rate of 0.5 mL/min and an oven temperature of 50 °C.

After the acetic anhydride peaks completely passes through the sensor, only inert helium is again present and the reaction producing cyanide ions stops. The potential of the sensor then begins to slowly decay back towards the original baseline due to the diffusion of cyanide ions from the highly concentrated region at the gas/liquid interface near the electrode into the bulk solution in the micro-channel.

Differentiating this potential signal gives the curve in figure 3.5. While the original open circuit potential signal was representative of the concentration of cyanide ions at the electrode surface, the differentiated signal represents the rate of change (production) of cyanide ions at the electrode. This mirrors the signal from the FID, which measures the rate of ions created from combustion in this sensor.

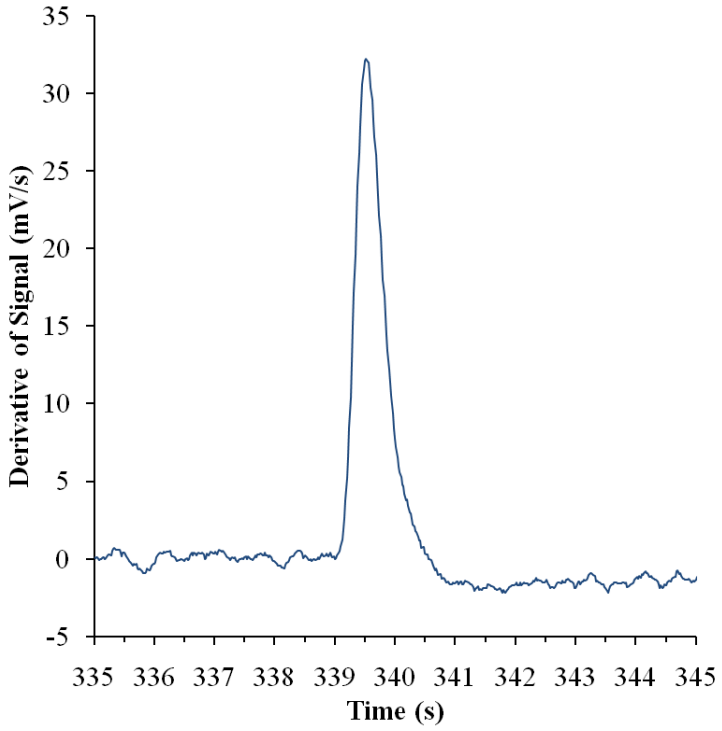

Figure 3.5: Derivative of oxime micro-sensor potential response signal from figure 3.4. Injection of 9.4×10^{10} molecules of acetic anhydride at a flow rate of 0.5 mL/min and an oven temperature of 50 °C.

This differentiated signal is created by averaging the original potential signal over a 0.3 second window, then differentiating the result over a 0.24 second interval. This removes the effect of most of the high frequency noise without compromising the accuracy of the data. It should be noted that the differentiated signal is slightly negative after the peak. This is due to the gradual decay in potential from cyanide diffusing away from the electrode which was mentioned previously. By using the differentiated response, the oxime sensor signals can now be analyzed in the same manner as the FID signals. This particular example has a peak height of 32.2 mV/s and a peak width at half height of 0.52 seconds. It should be noted that while the peak width from both sensors can be directly compared, peak height is measured in different units for each sensor and therefore cannot be easily compared without extensive calibration curves for both sensors. Therefore, figures which plot peak height data have the FID signal normalized in a way that allows for easy comparison of the trends in peak height change for both sensors.

Figure 3.6 shows the change of peak height and peak width at half height for both sensors as a function of carrier gas flow rate at an oven temperature of 35 °C. Figure 3.6A shows that the peak height behaves very similarly for both sensors, indicating the oxime micro-sensor response is proportional to the maximum acetic anhydride concentration in the "pulse" over the flow rate range tested. However, peak width at half height is substantially different between sensors. It can be seen from figure 3.6B that the true width (from the FID signal) of the acetic anhydride "pulse" is approximately 2 orders of magnitude shorter than the width of the peak from the oxime sensor signal. Additionally, the trend in peak width as flow rate increases is also significantly different. The trend in peak width from the FID signal seems to roughly follow the theoretically expected behavior of the acetic anhydride "pulse" to asymptotically approach zero as the flow rate increases. However, the oxime micro-sensor peak width appears to plateau at

just above 0.8 seconds for flow rates of 0.2 mL/min and greater, even though the width of the actual acetic anhydride "pulse" continues to decrease over the entire flow rate range.

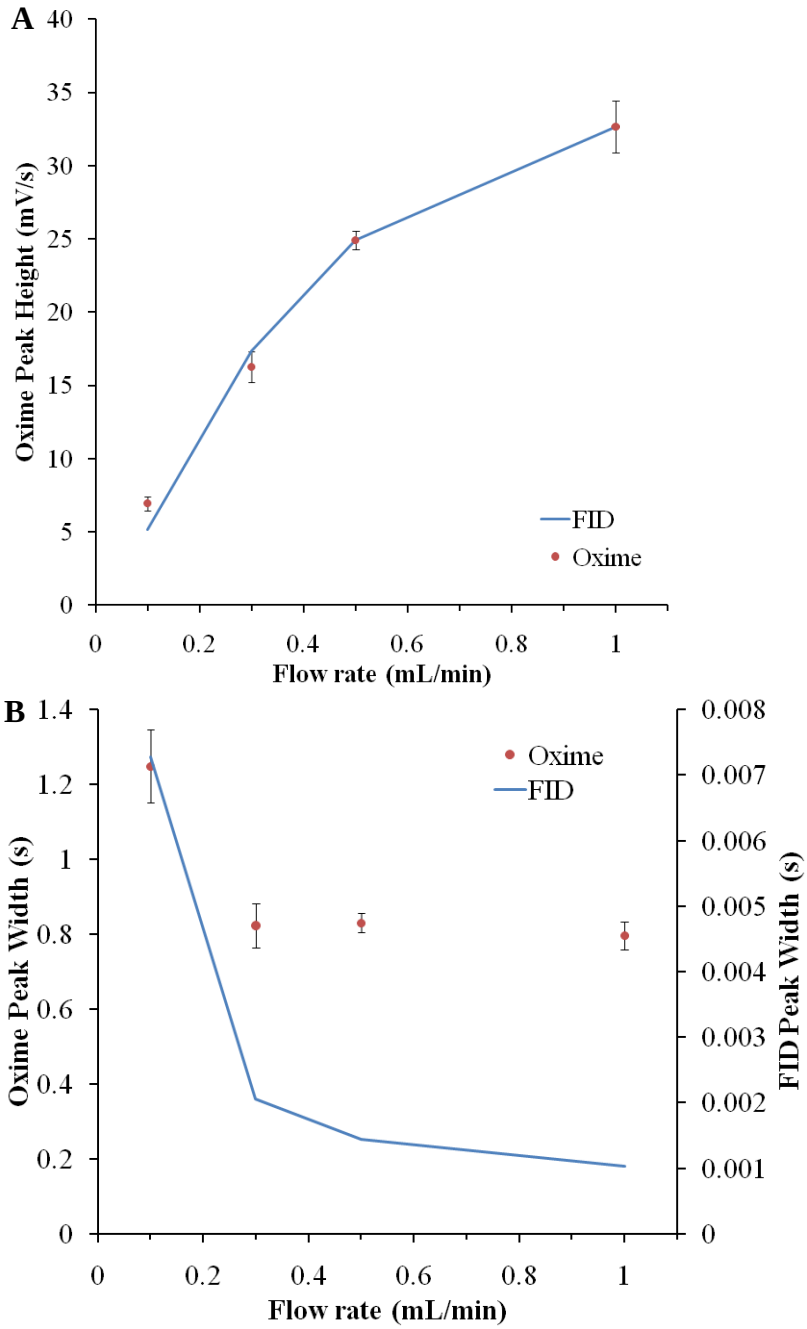

Figure 3.6: Effect of carrier gas flow rate on (A) peak height and (B) peak width at half height from the oxime micro-sensor and commercial GC FID. Performed at a constant oven temperature of 35 ºC.

Figure 3.7 shows the effect of oven temperature on the peak height and peak width at half height for both sensors, for flow rates of 0.1 mL/min and 0.5 mL/min. From figure 3.7A, the peak height of the FID signal can be seen to slowly increase as the oven temperature increases. Although there is no stationary phase in the capillary used to supply the sensor with the "pulse" of analyte, acetic anhydride still slightly adsorbs to the fused silica capillary walls. However this adsorption is reduced as the capillary temperature is increased. This decreases the spreading of the peak caused by mass transport to and from the wall of the capillary, allowing the "pulse" to travel through the capillary relatively undisturbed. Because the total amount of acetic anhydride injected is constant, peak height will increase as peak width decreases, thus conserving overall mass. Peak height of the oxime micro-sensor signal also increases as sensor temperature increases, however it does so more rapidly than the FID peak height and is most likely due to an increase in oxime reaction rate with acetic anhydride. This also corroborates the findings by our research group during the oxime micro-sensor design optimization that the device performance is fundamentally reaction rate limited [3]. At a carrier gas flow rate of 0.1 mL/min, the oxime signal height increases by 33% while the width at half height decreases by 29%. At a carrier gas flow rate of 0.5 mL/min the improvements were diminished, the oxime signal height increases by 19% while the width at half height decreases by 15%.

Unfortunately, temperatures above 50 °C could not be evaluated due to the excessive formation of gas bubbles in the aqueous oxime solution. Additionally, operating the oxime micro-sensor at the extremes of flow rate and temperature tested in this study produced a significant amount of variability in the signal peak height, as seen from the increasingly larger standard deviation bars as temperature increased for flow rates of 0.5 mL/min. This is most

likely a result of gas bubbles accumulating on portions of the membrane and partially interfering with the mass transport of acetic anhydride to the liquid phase.

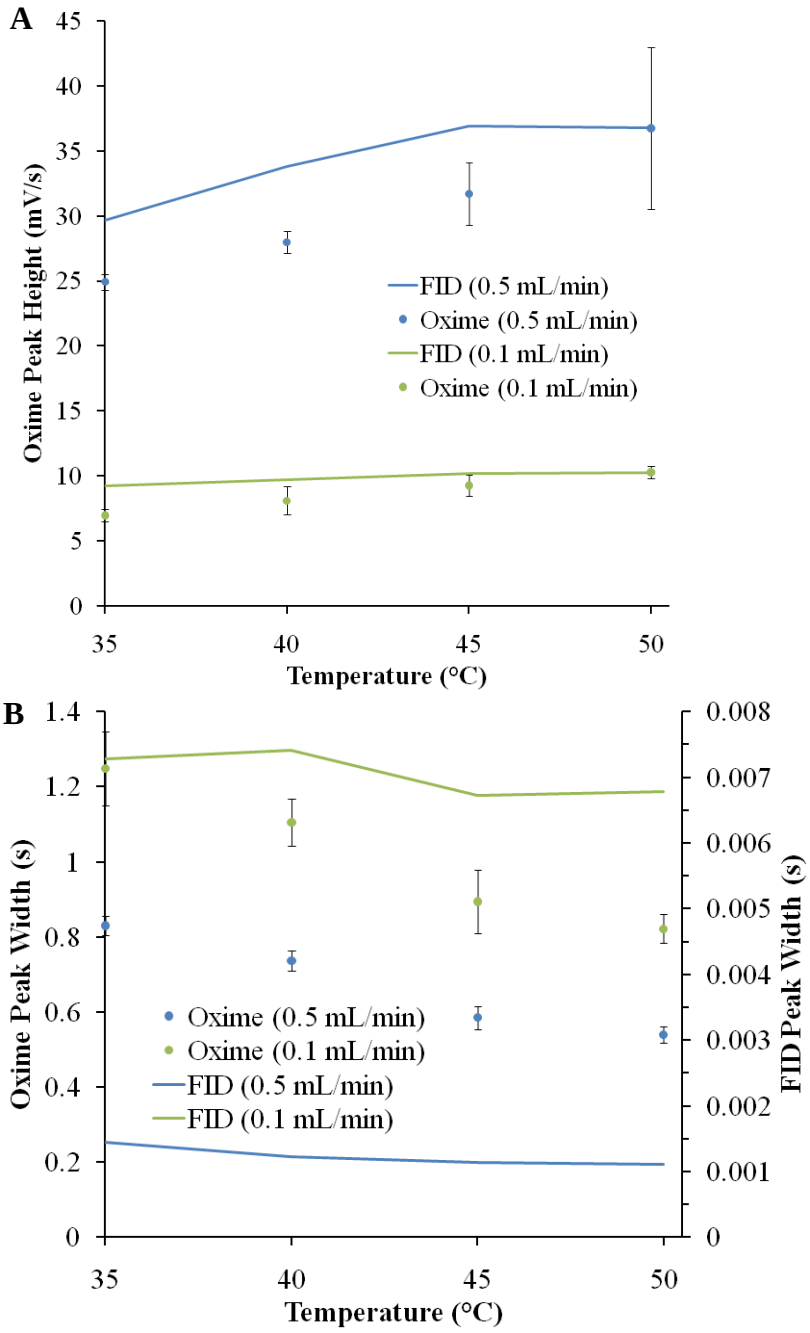

Figure 3.7: Effect of oven temperature on (A) peak height and (B) width at half height from the oxime micro-sensor and commercial GC FID. Performed at carrier gas flow rates of 0.1 and 0.5 mL/min.

Figure 3.7B shows the effect of temperature on the peak width at half height for both the oxime micro-sensor and the FID. For both flow rates measured, we observe the expected decrease in peak width from the FID signal as temperature increases due to the diminished adsorption of acetic anhydride within the capillary. Although the peak width from the oxime sensor signal is again much larger than the true width of the acetic anhydride "pulse", it is decreasing at a faster rate as temperature increases. This behavior can also be attributed to the improvement in reaction kinetics. Because the analyte "pulse" is so narrow and the mass transport from the gas to liquid phase is so rapid, acetic anhydride accumulates in the aqueous solution at the gas-liquid interface. As a result of the slow reaction kinetics, the production of cyanide lags behind the actual passage of the analyte "pulse" through the sensor. By increasing the temperature of the sensor, we decrease the time required for the oxime to react with the accumulated acetic anhydride and this consequently improves the sensors detection time.

3.3.3 Oxime micro-sensor integrated with commercial fused silica GC column

The next step to evaluating this oxime micro-sensor as a possible detector in a complete gas chromatography system is to integrate it with a commercial fused silica GC column. To show the ability of the oxime micro-sensor to detect the acetylcholinesterase simulant in a mixture of interferents, a solution of acetic anhydride, as well as several of its chemical isomers in an acetone solvent will be separated and sent to the sensor for analysis. A 30 meter fused silica GC column with a stationary phase consisting of 5%-phenyl-methylpolysiloxane was used for all experiments in this section (30 m × 0.25 mm × 0.25 µm, HP-5MS, 19091S-433, Agilent). These tests were conducted at 50 °C with helium carrier gas flow rates of 0.5 and 1.0 mL/min. The sample mixture contained 3.5 mM acetic anhydride, 3.7 mM methyl pyruvate, 3.9 mM ethyl

oxoacetate and 3.1 mM toluene dissolved in an acetone solvent. Toluene is present in this mixture because ethyl oxoacetate could only be purchased in a 50% by volume solution in toluene. The automatic injector assembly samples 0.2 µL of this mixture and dilutes it with a split flow of 300:1. After dilution with helium, approximately 1.40×10^{12} molecules of acetic anhydride, 1.48×10^{12} molecules of methyl pyruvate, 1.56×10^{12} molecules of ethyl oxoacetate and 1.24×10^{12} molecules of toluene are routed to the oxime micro-sensor.

Figure 3.8 compare the FID and oxime micro-sensor signals of the separated mixture at flow rates of 0.5 and 1.0 mL/min. Again, due to the dissimilar units for both sensor signals, the FID signal was normalized such that the acetic anhydride peak is of identical height to corresponding peak in the oxime micro-sensor signal. However, the time scales from both signals were not altered in any way. All compounds in the mixture were detected by the FID due to its non-selective behavior. From left to right, the peaks correspond to acetone, methyl pyruvate, acetic anhydride, ethyl oxoacetate and toluene.

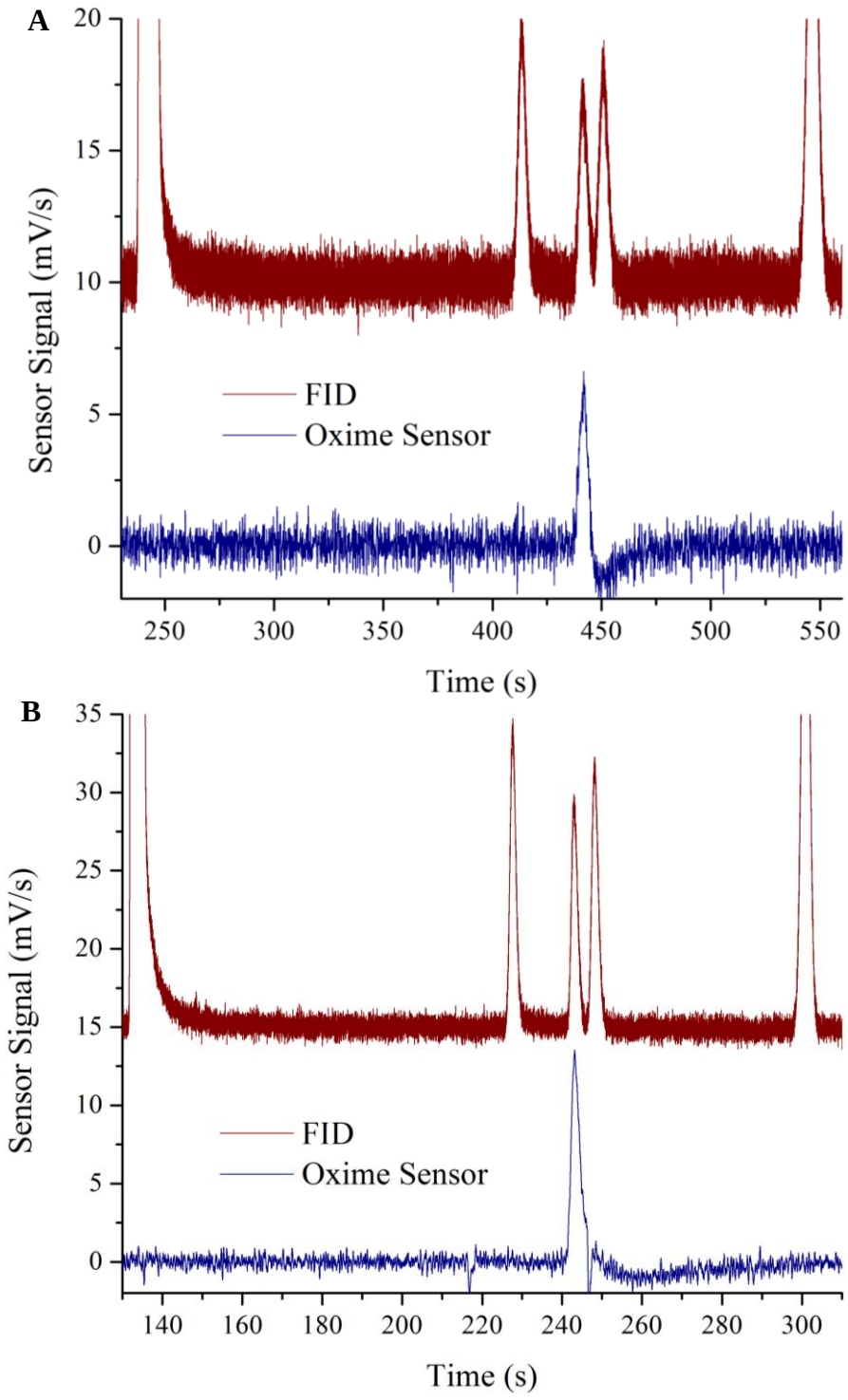

Figure 3.8: Oxime micro-sensor and normalized FID signal for separated sample. Gas flow rates of (A) 0.5 and (B) 1.0 mL/min, with a temperature of 50 °C. From left to right, the peaks in the FID signal are acetone, methyl pyruvate, acetic anhydride, ethyl oxoacetate and toluene.

For both carrier gas flowrates, the differentiated potential signal from the oxime micro-sensor shows no reaction to all other species except for the acetylcholinesterase simulant acetic anhydride. Additionally, both acetic anhydride peaks from the oxime micro-sensor signal are nearly identical in shape to the acetic anhydride peak from the FID signal. This is in contrast to the previous section, where experimental results showed the oxime sensor peak was significantly broader that the true "pulse" width. Table 3.2 shows the peak width at half height for FID and oxime sensor at both flow rates tested.

Flow rate	FID	Oxime Sensor
0.5 mL/min	4.75 s	4.5 s
1.0 mL/min	1.90 s	2.4 s

Table 3.2: Width at half height of the acetic anhydride peak from both the oxime micro-sensor and FID signals shown in figure 3.8.

The broader the acetic anhydride "pulse" in the carrier gas, the slower the acetic anhydride concentration changes as it passes through the oxime micro-sensor. At a certain point, the kinetic limitations of the sensor become negligible compared to the time required for the acetic anhydride "pulse" to traverse the micro-channel. This is the situation taking place in the experiments performed in this section. As a result, the oxime micro-sensor has equivalent detection capabilities as the FID, and has the ability to individually detect all target compounds provided they are not co-eluted from the GC column. As we will see in the following section, even if a target compound is co-eluted with an interferent compound, the oxime sensor will only respond to the target and will resolve its peak individually. Finally, it should also be noted that the signal to noise ratio is higher for the oxime micro-sensor than it is for the FID, which allows the oxime sensor to detect lower concentrations of its target compounds.

3.3.4 Oxime micro-sensor integrated with silicon GC micro-column

The final step in creating a complete micro-gas chromatograph system is the integration of the oxime micro-sensor with the micro-GC column fabricated in-house. This integration will allow for the rapid identification of various acetylcholinesterase inhibitors in a complex vapor mixture containing many interferents. The fabrication of this 34 cm long partially-buried micro-column (PBMC) was detailed in section 3.2.4. These studies were performed at a flow rate of 0.2 mL/min because previous development work had shown that the micro-column operated most effectively at this flow rate [9]. The oven temperature for these experiments was set at 50 °C to maximize the speed and magnitude of the potential response from the oxime micro-sensor. Acetic anhydride could not be used in this experiment as it is highly reactive with the column coating. Instead, the acid anhydrides isopropyl sulfonyl chloride (IPSC) and methyl sulfonyl chloride (MeSC) were used as simulants in this study. A mixture containing 4.3 mM of both IPSC and MeSC, along with 1.2 mM of each n-alkanes C_7-C_{11} as interferents was prepared in a pentane medium. The GC system injected 1 µl of this mixture and diluted it with an injector split ratio of 1500:1. After dilution, the sensor is exposed to approximately 1.7×10^{12} molecules of both IPSC and MeSC, as well as 5.0×10^{11} molecules of the C_7-C_{11} n-alkane interferents.

Figure 3.9(A) shows the FID response to the separated mixture eluted from the micro-GC column. Due to the much shorter length of the micro-column, compounds are eluted more rapidly with less time separating individual peaks. It is important to note that the C_7 and MeSC peaks have actually been co-eluted from the micro-column and the FID is unable to resolve the two individual peaks of these compounds. Before the oxime micro-sensors was exposed to the separated mixture, sensor response to individual injections of MeSC and IPSC was performed to determine their respective elution times.

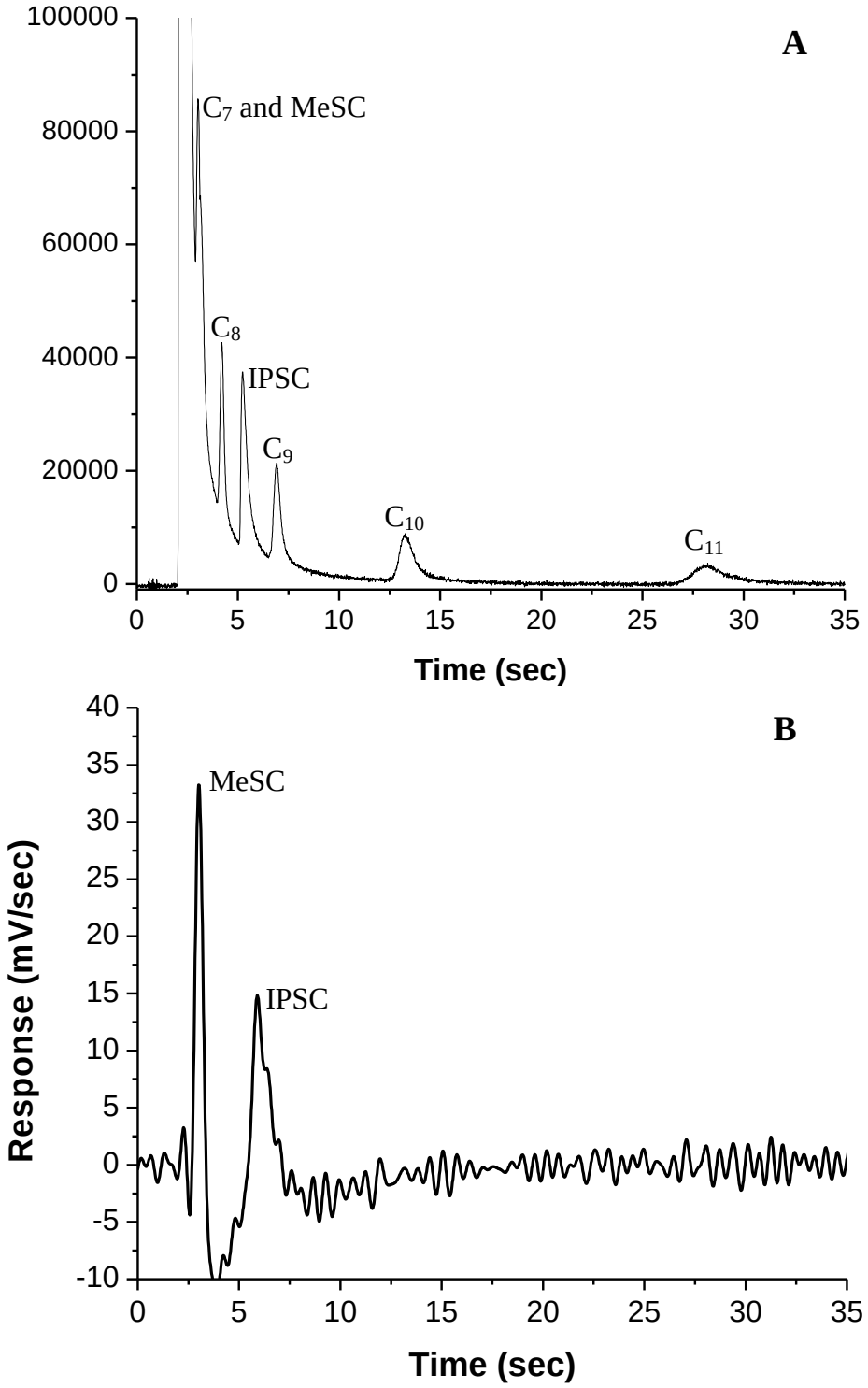

Figure 3.9: (A) FID signal and (B) oxime micro-sensor signal to a separated mixture of MeSC, IPSC and C_7-C_{11} n-alkanes in n-pentane. This mixture was separated using the 34 cm PBMC at a carrier gas flow rate of 0.2 mL/min and a temperature of 50 °C.

The response of the oxime sensor to the same injection mixture is shown in figure 3.9(B). Only two peaks are present in the signal from the oxime micro-sensor and they correspond to the elution times of MeSC and IPSC determined previously. Although the sensor was exposed to considerably more pentane than either of the two simulants, no potential response was observed. No peaks were observed for any of the other n-alkane interferents eluted from the micro-column either. It is also important to note that the MeSC peak in both the FID and the oxime sensor signal are very similar in shape. However, the IPSC peak from the oxime sensor is considerably broader. This is either a result of sluggish reaction kinetics with the oxime reagent or due to the interaction of IPSC with the non-inert polycarbonate side walls in the gas channel of the device. Adsorption and desorption of IPSC from the micro-sensor walls before it reacts with the oxime introduces a lag in the detection process and can lead to a peak broadening in the sensor signal.

3.4 Conclusions and recommendations

The studies detailed in this chapter build off of previous work conducted by our research group related to the development of the oxime micro-sensor as well as in the area of micro-columns for gas chromatography systems. Previous work in our research group has shown that the aqueous oxime based chemistry used in the micro-sensor is selective to organophosphates, acetylcholinesterase inhibitors and other highly reactive acid anhydrides. In this chapter we tested the oxime micro-sensors against the standard TO-15 EPA mixture of the 62 most common compounds in the atmosphere and found that all of these possible interferents had no effect on the potential response of the detector. Including past work in our research group, this oxime chemistry has been found to be unaffected by over 80 different compounds[1, 2].

Coupling this oxime micro-sensor with a gas chromatography system will enable accurate analysis of complex mixtures. The selective nature of this oxime based chemistry combined with the elution times of each individual species from the gas chromatography column will allow quick identification of the number, possible identity and concentration of any acetylcholinesterase inhibitors or simulants present in a mixture. To this end, the micro-sensors' response to an individual compound was evaluated at a variety of carrier gas flow rates and temperature to better understand the behavior of this device. Experiments showed that the peak height of the differentiated oxime signal increased as flow rate increased. This mirrored the trend in FID peak height and was simply a result of the decreased residence time as carrier gas flow rate is increased. While the sensitivity of the oxime sensor was unaffected by changes in flow rate; due to the fundamental kinetic limitations of the oxime chemistry, the sensor was not able to react with the acetic anhydride simulant as rapidly as the "pulse" of analyte passed through the device. As a result, the peak width at half height from the oxime sensor signal was more than 2 orders of magnitude greater than the width of the actual analyte "pulse". This also caused the peak width from the oxime sensor signal to plateau at 0.8 seconds instead of asymptotically decreasing towards zero as flow rate increases. The kinetic limitations of this oxime micro-sensor were again apparent in the experiments investigating temperature effects. As temperature increases, peak height is expected to increase and peak width at half height is expected to decrease due to diminished adsorption of analyte on the walls of the passivated capillary connecting the sensor to the injector. This behavior is also observed in the oxime sensor signal, however both height and width trends occur at a more rapid rate compared to the FID signal. This increase in sensitivity and corresponding decrease in detection time are a result of the improved oxime reaction kinetics from the elevated temperature. However, these

improvements in sensor performance come at the expense of detector reliability. High temperatures cause gas bubble formation in the aqueous oxime solution. Operating this micro-fluidic device at the extremes of temperature and flow rate evaluated in this study leads to high variability of the peak height and negatively effects detector sensitivity.

The oxime micro-sensor was then coupled to a commercial gas chromatograph column evaluate its ability to detect the target molecule without being affected by other eluted interferents. A commercial column was used to separate a mixture of acetic anhydride and two of its isomers in an acetone matrix. Acetic anhydride and its isomers were eluted from the column as three discrete peaks in quick succession of each other; however, due to the selective nature of the oxime chemistry, only acetic anhydride produced a response in the sensor. The two isomers, as well as toluene and the large solvent peak from acetone did not interfere with the oxime micro-sensor signal in any way. The individual acetic anhydride peak eluted from the commercial column has a width at half height measured by the FID of 4.75 and 1.90 seconds for gas flow rates of 0.5 and 1.0 mL/min, respectively. This is significantly broader than the acetic anhydride "pulse" observed when directly connecting the sensor to the GC injector and is expected due to axial diffusion of the analyte in the helium carrier flow. These broad acetic anhydride "pulses" take a much longer time to pass completely through the sensor and as a result, the kinetic limitations of the oxime chemistry have a negligible impact on the peak width of the micro-sensor signal. The peak width at half height as measured by this sensor was 4.5 and 2.4 seconds for gas flow rates of 0.5 and 1.0 mL/min, respectively.

The final stage of this work was to integrate the oxime micro-sensor with a gas chromatography micro-column which was also designed and fabricated in our research group. This forms the analytical backbone of a complete micro-gas chromatography system designed

specifically to detect acetylcholinesterase inhibitors. In combination with a microfabricated gas sample pre-concentrator unit, this system becomes a powerful, highly portable gas analyzer. A mixture containing two acetylcholinesterase simulants (MeSC and IPSC) as well as 5 interferents (C_7 through C_{11} n-alkanes) in a pentane solvent was used to test this integrated micro-column and oxime micro-sensor. Although the micro-column was operated at its optimal flow rate, it was unable to resolve the methyl sulfonyl chloride peak from the C_7 peak. The oxime micro-sensor on the other hand only responded to the simulants MeSC and IPSC and ignored all other compounds. The IPSC peak in the oxime sensor was broader than its corresponding peak in the FID signal and could be a result of either slow reaction kinetics with oxime reagent or strong adsorption interactions with the non-passivated polymer walls of the micro-channel.

In combination with previous work from our lab, these studies have shown that this oxime micro-sensor is a highly sensitive and selective detector of acetylcholinesterase inhibitors. Although the oxime micro-sensor cannot respond as rapidly as the FID which is commonly used in GC systems, our test have shown that under typical chromatography conditions, the oxime sensor is more than capable of accurately measuring the peak height and width of an analyte "pulse". These studies have also shown that the oxime sensor is responsive enough to resolve the peaks of two target compounds eluted in quick succession of each other while ignoring all interferent peaks.

The performance of this oxime micro-sensor can possibly be improved further. Currently the sensor is constructed entirely from non-passivated polycarbonate materials, including the nano-porous membrane. This polymer material may irreversibly capture target molecules into the side walls of the vapor microchannel or introduce lag in the sensor signal from these adsorption processes. In the following chapter, I will discuss the design and fabrication of an all

silicon microsensor even smaller than the current polymer based design. This silicon oxime sensor is incorporated into an array of solid-state sensors to boost the analytical power of the system. Another benefit of an all silicon design will be that the gas/liquid membrane will be far more rigid and able to handle higher gas flow rates. It may also be possible, although much more difficult, to improve on the fundamental oxime chemistry in a way that increases reaction kinetics or allows the sensor to operate a higher temperatures.

3.5 References

1. Oh, I. and R.I. Masel, *Electrochemical organophosphate sensor based on oxime chemistry.* Electrochemical and Solid State Letters, 2007. **10**(2): p. J19-J22.
2. Oh, I., C.N. Monty, and R.I. Masel, *Electrochemical multiphase microreactor as fast, selective, and portable chemical sensor of trace toxic vapors.* Ieee Sensors Journal, 2008. **8**(5-6): p. 522-526.
3. Monty, C.N., I. Oh, and R.I. Masel, *Optimization of a multiphase sensor for detection of phosphonates in air.* Aiche Journal, 2010. **56**(1): p. 241-247.
4. Yeom, J., et al., *The design, fabrication and characterization of a silicon microheater for an integrated MEMS gas preconcentrator.* Journal of Micromechanics and Microengineering, 2008. **18**(12): p. 12.
5. Shortt, B.J., et al., *Miniaturized system of a gas chromatograph coupled with a Paul ion trap mass spectrometer.* Journal of Mass Spectrometry, 2005. **40**(1): p. 36-42.
6. Bessoth, F.G., et al., *Towards an on-chip gas chromatograph: the development of a gas injector and a dc plasma emission detector.* Journal of Analytical Atomic Spectrometry, 2002. **17**(8): p. 794-799.
7. Orient, O.J. and A. Chutjian, *A compact, high-resolution Paul ion trap mass spectrometer with electron-impact ionization.* Review of Scientific Instruments, 2002. **73**(5): p. 2157-2160.
8. Radadia, A.D., et al., *Micromachined GC columns for fast separation of organophosphonate and organosulfur compounds.* Analytical Chemistry, 2008. **80**(11): p. 4087-4094.
9. Radadia, A.D., et al., *Partially buried microcolumns for micro gas analyzers.* Analytical Chemistry, 2009. **81**(9): p. 3471-3477.
10. Radadia, A.D., et al., *The effect of microcolumn geometry on the performance of micro-gas chromatography columns for chip scale gas analyzers.* Sensors and Actuators B-Chemical, 2010. **150**(1): p. 456-464.
11. Radadia, A.D., et al., *The fabrication of all-silicon micro gas chromatography columns using gold diffusion eutectic bonding.* Journal of Micromechanics and Microengineering, 2010. **20**(1).
12. Chiriac, R.E., et al., *Development of a pre-concentrator-thermo-desorber/micro-gas chromatograph/mass spectrometer coupling for on-site analyses of emissions of volatile organic compounds from landfills.* International Journal of Environmental Analytical Chemistry, 2007. **87**(1): p. 43-55.
13. Lu, C.J., C.G. Jin, and E.T. Zellers, *Chamber evaluation of a portable GC with tunable retention and microsensor-array detection for indoor air quality monitoring.* Journal of Environmental Monitoring, 2006. **8**(2): p. 270-278.
14. Lu, C.J., et al., *Portable gas chromatograph with tunable retention and sensor array detection for determination of complex vapor mixtures.* Analytical Chemistry, 2003. **75**(6): p. 1400-1409.
15. Zhong, Q., W.H. Steinecker, and E.T. Zellers, *Characterization of a high-performance portable GC with a chemiresistor array detector.* Analyst, 2009. **134**(2): p. 283-293.

16. Wanekaya, A.K., et al., *Multicomponent analysis of alcohol vapors using integrated gas chromatography with sensor arrays.* Sensors and Actuators B-Chemical, 2005. **110**(1): p. 41-48.
17. Chapman, P.J., et al., *Facile hyphenation of gas chromatography and a microcantilever array sensor for enhanced selectivity.* Analytical Chemistry, 2007. **79**(1): p. 364-370.
18. Shopova, S.I., et al., *On-column micro gas chromatography detection with capillary-based optical ring resonators.* Analytical Chemistry, 2008. **80**(6): p. 2232-2238.
19. Sun, Y.Z., et al., *Rapid tandem-column micro-gas chromatography based on optofluidic ring resonators with multi-point on-column detection.* Analyst, 2010. **135**(1): p. 165-171.
20. Lee, C.Y., et al., *On-chip micro gas chromatograph enabled by a noncovalently functionalized single-walled carbon nanotube sensor array.* Angewandte Chemie-International Edition, 2008. **47**(27): p. 5018-5021.
21. Cruz, D., et al., *Microfabricated thermal conductivity detector for the micro-ChemLab (TM).* Sensors and Actuators B-Chemical, 2007. **121**(2): p. 414-422.
22. Terry, S.C., J.H. Jerman, and J.B. Angell, *Gas-chromatographic air analyzer fabricated on a silicon-wafer.* Ieee Transactions on Electron Devices, 1979. **26**(12): p. 1880-1886.
23. Sanchez, J.B. and F. Berger, *Towards a hybrid micro-device allowing the selective detection of hydrogen fluoride vapours in a complex mixture.* Talanta, 2009. **80**(1): p. 385-389.
24. Dori, L., et al., *A gas chromatographic-like system for the separation and monitoring of benzene, toluene and xylene compounds at the ppb level using solid state metal oxide gas sensors.* Sensors and Materials, 2000. **12**(3): p. 163-174.
25. Lewis, P.R., et al., *Recent advancements in the gas-phase MicroChemLab.* Ieee Sensors Journal, 2006. **6**(3): p. 784-795.
26. Akao, S., et al., *Development of microseparation column for ball surface acoustic wave gas chromatograph.* Japanese Journal of Applied Physics, 2008. **47**(5): p. 4086-4090.
27. Yamamoto, Y., et al., *Development of packed column for surface acoustic wave gas chromatograph using anodically bonded silicon-glass structure with a compression jacket.* Japanese Journal of Applied Physics, 2009. **48**(7).
28. Lambertus, G.R., et al., *Silicon microfabricated column with microfabricated differential mobility spectrometer for GC analysis of volatile organic compounds.* Analytical Chemistry, 2005. **77**(23): p. 7563-7571.
29. Lu, C.J., et al., *First-generation hybrid MEMS gas chromatograph.* Lab on a Chip, 2005. **5**(10): p. 1123-1131.
30. Ohira, S.I., et al., *Hybrid microfabricated device for field measurement of atmospheric sulfur dioxide.* Analytical Chemistry, 2002. **74**(22): p. 5890-5896.
31. Toda, K., et al., *Micro-gas analysis system for measurement of nitric oxide and nitrogen dioxide: Respiratory treatment and environmental mobile monitoring.* Analytica Chimica Acta, 2007. **603**(1): p. 60-66.
32. Takabayashi, Y., et al., *Development and optimization of a lab-on-a-chip device for the measurement of trace nitrogen dioxide gas in the atmosphere.* Analyst, 2006. **131**(4): p. 573-578.
33. Timmer, B.H., et al., *Miniaturized measurement system for ammonia in air.* Analytica Chimica Acta, 2004. **507**(1): p. 137-143.
34. Ohira, S.I. and K. Toda, *Micro gas analyzers for environmental and medical applications.* Analytica Chimica Acta, 2008. **619**(2): p. 143-156.

Chapter 4:

Oxime and Single-Walled Carbon Nanotube Based Sensors Integrated into a Micro-Machined Silicon Array

4.1 Introduction

In the previous chapter, I discussed the selective nature of the aqueous oxime based detection chemistry and its ability to respond to organophosphates, acetylcholinesterase inhibitors, and reactive acid anhydrides without being affected by the presence of other interferent species [1]. I also briefly described the design and optimization of the oxime micro-sensor developed by our research group and the improvements in performance as a result of transitioning to this micro-fluidic platform [2, 3]. Finally I went into detail on the studies performed to effectively couple this oxime micro-sensor with a gas chromatography (GC) system, particularly a micro-fabricated GC column which was also developed in our research group [4]. All the successful research shown thus far has laid the ground work for this chapter, in which the oxime micro-sensor will be further miniaturized by micro-fabricating the entire device out of silicon. This all silicon oxime micro-sensor will be integrated on-chip with several polymer coated single-walled nanotube-based (SWNT) sensors which have also been developed in our research group. Together, this micro-fabricated array of sensors will form a powerful detector package which will be capable of identifying a large variety of compounds. Ultimately, a comprehensive and portable analytical system could be created once this micro-sensor array is coupled with a GC micro-column.

4.1.1 Electronic noses

Sensor arrays for the detection of gaseous analytes are often referred to as electronic noses because of the parallels they draw with their biological counterparts. Biological olfaction systems consist of millions of receptor neurons which detect the presence of various types of compounds. Individually, an olfactory receptor (or sensor) is not particularly sensitive or selective to a specific chemical species. However, by utilizing the signals from millions of different receptors and analyzing this information with the processing power of the brain, the organism can detect and identify a remarkable number of compounds. Electronic noses seek to improve detection capability in a very similar manner. By combining several semi-selective sensors together in one package and analyzing their output with some type of pattern recognition software, much more information on the chemical identity of a sample can discerned compared to the case when an individual sensor used.

One of the first examples of electronic noses involved the research done by Persaud and Dodd using an array of three different commercial SnO_2 semiconductor sensors to identify the chemical signatures of compounds such as ethanol, amyl acetate and even coriander oil [5]. Since their research, electronic noses have been developed using almost every conceivable gas sensor technology available. Due to their commercial popularity, the use of metal oxide semiconductor sensors in arrays has been widely reported in literature. For example, Heilig *et al.* created a micro-fabricated array of six SnO_2 semiconductor sensors with an integrated heater system to detect CO and NO_2 in air [6]. Other semiconductor based sensor arrays have also been reported, such as a light addressable potentiometric sensor system integrated with live olfactory neurons for the detection of glutamic acid and other biological compounds [7]. Noble metal gas sensors have also been employed in electronic noses, such as the array of 4 gold and platinum sensors

created by Stetter *et al.* for the analysis of grain stock quality [8]. Chemi-resistive sensor technology is also used extensively in electronic noses. Fruend *et al.* created an array of 14 conductive polymer sensors for the detection of various volatile organic compounds (VOCs) such as acetone, benzene and ethanol. Other examples utilizing chemi-resistive sensors include a 3 sensor array using thin films of functionalized gold nanoparticles [9], as well as an array of four sensors created from different concentrations of conductive carbon black particles within insulating polymer fibers [10]. Examples of mass balance type sensor technology include the work by Senesac *et al.* to created a micro-fabricated array of 10 polymer functionalized micro-cantilever beam sensors for the detection of dioxane, dichloromethane, various alcohol [11]. Di Natale *et al.* used a series of 8 metalloporphyrin functionalized quartz crystal micro-balances as a rapid screening method for the detection of lung cancer by analyzing the VOCs emitted from patients' lungs [12]. Surface acoustic wave (SAW) sensors are another commonly used technology found in electronic noses. For example, an array of 4 polymer coated SAW sensors was used to detect organophosphate and organosulfate compounds [13], while various dendrimer molecules were used to functionalize an array of 5 SAW sensors for the detection of VOCs [14]. Even optical based sensor methods have be used in electronic noses. Rakow and Suslick created 11 different metalloporphyrins immobilized in both silica and micro-fabricated polymer films, and measured the resulting color change of the array when exposed to pyridine, acetone, ethanol, benzene and other VOCs (figure 4.1) [15]. Absorption or fluorescent based micro-sensor arrays can also be easily fabricated by individually functionalizing the terminating ends of optical fibers with dyes or other optically active reagents in a polymer matrix [16, 17]. This list is by no means comprehensive and only covers a small portion of the various sensor arrays which have been developed thus far [18, 19].

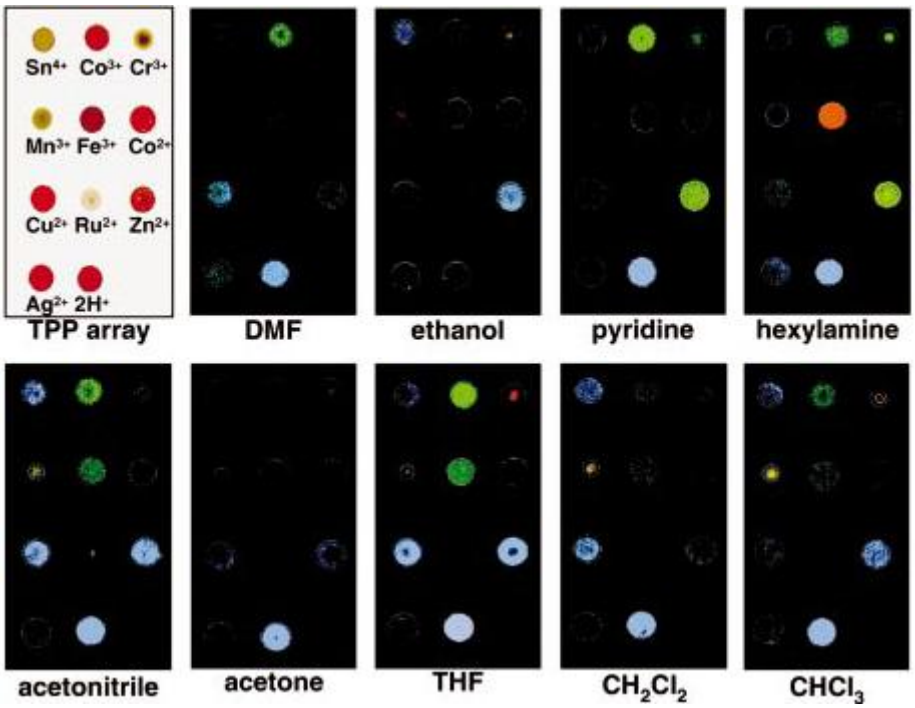

Figure 4.1: Optical absorption based sensor array utilizing various metalloporphyrin compounds created by Rakow and Suslick [15]. Array undergoes color change when exposed to various compounds.

The detection capabilities of electronic noses have been evaluated in many real world situations. Sensor arrays have been used to identify the type and/or quality of beer [20], milk and dairy products [21], grain [8], and other various food stuffs [22-24]. They have also been applied to health related detection issues. For example, Gardner *et al*. used a commercially developed array of semiconductor sensors for bacterial infection identification in both cow and human subjects [25]. Sensor arrays have been employed to address environment problems, such as waste water odor quantification [26]. Electronic noses have clearly demonstrated their potential in these examples as well as in a number of other real world applications [18, 19, 27].

Due to the analytical power of these sensor arrays and signal processing techniques, most electronic noses are operated without the use of any mixture separation or chromatographic equipment. This simplifies their operation, minimizes their total device footprint and cost, and reduces the number of system parameters which must be optimized for a given detection situation. In fact, operating in a continuous detection mode without a chromatography system is required when the response time of individual sensors are either too slow or differ greatly from each other. For our research however, the oxime and SWNT-based sensors which will be used in the integrated silicon array can respond very rapidly to the presence of an analyte. Although not studies in this chapter, the ultimate goal for this micro-fabricated sensor array is to couple it with a GC column such as the micro-fabricated one created in our research group [4, 28-30]. This will allow the sensor array to analyze compounds individually; increasing the detection accuracy and simplifying the signal processing algorithm needed.

4.1.2 Signal processing for sensor arrays

Signal processing is outside the scope of our research on this integrated silicon micro-sensor array; however for the sake of completeness I will briefly discuss the major techniques used. Electronic noses consist of multiple individual sensors created or operated in some fashion that makes each unit partially unique. Most sensor technology used in these arrays is semi-selective. That is to say, an individual sensor will preferentially respond to a particular compound or functional group within a molecule, however it will still respond to other compounds to a lesser degree. Within an electronic nose, several sensors may respond at different magnitudes when exposed to a single compound. This cross-sensitivity inherent in

most sensor arrays is what necessitates the use of complex statistical signal processing techniques.

As was mentioned earlier, most electronic noses are operated in a continuous sample flow mode. The response of the array is then taken from the steady-state values of the individual sensors, ignoring the more complex and difficult to analyze transient behaviors. Drawbacks of this operation mode include lengthy detection times required for all sensors to reach a steady-state, response from slow sensors being difficult to distinguish from environmental drift, and the possibility that extended analyte exposure will permanently alter or damage the sensor response [31]. Additionally, the time-dependent aspects of a sensors' signal can also hold a great deal of information regarding the compound(s) being detected. In the case of the micro-fabricated sensor array being developed in this chapter, the system will be tested with "pulses" of analyte and therefore only transient signals will be measured from the individual detectors. In this situation, the maximum value of a sensors transient signal will be used as its response to a compound. Finally, before the output of a sensor array can be analyzed by a signal processing technique, some amount of pre-processing of the data is usually required. This can depend on whether the electronic nose is being used primarily in a quantitative versus qualitative manner, and can involve averaging, normalizing or linearizing of an individual sensors response [31].

If the electronic nose is being used to compare unknown samples to a single reference sample or between two reference samples, simple graphical representations can be used to visually analyze the data. For more complex situations, several statistical analysis techniques are available which rely on pattern recognition (PARC). These various techniques can be classified as linear or non-linear depending on how they combine the signals from all individual sensors, as well as supervised versus unsupervised depending on whether they utilize responses from known

samples to form the basis of the analysis model. Two common examples of these PARC methods include principle component analysis (PCA) and artificial neural networks (ANN) [23]. PCA is a linear, unsupervised analysis technique which reduces the dimensionality of the data down to a few "principle components" so that it can be easily mapped in 2 or 3-D space. The unknown data can then be plotted in this reduced dimensional space and visually grouped into discrete regions indicating similarity between unknowns [31]. ANN is a non-linear, supervised technique which attempts to simulate the analytical process of biological neural networks [23]. In an ANN, a set of various algorithms working in parallel are used to link the input and output signals of the method. The connectivity of the input, output, and "hidden" algorithms, which are collectively referred to as neurons, is determined using a set of known responses from the sensor array [31]. Through an iterative process, the ANN "learns" or adapts to the known data, and the connectivity between the various neurons is tuned [23]. Once this analytical network has been developed, it can then be used to evaluate unknown samples.

4.1.3 Single walled carbon nano-tube (SWNT) based sensors

Single wall carbon nanotubes (SWNTs) are unique fullerene materials with great mechanical strength, high thermal conductivity and tunable electronic properties. This makes them a popular research material in a variety of applications, including gas detection. The use of SWNTs in gas sensors originates from the work by Collins *et al.* and Kong *et al.*, who measured the change in capacitance of a thin film of this material when exposed to different gaseous compounds [32, 33]. Since this research was published, many other groups have developed various chemi-resistive [34-38] as well as chemi-capacitive SWNT-based gas sensors [37, 39]. Three electrode chemi-transistive SWNT-based sensors have also been developed in an effort to improve the

sensitivity and the adsorption reversibility of these types of detectors [40-42]. A great deal of the performance of any SWNT-based sensor is associated with the method used in fabricating the gas sensitive portion of the device. The common feature in all the sensor types just discussed is the thin film of SWNTs which is used to bridge a small gap between two metal electrodes on an insulating surface. Many methods have been used to fabricate this SWNT film, each with their own benefits and drawbacks. SWNT films can be deposited via solvent evaporation techniques which are relatively simple to implement, however this method yields poor film thickness uniformity within each sensor as well as between sensors [35, 43]. Chemical vapor deposition (CVD) can be used to physically grow the SWNT film directly on the sensor substrate in very specific regions [36]. While this method could easily be incorporated into sensor micro-fabrication processes, CVD is a complex technique which is difficult to control and a gives much lower yields compared to the previous deposition method. Another method for SWNT film creation is AC dielectrophoresis, which utilizes the two electrodes in the sensor to locally apply an electric field to a small drop of solution containing the SWNTs. The SWNTs will align with the electric field and deposit between the electrodes in an ordered, uniformly distributed fashion [41]. However, in practice this method is also difficult to use reliability due to the number of parameters involved which must be simultaneously optimized. Finally, films of SWNTs can also be deposited via a vacuum filtration and transfer method. This process involves vacuum filtering a solution of SWNTs onto a porous membrane. Once the membrane is dry, it can be cut to fit the desired region on the sensor, then the SWNTs can be transfer printed to the surface and the filtration membrane can be removed or dissolved [44, 45].

Theoretically, SWNTs-based sensors created with a reliable and robust fabrication method will all be identical to each other and respond equally to a given analyte. Several

techniques have been utilized to tune the selectivity of these SWNT-based sensors. Polymers can be incorporated directly into the films by adding them to the SWNT solution and then depositing the mixture via the solvent evaporation method, but again, this process suffers from uniformity issues [38, 46]. The SWNTs can also be covalently modified with polymer molecules to impart a degree of selectivity to the sensors, however this method can negatively affect the electronic properties of the SWNTs and degrades the sensor performance [47]. Finally, electropolymerization can be used to grow a thin layer of polymer over the previously deposited SWNT film [48, 49]. Using the sensor itself as the working electrode, a solution of the monomer can be held in place on the surface and the polymer can be grown by applying a voltage to the electrodes. The polymerization process is conveniently localized at the active area of the sensor, the thickness can be controlled electrochemically and the films produced have good uniformity.

The silicon array detailed in this chapter will incorporated a SWNT-based sensor fabrication process developed in our research group [50]. A schematic of a typical SWNT-based sensor created with our fabrication process is given in figure 4.2.

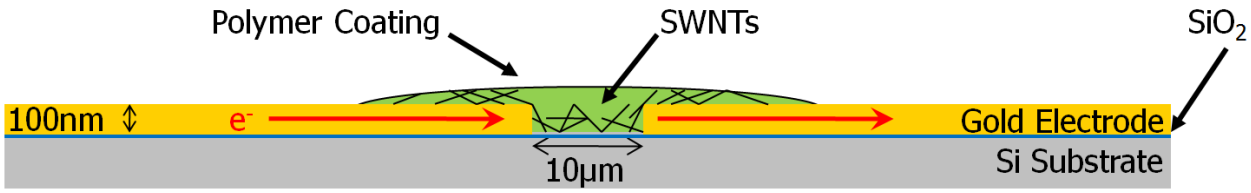

Figure 4.2: Typical SWNT-based sensor used in our silicon micro-sensor array. Not to scale.

This SWNT-based sensor is micro-fabricated on a silicon substrate with a thin layer of thermally grown SiO_2 on the surface to electrically isolate the gold electrodes. The SWNT film is then deposited over the 10 µm gap between electrodes using the vacuum filtration/transfer method discussed previously. Once the SWNT film has been successfully deposited, the active

area of the sensor can be coated by an electropolymerized layer to tune the detector selectivity. Detailed micro-fabrication steps will be given in section 4.3.1. Research in our group has shown that sensors micro-fabricated by this process are sensitive, respond rapidly and the analyte adsorption on their surface is highly reversible if operated at sufficient driving currents [51-53].

4.2 Integrated micro-sensor array design

The design requirements set forth for this silicon micro-sensor array were the following. The micro-sensor array must contain 7 SWNT-based sensors as well as 1 aqueous oxime based sensor. The integrated device can be as tall as necessary; however it must have a square footprint of 1.4 × 1.4 cm on each side. This would make it identical in size to the partially-buried micro-column (PBMC) previously developed in our group [4] and could later be easily coupled with this device to create a silicon micro-GC stack. All electronic connections to this array must originate from the top side of the device, while all fluidic connections, both gaseous and liquid, must originate from the bottom side of the device. This would allow for the PBMC to be directly bonded to the bottom of the micro-sensor array without interfering with the electrical connections. Independent testing of this array without a coupled micro-column is necessary, and therefore the fluidic connections were also designed to accommodate two varieties of fused silica capillaries. Inlet fluidic connections were designed to hold 360 μm O.D. (100 μm I.D., IP-deactivated, No. 10100, Restek) capillaries while the outlet fluidic connections were designed to hold larger 690 μm O.D. (530 μm I.D., IP-deactivated, No. 10043, Restek) capillaries. Finally, in an effort to ensure that the SWNT-based sensors could always be regenerated after exposure to a gas sample, a resistive heater element will be integrated beneath the 7 SWNT-based sensors. The studies performed in the previous chapter show that the oxime sensor has a maximum

operation temperature of approximately 50 °C, however the SWNT-based sensors have a much higher safe operating temperature of 80 °C. To prevent disruption of the oxime micro-sensor from the use of the integrated resistive heating element, the two types of sensors must be partially thermally isolated from one another.

There are many design challenges associated with the development of this micro-fabricated sensor array. This array will be tested by sending "pulses" of analyte through the device in an inert carrier gas flow. To maintain similar detection characteristics for all sensors in the array, the "pulse" of analyte should not significantly change as it travels through the device. In general for any micro-sensor array design, the gas channel within the device must have minimal and gradual channel cross-section expansions/changes, and dead-space volumes must be minimized. The ordering of the sensors in the array can be done in a parallel or series fashion. For parallel sensors, the analyte "pulse" must be divided up equally, however it has the benefit of preventing up-stream sensors from affecting down-stream sensors and detection will occur at roughly the same moment for all sensors. A series arrangement of sensors removes the need for a complex gas distribution manifold; however the order of detection is critical to prevent sensors from interfering with each other.

Unlike the individual SWNT-based sensors, research in our group on the aqueous oxime based sensor was successful in only partially micro-fabricating the device from silicon [54]. The bulk of this oxime sensor was created from micro-machined silicon however it still required the use of a polymer based porous membrane layer. Unfortunately, such a membrane will not be compatible with the design of this all silicon array. Finally, the design of this micro-sensor array will most likely require the use of several layers of micro-machined silicon wafers. Therefore, it will be necessary to develop a method of wafer bonding, either by using a polymer adhesive or

via a more direct silicon to silicon bonding process. It is also necessary to provide a minimum of 500 μm of separation between gas and/or fluidic channel features or between the channel and the edge of the device, in order to ensure there is sufficient surface area for bonding and prevent leakage from occurring.

The first iteration of the silicon micro-sensor array design after taking into account all the design requirements as well the inherent micro-fabrication limitations is shown in figures 4.3 – 4.6. This device is a 4 layer (4 micro-machined silicon wafers) stack with the sensors arranged in a series configuration. Unlike the SWNT-based sensors, the oxime based sensor will consume a portion of the analyte "pulse" it is exposed to due to the reaction with the aqueous oxime reagent. Additionally, the oxime sensor continuously releases a small amount of water vapor into the carrier gas stream due to evaporation. To prevent this sensor from interfering with the SWNT-based sensors, it is placed last in the series of detectors in the device.

Figure 4.3 shows a simplified depiction of the silicon micro-sensor array stack including fluidic and electrical connections. The layers are numbered 1 – 4 starting at the bottom most wafer. The gaseous stream is colored red while the aqueous streams are colored blue. All gold contacts/leads/electrodes are in yellow and the wafer itself is grey. This color scheme will be used for figures 4.3 – 4.6. Electrical connections originate from layer 1 and layer 3 for the SWNT-based sensors and oxime based sensor, respectively.

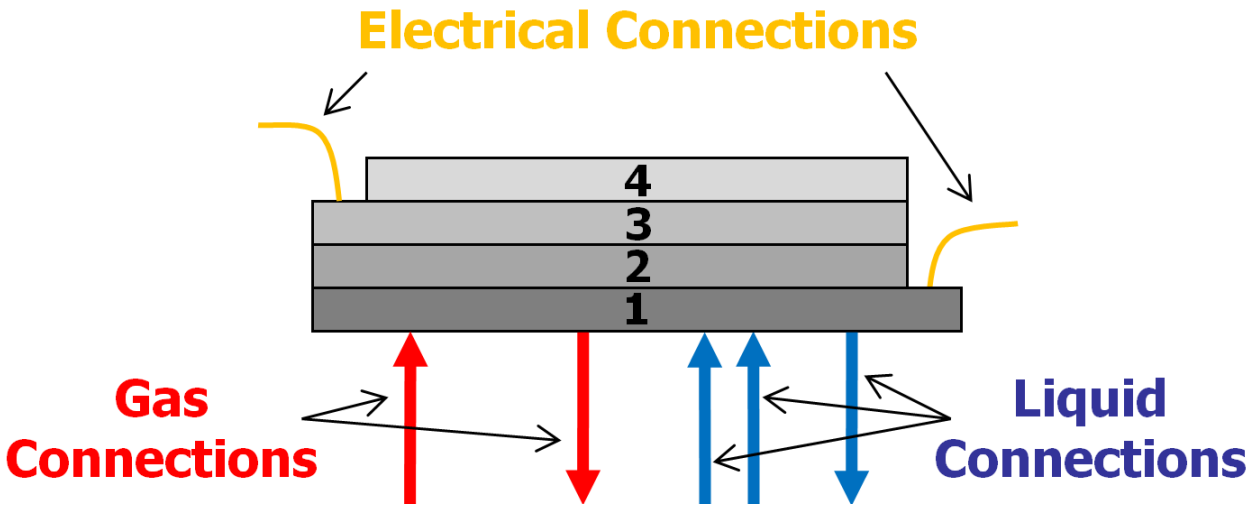

Figure 4.3: Simplified side profile of silicon micro-sensor array stack. Not to scale.

Figure 4.4 shows the configuration of the device between layers 1 and 2 (i.e. the top of layer 1 and the bottom of layer 2). The gas stream is seen entering the device from a small through-hole in the bottom of layer 1. It then proceeds to flow past the 7 SWNT-based sensors also located on layer 1. The view of the bottom of layer 2 shows the gas micro-channel directing this flow. The active area of these chemi-resistive sensors is obscured by the gas flow arrow and the 10 µm gap between electrodes would not be visible at this resolution even if the flow arrow were not present. It should be noted that each SWNT-based sensor has 4 gold leads connected to it (2 per electrode). This allows voltage to be measured using one pair of leads and current with the other two. The large gold squares at the end of the each lead are necessary to provide adequate surface area for the gold wire bonding process which will connect the device to external circuitry. Also not shown in this figure is the resistive heating element integrated into the silicon wafer below the array of SWNT-based sensors. However, one of the gold contact pads for this heating element is visible at the far corner of layer 1 while the other is located just out of view at the other end of the row of sensors.

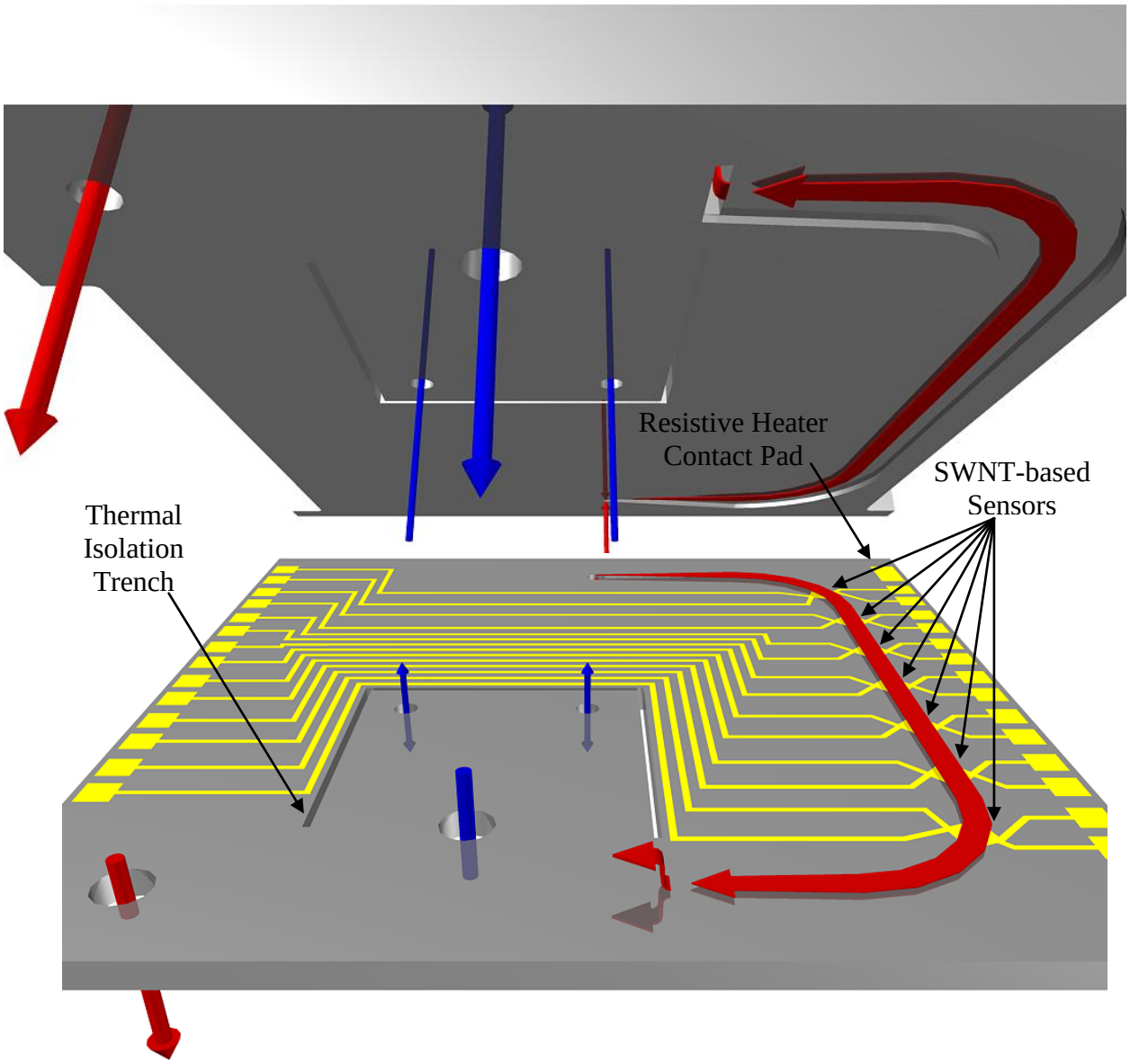

Figure 4.4: Rendering of micro-sensor array design between layers 1 and 2. This diagram is to scale.

After passing over all 7 SWNT-based sensors, the gas stream is diverted up through layer 2 towards the oxime sensor. Also shown in figure 4.4, there are 2 inlet liquid streams, one contain a solution of the oxime in ethanol and the other a basic aqueous buffer solution. These two solutions are a product of the research discussed in Chapter 1 and allow the oxime reagent to

be dissolved in a fluid while avoiding the long term degradation experienced in aqueous solutions. The third liquid stream is the waste from the oxime sensor. Finally, the thermal isolation trench can be seen which extends through all 4 layers of the device and partially surrounds the oxime sensor found in layers 3 and 4. This will shield the oxime sensor from the effects of the resistive heating element.

Figure 4.5 shows the configuration of the device between layers 2 and 3. After the gaseous stream has travelled through layer 2 the majority of it flows to the exit through-hole at the corner of the device. However, a portion of this stream diffuses up through a porous silicon "membrane" (not seen) in layer 3 and into the aqueous stream of the oxime sensor. What can be seen in the figure is the continuation of the gas micro-channel etched in the bottom of layer 3. In figure 4.5 we also see the thermal isolation trench and liquid streams continuing up through the device as well as the gold wire bonding contact pads exposed on either side of the stack.

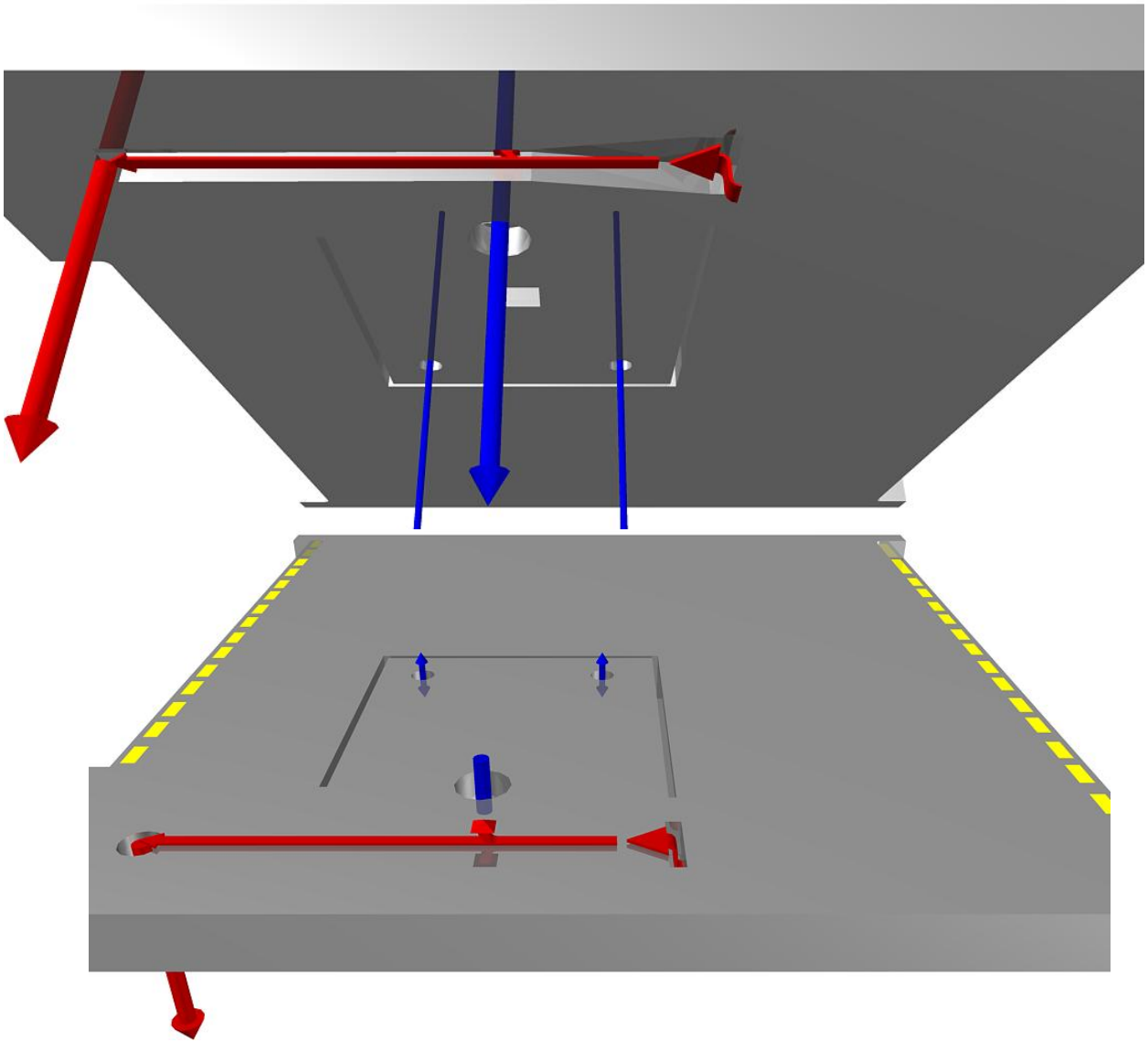

Figure 4.5: Rendering of micro-sensor array design between layers 2 and 3. This diagram is to scale.

Finally, figure 4.6 shows the structure of the micro-sensor array stack between layers 3 and 4. The "working" and "reference" electrode of the oxime sensor can be seen, each with a single lead that ends in a gold wire bonding contact pad just out of view on the left.

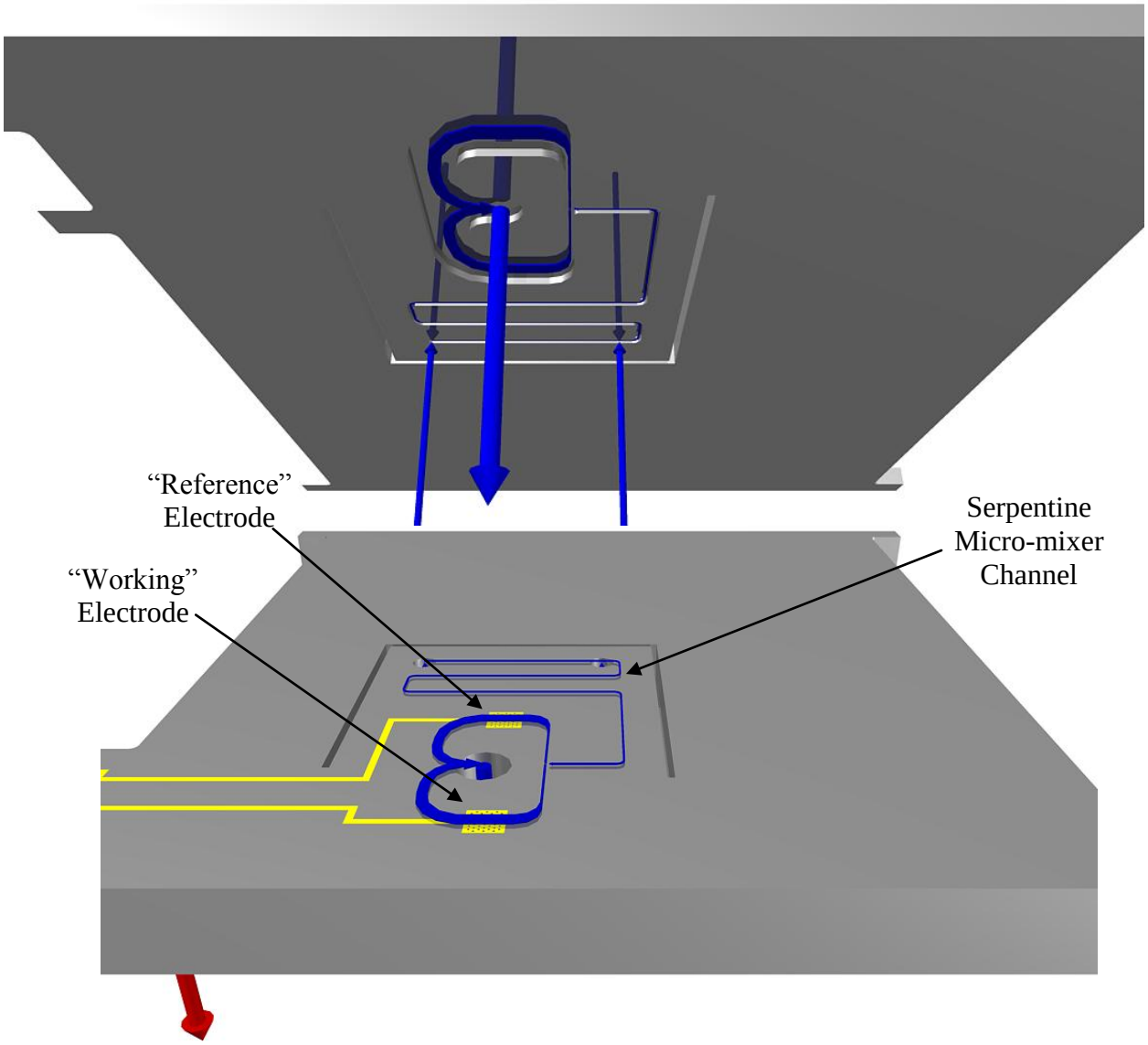

Figure 4.6: Rendering of micro-sensor array design between layers 3 and 4. This diagram is to scale.

Each electrode covers the surface of a porous silicon "membrane" consisting of holes 30 µm in diameter and 20 µm deep, spaced 70 µm apart. Although the polycarbonate membrane used in the stand alone oxime micro-sensor had 50 nm diameter pores, due to limitations in the etching technique, the smallest pore size which could be reliability fabricated was 30 µm. The

20 μm depth of the membrane is a result of the thickness of the device layer in the silicon on insulator (SOI) wafer used. Also integrated into the oxime sensor in this array is a serpentine micro-mixer channel, which serves to combine the oxime/ethanol solution with the aqueous buffer solution via diffusion.

4.3 Array fabrication process

4.3.1 Layer 1 (SWNT-based sensor layer)

Layer 1 was fabricated from a 550 μm thick <100> intrinsic silicon wafer (>1000 Ω×cm, p-doped, single side polished, Ultrasil). All photolithography steps for this layer were performed using plasma resistant photo-resist AZ-4620 (HD AZ Electronic Material). Alignment marks for the subsequent steps were first patterned onto the top side of this wafer using standard photolithography techniques and then inductively coupled plasma deep reactive ion etching (ICP-DRIE) was used to cut the pattern 10 μm into the surface. The resist was then removed and the wafer was placed into a dry oxidation furnace to grow a 500 nm layer of SiO_2 (1150 °C, 6 sccm O_2) (figure 4.7A). The resistive heating element profile was patterned onto the top side of the wafer and the SiO_2 layer was selectively removed using a buffered oxide etch (BOE). The resist layer is once again removed and the wafer is placed into a boron tube furnace for diffusive doping. The remaining SiO_2 on the wafer serves as a diffusion mask for this doping step. A p-type resistive heating element was created using a solid boron doping source in the tube furnace (40 minutes, 1000 °C, 6 sccm N_2) (figure 4.7B). The remaining SiO_2 layer was completely removed via a BOE then re-grown to a thickness of 500 nm in the dry oxidation furnace (1150 °C, 6 sccm O_2). This layer of SiO_2 will serve to electrically insulate the SWNT-based sensors from each other and prevent any shorts. Heater contact pads were photolithographically

patterned on the surface over top of the ends of the p-type heater element. The wafer was then subjected to a BOE to selectively remove the SiO_2 layer and reveal the doped silicon of the heater element. A 0.1 µm thick layer of chromium was sputtered on the top of the wafer to act as an adhesion promoter for the gold contact pads. This was subsequently followed by the deposition of a 1 µm thick layer of sputtered gold. The unneeded metal, as well as the resist were then removed in a lift-off technique. The wafer was then annealed in a tube furnace to create ohmic contacts between the gold pads and the p-type silicon of the heater element (15 minutes, 370 °C, 4 sccm N_2) (figure 4.7C). The top of the wafer was again patterned via photolithography for the SWNT-based sensor electrodes/leads/contact pads. Chromium and gold were once again sputtered onto the top surface of the wafer at 0.1 µm and 1 µm thickness, respectively. Resist lift-off was then performed to remove the unneeded metal layers as well as the photo-resist (figure 4.7D). The wafer was cleaned in SC-1 solution (10:2:1 ratio of H_2O:H_2O_2:NH_4OH) and a self assembled monolayer (SAM) of 3-aminopropyl triethoxysilane (APTES) was grown on the wafer to increase SWNT adhesion (solution of 1 ml APTES in 200 ml acetone). Photo-resist was applied to both sides of the wafer and the back side was patterned for the various fluidic through-holes, the thermal isolation break and the die edges. Then using ICP-DRIE, the capillary through-holes, the thermal isolation break and the die edges were etched all the way through to the other side of the wafer (figure 4.7E).

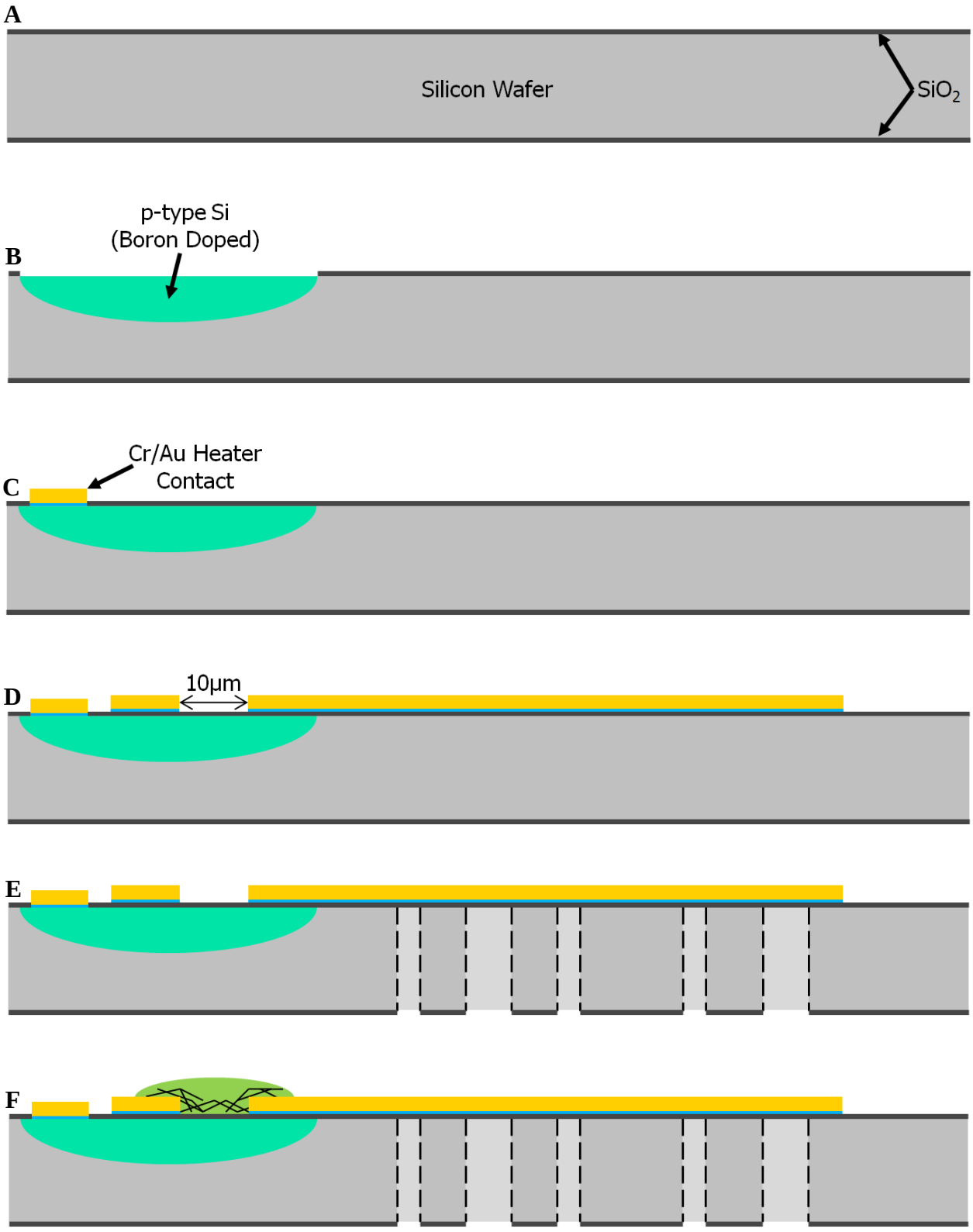

Figure 4.7: Cross-sectional diagram of layer 1 at various steps in the micro-fabrication process.

Not to scale.

With cleanroom micro-fabrication on layer 1 complete, the individual SWNT-based sensors could now be fabricated. First, 10 mg of purified SWNTs are suspended in 100 mL of an aqueous solution containing 1% sodium dodecyl sulfate (SDS) as a surfactant. This solution is sonicated and stirred multiple times, then centrifuged for 6 hours at 4100 RPM (2800 g). The liquid phase is decanted off and vacuum filtered onto a mixed cellulose ester (MCE) membrane (47 mm diameter, 0.22 micron pore size, Millipore). Care was taken during the filtration process to not introduce bubbles which would lead to non-uniformities in the SWNT film. After the MCE membrane had dried, it was washed with water using the vacuum filtration system until all traces of SDS were removed. A 1 mm diameter circle of SWNT-MCE membrane was removed from the vacuum filtered film using a hole punch. Using the wetting surface tension effects from a drop of water, the 1 mm MCE membrane punch out was inverted and aligned over the gap between the two electrodes of an individual sensor. Once the MCE membrane firmly in place, it was dissolved with an acetone vapor bath for ~4 minutes leaving only the SWNT film. This was followed by a liquid acetone bath for 10 minutes, a nitrogen dry, and back into the acetone bath for an hour. Finally, the sensor is washed briefly in methanol, 2-propanol, water, and dried with nitrogen to ensure the complete removal of the MCE membrane. Electropolymerization was performed using a syringe containing the monomer in an aqueous buffer solution. A drop of this solution was held in place over the SWNT-based sensor between the surface of the wafer and the tip of the syringe which was in close proximity. The hydrophobicity of the APTES coated silicon surface prevents the droplet from spreading out across the wafer. Integrated into the syringe are a Ag/AgCl reference electrode and a platinum (Pt) counter electrode. Electropolymerization was performed using cyclic voltametry (CV) over a potential range specific to the monomer being utilized. Figure 4.7F shows the finished state of layer 1.

Photographs of the top and bottom of a typical layer 1 affixed into the device holder and wire bonded to the external pins is given in figure 4.8.

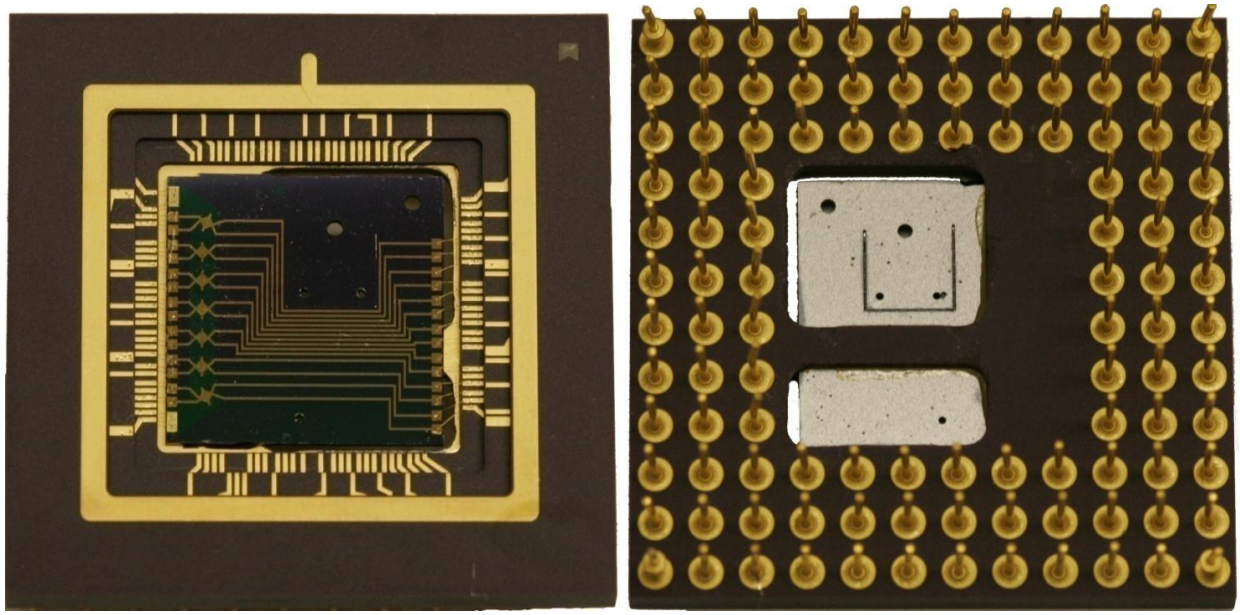

Figure 4.8: Photograph of the top and bottom of a completed layer 1.

4.3.2 Layer 2 (Gas micro-channel layer)

Layer 2 was fabricated from a 400 µm thick <100> p-doped silicon wafer (10 Ω×cm, double side polished, Ultrasil). All photolithography steps for this layer were performed using plasma resistant photo-resist AZ-4620 (HD AZ Electronic Material). The top side of the wafer was patterned for the fluidic through-holes, the thermal isolation break and the die edges, while the bottom side of the wafer was patterned for the gas micro-channel (figure 4.9A). Using ICP-DRIE, the gas micro-channel was created by etching 100 µm into the bottom of the wafer (figure 4.9B) while the fluidic through-holes, the thermal isolation break and the die edges were etched from the top all the way through to the bottom of the wafer. Once this was complete, the remaining resist was removed (figure 4.9C). A photograph of the top and bottom of a typical layer 2 is given in figure 4.10.

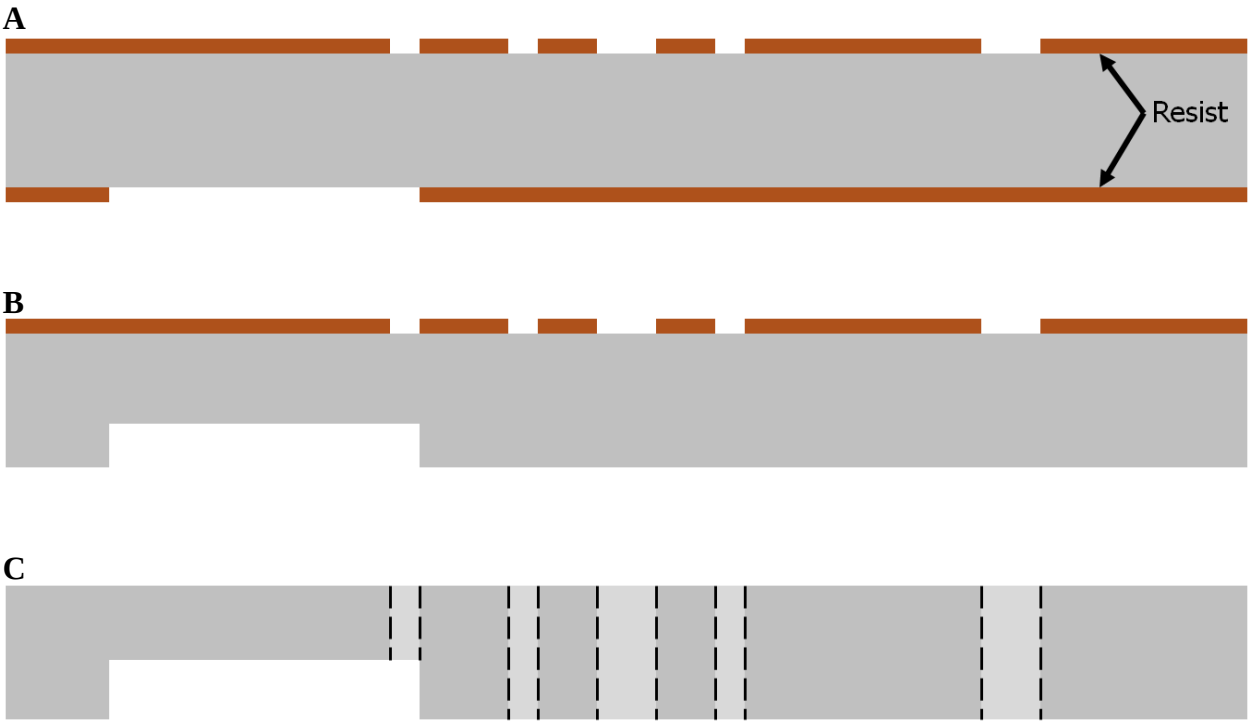

Figure 4.9: Cross-sectional diagram of layer 2 at various steps in the micro-fabrication process.

Not to scale.

Figure 4.10: Photograph of the top and bottom of a completed layer 2.

4.3.3 Layer 3 (Oxime sensor and gas/liquid membrane layer)

Layer 3 was fabricated from a silicon on insulator (SOI) wafer with a 400 µm thick <100> p-type handle wafer and a 20 µm thick <100> p-type device wafer separated by a 1 µm buried oxide (BOX) layer (Double side polished, Ultrasil) (figure 4.11A). All photolithography steps for this layer were performed using plasma resistant photo-resist AZ-4620 (HD AZ Electronic Material). The wafer was first placed into a dry oxidation furnace to grow a 500 nm layer of SiO_2 (1150 °C, 6 sccm O_2) (figure 4.11B). This layer of SiO_2 will serve to electrically insulate the oxime electrodes from the bulk silicon and prevent a short. Photo-resist was then applied to the top of the wafer and patterned for the oxime sensor electrodes, leads and contact pads. Chromium and gold were sputtered onto the top surface of the wafer at 0.1 µm and 1 µm thickness, respectively. Resist lift-off was then performed to remove the unneeded metal layers as well as the remaining photo-resist (figure 4.11C). After this, both sides of the wafer were coated in resist; the top is patterned for the membrane pores as well as the fluidic through-holes, the thermal isolation break and the die edges, while the bottom is patterned for the gas micro-channel as well as the fluidic through-holes, the thermal isolation break and the die edges. The exposed portions of the oxime electrodes are removed using chromium and gold etching solution. The thermal oxide layer on both sides of the wafer is then etched using Freon reactive ion etching (RIE) (24 sccm CF_4, 3 sccm O_2). ICP-DRIE is used to etch the top of the wafer 20 µm through the silicon device layer to the BOX layer which acts as a precise etch stop (figure 4.11D). The bottom of the wafer is then etched approximately 400 µm through the silicon handle layer to the BOX layer using ICP-DRIE. By utilizing the BOX layer of an SOI wafer as an etch stop, we can ensure the oxime sensor membrane is of uniform thickness and can be reliability produced. Finally, the 1 µm BOX layer is removed via Freon RIE (24 sccm CF_4, 3

sccm O_2) to connect the top and bottom of the layer and all of the remaining resist is removed (figure 4.11E). A photograph of the top and bottom of a typical layer 3 is given in figure 4.12.

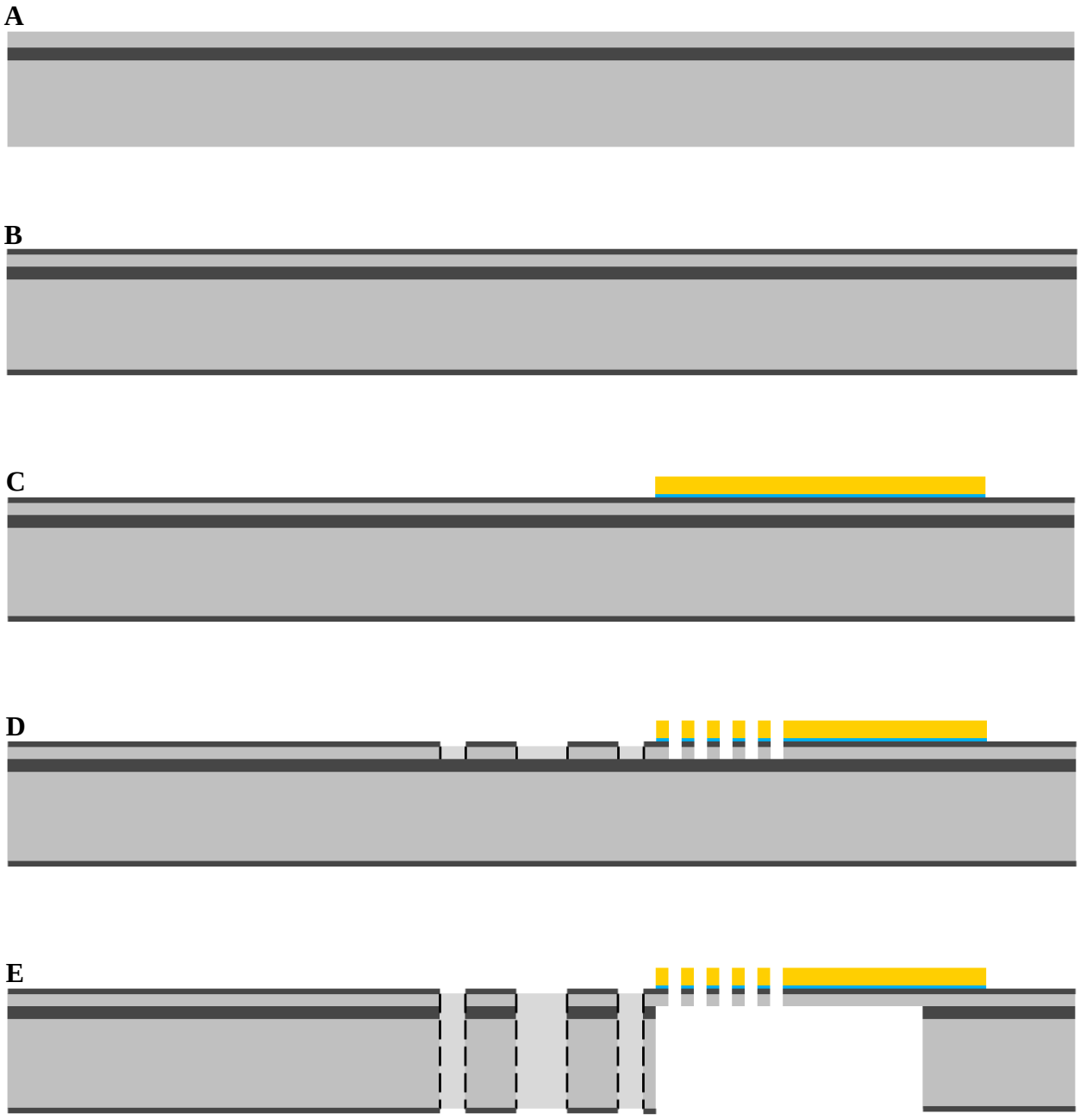

Figure 4.11: Cross-sectional diagram of layer 3 at various steps in the micro-fabrication process. Not to scale.

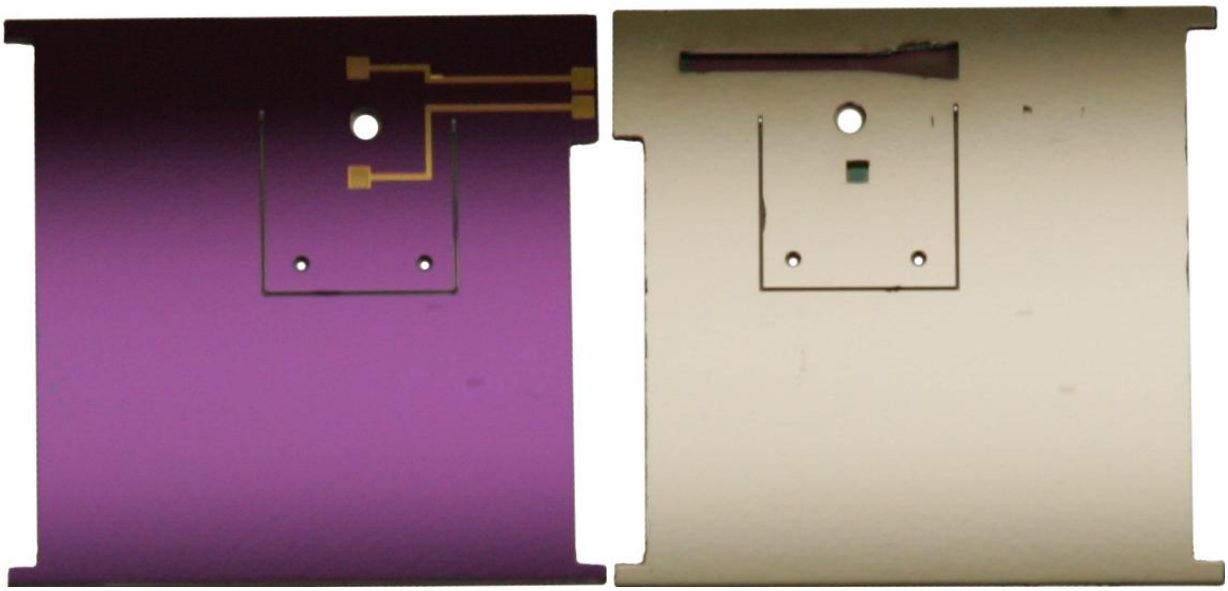

Figure 4.12: Photograph of the top and bottom of a completed layer 3.

4.3.4 Layer 4 (Liquid micro-channel layer)

Layer 4 was fabricated from a 400 µm thick <100> p-doped silicon wafer (10 Ω×cm, double side polished, Ultrasil). All photolithography steps for this layer were performed using plasma resistant photo-resist AZ-4620 (HD AZ Electronic Material). Photo-resist was applied to both sides of the wafer; the bottom was patterned for the liquid micro-channel while the top was patterned for the thermal isolation break and the die edges (figure 4.13A). Using ICP-DRIE, the liquid micro-channel was created by etching 100 µm into the bottom of the wafer while the thermal isolation break and the die edges were etched from the top all the way through to the bottom of the wafer. Once this was complete, the remaining resist was removed (figure 4.13B). A photograph of the top and bottom of a typical layer 3 is given in figure 4.14.

A complete list of the fabrication steps for all layers is given in appendix A. All photolithography mask used in the fabrication of this device are shown in appendix B.

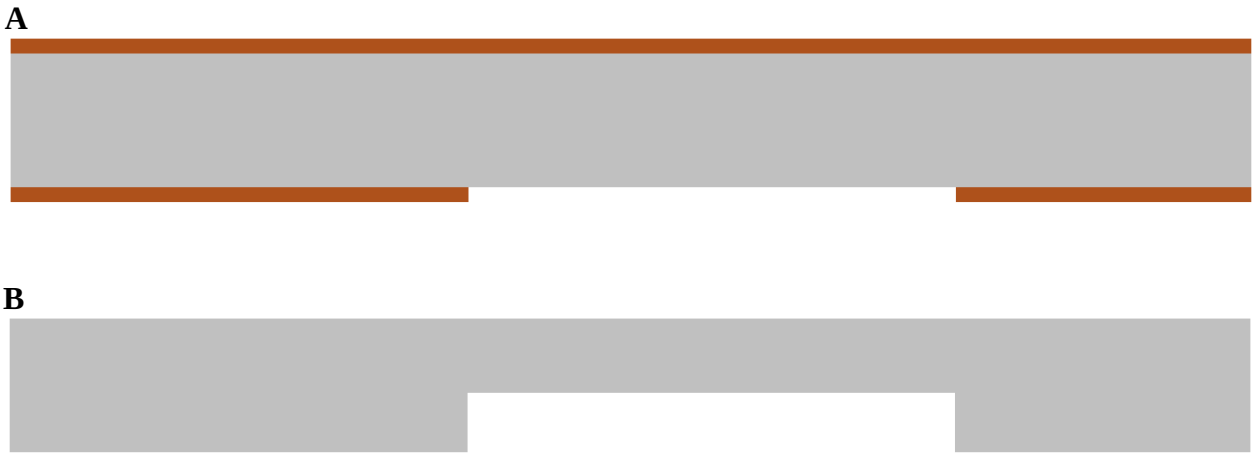

Figure 4.13: Cross-sectional diagram of layer 4 at various steps in the micro-fabrication process. Not to scale.

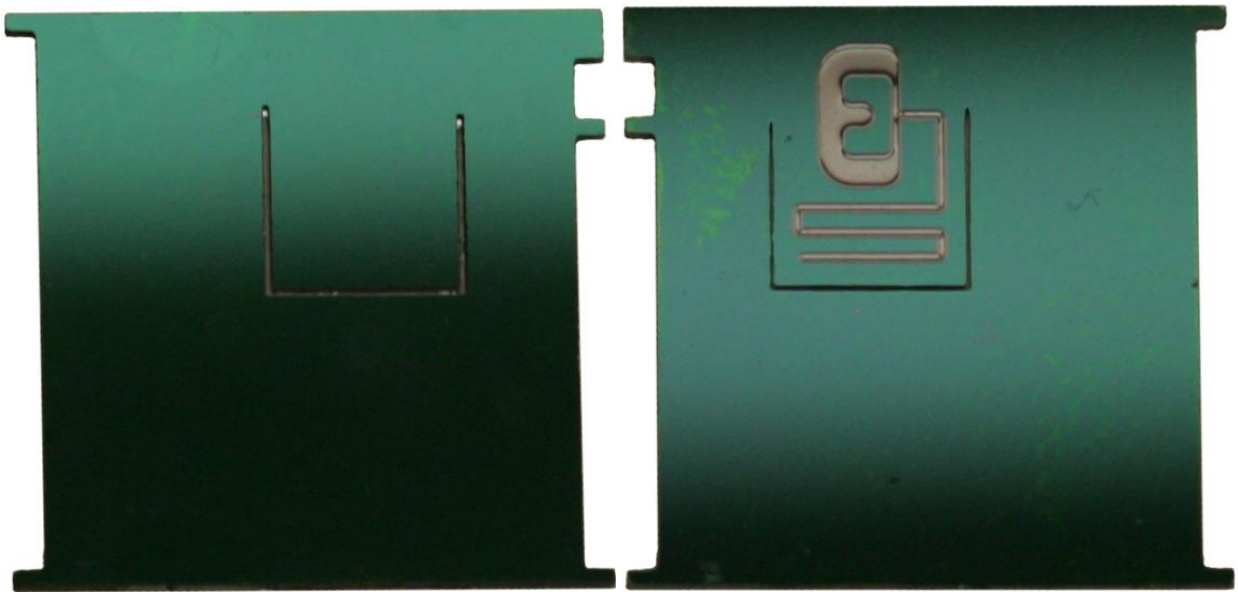

Figure 4.14: Photograph of the top and bottom of a completed layer 4.

4.3.5 Device assembly

The silicon micro-sensor array has a total of 32 gold contact pads which must be individual addressed. To do so, a commercial pin grid array (PGA) integrated circuit (IC) package was modified to accommodate the micro-sensor array stack. A portion of the bottom of the PGA package was removed to allow for access to the fluidic through-holes on the device. Layer 1 is then affixed to the PGA package with conductive silver epoxy (Epotek, h20e). Once the epoxy has cured, the gold contact pads from layer 1 are connected to the corresponding gold contacts on the PGA package using a gold wire bonding machine (4524 K&S gold wire ball bonder). Figure 4.8 shows layer 1 attached and fully wire bonded into the PGA package.

High temperature wafer bonding techniques could not be utilized to assemble the array stack as this would damage the SWNT-based sensors. Instead, a polymer adhesive bonding process would be used, so long as it did not require curing the adhesive at temperatures higher than 80 °C. Additionally, the use of a polymer adhesive would also ensure the gold electrical contacts/leads remained electrically isolated from each other. After much trial and error testing of various products, a silicone based adhesive (GE RTV108 Silicon Adhesive) was finally chosen for the die bonding process due to the ease in which it could be applied to a PDMS puck in a uniform and thin manner, as well as its ability to transfer from the puck to the surface of the die without obstructing the micro-channels. The silicon adhesive was applied via this transfer process to the bottom of layer 4, and bonded to layer 3. Silicon adhesive was then transferred to the bottom of this stack and layer 2 was bonded. Finally, adhesive was applied to the bottom of the layer 2 – 4 stack and this was bonded with layer 1 in the PGA package. The adhesive was allowed to cure over night and then the 2 remaining gold contact pads from the oxime sensor were wire bonded to the contacts in the PGA package.

The final stage in assembling this micro-sensor array was the connection of the capillaries for liquid and gas streams. The micro-machined through-holes in the device stack were designed to accommodate the 2 different diameter capillaries used in this project and allowed these capillaries to be fully inserted into the stack without concern for obstructing flow. Unfortunately, the maximum insertion depth of these capillaries into the stack is ~1.5 mm which does not provide sufficient mechanical support to anchor them in place. Nanoport ferrules were used to provide a gas tight fit between the 360 µm O.D. fused silica capillary and the micro-machined silicon stack of the sensor array. Pieces of GC septum are used instead of ferrules for the larger 690 µm O.D capillaries. Epoxy was applied to the ferrule, which was then slid into place over the capillary. With the capillary supported vertically, it is inserted into the appropriate through-hole in the stack, the ferrule was manually pushed into place and the adhesive was allowed to cure. This process was repeated for all 5 capillary connections to the device. To enhance the gas seal and provide mechanical support for the capillaries, freshly prepared polydimethylsiloxane (PDMS) was then poured to a depth of approximately 0.5 cm into a PDMS reservoir surrounding the capillaries on the bottom of the package. Figure 4.15 shows the final assembled device stack in the PGA packaging with the all fluidic connections in place. The clear, transparently block of PDMS is apparent and the ferrules (or green GC septum) can be seen within it. It should be noted that the sensor was not tested using the two part liquid being mixed via diffusion, therefore only 1 liquid capillary connection was installed on the device.

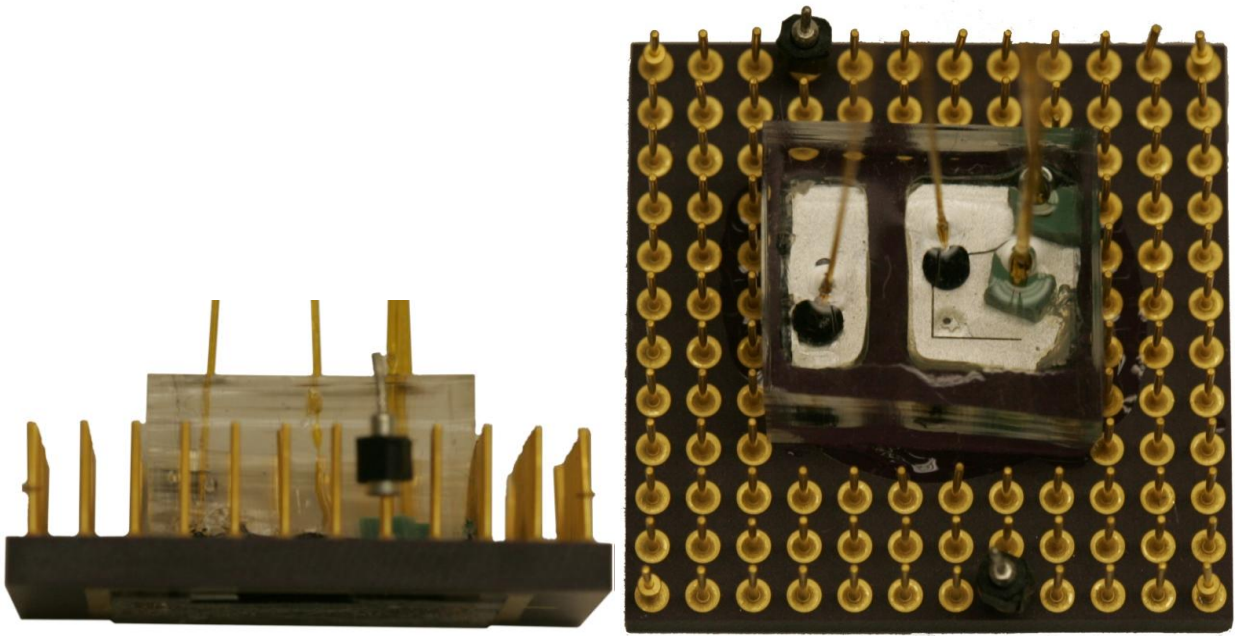

Figure 4.15: Photograph of the side and bottom of the final assembled micro-sensor array in its PGA package with all capillaries attached.

4.4 Preliminary sensor array performance

The final assembled device was first tested to verify that the gas and liquid channels were not blocked and fluid was able to pass from inlet to outlet freely. It was also tested to ensure no gas or liquid leakage was taking place, either at the capillary/device bonds, from the bond between the individual layers or from gas to liquid channels. Once the device was found to be mechanically operational, the sensor performance was evaluated. As the electronic hardware and software were not available at the time this device was assembled, the sensors could only be studied individually. Additionally, the SWNT-based sensors were not polymer coated for this first prototype to reduce the overall fabrication time. The response of a typical SWNT-based sensor to 6.72×10^{13} molecules (10 ppm) of dimethyl methyl phosphonate (DMMP) is shown in figure 4.16. The sensor was operated with a drive current of 0.1 mA and 1.0 mL/min of helium

carrier gas was used to supply the sample "pulse". It should be noted that the resistances of the SWNT-based sensors in the micro-fabricated array were much higher than for the individual sensors, which are typically in the range of 5 – 10 kΩ for the stand-alone sensors. This makes it difficult to operate the sensor at higher drive currents and produces a highly noisy signal. This is most likely due to poor electrode gap distance uniformity as a result of sputtering/resist lift-off processes during micro-fabrication. The layer assembly process also played a role in increasing the SWNT-based sensor resistance although the exact cause is unknown.

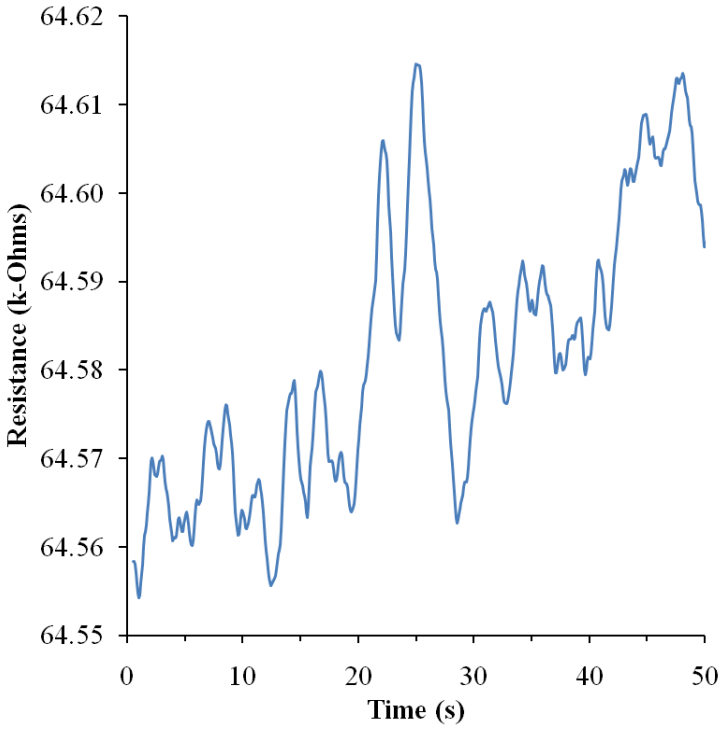

Figure 4.16: Response of a SWNT-based sensor in the silicon array to a "pulse" of 10 ppm DMMP at 1 mL/min. The sensor was operated at a drive current of 0.1 mA.

A typical response of the oxime sensors sensor is shown in figure 4.17. The oxime sensor was operated at 30 °C using a helium carrier gas flow rate of 0.2 mL/min. It was exposed to a "pulse" of 1.1×10^{13} molecules of acetic anhydride. The oxime sensor in the silicon array has

significantly lower sensitivity, roughly 2 orders of magnitude less, compared to the oxime micro-sensor individually fabricated from polycarbonate. This is most likely due to the difference in the gas-liquid membrane between the two devices. The micro-sized pores combined with the thick nature of the silicon micro-fabricated membrane make it difficult to "pin" the gas-liquid interface at the entrance of the pore were the gold electrodes are located. Shifting the gas-liquid interface away from the electrodes greatly decrease the sensitivity of the sensor. Although it is not possible to directly observe what is taking place within the device, it was noticed during testing that the gas flow could be re-directed across the membrane fairly easily by increasing its flow-rate and thus the pressure. Therefore care was taken during testing to use a low gas flow-rate as well as liquid flow-rate when introducing the oxime solution.

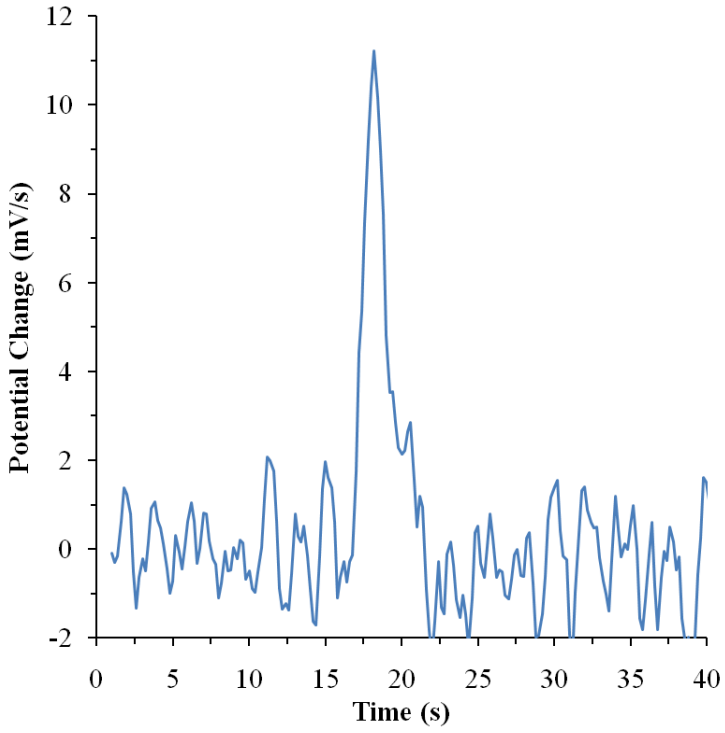

Figure 4.17: Response of the oxime based sensor in the silicon array to a "pulse" of acetic anhydride at 0.2 mL/min. The sensor was operated at a temperature of 30 ºC.

4.5 Conclusions and recommendations

By combining individual semi-selective sensors together into an array as an electronic nose has been found in literature to greatly increase the qualitative as well as quantitative power of the detector. Electronic noses have been created using numerous different types of solid-state sensors, which have been monitored both electrically and optically. These sensor arrays have been used to evaluate everything from simple inorganic gases to complex mixtures of VOCs emitted from food stuffs, bacteria, cancer and a large variety of other applications. Coupled with a well designed signal processing technique, these devices can handle a wide assortment of "odors" without the need for any chromatographic or gas separation equipment.

The goal of our research was to combine 7 solid-state chemi-resistive SWNT-based sensors with an aqueous oxime based sensor in a single micro-fabricated device. This miniaturized sensor array could then be eventually coupled with a micro-GC column to create a complete gas separation/analysis micro-platform. Design requirements of this array also included footprint size, electrical and fluidic connection locations, capillaries sizes and an integrated resistive heater for the SWNT-based sensors. After taking into account all design goals as well as the limitations of the individual sensors and of the micro-fabrication processes involved, the first version of the micro-sensor array consisted of a 4 layer stack of micro-machined silicon wafers. The array contained the 7 SWNT-based sensors in series, followed by the oxime based sensor to minimize interference between sensors. A thermal isolation break extended through all 4 layers of the device and shielded the oxime sensor from temperature changes in the other sensors. The gas-liquid membrane for the oxime sensor was created from the device layer of an SOI wafer and was 20 μm thick, with "pores" 30 μm in diameter spaced 70 μm apart.

Micro-fabrication of the array required extensive use of standard photolithography techniques, metal sputtering and ICP-DRIE. Tube furnaces were also used frequently to growth thermal SiO_2 layers as well as for boron doping of the resistive heating element. Buffered oxide etchant solution and gas phase Freon RIE were utilized at times for selective removal of SiO_2 layers. SWNT film deposition for the individual chemi-resistive sensors was performed manual according to the procedure previously developed in our research group. Once the fabrication was complete on the individual layers, the device stack was assembled using a silicone based adhesive through a PDMS transfer technique. This assembled stack was then bonded with a standard IC PGA package and electrical connections were then made to the package via gold wire bonding. Finally, fluidic capillary connections were made by first creating a gas tight seal at their base then pouring a large PDMS anchor block to provide mechanical stability.

Unfortunately, testing of this micro-sensor array was limited. Project funding ended unexpectedly just as the first working proto-type of the micro-sensor array has been fully assembled. This prevented the completion of the electronic hardware and software necessary to monitor all 8 sensor signals simultaneously. Testing the sensors in the array individually showed them to be functional; however their performance was significantly reduced in comparison to their stand-alone counterparts. For the oxime sensor, this was attributed to the large pore size and thickness of the gas-liquid membrane. This silicon based micro-membrane was not able to effectively maintain the gas-liquid interface at the surface of the pores near the gold electrode and as a result, sensitivity was negatively affected. For the SWNT-based sensors, micro-fabrication issues in the sputtering and/or resist lift-off processes created non-uniform electrode gap distances. After SWNT film deposition, the sensor resistances were abnormally high and were subsequently increased further during the device stack assembly process, although the

reason for this is unknown. The high resistances of the SWNT-based sensors made them difficult to operate at the normal drive currents and yielded noisy signals. As a result, sensitivity for these sensors was also reduced.

If development on this project were to have continued, it would have been focused in two areas; improvement of the gas-liquid membrane of the oxime based sensor and addressing the fabrication issues which resulted in high SWNT-based sensor resistances. The existing samples of layer 3 could be modified using a hydrophobic self assembling monolayer which would help prevent liquid from entering the membrane pores. A polymer coating could also be utilized in the same manner and could have the additional benefit of decreasing pore size. Because this oxime sensor is kinetically limited, this decrease in pore size should not decrease sensitivity but would help prevent liquid from flooding the membrane. Reducing the thickness of the device layer in the SOI wafer would allow for thinner membranes to be fabricated, however 20 μm seemed to be the limit of what was commercially available at the time. Improvements or the use of different lithography and etching processes would be necessary to reach small membrane pore sizes, however this may come at the expense of device yield. As a last resort, the silicon membrane could be scrapped in favor of a more effective polymer based membrane. Such a membrane would be sandwiched between silicon layers and as a result, a new layer bonding adhesive and technique may need to be developed to effective bond the device together. Additionally, electrical contacts to this polymer membrane may not be possible using wire bonding and a different technique would have to be utilized. For the SWNT-based sensors, equipment parameters and conditions would need to be optimized to ensure accurate, uniform electrode gaps were produced. The effects of layer assembly would also have to be investigated, to determine how curing temperature and adhesive choice changes the sensor resistances.

Further development on this sensor array should also include the effect of the gas micro-channel geometry on the shape of the analyte "pulse", as well as ensuring a minimal lose of analyte through adsorption to the channel walls or the bonding adhesive. Finally, the electronic hardware and software must be developed to collect and analyze all 8 sensor signals simultaneously. At this point a micro-sensor array response map could be created for a variety of common gaseous analytes.

4.6 References

1. Oh, I. and R.I. Masel, *Electrochemical organophosphate sensor based on oxime chemistry.* Electrochemical and Solid State Letters, 2007. **10**(2): p. J19-J22.
2. Monty, C.N., I. Oh, and R.I. Masel, *Optimization of a multiphase sensor for detection of phosphonates in air.* Aiche Journal, 2010. **56**(1): p. 241-247.
3. Oh, I., C.N. Monty, and R.I. Masel, *Electrochemical multiphase microreactor as fast, selective, and portable chemical sensor of trace toxic vapors.* Ieee Sensors Journal, 2008. **8**(5-6): p. 522-526.
4. Radadia, A.D., et al., *Partially buried microcolumns for micro gas analyzers.* Analytical Chemistry, 2009. **81**(9): p. 3471-3477.
5. Persaud, K. and G. Dodd, *Analysis of discrimination mechanisms in the mammalian olfactory system using a model nose.* Nature, 1982. **299**(5881): p. 352-355.
6. Heilig, A., et al., *Gas identification by modulating temperatures of SnO2-based thick film sensors.* Sensors and Actuators B-Chemical, 1997. **43**(1-3): p. 45-51.
7. Liu, Q.J., et al., *Olfactory cell-based biosensor: A first step towards a neurochip of bioelectronic nose.* Biosensors & Bioelectronics, 2006. **22**(2): p. 318-322.
8. Stetter, J.R., et al., *Quality classification of grain using a sensor array and pattern recognition.* Analytica Chimica Acta, 1993. **284**(1): p. 1-11.
9. Kim, Y.J., et al., *Mixed-ligand nanoparticles of chlorobenzenemethanethiol and n-octanethiol as chemical sensors.* Sensors and Actuators B-Chemical, 2005. **106**(1): p. 189-198.
10. Kessick, R. and G. Tepper, *Electrospun polymer composite fiber arrays for the detection and identification of volatile organic compounds.* Sensors and Actuators B-Chemical, 2006. **117**(1): p. 205-210.
11. Senesac, L.R., et al., *Analyte species and concentration identification using differentially functionalized microcantilever arrays and artificial neural networks.* Analytica Chimica Acta, 2006. **558**(1-2): p. 94-101.
12. Di Natale, C., et al., *Lung cancer identification by the analysis of breath by means of an array of non-selective gas sensors.* Biosensors & Bioelectronics, 2003. **18**(10): p. 1209-1218.
13. Grate, J.W., et al., *Smart sensor system for trace organophosphorus and organosulfur vapor detection employing a temperature-controlled array of surface-acoustic-wave sensors, automated sample preconcentration, and pattern-recognition.* Analytical Chemistry, 1993. **65**(14): p. 1868-1881.
14. Crooks, R.M. and A.J. Ricco, *New organic materials suitable for use in chemical sensor arrays.* Accounts of Chemical Research, 1998. **31**(5): p. 219-227.
15. Rakow, N.A. and K.S. Suslick, *A colorimetric sensor array for odour visualization.* Nature, 2000. **406**(6797): p. 710-713.
16. Dickinson, T.A., et al., *A chemical-detecting system based on a cross-reactive optical sensor array.* Nature, 1996. **382**(6593): p. 697-700.
17. Walt, D.R., *Fiber optic imaging sensors.* Accounts of Chemical Research, 1998. **31**(5): p. 267-278.

18. James, D., et al., *Chemical sensors for electronic nose systems.* Microchimica Acta, 2005. **149**(1-2): p. 1-17.
19. Vlasov, Y. and A. Legin, *Non-selective chemical sensors in analytical chemistry: from "electronic nose" to "electronic tongue".* Fresenius Journal of Analytical Chemistry, 1998. **361**(3): p. 255-260.
20. Pearce, T.C., et al., *Electronic nose for monitoring the flavor of beers.* Analyst, 1993. **118**(4): p. 371-377.
21. Ampuero, S. and J.O. Bosset, *The electronic nose applied to dairy products: a review.* Sensors and Actuators B-Chemical, 2003. **94**(1): p. 1-12.
22. Deisingh, A.K., D.C. Stone, and M. Thompson, *Applications of electronic noses and tongues in food analysis.* International Journal of Food Science and Technology, 2004. **39**(6): p. 587-604.
23. Schaller, E., J.O. Bosset, and F. Escher, *'Electronic noses' and their application to food.* Food Science and Technology-Lebensmittel-Wissenschaft & Technologie, 1998. **31**(4): p. 305-316.
24. Di Natale, C., et al., *The exploitation of metalloporphyrins as chemically interactive material in chemical sensors.* Materials Science & Engineering C-Biomimetic Materials Sensors and Systems, 1998. **5**(3-4): p. 209-215.
25. Gardner, J.W., H.W. Shin, and E.L. Hines, *An electronic nose system to diagnose illness.* Sensors and Actuators B-Chemical, 2000. **70**(1-3): p. 19-24.
26. Gostelow, P., S.A. Parsons, and R.M. Stuetz, *Odour measurements for sewage treatment works.* Water Research, 2001. **35**(3): p. 579-597.
27. Gardner, J.W. and P.N. Bartlett, *A brief-history of electronic noses.* Sensors and Actuators B-Chemical, 1994. **18**(1-3): p. 211-220.
28. Radadia, A.D., et al., *Micromachined GC columns for fast separation of organophosphonate and organosulfur compounds.* Analytical Chemistry, 2008. **80**(11): p. 4087-4094.
29. Radadia, A.D., et al., *The effect of microcolumn geometry on the performance of micro-gas chromatography columns for chip scale gas analyzers.* Sensors and Actuators B-Chemical, 2010. **150**(1): p. 456-464.
30. Radadia, A.D., et al., *The fabrication of all-silicon micro gas chromatography columns using gold diffusion eutectic bonding.* Journal of Micromechanics and Microengineering, 2010. **20**(1).
31. Hines, E.L., E. Llobet, and J.W. Gardner, *Electronic noses: a review of signal processing techniques.* Iee Proceedings-Circuits Devices and Systems, 1999. **146**(6): p. 297-310.
32. Collins, P.G., et al., *Extreme oxygen sensitivity of electronic properties of carbon nanotubes.* Science, 2000. **287**(5459): p. 1801-1804.
33. Kong, J., et al., *Nanotube molecular wires as chemical sensors.* Science, 2000. **287**(5453): p. 622-625.
34. Lee, C.Y., et al., *On-chip micro gas chromatograph enabled by a noncovalently functionalized single-walled carbon nanotube sensor array.* Angewandte Chemie-International Edition, 2008. **47**(27): p. 5018-5021.
35. Li, J., et al., *Carbon nanotube sensors for gas and organic vapor detection.* Nano Letters, 2003. **3**(7): p. 929-933.
36. Novak, J.P., et al., *Nerve agent detection using networks of single-walled carbon nanotubes.* Applied Physics Letters, 2003. **83**(19): p. 4026-4028.

37. Snow, E.S. and F.K. Perkins, *Capacitance and conductance of single-walled carbon nanotubes in the presence of chemical vapors.* Nano Letters, 2005. **5**(12): p. 2414-2417.
38. Wang, F., H.W. Gu, and T.M. Swager, *Carbon nanotube/polythiophene chemiresistive sensors for chemical warfare agents.* Journal of the American Chemical Society, 2008. **130**(16): p. 5392-+.
39. Snow, E.S., F.K. Perkins, and J.A. Robinson, *Chemical vapor detection using single-walled carbon nanotubes.* Chemical Society Reviews, 2006. **35**(9): p. 790-798.
40. Heller, I., et al., *Identifying the mechanism of biosensing with carbon nanotube transistors.* Nano Letters, 2008. **8**(2): p. 591-595.
41. Lee, C.Y., et al., *Charge transfer from metallic single-walled carbon nanotube sensor arrays.* Journal of Physical Chemistry B, 2006. **110**(23): p. 11055-11061.
42. Lee, C.Y. and M.S. Strano, *Amine basicity (pK(b)) controls the analyte blinding energy on single walled carbon nanotube electronic sensor Arrays.* Journal of the American Chemical Society, 2008. **130**(5): p. 1766-1773.
43. Valcarcel, M., S. Cardenas, and B.M. Simonet, *Role of carbon nanotubes in analytical science.* Analytical Chemistry, 2007. **79**(13): p. 4788-4797.
44. Wu, Z.C., et al., *Transparent, conductive carbon nanotube films.* Science, 2004. **305**(5688): p. 1273-1276.
45. Zhou, Y.X., L.B. Hu, and G. Gruner, *A method of printing carbon nanotube thin films.* Applied Physics Letters, 2006. **88**(12): p. 3.
46. Wang, H.C., Y. Li, and M.J. Yang, *Sensors for organic vapor detection based on composites of carbon nonotubes functionalized with polymers.* Sensors and Actuators B-Chemical, 2007. **124**(2): p. 360-367.
47. Zhang, T., et al., *Poly(m-aminobenzene sulfonic acid) functionalized single-walled carbon nanotubes based gas sensor.* Nanotechnology, 2007. **18**(16): p. 6.
48. Zhang, T., et al., *Electrochemically functionalized single-walled carbon nanotube gas sensor.* Electroanalysis, 2006. **18**(12): p. 1153-1158.
49. Zhang, X.T., J. Zhang, and Z.F. Liu, *Conducting polymer/carbon nanotube composite films made by in situ electropolymerization using an ionic surfactant as the supporting electrolyte.* Carbon, 2005. **43**(10): p. 2186-2191.
50. Field, C.R., et al., *Robust fabrication of selective and reversible polymer coated carbon nanotube-based gas sensors.* Sensors and Actuators B-Chemical, 2010. **148**(1): p. 315-322.
51. Salehi-Khojin, A., et al., *Sensitivity of nanotube chemical sensors at the onset of Poole-Frenkel conduction.* Applied Physics Letters, 2010. **96**(16).
52. Salehi-Khojin, A., et al., *On the Sensing Mechanism in Carbon Nanotube Chemiresistors.* Acs Nano, 2011. **5**(1): p. 153-158.
53. Salehi-Khojin, A., et al., *Nonthermal Current-Stimulated Desorption of Gases from Carbon Nanotubes.* Science, 2010. **329**(5997): p. 1327-1330.
54. Sayyah, M., et al., *Electrochemical multiphase microsensor for detection of organophosphates.* Journal of Micromechanics and Microengineering, 2011. **21**(1): p. 7.

Chapter 5:

A Critical Review of Existing Non-Biological Inhibition Based Sensing (NIBS) Mechanisms

5.1 Introduction

5.1.1 Chemical amplification

One method of increasing the sensitivity of a chemical detection method is by employing a catalytic reaction which is either enhanced or inhibited by the presence of the analyte molecule which is the target of the detection mechanism. Modulation of the production (or consumption) of many molecules by introduction of a few analyte molecules is thus the essence of any chemical amplification detection mechanism.

Chemical amplification by way of increasing catalytic activity was pioneered by Blaedel, who used the analyte itself as a catalyst in another main reaction [1-5]. This main reaction would only take place when exposed to a sample containing the desired catalytic analyte. The concentration of analyte could then be determined by the increase in reaction rate that occurred. This method of chemical amplification can thus yield a thousand fold increase in the sensitivity of the analyte detection. An example of this type of chemical amplification is in the detection of iodide and iodine containing thyroid hormones. Iodide ions can be used to catalyze the simple redox reaction between ceric and arsenious ions shown in equation 5.1:

$$2Ce^{+4} + As^{+3} \rightarrow 2Ce^{+3} + As^{+5} \qquad 5.1$$

Adding a sample containing iodide ions rapidly increases the rate of this reaction, which can be monitored spectroscopically by the consumption of the ceric ions, allowing detection of

nanogram quantities of various iodine compounds [6]. Blaedel's methods have also been successfully employed in atmospheric analysis and many other systems [7-11].

Enzymes are powerful biological catalysts which often utilize very specific reactants (substrates). The catalytic activity of many enzymes can also be modulated, either by enzyme specific inhibitor or activator compounds. Enzyme inhibition is a naturally occurring process within biological organisms as part of their normal regulatory balance; however inhibitors can be introduced from external sources as poisons to disrupt biological functions. Organophosphate nerve agents work in such a way by inhibiting the enzyme acetylcholinesterase in nerve synapses. These nerve agents prevent acetylcholine from being hydrolyzed by the enzyme, causing an accumulation of this compound at nerve synapses and which leads to excessive neuron activity and muscle paralysis. Many inhibition based chemical amplification detection mechanisms have been created using acetylcholinesterase as a catalyst which is then inhibited by organophosphates nerve agents or pesticides [12-30]. An example of a sensor using such an amplification method is the one created by Monty *et al.* [31]. This device utilized electric eel acetylcholinesterase to catalyze the hydrolysis of acetylthiocholine to thiocholine and acetate. Thiocholine is then detected amperometrically as it oxidized at a gold working electrode. The acetylcholinesterase is immobilized in a microchannel of the sensor with an aqueous solution of acetylthiocholine flowing over it. The liquid microchannel is separated by a nano-porous membrane from a gas microchannel which delivers the sample to be analyted. As an acetylcholinesterase inhibitor passes through the gas channel, it diffuses across the membrane into the liquid channel and permanently inhibits the enzyme (figure 5.1).

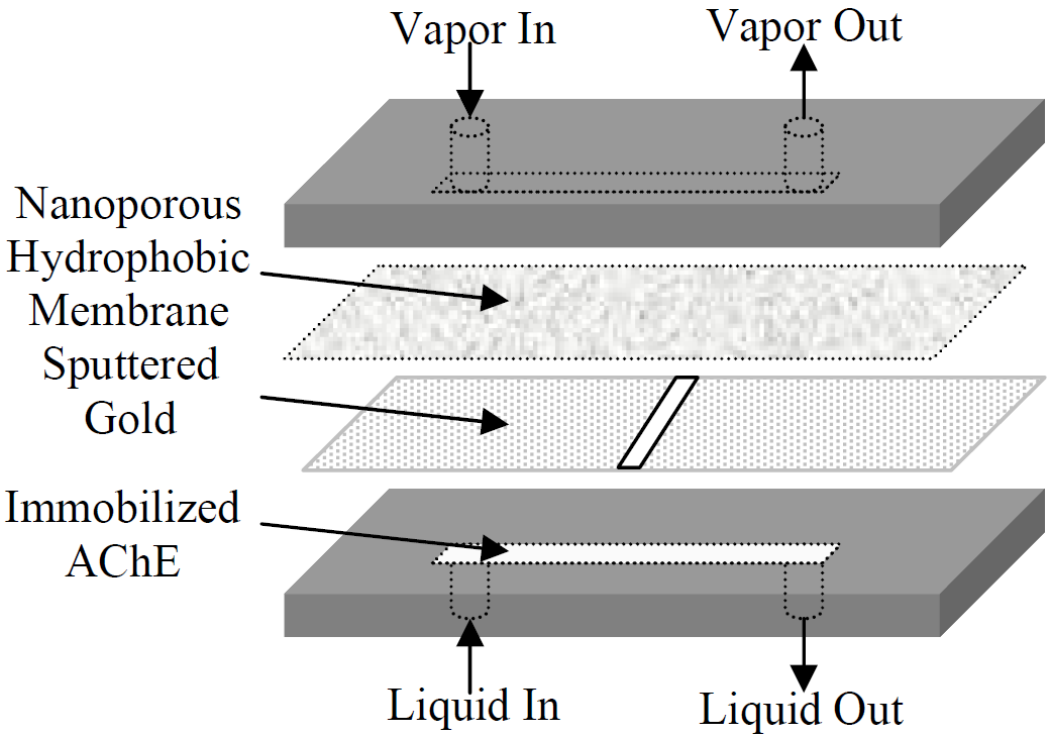

Figure 5.1: Schematic of the dual microchannel/membrane system. Vapor flows through the top microchannel and is separated from the liquid microchannel by a nanoporous membrane with 40-nm thick layer of sputtered gold on the liquid side. The gold layer is separated into a working and a counter electrode by using a shadow mask during sputtering. A thin film of AChE is immobilized inside the liquid microchannel in a cross-linked gel with glutaraldehyde [31].

This causes the rate at which thiocholine is produced to drop, which in turn lowers the current measured from thiocholine oxidation. Enzyme inhibition based chemical amplification schemes have also been utilized to detect various types of heavy metals such as mercury and cadmium [32-39].

Enzymes can also be used in more complex chemical amplification schemes, such as the following example for detection of the co-enzyme $NADP^+$, which acts as a sort of enzyme activator. This mechanism requires two types of enzymes; glutamate dehydrogenase (GDH) and

glucose-6-phosphate dehydrogenase (G6PDH). GDH catalyzes the conversion of ketoglutarate to glutamate, while G6PDH catalyzed the conversion of glucose-6-phosphate to 6-phosphogluconate. Both enzymes require the co-enzyme $NADP^+$/NADPH to function (figure 5.2).

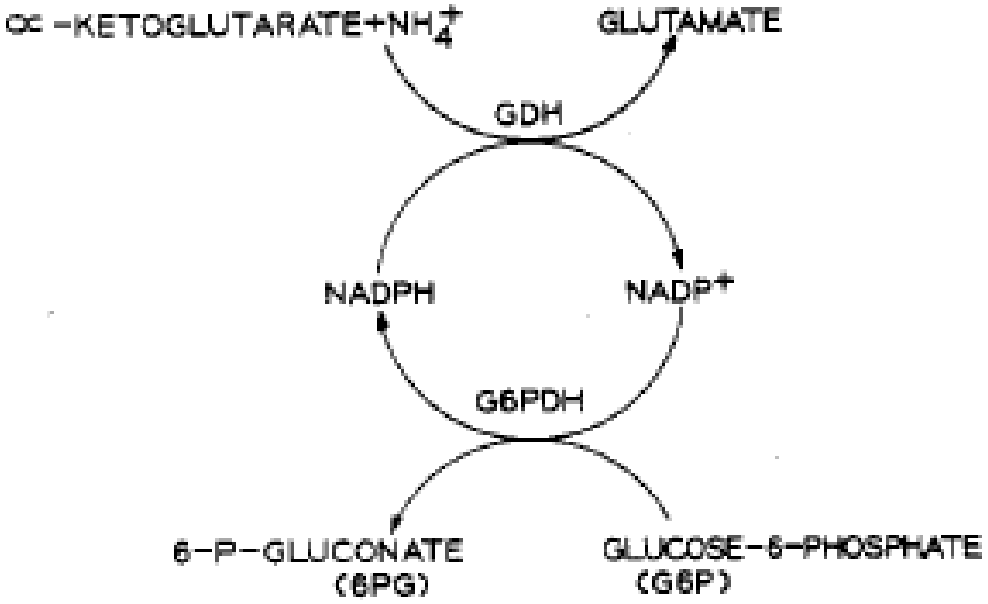

Figure 5.2: Chemical amplification mechanism using $NADP^+$ to active two enzymes which facilitates the production of 6-phosphogluconate [40].

Adding a sample containing a small amount of $NADP^+$ to a solution of the enzymes and reactants (substrates) allows all the overall mechanism to take place. After a set time, the amount of 6-phosphogluconate produced is measured via another, rapid enzymatic indicator [40]. The rate of production of 6-phosphogluconate can then be correlated to the concentration of $NADP^+$ in solution.

5.1.2 Non-Biological Inhibition Based Sensing (NIBS) mechanisms

All the chemical amplification detection schemes discussed in the previous section are both selective for a specific type of analyte and highly sensitive due to the nature of the amplification mechanisms involved. The biological, enzyme inhibition based methods are particularly popular for several reasons. Accurate, sensitive measurements of enzyme inhibitors are of great importance due to their capability of controlling or disrupting biological activity. Additionally, the large variety of enzymes with different functionalities and the types of inhibitors which are being detected gives a high degree of flexibility when designing a sensing mechanism.

There are several disadvantages to the use of enzyme or other biological material in sensor systems; namely shelf life and operating condition issues. Enzymes are complex, folded proteins which derive their catalytic activity from both the type of amino acids present in their structure as well as the orientation of these amino acids relative to each other. Due to the lack of covalency of protein folding interactions, enzymes can easily unfold or denature, and in the process partially or completely lose their catalytic activity. Enzymes will slowly denature over time, however this process is accelerated at high temperatures. Enzymes are also sensitive to their chemical environment and in many cases denature in the presence of a strong acid or base, concentrated salt solutions or various organic solvents. Enzyme denaturing can be reversed in some conditions, but the process is not trivial. These issues, as well as the higher cost of enzymes compared to non-biological materials limits their use in chemically amplification mechanism.

In an effort to avoid these limitations inherent in biological detection schemes, research by Monty has attempted to develop another type of inhibition based chemically amplified

detection mechanism which forgoes the use of enzymes for simpler, non-biological catalysts [41, 42]. This type of detection scheme, which is has be named Non-Biological Inhibition Based Sensing (NIBS) follows the same basic ideas as its enzymatic counterpart. The NIBS mechanism will have a main reaction of substrate(s) being converted to product(s), which only takes places at an appreciable rate in the presence of a specific catalyst. The analyte of interest and the catalyst for a particular mechanism are chosen such that the analyte molecule binds or interacts with the catalyst in a way that decreases its catalytic activity for the main reaction (figure 5.3).

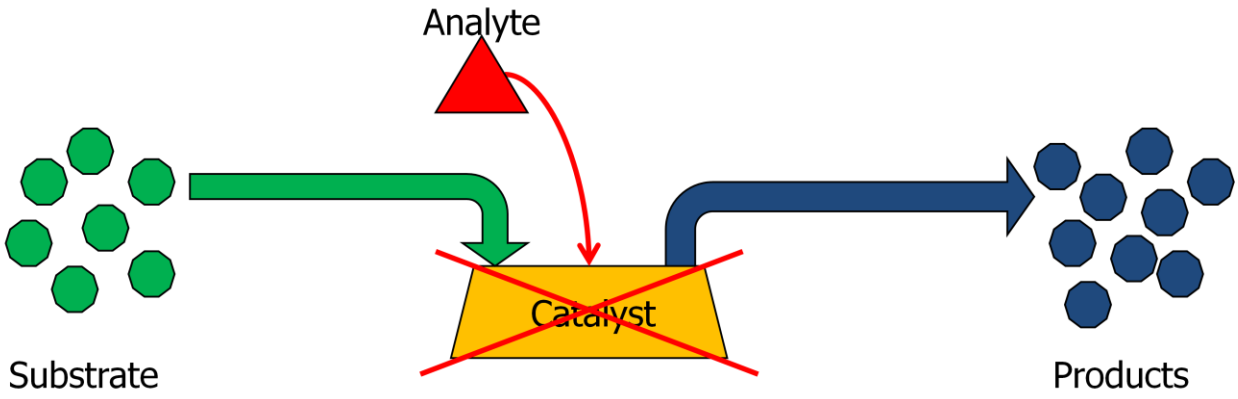

Figure 5.3: General form of a Non-Biological Inhibition Based Sensing (NIBS) mechanism. Substrates are converted to produces by the catalyst. Addition of the analyte molecule inhibits the catalyst and prevents the substrate conversion from taking place.

The general process for developing a specific example of a NIBS mechanism is relatively straightforward. First one must find an appropriate analyte/catalyst combination. Drager or Stain tubes are a good source of selective, colorimetric reactions between various analytes and reagents. Colorimetric reactions can also be found in the literature and are usually selective to specific compounds. Focusing on colorimetric reactions maximizes the probability that the

analyte changes the catalytic activity of reagent, as most colorimetric reactions involve some type of electronic change in the reagents or charge transfer between species.

The next step involves finding the main reaction which will be catalyzed by the reagent in the colorimetric detection method identified previously. This main reaction should ideally be as simple as possible and used a minimal number of substrates, as well as not undergo any side reactions, especially involving the analyte. These NIBS mechanisms should ideally be measured electrochemically to maximize their sensitivity and ease of use. As a result, the main reaction should contain at least one electroactive compound, which can be monitored as it is produced or consumed.

Monty used the process detailed above to develop two examples of NIBS mechanisms. The first mechanism was designed to detect various toxic sulfide compounds through the use of a copper (II) acetate catalyst to oxidize formic hydrazide [41]. The other mechanism was designed to detect an arsenic based riot control agent called Adamsite using silver nitrate as the catalyst in a main reaction between phenylenediamine and acetone [42]. These reaction mechanisms were both developed on the beaker scale and goal of my research was to design microfluidic sensors platforms for the use of these NIBS mechanisms in the hope of further improving their sensitivity, reliability and ease of use. Unfortunately, I encountered significant difficulty in replicating the basic behavior of these two mechanisms which prevented me from evaluating any microfluidic sensor designs. I found several issues with the data presented on the beaker cell development of these methods, and additional experimentation indicates the reaction mechanisms are more complex than originally anticipated. I will detail these issues, my experimental findings, and make recommendations for the future of both NIBS mechanisms in the following sections.

5.2 NIBS for the detection of toxic sulfide compounds

Toxic sulfide compounds, such as sulfur mustard chemicals are of particular interest for detection as they are dangerous blister agents. These compounds' toxicity comes from their ability to alkylate the guanine nucleotide in DNA, causing irreversible damage to the DNA. This can lead to cancer or outright cellular death. Because of the large amount of cellular damage, these compounds are powerful vesicants, causing chemical burns and blisters on the skin, similar in severity to ordinary burns. Since the effects of blister agents can take up to a day to manifest themselves in humans, sensitive and selective sensors are essential to detect and prevent exposure to toxic levels of these compounds.

This NIBS mechanism was developed by utilizing a selective colorimetric reaction between toxic sulfides and copper (II) acetate discovered by Brinkley *et al.* [43]. In this colorimetric reaction, copper (II) acetate in solution goes from a sky blue color to a yellow color upon addition of the toxic sulfide simulant 2-chloroethyl methyl sulfide (CEMS). Using this colorimetric detection method only, the detection limit for CEMS is ~200 μM [43]. To complete the NIBS mechanism, this colorimetric reaction is then coupled with a main reaction. Copper acetate is a known catalyst for the oxidation of hydrazides to their corresponding carboxylic acids [44, 45]. By using a main reaction of formic hydrazide to formic acid, the presence of CEMS should be chemically amplified by electrochemically measuring the decrease in the rate of formic acid production (figure 5.4) [41].

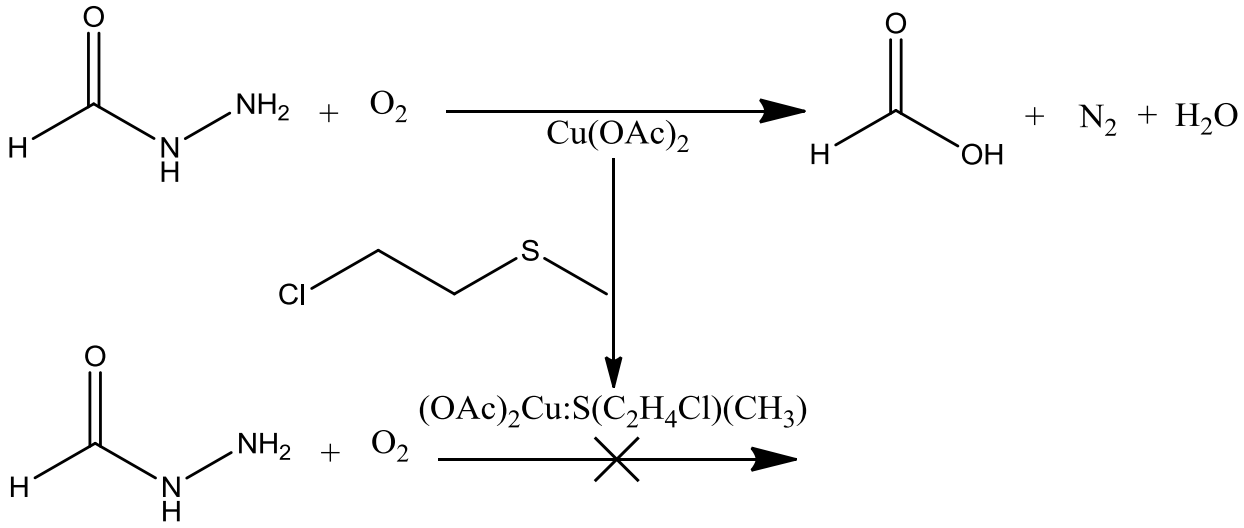

Figure 5.4: Theorized NIBS mechanism for the detection of toxic sulfide compounds.

5.2.1 Chemicals and materials

2-Chloroethyl methyl sulfide (CEMS, 97%, Aldrich), copper (II) acetate (Aldrich), formic hydrazide (Aldrich), tetrabutyl ammonium perchlorate (Fluka), silver nitrate (Aldrich), methanol (Fisher). Platinum disc working electrode (MF-2013) and non-aqueous reference electrode (MF-2062) were purchased from BASi.

5.2.2 Experimental procedures

Intermediate solutions of formic hydrazide (6 mg in 10 mL methanol), copper (II) acetate (11.4 mg in 10 mL methanol) and CEMS (4 µL in 4 ml methanol) were prepared fresh daily. The non-aqueous reference electrode was prepared using methanol, tetrabutyl ammonium perchlorate and silver nitrate following the procedures given from BASi. This reference electrode solution was also created fresh daily. For a particular experiment, a given amount of formic hydrazide intermediate solution was diluted with methanol to 10 mL. CEMS solution is then added if the effects of catalyst inhibition are being studied. Finally, a given amount of

copper (II) acetate solution is added, the resulting solution is mixed manually for several seconds and then placed onto a stirring plate operating at 100 rpm. The working and reference electrodes are quickly inserted and the open circuit potential of the solution is monitored for 1000 s.

5.2.3 Results and discussion

Monty conducted research on this NIBS mechanism to determine the optimal solvent for this detection method to occur in, as well as the optimal concentration ratio of catalyst to substrate (copper acetate to formic hydrazide) [41]. These studies then allowed her to determine the optimal conditions for operation of the NIBS mechanism to quickly detect low concentrations of sulfides. The optimal solution was found to be 0.4 µL of formic hydrazide and 50 µL of copper (II) acetate intermediate solutions in 10 mL of methanol, and allowed the detection of CEMS in a range of 2 – 30 µM. An example of a typical potential response from the NIBS mechanism as seen by Monty is shown in figure 5.5 [41]. Converting the mass concentrations to molar concentrations for this optimal detection condition gives 0.4 µM of formic hydrazide and 31.4 µM of copper (II) acetate.

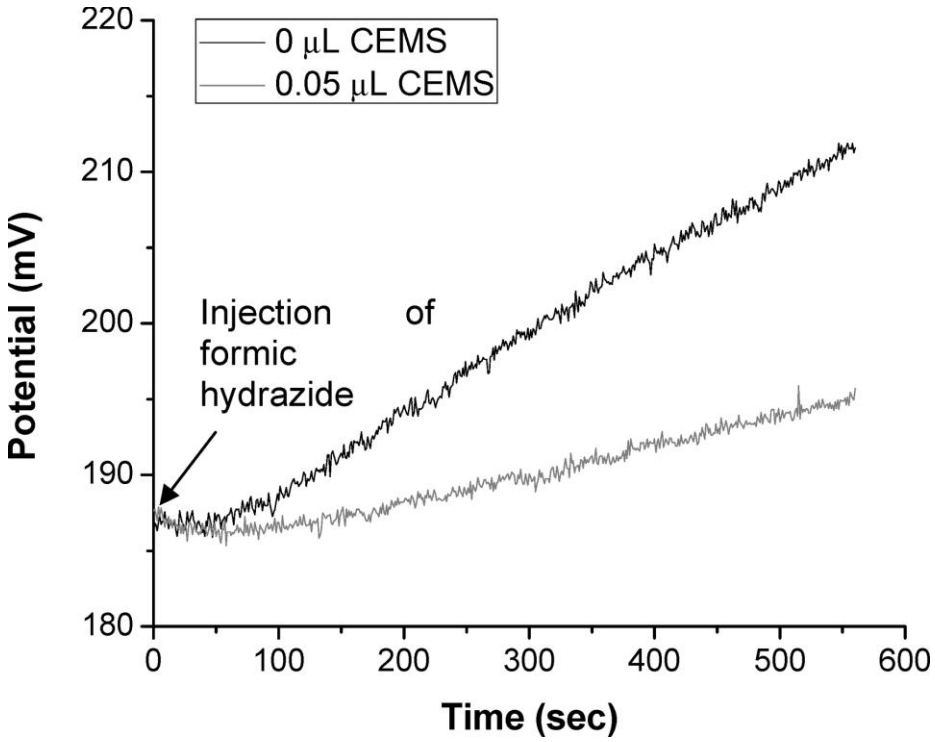

Figure 5.5: Open circuit potential response of the NIBS sulfide detection mechanism as measured by Monty [41]. 0.4 µM of formic hydrazide and 31.4 µM of copper (II) acetate in methanol, with and without the presence of CEMS.

At these conditions, both the concentration of the catalyst as well as the CEMS used to inhibit it are several orders of magnitude greater than the substrate (formic hydrazide) in the main reaction. This would seem to defeat the purpose of the NIBS mechanism to chemically amplify the presence of toxic sulfide if it requires 10 to 100 molecules of CEMS to effect the production of 1 molecule of formic acid. It is possible that the production of formic acid has a much greater contribution electrochemically than the toxic sulfide compounds, however my own attempts to replicate the open circuit potential response have shown otherwise (figure 5.6).

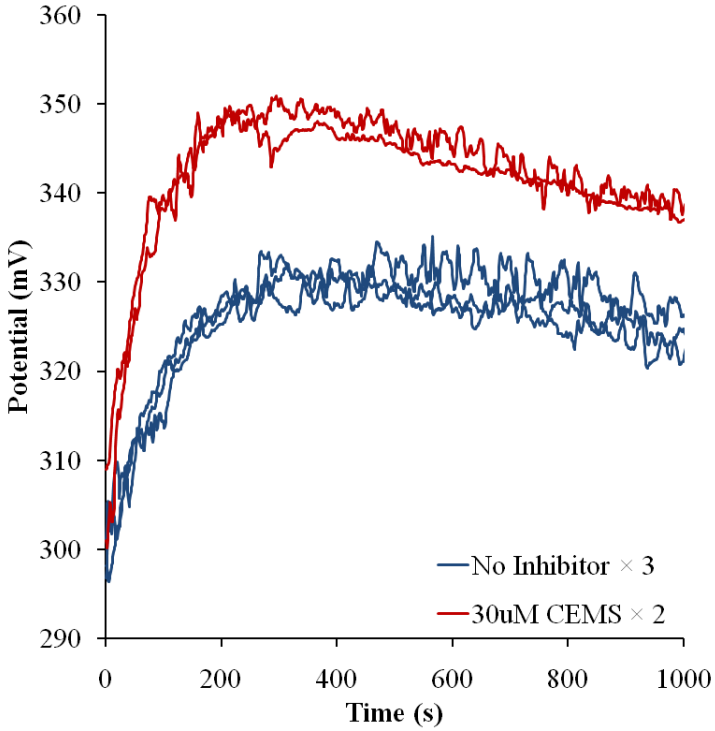

Figure 5.6: Open circuit potential response of the NIBS mechanism. 0.4 µM of formic hydrazide and 31.4 µM of copper (II) acetate in methanol, with and without the presence of CEMS.

Instead of a gradual, linear increase in potential over the time period measured as seen in figure 5.5, there is a more rapid initial increase in potential followed by a gradual decrease after approximately 200 s. The addition of CEMS seems to simply shift the solution to a higher potential, however it also increases the initial rate of potential change. This initial potential increase could however simply be a result of the reference and working electrode acclimating to the solution and not indicative of an actual chemical reaction taking place in the bulk solution. The response of this NIBS chemistry as measured after 10 min would be the difference in potential between the inhibited and non-inhibited curves, which according to my data in figure

5.6, appears to be solely due to the electrochemical contribution of CEMS to the potential and not from any change in the rate of the main reaction.

A NIBS mechanism functions most effectively when the substrate-to-inhibitor ratio is as high as possible. The concentration of the limiting reactant in the main reaction should at least be on the same order as the maximum concentration of inhibitor the mechanism has been designed to detect, if not several orders of magnitude greater. Figures 5.7 and 5.8 show the potential response of the solution using 40 µM and 400 µM formic hydrazide, respectively. Both experiments used the same about of catalyst and inhibitor as figure 5.6 (31.4 µM of copper (II) acetate and 30 µM CEMS).

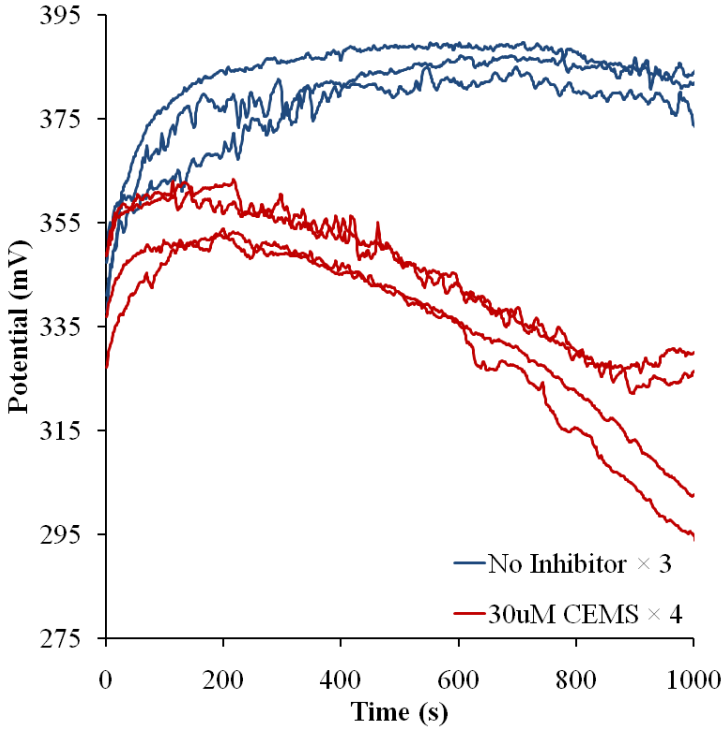

Figure 5.7: Open circuit potential response of the NIBS mechanism. 40 µM of formic hydrazide and 31.4 µM of copper (II) acetate in methanol, with and without the presence of 30 µM CEMS.

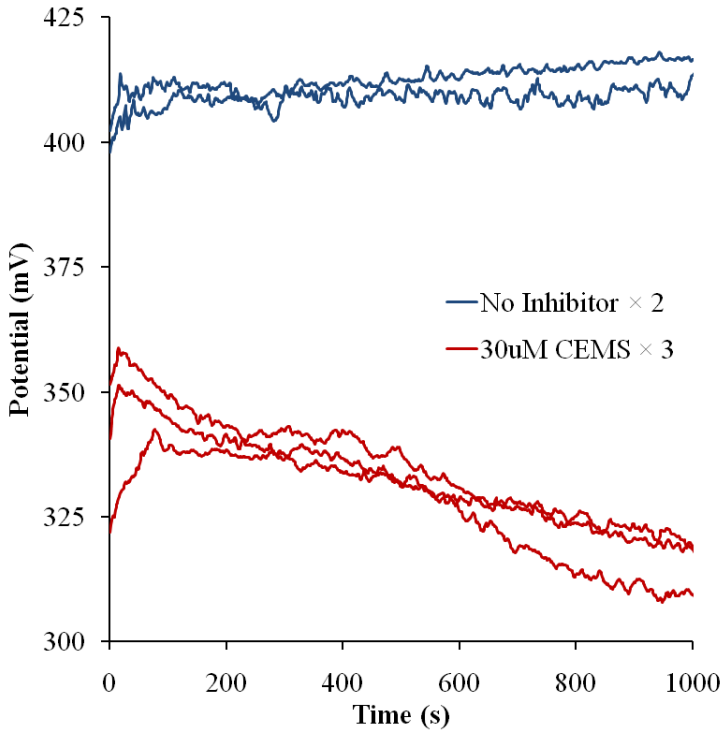

Figure 5.8: Open circuit potential response of the NIBS mechanism. 40 µM of formic hydrazide and 31.4 µM of copper (II) acetate in methanol, with and without the presence of 30 µM CEMS.

Both figures 5.7 and 5.8 show a reaction may possibly be taking place, however seemingly in the opposite fashion as expected from a NIBS mechanism. The potential curves for both formic hydrazide concentrations in the absence of inhibitor show little change, however in the presence of 30 µM CEMS, the potential of the solution gradually decreases over the period of time measured. It appears as though a reaction is taking place in the solution when CEMS is added, possibly between CEMS and the formic hydrazide itself. Such a side reaction between these two species would effectively circumvent the normal NIBS mechanism and prevent any chemical amplification from taking place.

Several other issues arise when examining the development work on this NIBS mechanism by Monty. These issues include the experimental methodology used to determine the

optimal catalyst to substrate (copper (II) acetate to formic hydrazide) ratio, conflicting experimental results in the data presented, inconsistencies in the concentrations of the various species used in the studies and a misunderstanding of the mechanism of the main reaction. I will use the rest of this section to address in detail these issues, as well as the difficulties present in realizing this NIBS mechanism.

As noted already, methanol was chosen by Monty as the ideal solvent for this NIBS mechanism [41]. This was based on the high rate of the main reaction in methanol as measured by the change in the solution potential over a period of 10 minutes. However, methanol was also chosen because it was shown that changes in catalyst concentration had a greater impact on reaction rate in this solvent, thus maximizing the effect of catalyst inhibition and the sensitivity of this detection method (figure 5.9) [41].

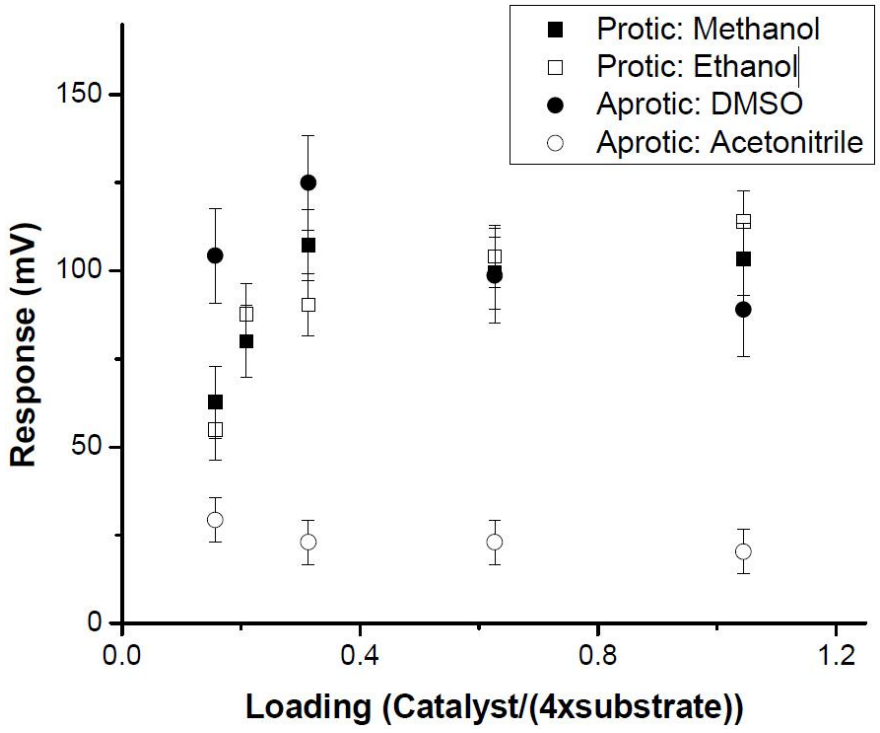

Figure 5.9: Effect of catalyst/substrate ratio on potential response of NIBS mechanism for both protic and aprotic solvents [41].

From figure 5.9, it can be seen why methanol was chosen as the optimal solvent. A decrease in available catalyst must trigger a decrease in the rate of the main reaction so that the presence of the inhibitor can be observed. According to Monty, at a catalyst/4×substrate ratio of approximately 0.33, the rate of the main reaction begins to decrease when methanol (or ethanol) is used as a solvent [41]. This behavior was not observed for aprotic solvents DMSO and acetonitrile.

The procedure used by Monty to obtain these data however involved varying the substrate (formic hydrazide) concentration while keeping the catalyst concentration fixed. This would imply that reaction rate would remain constant as the concentration of formic hydrazide increased until past a certain threshold, whereby the reaction rate would begin to decrease. This observation is not only highly unusual; it is also seemingly contradicted in one of the subsequent figures created by Monty. Figure 5.10 is a Lineweaver-Burke plot of inverse substrate concentration to inverse reaction rate for various concentrations of inhibitor which shows that the reaction kinetics of this NIBS mechanism can be analyzed using the Michaelis-Menton enzyme kinetic model [41].

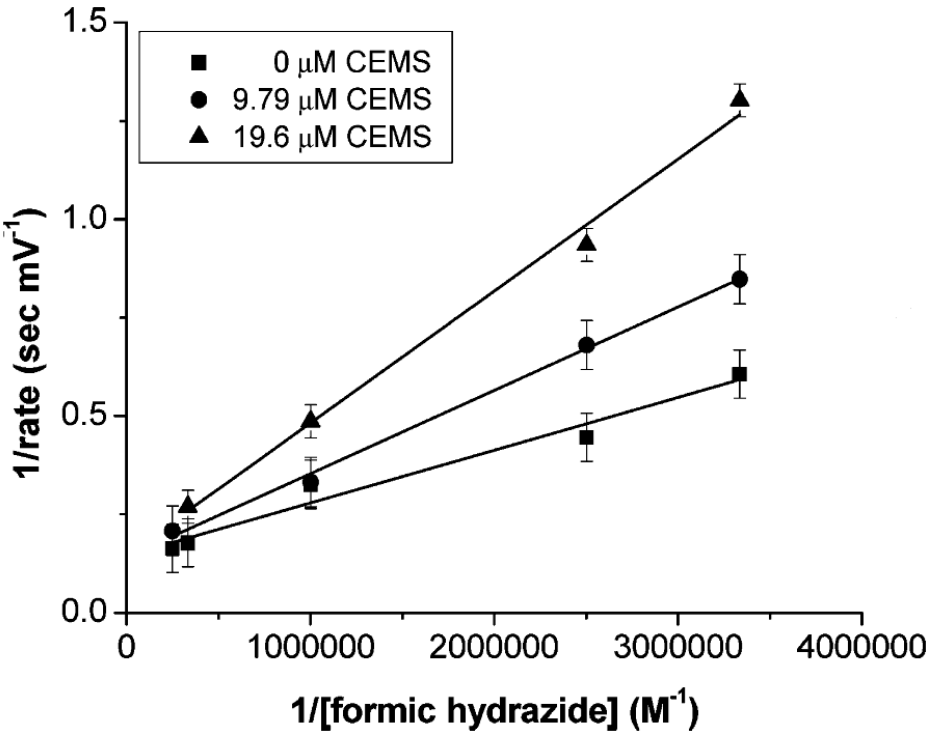

Figure 5.10: Lineweaver-Burke plot of inverse reaction rate versus inverse formic hydrazide concentration [41].

The data shown in figure 5.10 was created in the same way as figure 5.9, in that the catalyst concentration remained fixed and the amount of formic hydrazide was varied. In this case however, the lowest curve shows that in the absence of CEMS, reaction rate increased steadily as formic hydrazide concentration increased. It should be noted that the catalyst concentration in figure 5.10 was 30.4 μM, and formic hydrazide was varied from 0.3 - 4 μM, which is very similar to the optimal reaction concentrations found by Monty of 31.4 μM of catalyst and 0.4 μM of formic hydrazide. However, the catalyst concentration in figure 5.9 was 6.3 mM and formic hydrazide concentration was varied over a range of 9.3 – 1.5 mM; both several orders of magnitude greater than the optimal concentrations. While it is possible that at higher catalyst and substrate concentrations the reaction rate no longer follows the usual

behavior which is seen in the Lineweaver-Burke plot in figure 5.10, the sudden decrease in reaction rate is still odd behavior. This data could possibly be explained by the logarithmic nature of species concentration to solution potential. For a fixed amount of formic acid produced, the absolute contribution to the potential of the solution will be less at higher concentrations of formic hydrazide compared to lower concentrations, thus causing the observed drop in the rate of potential increase seen in figure 5.9. The effect of concentration on overall solution potential could also possibly explain the behavior seen in the Lineweaver-Burke plot (figure 5.10). Even in the absence of any reaction taking place, increasing the concentration of formic hydrazide and CEMS would increase the solution potential. However, due to the logarithmic nature of the concentration to potential dependence, CEMS would not have as great a contribution to the solution potential at high formic hydrazide concentrations as it would at low concentrations.

As the concentrations used in figure 5.9 were significantly different than those used for the optimal condition, it is also not surprising that the optimal conditions found by Monty do not use a catalyst/4×substrate ratio less than the 0.33 threshold reportedly found from figure 5.9. The catalyst/4×substrate ratio for the optimal conditions is in fact 19, much far great than the 0.33 threshold and larger than any ratio tested in figure 5.9.

The ratio of catalyst/4×substrate defined by Monty is itself important as it hints at a much more fundamental issue regarding the design of the main reaction in this NIBS mechanism. This ratio was defines as such because "stoichiometrically, there are 4 moles of catalyst needed for every one mole of hydrazide" as pointed out by Monty [41]. However this is only partially correct, as Tsuji *et al.* stated that "It was confirmed that at least four moles of Cu^{+2} salt are necessary for the oxidation of one mole of hydrazides in the absence of oxygen" [45]. The key difference is that

in the absence of oxygen or low oxygen concentration situations, the Cu^{+2} salt does not function as a catalyst. Instead it acts as another reactant and is subsequently consumed as the oxidation reaction proceeds. Tsuji *et al.* postulate that this non-catalytic hydrazide oxidation process takes place via the following mechanism (reactions 1 -3), whereby 4 moles of the Cu^{+2} salt first form the corresponding acyl cation from the hydrazide [45]. This acyl cation then goes on to react with any water, hydroxide ions, alcohols or alkoxide ions, or amines present.

1) $RCONHNH_2 + 4Cu^{+2} \rightarrow RCO^+ + 4Cu^{+1} + 3H^+ + N_2$
2) $RCO^+ + HX \rightarrow RCOX + H^+$

   or

3) $RCO^+ + X^- \rightarrow RCOX$

   where X = OH, OR or NR_2

It is well known that molecular oxygen readily oxidizes Cu^{+1} ions to Cu^{+2}. The specific mechanism for this reaction is complex, however it most likely involves a Cu – dioxygen adduct as an intermediate which then proceeds to react further with either the acyl cation and/or any H^+ available to produce the carboxylic acid and hydroxide anion, respectively [46]. After this takes place, copper is returned to its +2 oxidation state and can go on to react with more hydrazide, thus completing a catalystic cycle. When oxygen is present in excess by bubbling it through the solution, Tsuji *et al.* showed that a smaller, non-stoichiometric amount of Cu^{+2} salt was necessary to carry out the hydrazide oxidation to completion indicating that the copper salt was functioning catalytically [45].

In the case of the NIBS mechanism, no external source of oxygen is introduced. The oxidation reaction relies solely on the oxygen already dissolved in the methanol. However, oxygen solubility in methanol at atmospheric conditions is roughly 4 µM. Due to this low oxygen solubility, the large excess of copper (II) acetate and the likelihood that water is also present in the solution from traces amounts absorbed by the solid reagents used to create the solution, the Cu^{+2} ions are likely predominately functioning in a non-catalytic manner. Even if the amount of water present is negligible, the acyl cations produced will react with the solvent itself, albeit at a slower rate [45].

It is still possible that the NIBS mechanism may work as intended, as the colorimetric reaction is a result of the CEMS creating and stabilizing the Cu^{+1} ion in a charge transfer complex. If the CEMS can convert a small, catalytic amount of Cu^{+2} to Cu^{+1} relative to the reactants and prevent it from being re-oxidized, then the main hydrazide oxidation reaction should be significantly inhibited. I attempted to create a NIBS mechanism that not only had a higher substrate-to-catalyst ratio (for proper chemical amplification) but also had similar formic hydrazide and oxygen concentration to ensure the reaction went to completion. However, my initial attempts at creating this NIBS mechanism did not yielded much success. Figure 5.11 show the potential response of the NIBS sulfide mechanism using 4 µM formic hydrazide and 0.3 µM copper (II) acetate, with and without the presence of 0.5 µM CEMS.

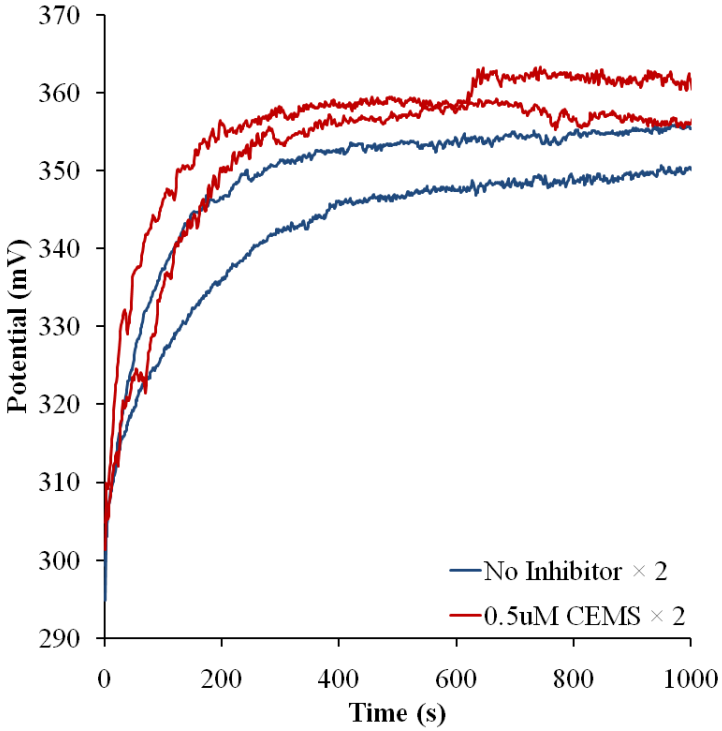

Figure 5.11: Open circuit potential response of the NIBS mechanism. 4 µM of formic hydrazide and 0.3 µM of copper (II) acetate in methanol, with and without the presence of 0.5 µM CEMS.

Unfortunately, there does not seem to be a significant difference between the non-inhibited and inhibited potential response curves. Although the low concentration of dissolved oxygen severely limits the amount of hydrazide, and thus catalyst and inhibitor which can be used, there is still some room to adjust concentrations to possibly give a functional NIBS mechanism.

Further experimental work must be done to determine if there are any side reactions taking place, especially between the substrates and CEMS. If possible, a secondary method of monitoring the progress of the main reaction can be found to confirm the electrochemical measurements of the solution. Because of the limited solubility of oxygen in methanol, it may be possible to introduce a different chemical source of available oxygen which could be used in

higher concentrations. This would allow for higher concentrations of formic hydrazide, and thus give more flexibility in catalyst and inhibitor concentrations to design a working NIBS mechanism for the detection of these toxic sulfides. Finally, care must be taken in relating potential change of the solution to an absolute measure of the rate of the main reaction. Multiple species contribute to the potential of the solution and direct comparisons of solution at difference concentration conditions cannot usually be made.

5.3 NIBS for the detection of the riot control agent Adamsite

Adamsite, or phenarsazine chloride, is a type of riot control agent. It was developed in 1918 by Roger Adams at the University of Illinois at Urbana-Champaign. Riot control agents such as Adamsite affect the lungs and mucous membranes of a person, causing intense crying, sneezing, burning sensations and even vomiting. In its pure state, Adamsite is a yellow crystalline substance with a low vapor pressure. Because of its solid nature, it is typically delivered in an aerosolized form and its effects on humans are slower developing, yet last longer than more modern riot control agents. This combined with the toxic nature of arsenic compounds in general has led to obsolescence of Adamsite use. However, large amounts of Adamsite still remain in the environment in areas of some European countries due to unsafe disposal practices [47-50]. Due to the high toxicity and adverse physiological reactions to Adamsite, sensitive and selective sensors are needed to deal with any abandoned stockpiles of this chemical.

The NIBS mechanism developed by Monty for the detection of Adamsite was based on a selective colorimetric reaction discovered by Delga *et al.* [51]. Delga found that by heating a mixture of Adamsite, silver nitrate and acetic acid in water, a yellow colored solution was

produced. This method of sensing Adamsite was experimentally determined to have a detection limit of 30 µM [51]. To complete the NIBS mechanism, this colorimetric reaction is then coupled with a main reaction. Silver nitrate can be used as a catalyst for the synthesis of 1,5-benzadiazepine derivates from phenylenediamine and the appropriate ketone [52, 53]. By using a main reaction of phenylenediamine with acetone to form its corresponding 1,5-benzadiazepine derivative, the presence of Adamsite should be chemically amplified by electrochemically measuring the decrease in the rate of phenylenediamine consumption (figure 5.12) [42].

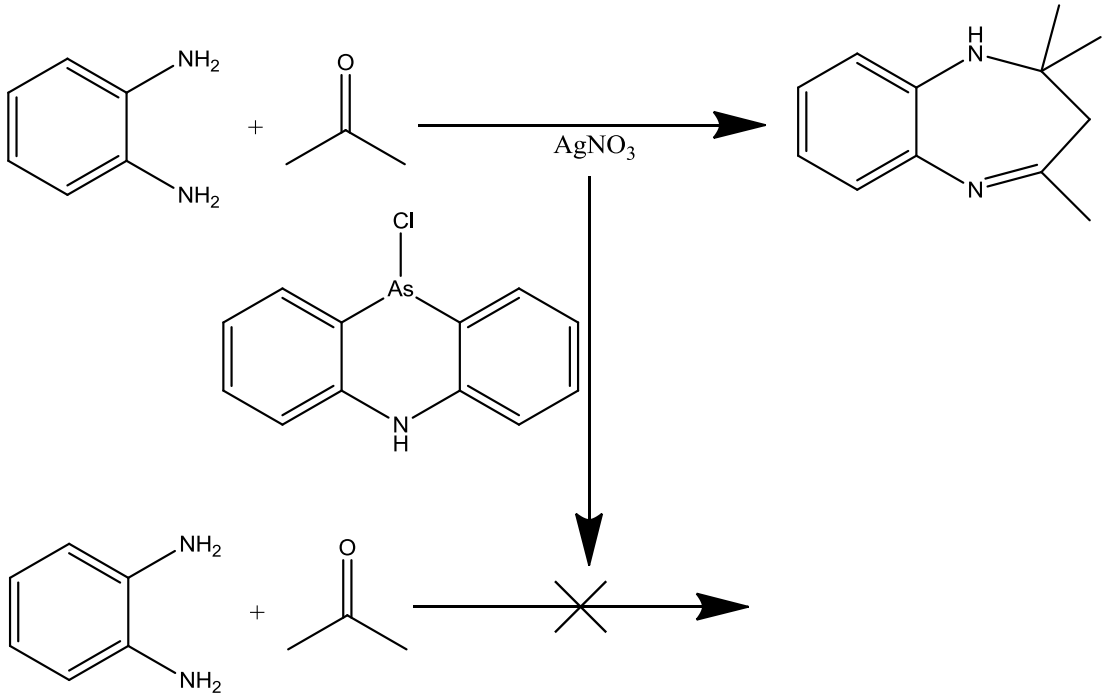

Figure 5.12: Theorized NIBS mechanism for the detection of Adamsite.

5.3.1 Chemicals and materials

Phenarsazine chloride (City Chemicals, LLP), phenylenediamine (Sigma–Aldrich), silver nitrate (Sigma–Aldrich), acetone (Sigma–Aldrich), and methanol (Fluka) were used as received. Platinum disc working electrode (MF-2013) and RE-5B Ag/AgCl reference electrode (MF-2052) were purchased from BASi.

5.3.2 Experimental procedures

Intermediate solutions of phenylenediamine (13.5 mg in 5 mL Millipore water), acetone (370 µL in 20 mL Millipore water) and silver nitrate (10 mg in 5 ml Millipore water) are prepared. An intermediate solution of Adamsite is created in methanol (11.2 mg in 20 mL methanol) due to its low solubility in water. The intermediate solutions of phenylenediamine and silver nitrate were prepared fresh daily to avoid any possible degradation in these reagents.

For an electrochemical experiment, a given amount of phenylenediamine and acetone intermediate solutions are combined and diluted with Millipore water to 10 mL. Adamsite solution is then added if the effects of catalyst inhibition are being studied. Finally, a given amount of silver nitrate solution is added, the resulting solution is mixed manually for several seconds and then placed onto a stirring plate operating at 100 rpm. The working and reference electrodes are quickly inserted and the open circuit potential of the solution is monitored for 1500 s.

For a spectroscopic experiment, various amounts of phenylenediamine, acetone and Adamsite (if inhibition is being studied) are combined in a quartz cuvette. The mixture is diluted with Millipore water such that when the catalyst is added; the total solution volume becomes 3 mL. Once the silver nitrate catalyst is added, the cuvette is briefly covered, manually mixed, then uncovered and loaded into the spectrometer for analysis. If the sample is not being continuously analyzed, it is removed from the spectrometer and covered to prevent excessive evaporation of the solvent between tests.

5.3.3 Results and discussion

For this NIBS mechanism, no solvent optimization studies were performed by Monty due to the speed of the main reaction in water as stated in literature. This permitted a more convenient experimental setup and allows for easy analysis of possible water based environmental samples once this NIBS mechanism is incorporated into a sensor platform. Monty did however perform catalyst to substrate loading optimization studies [42]. Unlike the study performed for the previous NIBS mechanism, these optimization experiments were conducted by adding varying amounts of the silver nitrate catalyst to a fixed concentration of the two reactants and monitoring the potential increase of the solution over a period of 20 min. In all experiments for this NIBS mechanism, acetone was always present in excess amounts to ensure complete conversion of phenylenediamine. Catalyst loading optimization studies were performed at 100 mM phenylenediamine (250 mM acetone) and 1 mM phenylenediamine (2.5 mM acetone) concentrations. From these catalyst loading studies, Monty found an optimal ratio of 0.027 g silver nitrate per g acetone which would ensure that a drop in available catalyst would have a significant effect on the main reaction rate figure 5.13 [42].

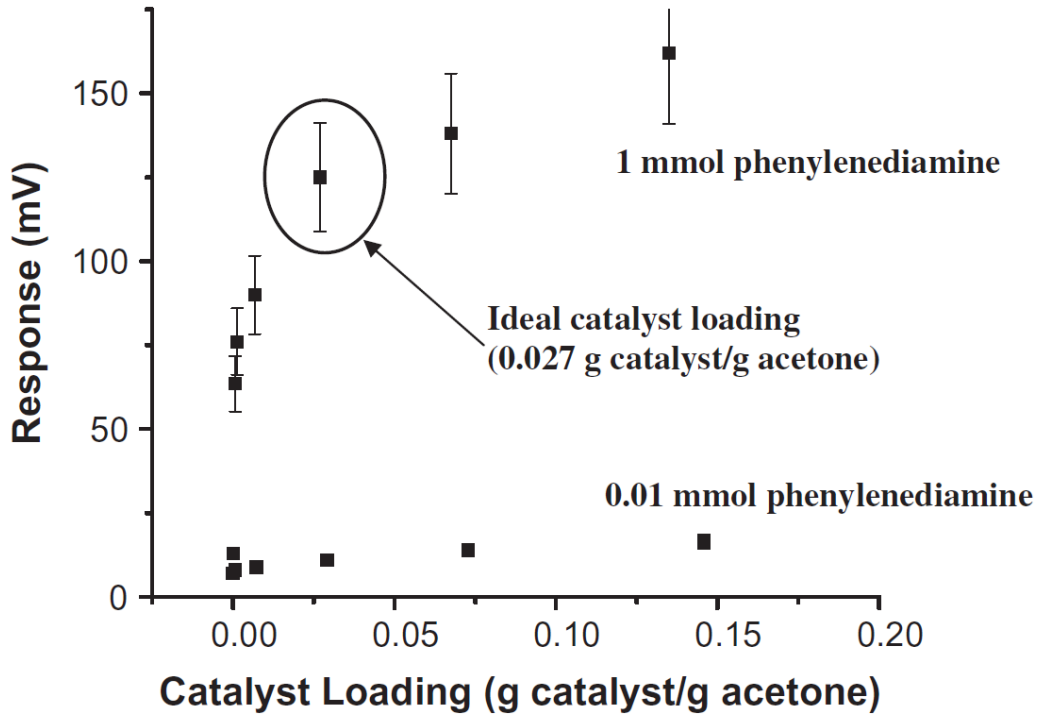

Figure 5.13: Effect of catalyst/substrate ratio on potential response of NIBS mechanism for both 100 mM and 1 mM phenylenediamine (250 mM and 2.5 mM acetone, respectively) [42].

Once the optimal catalyst loading was determined, Monty further tweaked the reactant concentrations to yield a NIBS mechanism capable of detecting micromolar amounts of Adamsite. The optimal solution concentrations for this NIBS mechanism to detect Adamsite were found to be 0.25 mM Adamsite, 2.5 mM acetone and 23.5 µM silver nitrate [42]. This gave an Adamsite detection range of 0.4 – 6 µM. Unlike the NIBS mechanism for the detection of toxic sulfides, this NIBS mechanism has been designed with reactant concentrations several orders of magnitude greater than the Adamsite concentration, thus ensuring a chemical amplification process will take place when the catalyst is inhibited. Although not performed at the optimal detection concentrations, figure 5.14 shows a typical potential response of this NIBS mechanism to the presence of the inhibitor Adamsite [42]. The addition of 1.8 µM Adamsite

causes a faster decrease in the solution potential compared to case with no Adamsite present. The sensor response of this NIBS mechanism is again found by the difference in potential between inhibited and non-inhibited curves after 30 minutes.

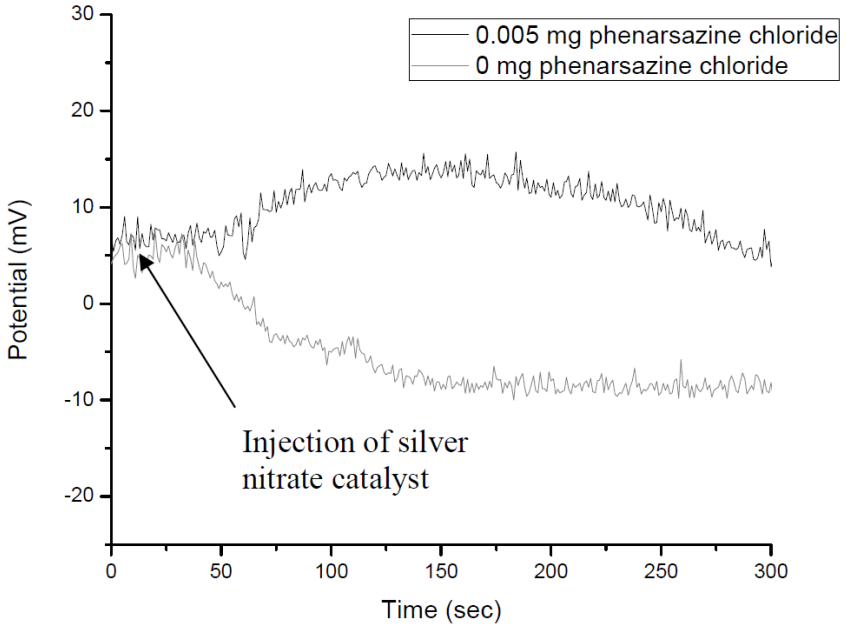

Figure 5.14: Open circuit potential response of the NIBS Adamsite detection mechanism as measured by Monty [XXX]. 1 mM phenylenediamine, 2.5 mM acetone, and 2 µM silver nitrate in water with and without the presence of 1.8 µM Adamsite [42].

Using the optimal concentrations found by Monty, I once again observe very different results for the potential response of the NIBS mechanism, both with and without the presence of Adamsite (figure 5.15).

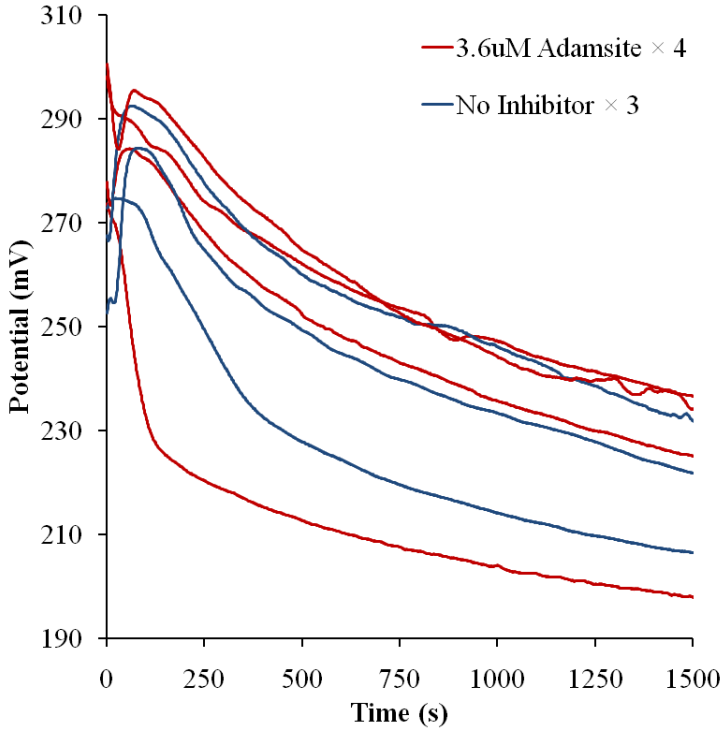

Figure 5.15: Open circuit potential response of the NIBS Adamsite detection mechanism. 0.25 mM phenylenediamine, 2.5 mM acetone, and 23.5 µM silver nitrate in water with and without the presence of 3.6 µM Adamsite.

The response of this NIBS mechanism was tested throughout the course of a day by alternating between inhibited and non-inhibited cases and seems to show an overall increase in the potential of the solution for each subsequent test. However, after approximately 4 hours of experiments the curves begin to converge. At this point it would appear that there is no significant difference is seen between the inhibited and non-inhibited responses.

One issue which could be possibly account for the overall increase in potential over time is the degradation of phenylenediamine. When initially prepared, the intermediate solution of phenylenediamine in water is clear and colorless. However over the course of several hours, this solution becomes noticeably yellow. The spectrum of this solution shows the bulk of the

absorbance comes from a peak centered at 417 nm. Figure 5.16 shows the absorbance at 417nm of a 25 mM aqueous phenylenediamine intermediate solution over time. The absorbance of this solution increases nearly linearly over a period of 48 hours after being prepared. The concentration of the phenylenediamine intermediate solution used in my experiments is 4 times more dilute than the one prepared by Monty and it is probable that this degradation process occurred at an even faster rate in her experiments.

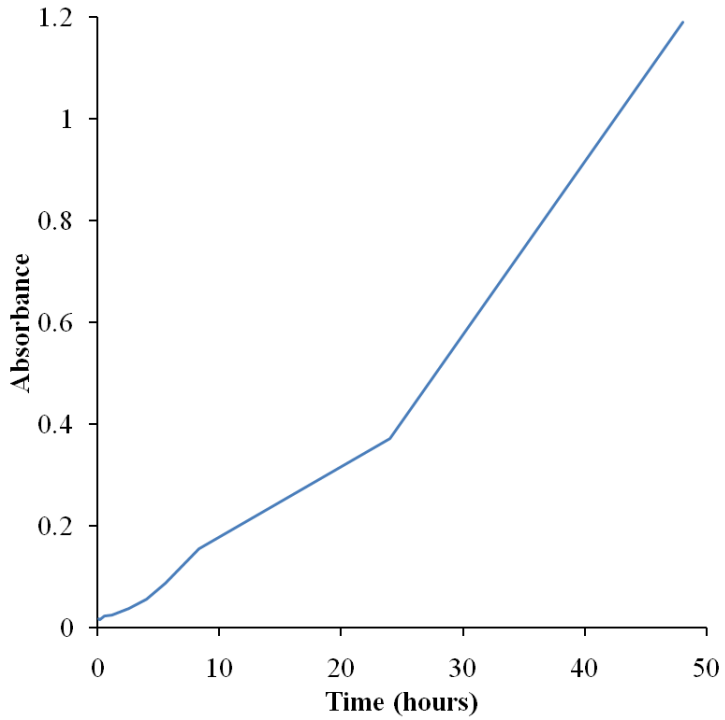

Figure 5.16: Absorbance at 417 nm of a 25 mM solution of phenylenediamine in water over a period of 48 hours.

Phenylenediamine is a commonly used monomer in chemical and electrochemical polymerization and the yellowing of this aqueous solution is most likely a result of phenylenediamine forming dimers, trimers or even larger oligomer molecules [54-57]. In fact, when this solution is left undisturbed for several days, thin strands of what appear to be

phenylenediamine polymer begin to form. However, because the polymerization of phenylenediamine takes place constantly over several days, it is not likely the cause of the overall potential increase seen taking place over the first 4 hours of experimentation. However, this polymerization would most likely effect the rate of the main reaction and is therefore a major issue in the correct operation of this NIBS chemistry.

Unlike the NIBS mechanism for detecting toxic sulfides, the main reaction in this NIBS mechanism can be monitored colorimetrically. In an effort to better understand what was happening in this NIBS mechanism, I conducted spectroscopic studies to determine if the main reaction as well as the inhibition reaction were in fact taking place. The concentration of all species for these initial spectrometric experiments was increased by a factor of roughly 33.3 (8.33 mM phenylenediamine, 83.3 mM acetone, 783 µM silver nitrate and 120 µM Adamsite) in order to quickly screen various conditions and clearly observe any side reactions taking place. At these elevated concentrations, the reactions proceed very quickly and are essentially complete within 5 minutes. Figure 5.17 shows the fully developed spectrums after ~25 minutes of the NIBS mechanism, both with and without the presence of Adamsite. It also includes a third spectrum which shows the contribution of the silver nitrate-Adamsite interaction in the absence of the main reaction (no phenylenediamine or acetone present).

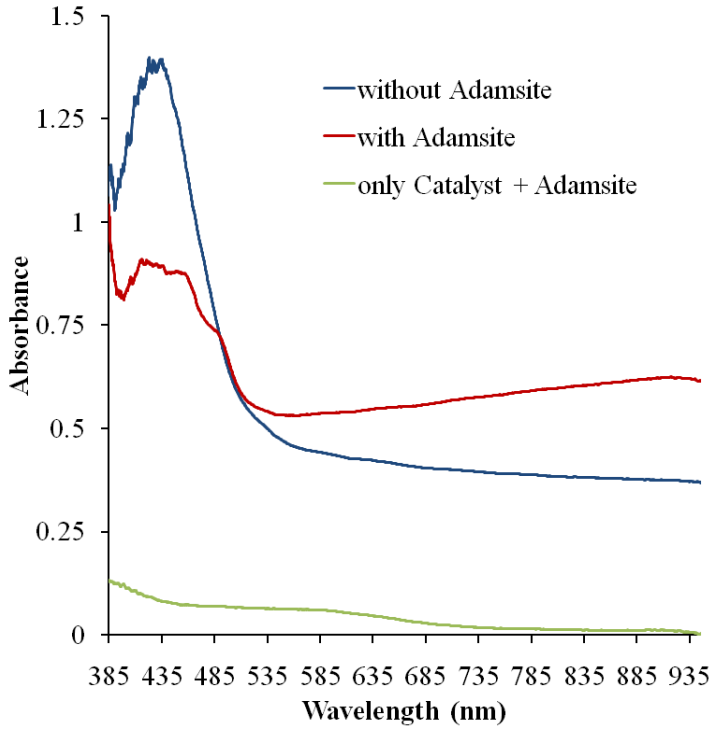

Figure 5.17: Absorbance spectrum of the NIBS mechanism after 25 minutes. 8.33 mM phenylenediamine, 83.3 mM acetone, 783 µM silver nitrate and 120 µM Adamsite present depending on the experimental conditions.

The spectrum of the main reaction in the absence of any Adamsite shows a clear, major absorbance peak at 434 nm which most likely corresponds with the benzodiazepine derivative which is expected to be produced under these conditions. The spectrum of the main reaction with Adamsite present does not have a very well defined peak but maximum absorbance takes place from approximately 430 – 470 nm and there is a shoulder peak at approximately 485 nm. Another important aspect to note is the much higher overall absorbance of the solution when Adamsite is present. Although the chemical interaction between Adamsite and silver nitrate produces a color change, the third spectrum shows that this cannot account for the higher absorbance seen from 580 – 935 nm.

In fact, very little color change actually occurs when Adamsite and silver nitrate are combined by themselves in solution and the bulk of the absorbance of this third spectrum is solely due to the green color of Adamsite in solution. As was previously mentioned, the Adamsite-silver nitrate inhibition reaction is based off a colorimetric detection technique developed by Delga [51]. All work conducted on this NIBS mechanism has the Adamsite and silver nitrate combined at room temperature in a neutral aqueous medium just as you begin to monitor the experiment. However, in the work by Delga, the color change requires a third reagent, glacial acetic acid as well as heating the total mixture for 10 minutes at temperatures close to 100 °C [51]. This information as well as the spectrometric studies indicates that the color change reaction between these two species may not be taking place, and as a result, no catalyst inhibition is occurring.

The higher overall absorbance seen from the solution with the main reaction + Adamsite is actually most likely due to an unknown side reaction taking place. Spectroscopic experiments to further understand side reactions are shown in figure 5.18 and 5.19. As noted in the procedure, Adamsite must be initially diluted in methanol due to its poor solubility in water. This Adamsite/methanol intermediate solution is what is then added to the final solution to obtain the correct concentrations. As a result, a significant amount of methanol is present during any experiment using Adamsite. Figure 5.18 shows the effect of adding an equivalent volume of pure methanol in place of the intermediate Adamsite/methanol solution.

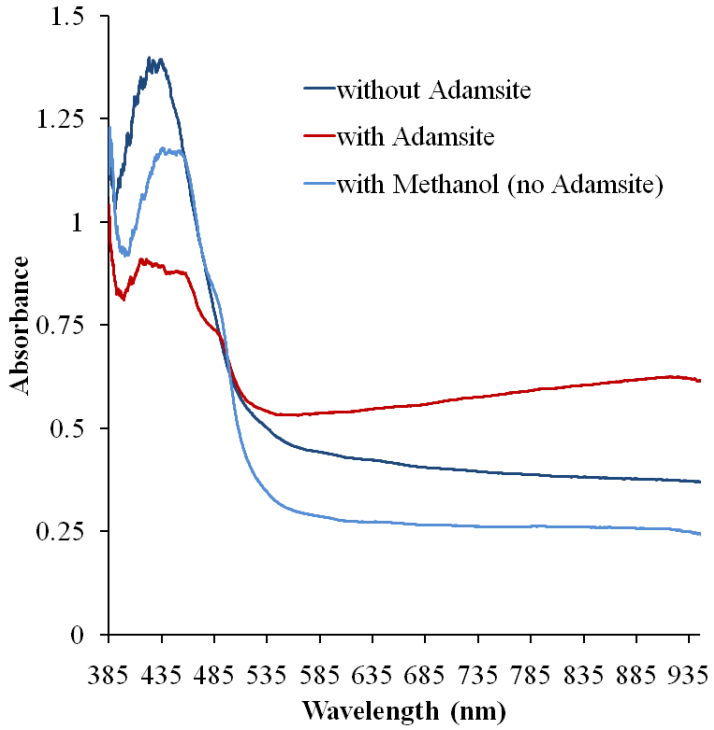

Figure 5.18: Absorbance spectrum of the solutions containing 8.33 mM phenylenediamine, 83.3 mM acetone and 783 µM silver nitrate after 25 minutes. The concentration of methanol in the one experiment is 494 mM. No Adamsite is present in any of these experiments.

The presence of methanol can be seen to have a fairly significant effect on the reactions taking place. Methanol lowers both the maximum absorbance as well as the absorbance from 580 – 935 nm compared to the spectrum without methanol present. Additionally, methanol cannot account for the high absorbance from 580 – 935 nm observed when Adamsite is present. Because of the wavelength shift for maximum absorbance, methanol is likely involved in a chemical reaction and is not simply slowing the rate of reaction between acetone and phenylenediamine.

In the absence of one of the reactants in the NIBS mechanism (phenylenediamine or acetone) the main reaction should not take place. No colorimetric change occurred in the

solution in the absence of phenylenediamine, however there was significant colorimetric activity in the solution in the absence of acetone. Figure 5.19 shows the effect of the removal of acetone on the spectrum of the solution 25 minutes after the catalyst was introduced.

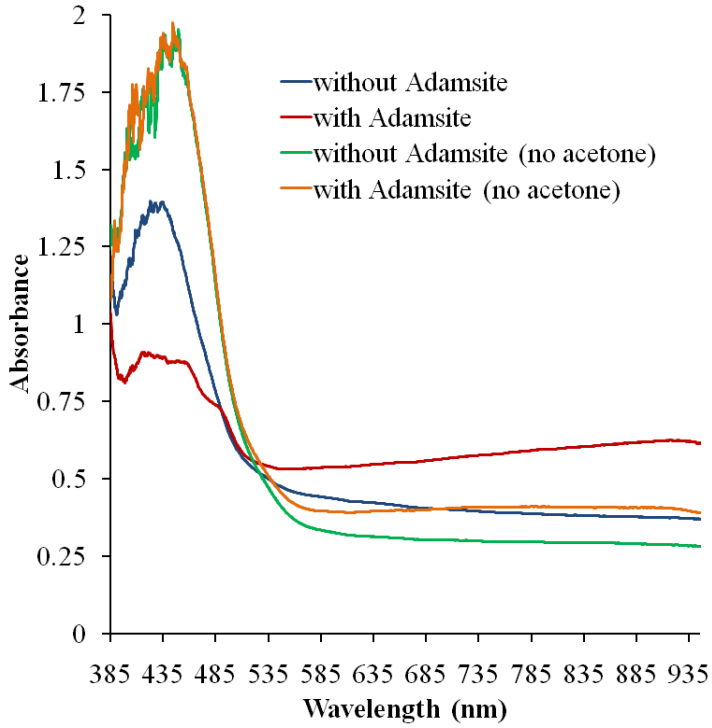

Figure 5.19: Absorbance spectrum of the solutions containing 8.33 mM phenylenediamine, and 783 µM silver nitrate after 25 minutes. Acetone concentration is either 0 mM or 83.3 mM, depending on the experiment.

In the absence of acetone, it would seem that phenylenediamine is reacting either with itself or with water. Interestingly, the presence of Adamsite does not affect the maximum absorbance or peak wavelength (~ 445 nm). It does however increase the overall absorbance of the solution from 580 – 935 nm, although not enough to completely account for the high absorbance seen from the main reaction in the presence of Adamsite. Figures 5.17 – 5.19 indicate that the chemical system used for this NIBS mechanism is much more complex than

originally imagined and several side reactions may be present. From this data, there appears to be a side reaction between Adamsite and the two reactants (phenylenediamine and acetone) which is catalyzed by silver nitrate. Additionally, there is possibly a side reaction involving the methanol which is used as a solvent of Adamsite. This added complexity makes it very difficult if not impossible to observe any catalyst inhibition properties of Adamsite.

It should be noted that in all the experiments conducted for figures 5.17 – 5.19, a very thin gray film covering the walls of the quartz cuvette was produced. This film absorbed light fairly uniformly across the wavelengths measured and its absorbance on average was approximately 0.02. After each experiment, the inside of the cuvette was wiped down to prevent build up and reset the absorbance by the cuvette to its normal levels. As a result, this film had negligible effect on these spectrometric tests. However, this film could be responsible for the overall increase in potential previously noted from figure 5.15. This film would have slowly accumulated on the working and reference electrodes over the course of several experiments at normal reactant, catalyst and inhibitor concentrations. After several experimental runs, this film could have been thick enough to impede mass transport to the electrode surface.

Colorimetric studies were also performed on the original, "optimal" concentrations for this NIBS mechanism. Figure 5.20 shows the solution absorbance at both 434 nm and 650 nm for the NIBS mechanism with and without the presence of Adamsite.

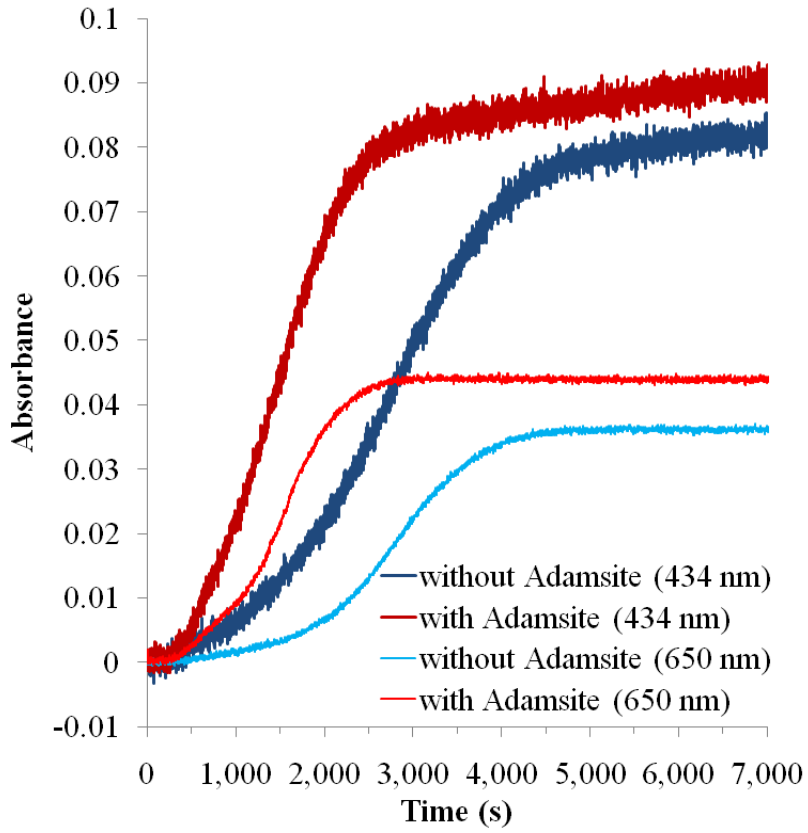

Figure 5.20: Absorbance of the NIBS mechanism over time at both 434 nm and 650 nm. 0.25 mM phenylenediamine, 2.5 mM acetone, 20.5 µM silver nitrate and 1.8 µM Adamsite present depending on the experimental conditions.

The 434 nm wavelength was chosen because this corresponds with the peak absorbance from the benzodiazepine derivative, while 650 nm was chosen to represent the wavelength which a minimum amount of absorbance takes place. In the presence of Adamsite, the solution absorbance is not only higher; the colorimetric change takes place more rapidly. Without Adamsite, the colorimetric change is essentially complete in 4,500 seconds (75 minutes). However with Adamsite, the reactions taking place finish after approximately 2,400 seconds (40 minutes). This increased absorbance and reaction rate are all most likely a result of Adamsite (and methonal) simply acting as a reactant in one or more side reactions.

This figure also raises another fundamental issue with the development of the NIBS mechanism by Monty. Although the concentration of reactants in her experiments varied by nearly 3 orders of magnitude, the potential response of the solution was always evaluated 30 minutes after catalyst was added [42]. My experiments however, show that increasing the concentration of all species present by a factor of 33.3 increases the reaction rate by approximately a factor of 20. If the potential difference measurement is performed too early, not enough of a potential change has occurred yet between inhibited and non-inhibited reactions, and the power of the chemical amplification process is not fully realized. If the measurement is performed too late, the effect of reaction rate inhibition may not be measured at all. Therefore it is critically important, both in this NIBS mechanism and others, to choose a final measurement time based on the concentration of reactants and thus the rate of the main reaction.

5.4 Conclusions and recommendations

Research into both of these NIBS mechanisms has discover multiple issues with the beaker scale development work which prevent these detection methods from operating correct and possibly indicate that they may not be entirely feasible. The development of the toxic sulfide NIBS mechanism has several critical problems associated with it, most important of which is the low substrate to inhibitor concentration ratio which appears to negate the purpose of chemical amplification. Experiments utilizing higher concentrations of the substrate formic hydrazide indicate the possibility of a side reaction between this compound and the inhibitor CEMS. Other development issues include the contradiction in the data presented on the effects of potential response as a function of catalyst to substrate ratio, as well as operating under conditions which promote stoichiometric as opposed to catalytic usage of copper (II) acetate.

The hydrazide oxidation reaction literature also illustrates a fundamental limitation with this NIBS mechanism. Without an excess of oxygen, copper (II) acetate will not act catalytically [45]. This greatly limits the useful concentration range for formic hydrazide in the main reaction due to the low solubility (< 2 μM) of molecular oxygen in methanol. With formic hydrazide concentrations in the low micro-molar range, this NIBS mechanism cannot effectively chemically amplify the target analyte.

The NIBS mechanism for the detection of Adamsite has its own set of unique issues. The overall drift in solution potential over the course of multiple electrochemical experiments combined with the substrate life-time issues from the polymerization of phenylenediamine make this chemistry difficult to reproduce accurately. Additionally, spectrometric experiments have shown that there are side reactions involving one or more of the substrates with Adamsite as well as the methanol used to dilute it with. A highly complex situation is present with various reactions taking place between numerous organic compounds present. The reaction products will also be varied and in some cases are not be soluble in the aqueous environment, as evidenced by the production of a thin film of material covering the reaction vessel. Such a film most likely plays a role in the poor reproducibility of the electrochemical measurements of this system. Spectrometric studies however are essentially unaffected by the film and clearly show that the presence of Adamsite actually increases the rate of color change talking place. The color change reaction between Adamsite and silver nitrate developed by Delga *et al.* takes place at elevated temperatures (100 °C) for prolonged periods of time (10 min) in the presence of a third reagent (acetic acid) [51]. However, the conditions used to evaluate this NIBS mechanism are at room temperature without acetic acid. Combined with the lack of color change detected spectrometrically between Adamsite and silver nitrate, it is likely that Adamsite is not effecting

silver nitrates' catalytic activity at all and no inhibition is taking place. Solid phase micro-extraction (SPME) coupled with GC-MS could be used to analyze the compounds produced under the various experiment conditions I examined in this chapter. This technique would qualitatively show if the correct benzodiazepine derivative is being produced, as well as if any other side reactions were taking place for various reaction conditions. The spectroscopic absorbance contribution of the compounds identified could then be determined if from standard solutions of the individual species.

There is a possibility that these two NIBS mechanisms can still function as intended but this will require a good deal of further research. The fundamental obstacle for a working NIBS sulfide mechanism is the ready supply of oxygen. Some possible ways of overcoming this limitation including bubbling oxygen through the solution possibly as the carrier gas for the gaseous sulfide sample, changing to a solvent that can dissolve high quantities of oxygen, or using an alternative source of oxygen for the main reaction which can be present in high concentrations in the solution. However, this alternative oxidant compound must still require the Cu+2 ions to effectively oxidize the hydrazide. The NIBS mechanism for the detection of Adamsite has even more significant limitations due to the side reactions and complex nature of the organic chemistry involved. The first step must be to determine under what temperature, pH and time conditions the colorimetric interaction between Adamsite takes places. It may be necessary for acetic acid or just another proton source to be present for this color change to take place. Only once these conditions are well understood can the main reaction be introduced. A new main reaction will also likely be needed as there are too many issues with the current phenylenediamine + acetone reaction. Even if a simpler main reaction can be found, there is no guarantee that Adamsite will actually inhibit the silver nitrate catalyst.

Unfortunately, it may be necessary to start from scratch to create a working NIBS mechanism. If this is indeed the case, development work should focus on creating a very simple, proof of principle system involving a non-biological catalyst with a well known inhibitor. The inhibitor-catalyst interaction should then be studied in detail at the concentrations relevant to a detection mechanism. At this point a simple main reaction can be chosen, preferably an in-organic reaction involving only one substrate and one product. This substrate(s) and product(s) in this reaction should first be tested with the target analyte to ensure no side reactions will take place. Then, this main reaction must be studied in great deal, both electrochemically and spectroscopically if possible. Solution potential readings cannot be directly interpreted and instead must be converted to species concentrations via standard calibration curves. A rate law for this reaction can then be created which will include both substrate and catalyst concentration effects. This rate law is critical in the effective design of the NIBS mechanism, specifically for the time require for maximum chemical amplification. Only once this development work has been carried out can the main reaction be combined with the inhibition reaction. At this point, it should only be a matter of verifying the behavior of the complete NIBS system and tweaking the concentration of the various species to reach the optimal conditions for use as a detection method. Further studies can then be done to build on the existing rate law and include the effect on inhibitor concentration.

5.5 References

1. Blaedel, W.J. and R.C. Boguslaski, *Chemical amplification in analysis - review.* Analytical Chemistry, 1978. **50**(8): p. 1026-1032.
2. Blaedel, W.J. and G.P. Hicks, *Analytical applications of continuous measurement of reaction rate - lactic dehydrogenase in blood serum.* Analytical Biochemistry, 1962. **4**(6): p. 476-&.
3. Blaedel, W.J. and G.P. Hicks, *Continuous analysis by measurement of rate of enzyme catalyzed reactions - glucose determination.* Analytical Chemistry, 1962. **34**(3): p. 388-&.
4. Blaedel, W.J. and C. Olson, *Continuous analysis by amperometric measurement of reaction rate.* Analytical Chemistry, 1964. **36**(2): p. 343-&.
5. Blaedel, W.J. and D.L. Petitjean, *Chemical analysis by measurement of reaction rate - determination of acetylacetone.* Analytical Chemistry, 1958. **30**(12): p. 1958-1965.
6. Knapp, G., H. Spitzy, and H. Leopold, *Separation and determination of thyroid hormones in blood serum.* Analytical Chemistry, 1974. **46**(6): p. 724-726.
7. Kuznetsov, V.V., et al., *Chemical amplification of the signal and the supramolecular factor in the flow determination of nanogram amounts of arsenic(V).* Journal of Analytical Chemistry, 2002. **57**(9): p. 843-851.
8. Rajagopalan, S.R., *Chemical amplification - A novel approach to ultratrace analysis.* Bull. Mater., 1983. **5**(3-4): p. 317-322.
9. Regehr, M.F. and F.E. Regnier, *Chemiluminescent detection for capillary electrophoresis and EMMA enzyme assays.* Journal of Capillary Electrophoresis, 1996. **3**(3): p. 117-124.
10. Van Antwerp, W.P., et al., *Detection of biological molecules using boronate-based chemical amplification and optical sensors along with application for implantable glucose monitor*. 1998, The Regents of the University of California and Minimed Inc.: United States of America.
11. Weinheimer, A.J., *Chemical methods: Chemiluminescence, chemical amplification, electrochemistry, and derivatization.* Anal. Tech. Atmos. Meas, 2006: p. 311-360.
12. Bachmann, T.T., et al., *Improved multianalyte detection of organophosphates and carbamates with disposable multielectrode biosensors using recombinant mutants of Drosophila acetylcholinesterase and artificial neural networks.* Biosensors & Bioelectronics, 2000. **15**(3-4): p. 193-201.
13. Bachmann, T.T. and R.D. Schmid, *A disposable multielectrode biosensor for rapid simultaneous detection of the insecticides paraoxon and carbofuran at high resolution.* Analytica Chimica Acta, 1999. **401**(1-2): p. 95-103.
14. Dzyadevych, S.V., et al., *Early-warning electrochemical biosensor system for environmental monitoring based on enzyme inhibition.* Sensors and Actuators B-Chemical, 2005. **105**(1): p. 81-87.
15. Gogol, E.V., et al., *Amperometric biosensors based on nafion coated screen-printed electrodes for the determination of cholinesterase inhibitors.* Talanta, 2000. **53**(2): p. 379-389.
16. Hendji, A.M.N., et al., *Sensitive detection of pesticides using a differential ISFET-based system with immobilized cholinesterases.* Analytica Chimica Acta, 1993. **281**(1): p. 3-11.

17. Jeanty, G. and J.L. Marty, *Detection of paraoxon by continuous flow system based enzyme sensor.* Biosensors & Bioelectronics, 1998. **13**(2): p. 213-218.
18. Longobardi, F., et al., *Use of electrochemical biosensor and gas chromatography for determination of dichlorvos in wheat.* Journal of Agricultural and Food Chemistry, 2005. **53**(24): p. 9389-9394.
19. Mionetto, N., J.L. Marty, and I. Karube, *Acetylcholinesterase in organic-solvents for the detection of pesticides - Biosensor application.* Biosensors & Bioelectronics, 1994. **9**(6): p. 463-470.
20. Mionetto, N., R. Rouillon, and J.L. Marty, *Inhibition of acetylcholinesterase by organophosphorus and carbamates compounds - studies on free and immobilized enzymes.* Journal for Water and Wastewater Research, 1992(3): p. 171-174.
21. Mulchandani, P., et al., *Biosensor for direct determination of organophosphate nerve agents. 1. Potentiometric enzyme electrode.* Biosensors & Bioelectronics, 1999. **14**(1): p. 77-85.
22. Palchetti, I., et al., *Determination of anticholinesterase pesticides in real samples using a disposable biosensor.* Analytica Chimica Acta, 1997. **337**(3): p. 315-321.
23. Shi, H.B., et al., *Fabricating of acetylcholine biosensor by a layer-by-layer deposition technique for determining trichlorfon.* Electroanalysis, 2005. **17**(14): p. 1285-1290.
24. Sotiropoulou, S., D. Fournier, and N.A. Chaniotakis, *Genetically engineered acetylcholine sterase-based biosensor for attomolar detection of dichlorvos.* Biosensors & Bioelectronics, 2005. **20**(11): p. 2347-2352.
25. Suprun, E., et al., *Acetylcholinesterase sensor based on screen-printed carbon electrode modified with prussian blue.* Analytical and Bioanalytical Chemistry, 2005. **383**(4): p. 597-604.
26. Amine, A., et al., *Enzyme inhibition-based biosensors for food safety and environmental monitoring.* Biosensors & Bioelectronics, 2006. **21**(8): p. 1405-1423.
27. Andreescu, S., et al., *Detection of organophosphorus insecticides with immobilized acetylcholinesterase - comparative study of two enzyme sensors.* Analytical and Bioanalytical Chemistry, 2002. **374**(1): p. 39-45.
28. Andreescu, S., et al., *Screen-printed electrode based on AChE for the detection of pesticides in presence of organic solvents.* Talanta, 2002. **57**(1): p. 169-176.
29. Belcher, R., *Amplification reactions.* Talanta, 1968. **15**(4): p. 357-366.
30. Botre, F., et al., *Cholinesterase based bioreactor for determination of pesticides.* Sensors and Actuators B-Chemical, 1994. **19**(1-3): p. 689-693.
31. Monty, C.N., I. Oh, and R.I. Masel, *Enzyme-based electrochemical multiphase microreactor for detection of trace toxic vapors.* Ieee Sensors Journal, 2008. **8**(5-6): p. 580-586.
32. Alexander, P.W. and G.A. Rechnitz, *Enzyme inhibition assays with an amperometric glucose biosensor based on a thiolate self-assembled monolayer.* Electroanalysis, 2000. **12**(5): p. 343-350.
33. Ciucu, A.A., C. Negulescu, and R.P. Baldwin, *Detection of pesticides using an amperometric biosensor based on ferophthalocyanine chemically modified carbon paste electrode and immobilized bienzymatic system.* Biosensors & Bioelectronics, 2003. **18**(2-3): p. 303-310.

34. de Melo, J.V., et al., *Urea biosensors based on immobilization of urease into two oppositely charged clays (Laponite and Zn-Al layered double hydroxides).* Analytical Chemistry, 2002. **74**(16): p. 4037-4043.
35. Han, S.B., et al., *A methylene blue-mediated enzyme electrode for the determination of trace mercury(II), mercury(I), methylmercury, and mercury-glutathione complex.* Biosensors & Bioelectronics, 2001. **16**(1-2): p. 9-16.
36. Kuswandi, B., *Simple optical fibre biosensor based on immobilised enzyme for monitoring of trace heavy metal ions.* Analytical and Bioanalytical Chemistry, 2003. **376**(7): p. 1104-1110.
37. Mourzina, I.G., et al., *Immobilization of urease and cholinesterase on the surface of semiconductor transducer for the development of light-addressable potentiometric sensors.* Microchimica Acta, 2004. **144**(1-3): p. 41-50.
38. Pirvutoiu, S., et al., *Flow injection analysis of mercury(II) based on enzyme inhibition and thermometric detection.* Analyst, 2001. **126**(9): p. 1612-1616.
39. Rodriguez, B.B., J.A. Bolbot, and I.E. Tothill, *Urease-glutamic dehydrogenase biosensor for screening heavy metals in water and soil samples.* Analytical and Bioanalytical Chemistry, 2004. **380**(2): p. 284-292.
40. Lowry, O.H., et al., *The measurement of pyridine nucleotides by enzymatic cycling* J. Biol. Chem., 1961. **236**: p. 2746-2755.
41. Monty, C.N., N.J. Londono, and R.I. Masel, *Non-Biological Inhibition Based Sensing (NIBS) demonstrated for the detection of toxic sulfides.* Analytical Chemistry, 2009. **81**(15): p. 6416-6421.
42. Monty, C.N., N.J. Londono, and R.I. Masel, *Non-Biological Inhibition Based Sensing (NIBS) demonstrated for the detection of toxic arsenic compounds.* Chemosphere, 2011. **82**(11): p. 1644-1648.
43. Brinkley, J.F., et al., *Charge-transfer complexes of Cu(II)/HD analogue in sol-gel sensors.* Chemical Physics Letters, 2003. **367**(1-2): p. 39-43.
44. Tsuji, J., et al., *Oxidative cleavage reaction of 3-substituted indoles catalyzed by CuCl-pyridine complex under oxygen.* Bulletin of the Chemical Society of Japan, 1981. **54**(8): p. 2369-2373.
45. Tsuji, J., et al., *Facile oxidative conversion of hydrazides of carboxylic-acids to corresponding acids, esters and amides using copper-compounds.* Tetrahedron, 1980. **36**(10): p. 1311-1315.
46. Karlin, K.D. and Y. Gultneh, *Binding and activation of molecular-oxygen by copper-complexes.* Progress in Inorganic Chemistry, 1987. **35**: p. 219-327.
47. Haas, R., et al., *Chromatographic determination of phenylarsenic compounds.* Fresenius Journal of Analytical Chemistry, 1998. **361**(3): p. 313-318.
48. Sanderson, H., et al., *PBT screening profile of chemical warfare agents (CWAs).* Journal of Hazardous Materials, 2007. **148**(1-2): p. 210-215.
49. Sanderson, H., et al., *Screening level fish community risk assessment of chemical warfare agents in the Baltic Sea.* Journal of Hazardous Materials, 2008. **154**(1-3): p. 846-857.
50. Sanderson, H., et al., *Human health risk screening due to consumption of fish contaminated with chemical warfare agents in the Baltic Sea.* Journal of Hazardous Materials, 2009. **162**(1): p. 416-422.
51. Delga, J., *New Colour Reaction of Phenarsazine Chloride.* J. Pharm. Chim., 1940. **132**: p. 73-76.

52. Krishnan, G.R., R. Sreerekha, and K. Sreekumar, *Three component Mannich reaction and 1,5-benzodiazepine synthesis catalyzed by a tetranitrile-silver complex.* Letters in Organic Chemistry, 2009. **6**(1): p. 17-21.
53. Kumar, R., et al., *An efficient synthesis of 1,5-benzadiazepine derivatives catalyzed by silver nitrate.* Green Chemistry, 2006. **8**(6): p. 519-521.
54. Chiba, K., et al., E*lectrochemical preparation of a ladder polymer containing phenazine rings.* Journal of Electroanalytical Chemistry, 1987. **219**(1-2): p. 117-124.
55. Huang, M.R., X.G. Li, and W. Duan, *Effect of polymerization conditions on o-phenylenediamine and o-phenetidine oxidative copolymers.* Polymer International, 2005. **54**(1): p. 70-82.
56. Premasiri, A.H. and W.B. Euler, S*yntheses and characterization of poly(aminophenazines).* Macromolecular Chemistry and Physics, 1995. **196**(11): p. 3655-3666.
57. Wu, L.L., J. Luo, and Z.H. Lin, *Spectroelectrochemical studies of poly-o-phenylenediamine .1. In situ resonance Raman spectroscopy.* Journal of Electroanalytical Chemistry, 1996. **417**(1-2): p. 53-58.

Chapter 6:

Thesis Summary and Recommendations for Future Research

A large variety of chemical sensors currently exist today, however the majority of these are solid state based technologies which detect species in a fairly non-selective manner. Biological components such as enzymes, antibodies or entire cells have been utilized to increase selectivity; however this usually comes at the expense of device life time and operating condition restrictions. Liquid based detection methods frequently involve non-biological, chemically selective reactions which produce an absorbance or fluorescence change in solution. Unfortunately these detection techniques usually have a much slower response time and decreased sensitivity compared to solid state sensors. The research in this thesis details the use and optimization of several different highly sensitive and selective liquid based detection chemistries. The majority of this thesis focuses on the use of an aqueous based chemistry utilizing an oxime reagent for the detection of acetylcholinesterases inhibitors, as well as the micro-fluidic sensor platform which enables this chemistry to be operated effectively. Alternative liquid detection chemistries following Non-Biological Inhibition Based Sensing (NIBS) mechanisms were also examined in greater detail in the final chapter of this thesis.

Research was initially conducted to improve the life time of the oxime reagent in solution in order to make it more competitive compared to biological based sensors. The oxime reagent decomposition in solution was studied electrochemically as well as by solid phase micro-extraction (SPME) analyzed through GC-MS. With this data, both an empirical kinetic rate law and likely decomposition mechanisms were established for the degradation process. The rate law was roughly 1^{st} order in oxime concentration, sub-1^{st} order for hydroxide concentration, and

the degradation mechanism is likely a rearrangement reaction where the oxime anion attacked itself. Therefore, dissolving the oxime in an organic solvent would prevent it from dissociating and thereby greatly suppressing degradation. The concentrated organic oxime solution could then be combined with a basic aqueous buffer just prior to being used in the detection process, thus suppressing degradation without significantly affecting electrochemical performance. Ethanol was chosen as the optimal organic solvent as it was able to increase the oxime life time in solution 10 fold, while causing minimal decreases in sensor sensitivity and response speed. Finally, in order to mix the aqueous and organic solutions on chip, a serpentine channel micro-mixer was created with the same dimensions and material as the original micro-sensor to allow for seamless integration.

The micro-fluidic platform previously developed for this oxime based chemistry enabled rapid and selective detection of acetylcholinesterase inhibitors. This selectivity was further demonstrated in this thesis by exposing this oxime micro-sensor to a wide variety of possible gaseous interferent compounds in the form of the EPA TO-15 mixture. Despite prolonged and repeated exposure, no response was observed from the sensor. Further characterization of this micro-sensor showed that although its response speed was fundamentally limited by the reaction rate of oxime with the analyte, performance could be increased roughly 25% by operating at a higher temperature. This did however come at the expense of sensor reliability caused by disruptions in the gas-liquid interface within the device. Regards of these issues, kinetic limitations had a negligibly affect on sensor performance if the device was coupled to a chromatography column for analysis of complex mixtures. The rapid, selective nature of the oxime micro-sensor allowed for quick evaluation of individual compounds, only responding to acetylcholinesterase inhibitors even if they are co-eluted with interferent compounds from the

GC column. Finally, this oxime micro-sensor was further miniaturized via a silicon micro-fabrication process. This allowed it to be integrated with 7 single walled carbon nano-tube (SWNT) based sensors on a single chip to form a complete micro-sensor array. This array had a footprint of 1.4 ×1.4 cm on each side, and was assembled as a stack from 4 micro-machined silicon wafers. Within the silicon micro-array there were gas and liquid micro-channels, a integrated resistive heater element for the SWNT-based sensors, and a thermal isolation break for the oxime sensor. Testing of the initially prototype found the sensors to be functional, however performance was diminished compared to their stand-alone counterparts.

The Non-Biological Inhibition Based Sensing (NIBS) mechanisms which were studied in this thesis are another example of selective liquid chemistries. These detection schemes are noticeably more complex than the oxime chemistry; utilizing the inhibition of a catalyst with the target analyte to dramatically slow the rate of a main reaction. This has the effect of chemically amplifying the presence of the analyte molecule by reducing the production of hundreds or thousands of molecules. Two such examples of this NIBS mechanism have been previously developed; one for the detection of toxic sulfides and one for the detection of the riot control agent Adamsite. However, research into both of these NIBS mechanisms has discover multiple issues with the beaker scale development work which prevent these detection methods from operating correct and possibly indicate that they may not be entirely feasible. The development of the toxic sulfide NIBS mechanism has several critical problems associated with it, most important of which is the low substrate to inhibitor concentration ratio which appears to negate the purpose of chemical amplification. Other development issues include operating under conditions which promote stoichiometric as opposed to catalytic usage of copper (II) acetate. The NIBS mechanism for the detection of Adamsite has its own set of unique issues. Reagent

lifetime issues exist as a result of the gradual polymerization of phenylenediamine. Additionally, spectrometric experiments have shown that there are likely side reactions involving one or more of the substrates with Adamsite as well as the methanol used to dilute it with. Combined with the lack of color change detected spectrometrically between Adamsite and silver nitrate, it is likely that Adamsite is not effecting silver nitrates' catalytic activity at all and no inhibition is taking place.

Development in the area of selective liquid based chemical sensors remains challenging due to the unique nature of each specific detection mechanism. Existing colorimetric detection mechanisms can possibly be adapted for use in electrochemical based sensor systems, although care must be taken to ensure that the selectivity of such mechanisms in not lost in the process. Chemical amplification techniques, specifically NIBS hold a great deal of promise for liquid based sensors; however the increased complexity of such systems introduces additional development challenges. Combining these liquid chemistries with an appropriately designed micro-sensor platform can not only improve the portability and reliability of the device, it should be able to increase the detection sensitivity and speed. Central to micro-sensor design is the gas-liquid interface. The power of the micro-fluidic platform for gas sensors is its ability to concentration the analyte and subsequently the chemical reaction to a thin region of liquid at the gas-liquid interface. By localizing the electrochemical measurements in this area, a large boost in detection sensitivity as well as response time can be realized. Therefore, further micro-sensor development should focus on membrane design and characterization. Membrane material, pore size, shape and hydrophobicity should all be studied in great detail. Techniques for *in-situ* monitoring of the gas-liquid interface and its interaction with the membrane would be particularly helpful when evaluating membrane performance.

Appendix A: Fabrication Steps for Silicon Micro-Array

Layer 1: SWNT-based Sensor Layer

Fabricated from 500 µm SSP intrinsic (>1000ohm*cm) silicon wafer

- PR on top side
- Pattern for alignment marks **(Mask 1a)**
- Very shallow etch of Si
- Remove PR
- Grow 500 nm SiO_2 (6 sccm O_2, 1150 °C)
- PR on top side
- Pattern PR for heating element **(Mask 1b)**
- Etch SiO_2
- Remove PR
- Diffusive doping of Boron for heating element (40 min, 1000 °C, 6 L/min N_2)
- Remove glass/SiO_2
- Grow 500 nm SiO_2 (6 sccm O_2, 1150 °C)
- PR on top side
- Pattern PR for heater electrical contacts **(Mask 1c)**
- Etch SiO2
- Sputter Cr/Au heater contacts (100/1000 nm Cr/Au)
- Remove PR
- Anneal at 375 °C for 15 min (under 4 L/min N_2)
- Pattern PR for SWNT sensor contacts/leads **(Mask 1d)**

- Sputter Cr/Au SWNT sensor contacts/leads (100/1000 nm Cr/Au)
- Remove PR
- SC-1 Cleaning
- PR on both sides
- Pattern bottom side with thermal breaks, die edges and through holes **(Mask 1e)**
- Coat wafer in APTES solution (~5% in Ethanol)
- DRIE through wafer on bottom side
- Remove PR
- Place SWNTs over all 7 electrode gaps (1 mm diameter disc)
- Acetone rinse to remove mixed cellulose ester (MCE) membranes
- Electropolymerize organic coating over SWNT sensors

Layer 2: Gas Micro-channel Layer

Fabricated from 400 µm DSP (p-type 10 ohm*cm) silicon wafer

- PR both sides
- Pattern top side with thermal breaks, die edges and through holes **(Mask 2a)**
- Pattern bottom side with gas channel **(Mask 2b)**
- DRIE 100 µm on bottom side
- DRIE through on top side
- Remove PR

Layer 3: Oxime Sensor Gas/Liquid Membrane Layer

Fabricated from DSP SOI wafer (400 µm handle, 20 µm <100> p-type, 1 µm BOX)

- Grow 500 nm SiO_2 (6 sccm O_2, 1150 °C)
- PR top side
- Pattern for sensor contacts/leads **(Mask 3a)**
- Sputter Cr/Au oxime sensor contacts/leads (100/1000 nm Cr/Au)
- Liftoff PR/Cr/Aug
- PR both sides
- Pattern top for membrane holes, thermal breaks, die edges and through holes **(Mask 3b)**
- Pattern bottom for gas channel, thermal breaks, die edges and through holes **(Mask 3c)**
- Etch Cr/Au from top
- Freon RIE to remove SiO_2 (24 sccm CF_4, 3 sccm O_2)
- DRIE top ~20 – 30 µm
- DRIE bottom ~400 µm
- Freon RIE to remove SiO_2 barrier between top and bottom (24 sccm CF_4, 3 sccm O_2)
- Remove PR

Layer 4: Liquid Micro-channel Layer

Fabricated from 400 µm DSP (p-type 10 ohm*cm) silicon wafer

- PR both sides
- Pattern top side with thermal breaks and die edges **(Mask 4a)**
- Pattern bottom side with liquid channel **(Mask 4b)**
- DRIE 100 µm on bottom side
- DRIE through on top side
- Remove PR

Appendix B: Photolithography Mask for Fabrication of Silicon Micro-Array

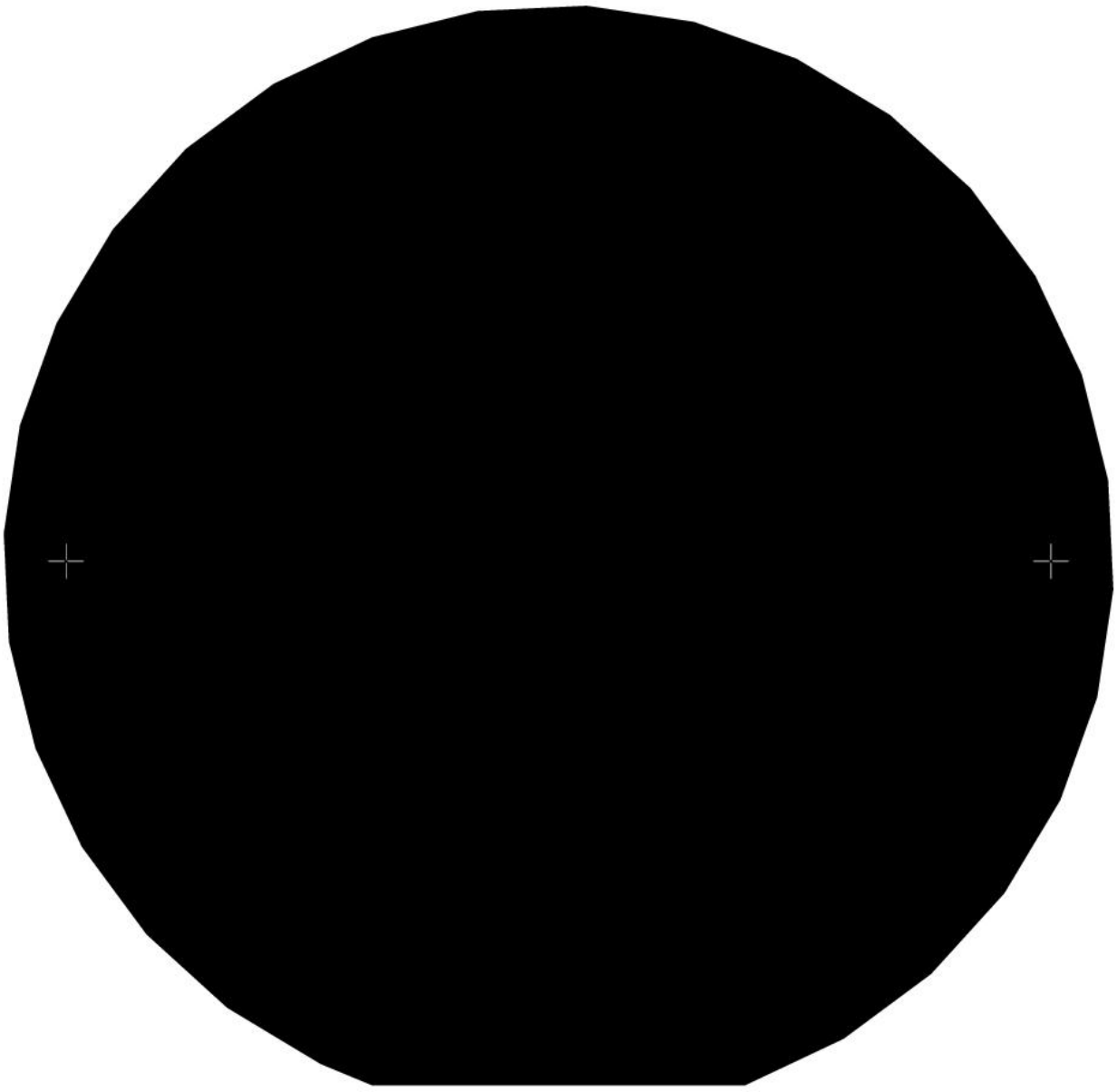

Figure B.1: Mask 1a – Pattern for alignment marks on top of layer 1.

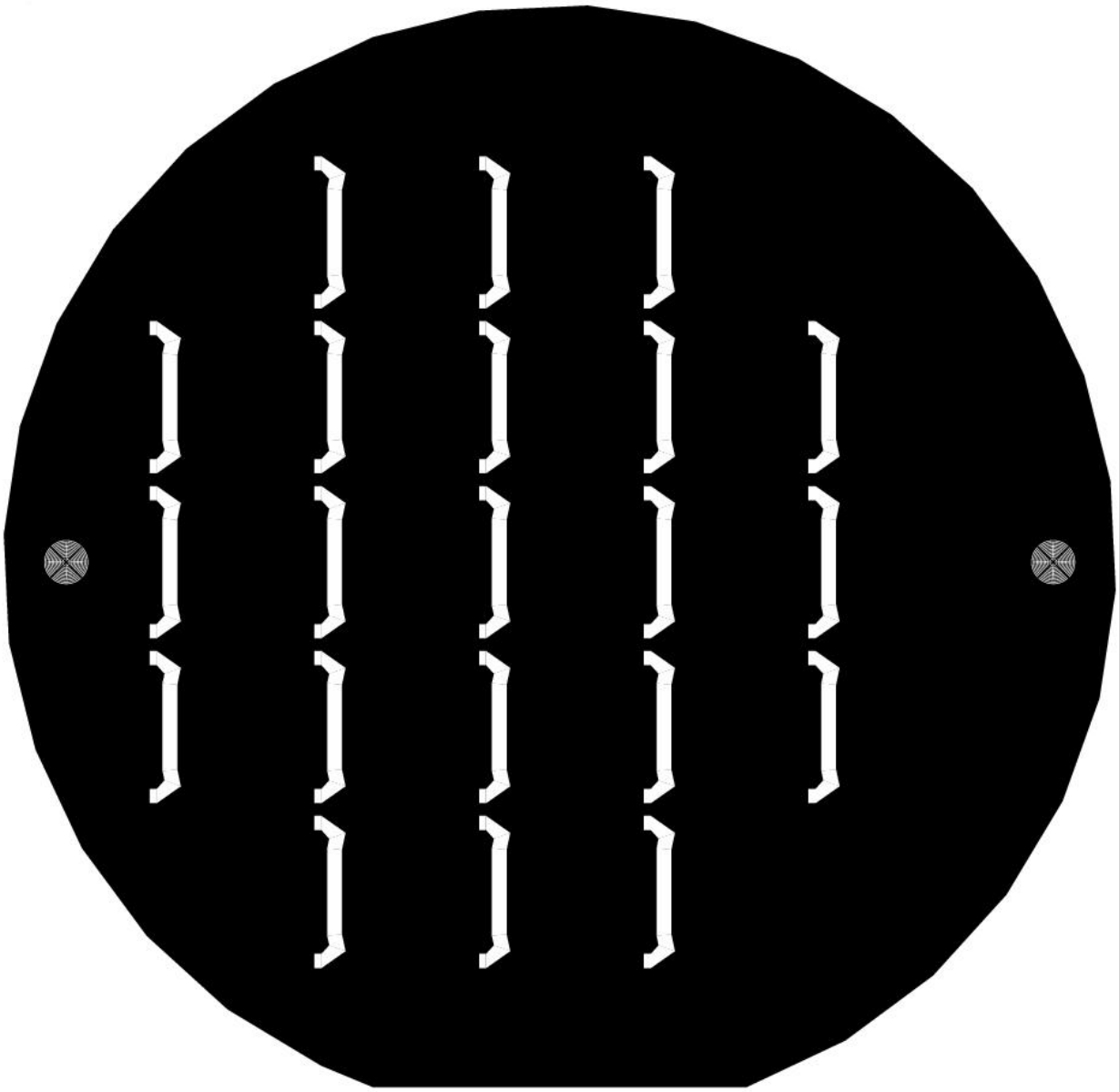

Figure B.2: Mask 1b – Pattern for integrated resistive heater element on top of layer 1.

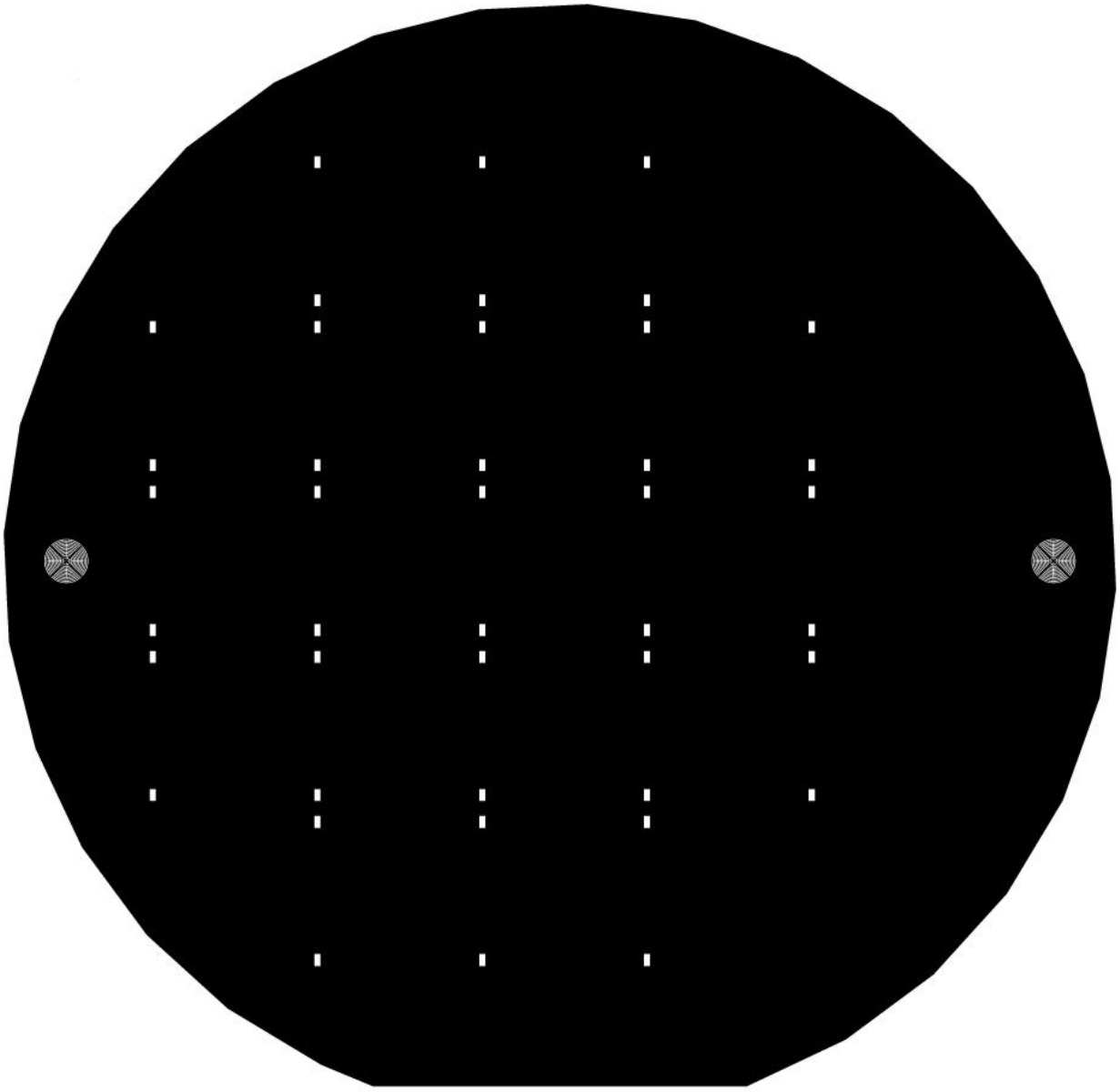

Figure B.3: Mask 1c – Pattern for gold contact pads for resistive heater element on top of layer 1.

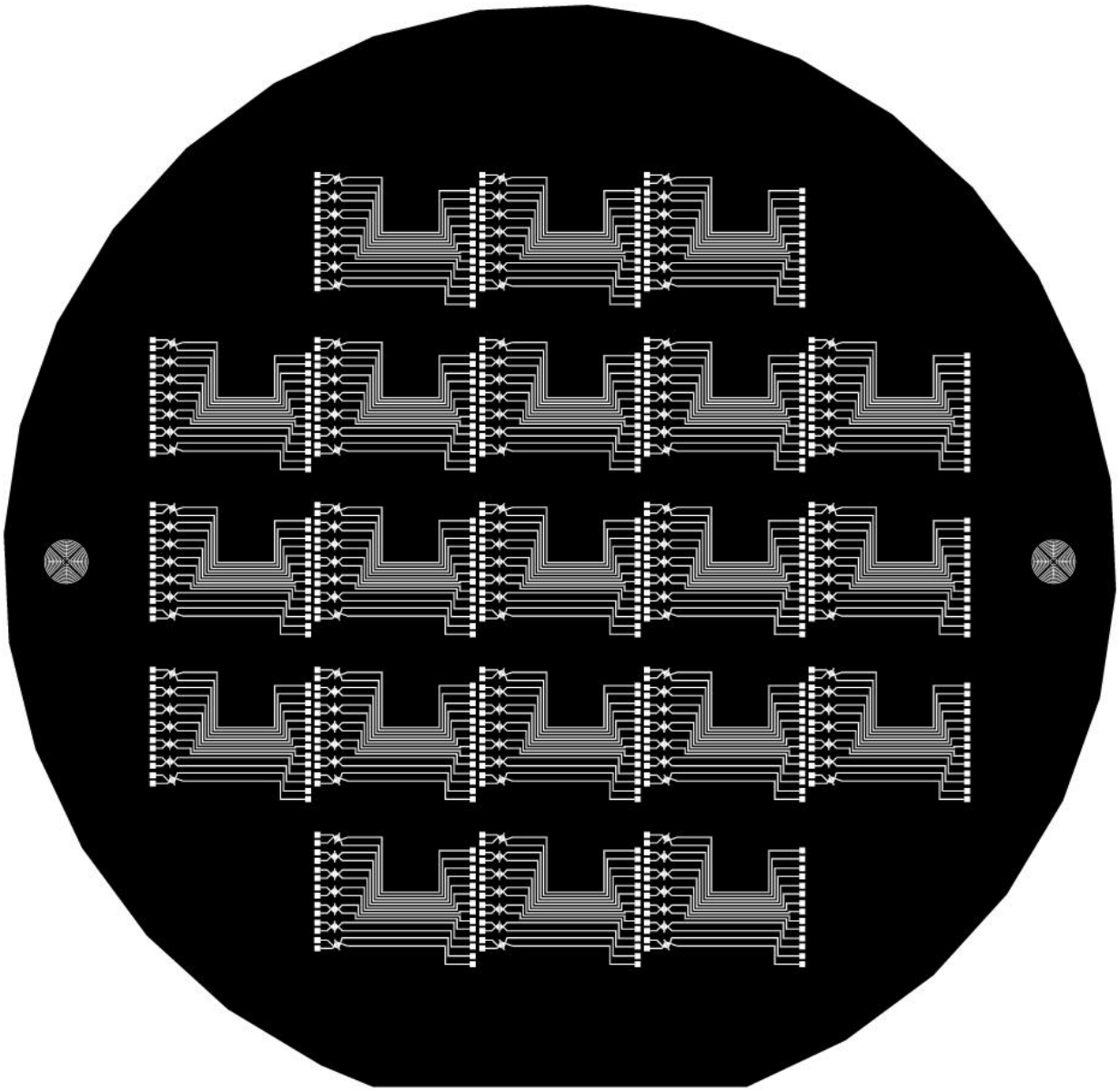

Figure B.4: Mask 1d – Pattern for gold electrodes/contact/leads for SWNT-based sensors on top of layer 1.

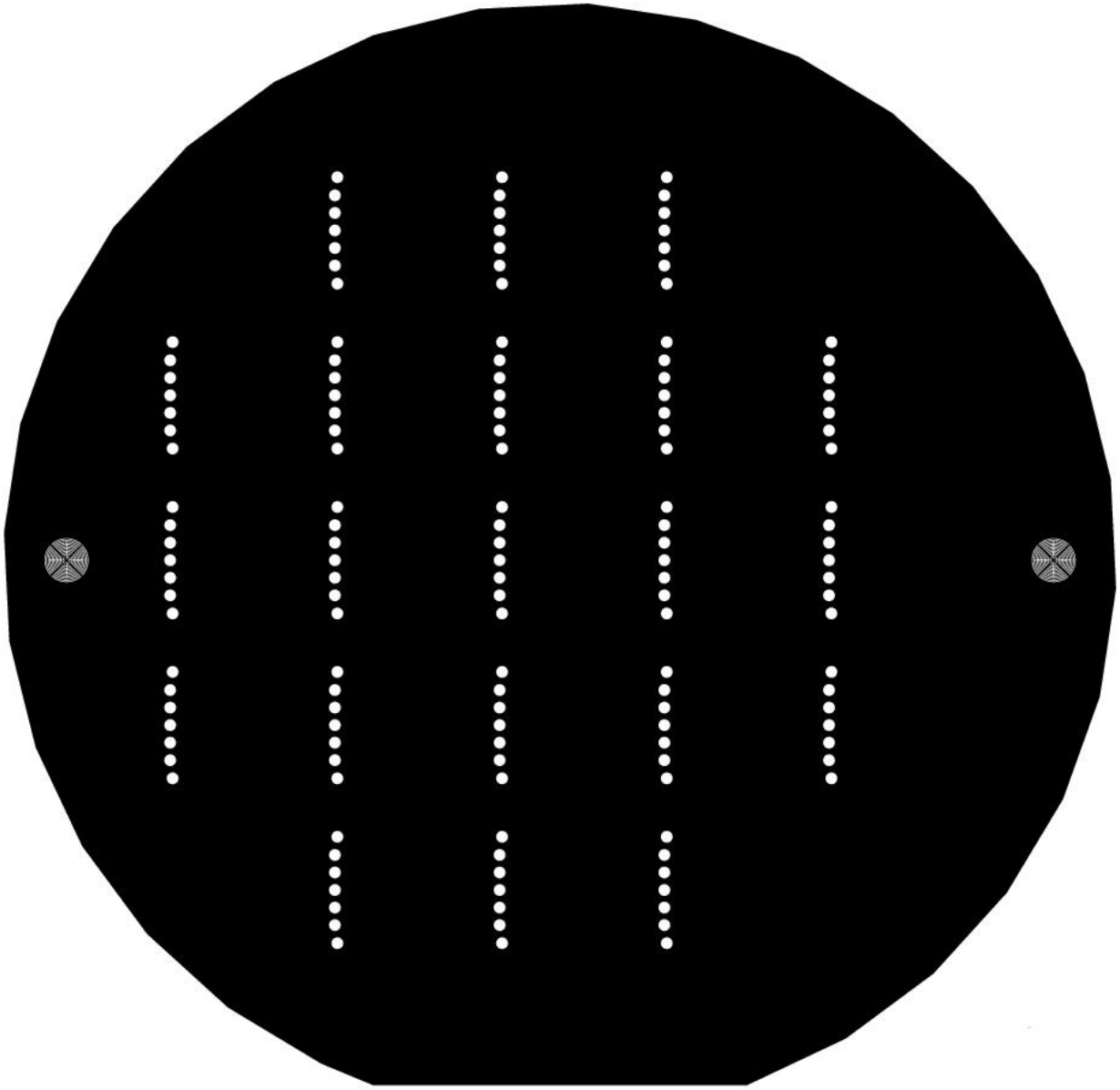

Figure B.5: Mask 1e – Optimal mask for SWNT film deposition alignment on top of layer 1.

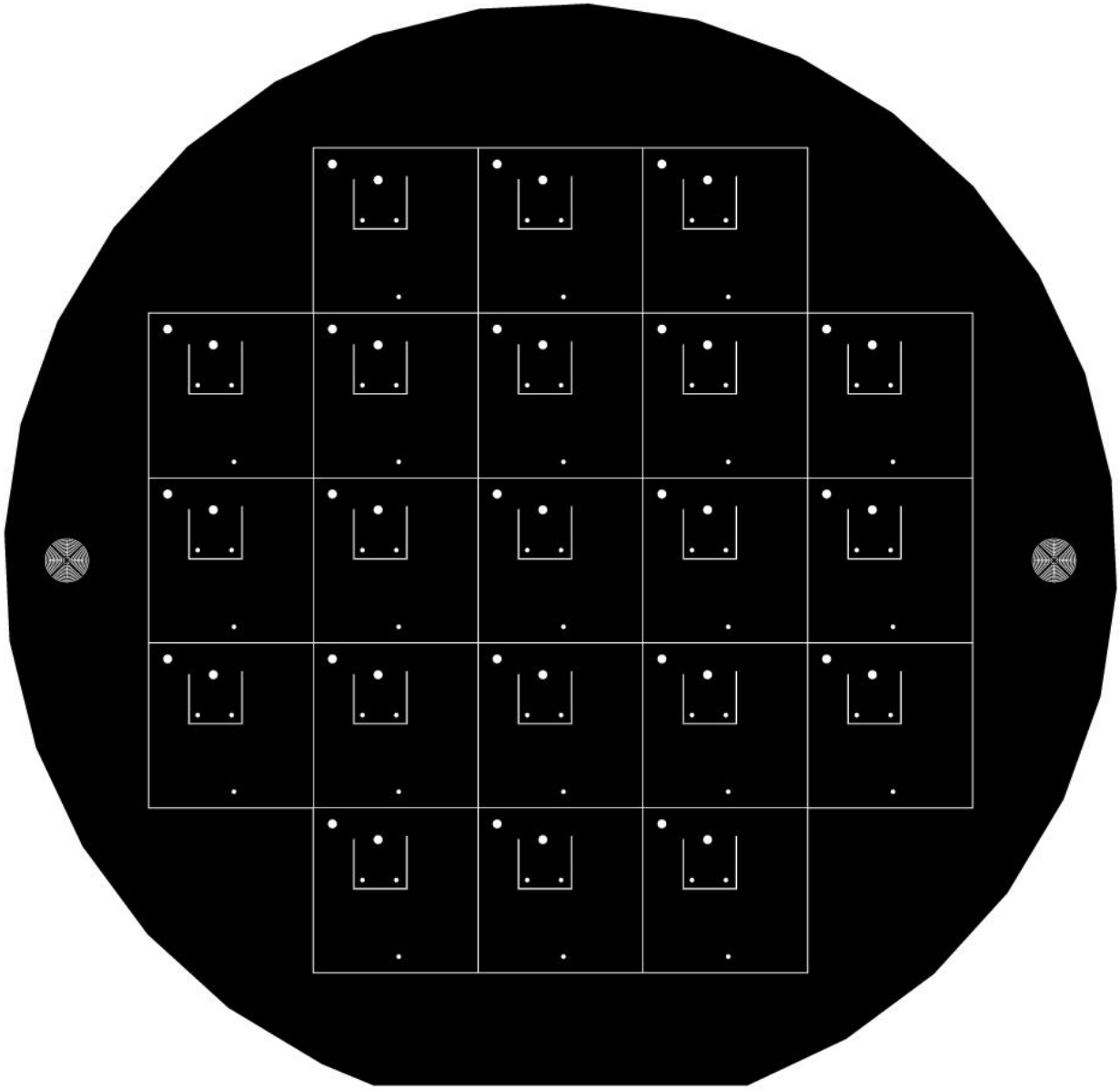

Figure B.6: Mask 1f – Pattern for through-holes, thermal break and die edges on bottom of layer 1.

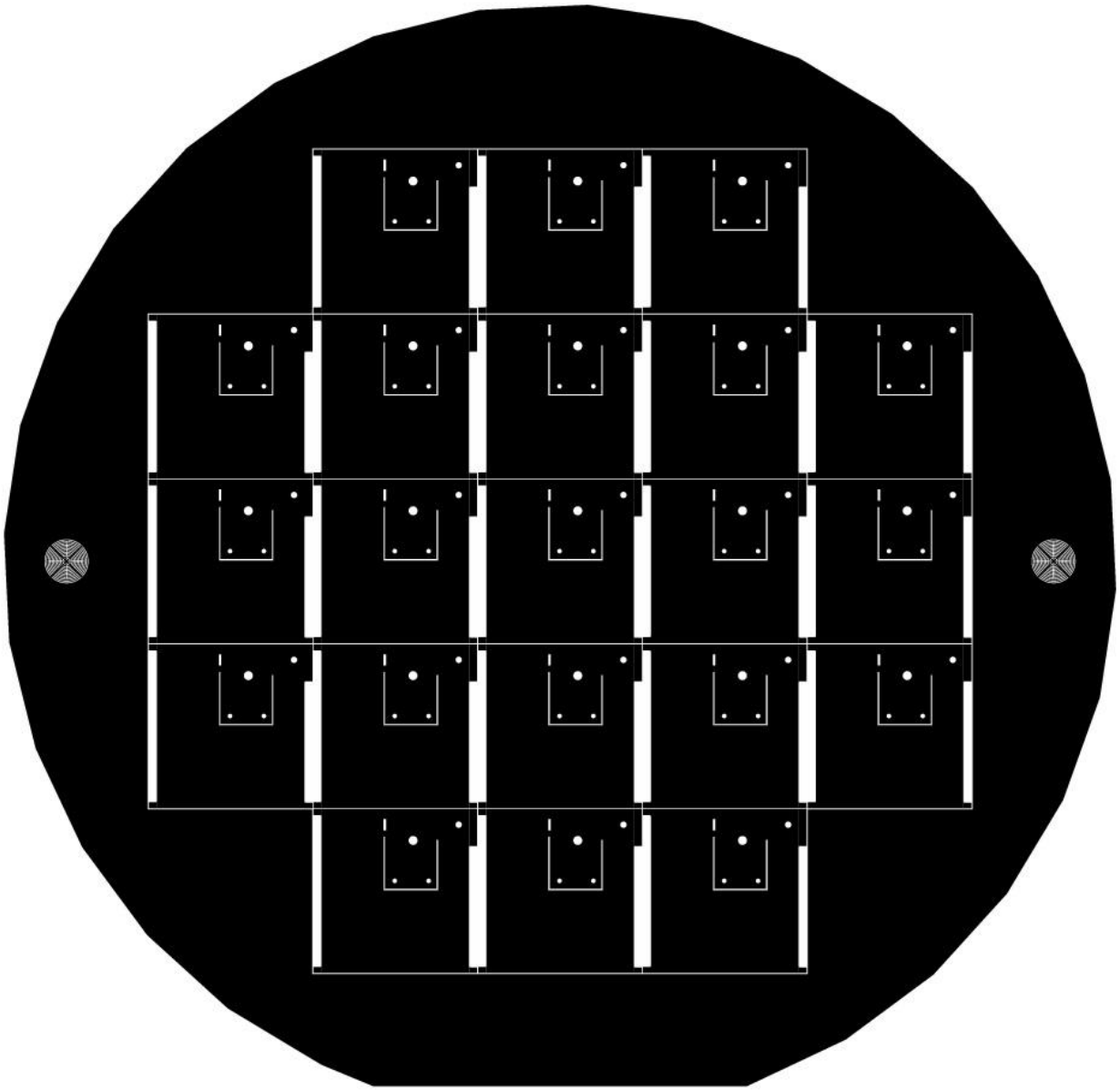

Figure B.7: Mask 2a – Pattern for through-holes, thermal break and die edges on top of layer 2.

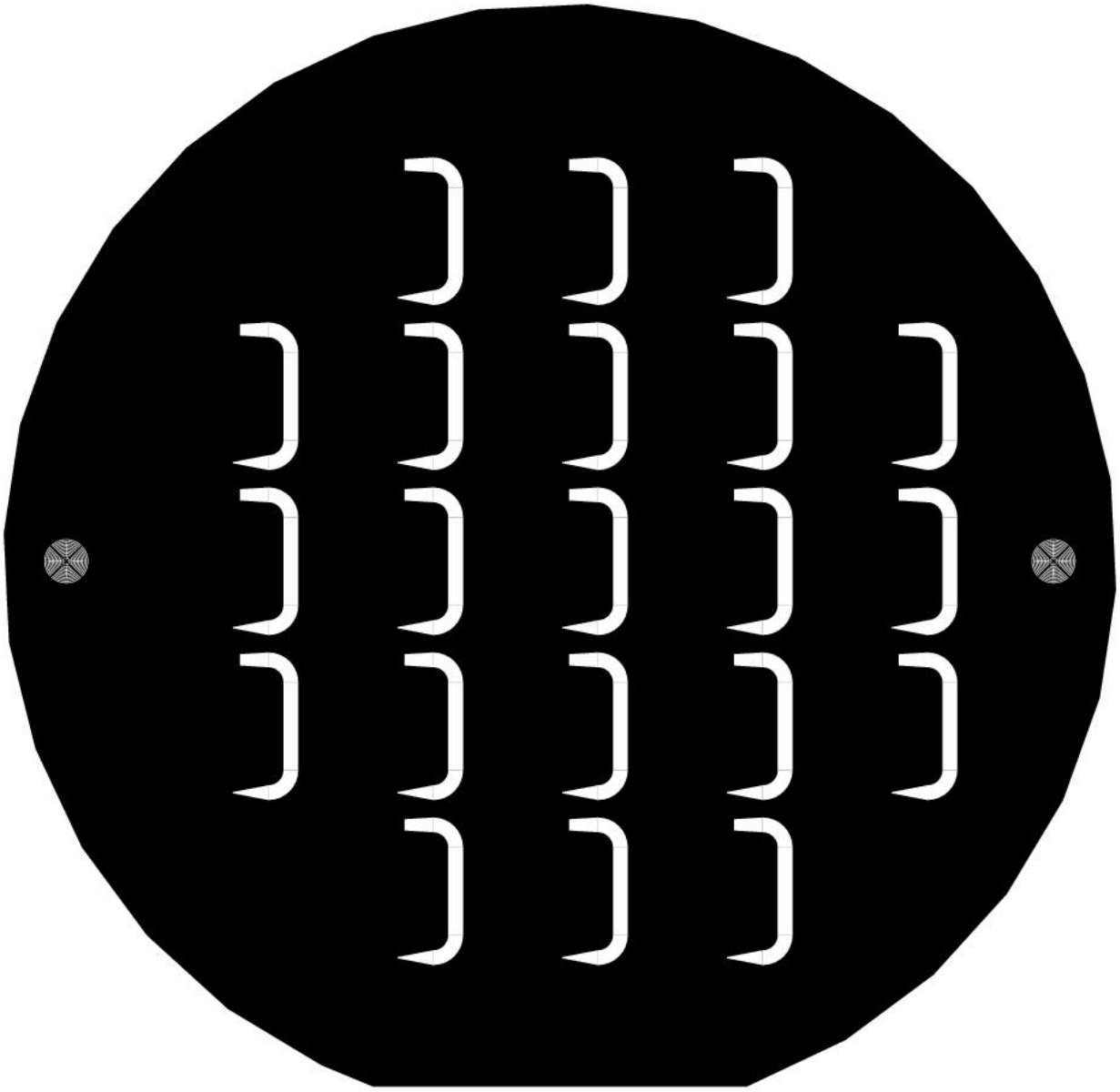

Figure B.8: Mask 2b – Pattern for gas micro-channel on bottom of layer 2.

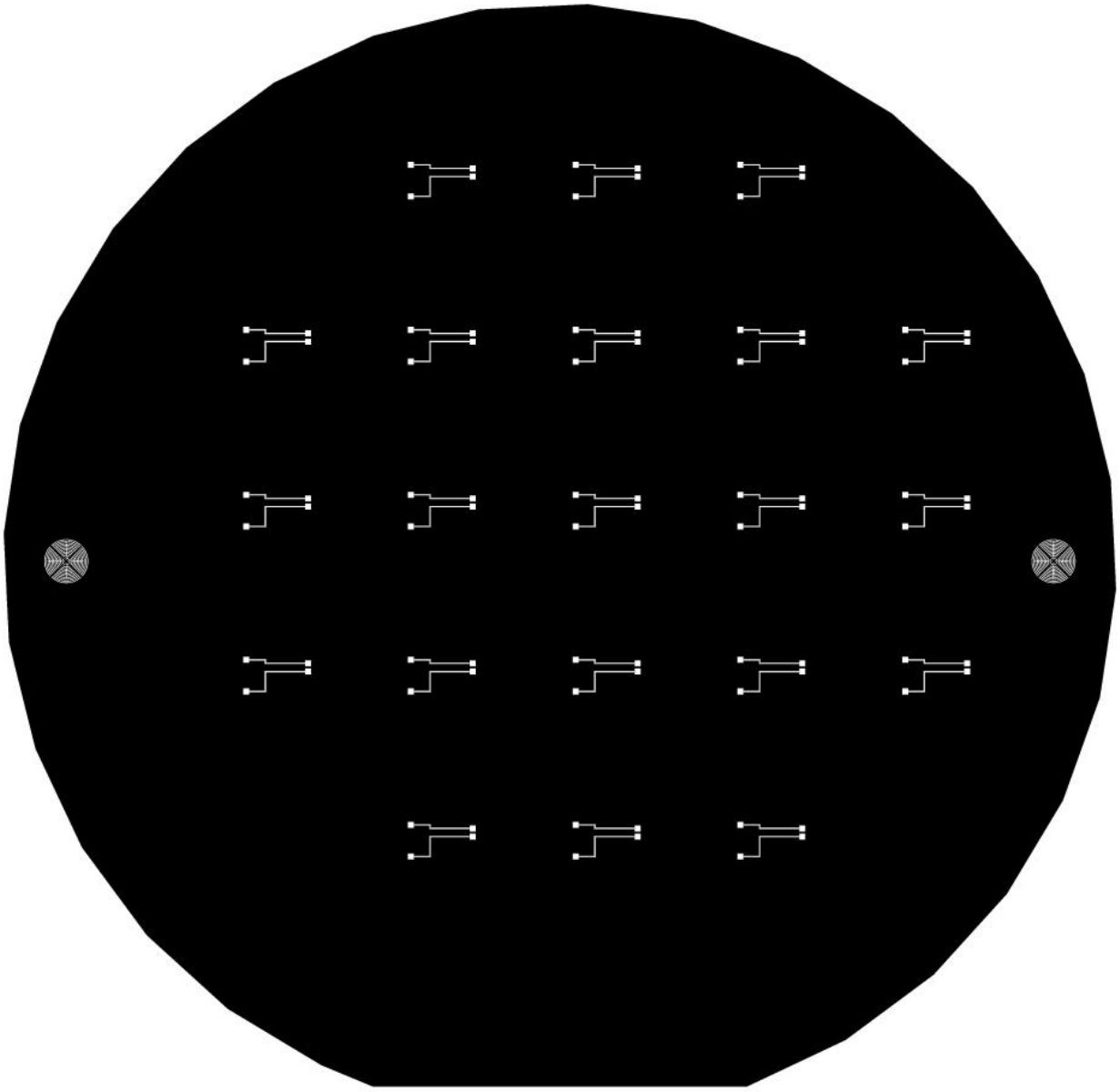

Figure B.9: Mask 3a – Pattern for gold electrode/leads/contacts for oxime sensor on top of layer 3.

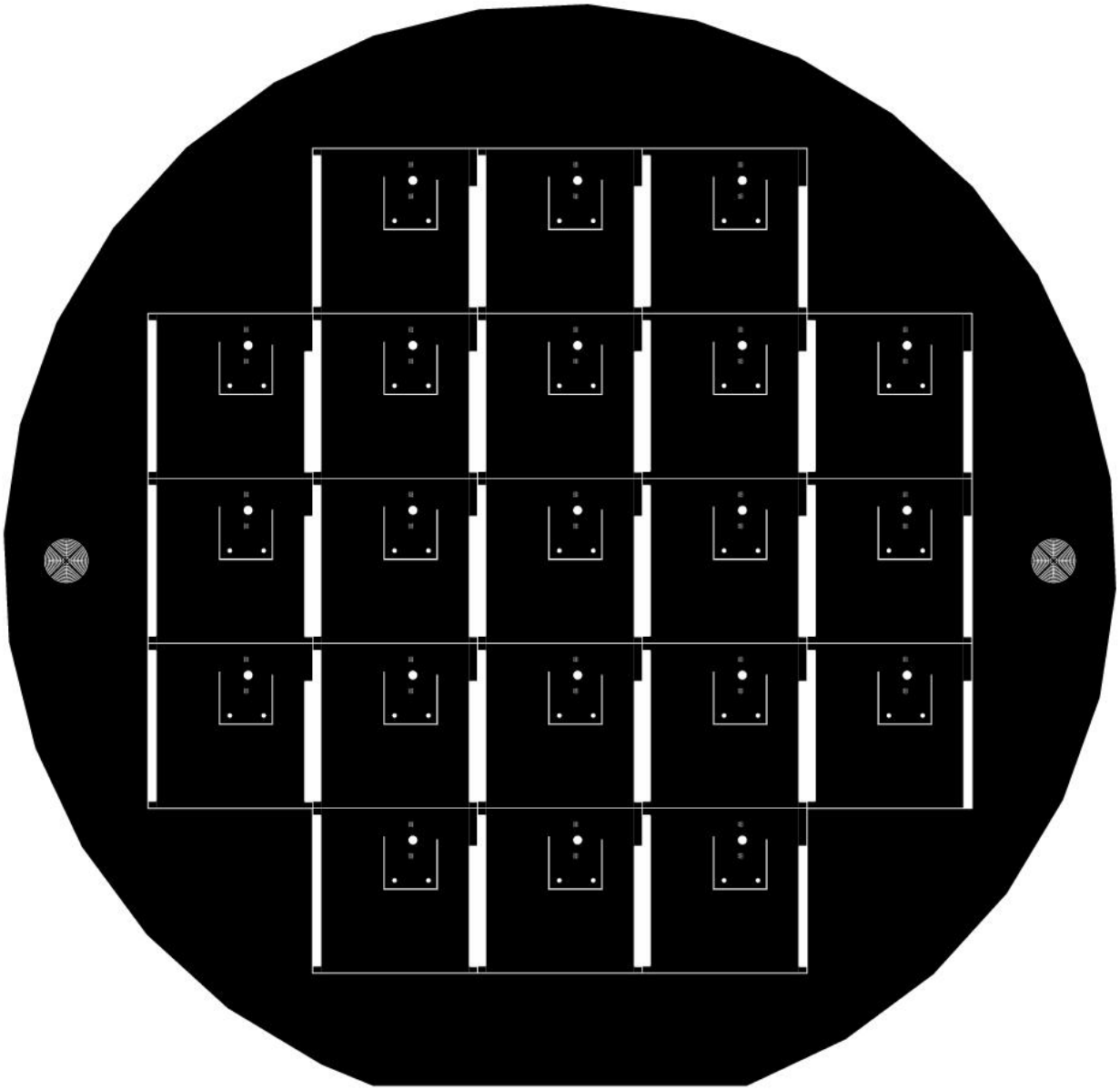

Figure B.10: Mask 3b – Pattern for membrane as well as through-holes, thermal break and die edges on top of layer 3.

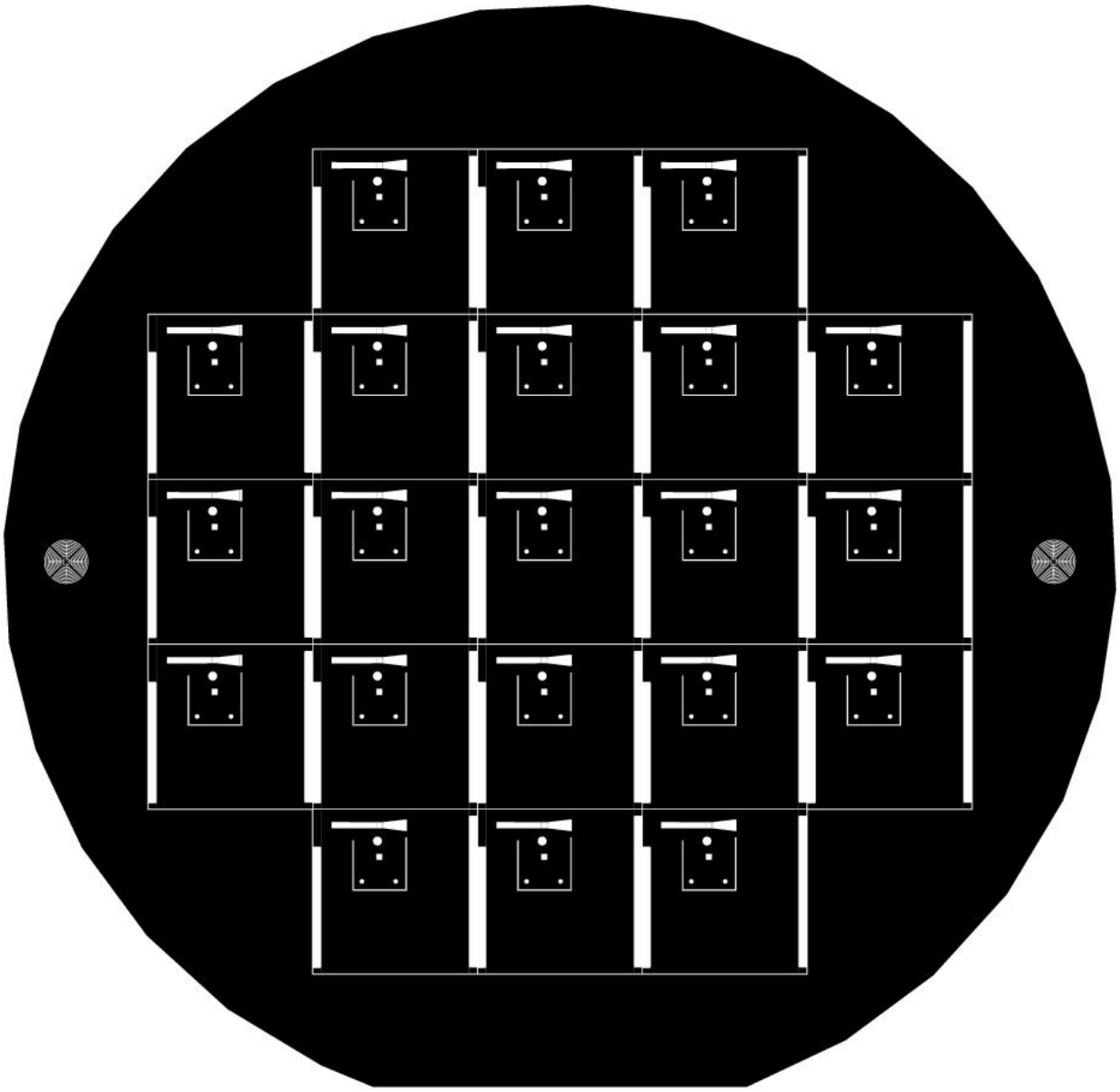

Figure B.11: Mask 3c – Pattern for gas micro-channel as well as through-holes, thermal break and die edges on bottom of layer 3.

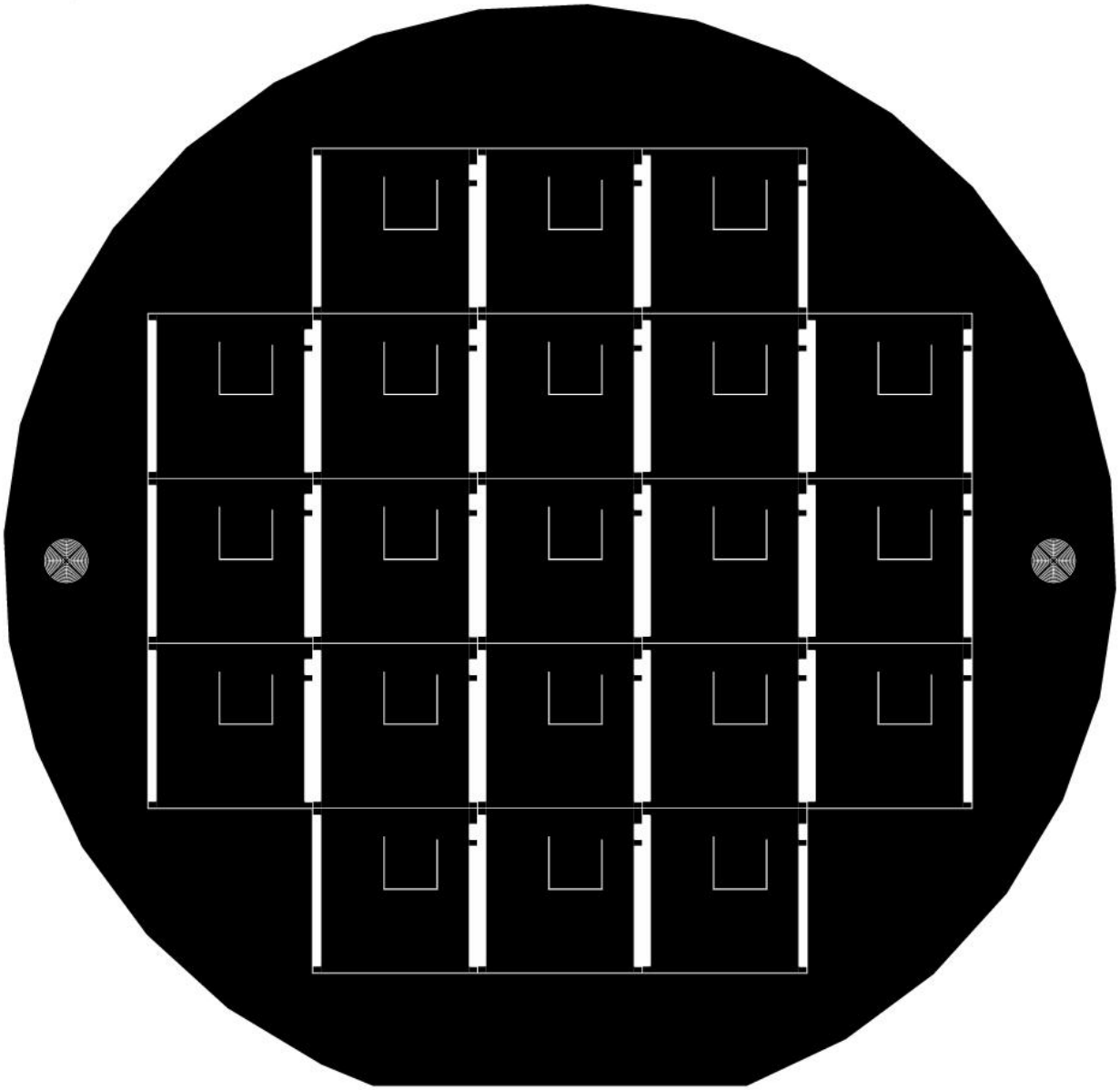

Figure B.12: Mask 4a – Pattern for thermal break and die edges on top of layer 4.

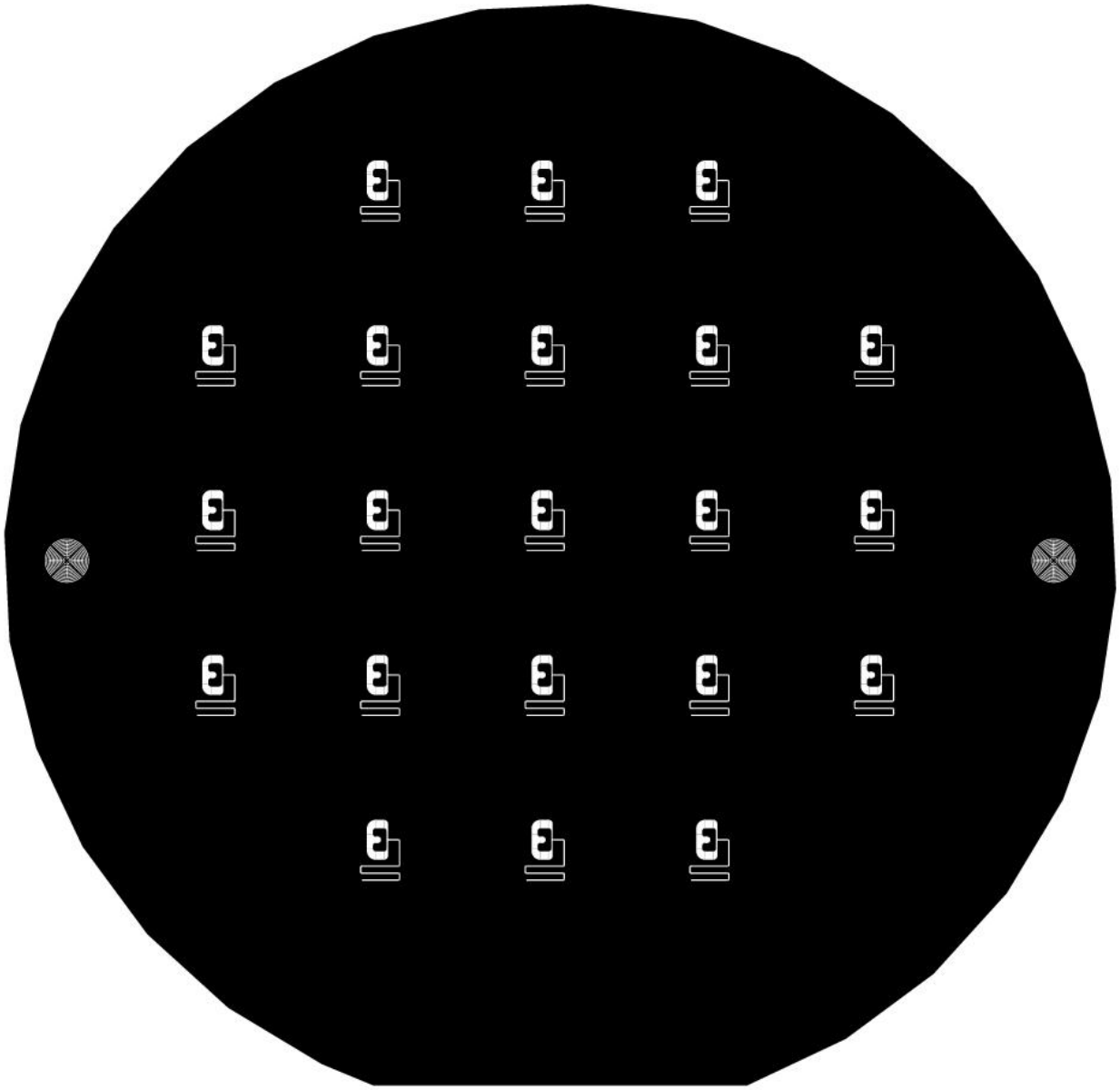

Figure B.13: Mask 4b – Pattern for liquid micro-channel on bottom of layer 4.

Appendix C: Experimental Procedures

Solid phase micro-extraction and analysis procedures

All solid phase micro extractions followed the general procedures outlined below.

1. The solution to be analyzed is first prepared and allowed to wait the specified amount of time. The oxime solution is prepared by dissolving 1mg of oxime per 1 ml of buffer solution (25 mM borate buffer solution, adjusted to pH 10 with concentrated NaOH). This solution is then allowed to sit for a specified amount of time before being sampled for analysis. Calibration solutions are prepared at various concentrations to form a calibration curve and are sampled immediately for analysis.
2. At the designated analysis time, 4 mL of solution is sampled into the 10ml vial and 1.25 g of NaCl (~23.8 wt%) is added to decrease the solubility of organics in solution. A small stir bar is also included in the vial to facilitate mixing.
3. The vial is immediately sealed with the GC septum, and then mixed by hand until the NaCl has completely dissolved.
4. The vial is then placed in a water bath at a temperature of 40 °C, and a stir rate of 450 rpm, and is allowed to equilibrate for 15 minutes.
5. To clean the polyacrylate fiber and prepare it for the extraction, the fiber needle is set to a depth of 3 cm and inserted into the GC injector port. The GC injector is set to 280 °C. The oven temperature is set at 250 °C to prevent contaminates

from the cleaning from collecting in the column. The fiber is cleaned in the GC for 15 minutes.

6. Once the fiber has been cleaned, it is quickly removed from the G, the needle depth readjusted to 2.8 cm, and then inserted into the vial containing the sample. At this depth, the fiber is completely submerged in the solution. The extraction is conducted at 40°C and a stir rate of 450 rpm for 50 minutes.
7. Once the extraction period is finished, the GC is prepped for the analysis run. Then the SPME fiber is removed from the sample, immediately set for a depth of 3 cm again and inserted into the injector port. The run is then started at this point. After 4 minutes into the run, the SPME fiber is removed from the injector.

Spectroscopic experiments on NIBS mechanism for Adamsite detection

1. Intermediate solutions of phenylenediamine (13.5 mg in 5 mL Millipore water), acetone (370 µL in 20 mL Millipore water) and silver nitrate (10 mg in 5 ml Millipore water) are prepared.
2. An intermediate solution of Adamsite is created in methanol (11.2 mg in 20 mL methanol) due to its low solubility in water.
3. The intermediate solutions of phenylenediamine and silver nitrate were prepared fresh daily to avoid any possible degradation in these reagents.

4. Phenylenediamine degradation was measured by simply using 3 mL of the intermediate solution in a quartz cuvette, then periodically loading the cuvette into the spectrometer to gather an absorbance spectrum.
5. For other experiments, various amounts of phenylenediamine were combined with acetone, Adamsite (if inhibition is being studied) or methanol in a quartz cuvette. The mixture is diluted with Millipore water such that when the catalyst is added; the total solution volume becomes 3 mL.
6. Once the silver nitrate catalyst is added, the cuvette is briefly covered, manually mixed, then uncovered and loaded into the spectrometer for analysis. If the sample is not being continuously analyzed, it is removed from the spectrometer and covered to prevent excessive evaporation of the solvent between tests.
7. After each experiment, the quartz cuvette is rinsed in methanol, water and then the interior is wiped down to remove any remain residues. Then the cuvette is dried to prepare for the next experiment.

Beaker scale electrochemical studies

Cyanide production kinetics for oxime based chemistry

1. Oxime solution to be studied is first prepared and allowed to wait the specified amount of time. The oxime solution is prepared by dissolving 1 mg, 0.5 mg or 0.25 mg of oxime per 1 ml of buffer solution giving a oxime concentration of 4.8 mM, 2.4 mM or 1.2 mM, respectively.

2. The buffer is a 25 mM borate solution, adjusted to pH 10 – 12 with concentrated NaOH, or pH 9 with concentration HCl solution.
3. At the designated analysis time, 20 mL of solution is sampled into the 60 mL electrochemical cell, and the Teflon® cap with the CN ISE is screwed on.
4. The Voltmaster potentiostat is connected to the 2 terminals of the CN ISE and set to measure an open circuit potential.
5. The electrode is allowed to reach equilibrium with the solution as evidenced by a constant open circuit potential reading. This value is recorded and the electrode is removed from the solution to a DI water beaker.
6. This is performed 2 more times to give an average open circuit potential reading from the CN ISE.
7. Calibration curves for cyanide concentration as a function of solution potential are created by preparing an identical oxime solution, then immediately measuring its open circuit potential with the CN ISE. During the measurement, standardized cyanide solution is added incrementally. Each time the potential reaches equilibrium, a measurement is taken, and then more cyanide solution is added. These measurements can then be used to form a calibration curve.

Organic solvent evaluation in oxime based chemistry

1. If an organic solvent is being tested, oxime is first dissolved in the organic solvent being tested in a 10 mg oxime per 1 mL solvent ratio. This solution is then

allowed to sit for a specified amount of time before being sampled for analysis. At the designated analysis time, the electrochemical cell is filled with 1 mL of the oxime/organic solvent solution and 9 mL of aqueous buffer solution (25 mM borate buffer solution, adjusted to pH 10 with concentrated NaOH). This results in a 4.8 mM oxime solution in the electrochemical cell. The solution is mixed thoroughly and the Teflon® cap with the CN ISE is screwed on.

2. If no organic solvent is being tested, 1 mg of oxime is directly dissolved in 1 ml of buffer solution (25 mM borate buffer solution, adjusted to pH 10 with concentrated NaOH). This solution creates a 4.8 mM oxime solution which is then allowed to sit for a specified amount of time before being sampled for analysis. At the designated analysis time, 10 mL of solution is sampled into the 60 mL electrochemical cell, and the Teflon® cap with the CN ISE is screwed on.
3. The Voltmaster potentiostat is connected to the 2 terminals of the CN ISE and set to measure an open circuit potential.
4. The electrode is allowed to reach equilibrium with the solution as evidenced by a constant solution potential reading. This represents the initial or baseline potential of the solution.
5. To initiate the reaction, 50 μL of a 21 mM solution of acetic anhydride (analyte) in acetone is injected into the cell, resulting in a final analyte concentration in solution of 50 μM.
6. Once the reaction has completed and the solution potential has once again stabilized, the final potential is recorded.

7. Before proceeding to the next experiment, the electrode is washed in DI water to remove any trace cyanide.

NIBS mechanism for toxic sulfide detection

1. Intermediate solutions of formic hydrazide (6 mg in 10 mL methanol), copper (II) acetate (11.4 mg in 10 mL methanol) and CEMS (4 μL in 4 ml methanol) were prepared fresh daily.
2. The non-aqueous reference electrode was prepared using methanol, tetrabutyl ammonium perchlorate and silver nitrate following the procedures given from BASi. This reference electrode solution was also created fresh daily.
3. For a particular experiment, a given amount of formic hydrazide intermediate solution was diluted with methanol to 10 mL. CEMS solution is then added if the effects of catalyst inhibition are being studied.
4. Finally, a given amount of copper (II) acetate solution is added, the resulting solution is mixed manually for several seconds and then placed onto a stirring plate operating at 100 rpm.
5. The working and reference electrodes are quickly inserted and the open circuit potential of the solution is monitored for 1000 s.
6. To minimize any extraneous cumulative effects on the open circuit potential of the solution, a set of experiments was usually run by alternative between inhibited and non-inhibited cases for the same reactant and catalyst concentrations.

7. Between experiments, the working and reference electrode were allowed to sit in pure methanol while the electrochemical cell was rinsed with methanol and water, and then wiped clean.

NIBS mechanism for Adamsite detection

1. Intermediate solutions of phenylenediamine (13.5 mg in 5 mL Millipore water), acetone (370 µL in 20 mL Millipore water) and silver nitrate (10 mg in 5 ml Millipore water) are prepared.
2. An intermediate solution of Adamsite is created in methanol (11.2 mg in 20 mL methanol) due to its low solubility in water.
3. The intermediate solutions of phenylenediamine and silver nitrate were prepared fresh daily to avoid any possible degradation in these reagents.
4. For a particular experiment, a given amount of phenylenediamine and acetone intermediate solutions are combined and diluted with Millipore water to 10 mL. Adamsite solution is then added if the effects of catalyst inhibition are being studied.
5. Finally, a given amount of silver nitrate solution is added, the resulting solution is mixed manually for several seconds and then placed onto a stirring plate operating at 100 rpm.
6. The working and reference electrodes are quickly inserted and the open circuit potential of the solution is monitored for 1500 s.

7. To minimize any extraneous cumulative effects on the open circuit potential of the solution, a set of experiments was usually run by alternative between inhibited and non-inhibited cases for the same reactant and catalyst concentrations.
8. Between experiments, the working and reference electrode were allowed to sit in DI water while the electrochemical cell was rinsed with water and acetone, and then wiped clean.

Oxime micro-sensor testing

Operation with gas chromatograph automatic injector assembly

These procedures apply to operation of both the polycarbonate oxime micro-sensor and the oxime sensor in the silicon micro-array.

1. A 4.8 mM oxime solution is prepared using an aqueous buffer solution (25 mM borate buffer solution, adjusted to pH 10 with concentrated NaOH).
2. If oxime degradation is being studied, the oxime solution is allowed to age the specified about of time before introducing it into the micro-sensor.
3. The solution is then loaded into a syringe and slowly introduced into the liquid channel of the sensor. During the test, the oxime solution remains static to maximize the potential response.
4. The micro-sensor, oxime containing syringe and the chromatography column (if present) are all loaded into the GC oven.

5. The oven temperature is set and the sensor is then allowed equilibrate for 20 – 30 minutes before any analyte is introduced.
6. The injection assembly temperature is set to 250 °C. Carrier gas flow rate, split ratio and sample volume are also set at this point.
7. When an injection is started, the sampling needle automatically draws in ambient air 6 times to "wash" the syringe. The vial containing the compound(s) to be tested is then sampled, either from the head space as a saturate vapor for individual compounds or directly from solution as a liquid for mixtures.
8. The sample is then injected, diluted by the split flow, and sent through a passivated capillary or a GC column to the micro-sensor as a "pulse" in the inert helium carrier flow.
9. The open circuit potential response of the micro-sensor is pre-processed by the 20× amplifier and low pass noise filter. The resulting signal is then measured by the external potentiostat unit.
10. Once a set of tests have been finished, the oven is opened and fresh oxime solution is again slowly flowed through the sensor to remove reaction products and reset the device.
11. After the oven is closed, the sensor again requires a short period of time to re-equilibrate before testing can resume.

Evaluation of organic solvents in micro-sensor

The procedure for this section is nearly identical to that of the previous section, with the exception of step #1 being replaced with the procedures given below.

1. Oxime is first dissolved in the organic solvent being tested in a 10 mg Oxime per 1 mL solvent ratio. This solution is then allowed to sit for a specified amount of time before being sampled for analysis.
2. At the designated analysis time, 9 mL of buffer solution (25 mM borate buffer solution, adjusted to pH 10 with concentrated NaOH) is mixed with 1 mL of the oxime/organic solvent solution, and thoroughly mixed. This results in a 4.75 mM oxime solution for use in the micro sensor.

Operation with continuous gas sample delivery

1. A 4.8 mM oxime solution is prepared using an aqueous buffer solution (25 mM borate buffer solution, adjusted to pH 10 with concentrated NaOH).
2. The solution is then loaded into a syringe and slowly introduced into the liquid channel of the sensor. During the test, the oxime solution remains static to maximize the potential response.
3. If a single compound is being tested, a saturated vapor sample is drawn into a 100 mL gas tight syringe and then diluted to the desired concentration with air. This syringe is then mounted onto a syringe pump and the pump speed is set to

1 mL/min. If a gaseous mixture is being tested, the cylinder containing the compounds is connected to the micro-sensor by way of a flow meter set to 1 mL/min.

4. The micro-sensor is allowed to reach equilibrium as evidenced by a constant open circuit potential reading, then the flow of the gas sample is started.
5. The open circuit potential response of the micro-sensor is pre-processed by the 20× amplifier and low pass noise filter. The resulting signal is then measured by the external potentiostat unit.
6. Once the sample exposure period has passed, the gas flow to the sensor is halted. If possible, air is passed through the sensor to remove any remaining sample.
7. The oxime solution is again slowly flowed through the sensor to remove reaction products and reset the device.
8. The sensor again requires a short period of time to re-equilibrate before testing can resume.

Micro-mixer evaluation

1. An organic solution of 11 mg oxime per 1 ml of ethanol is created fresh for the test. This solution is loaded into the 4.5 mm diameter syringe.
2. The 14 mm diameter syringe is loaded with 25 mM borate buffer solution, adjusted to pH 10 with concentrated NaOH.

3. Due to syringe pump limitations, the minimum reliable plunger speed is roughly 30 μm/min. This speed gives an aqueous buffer solution flow rate of 5.0 μL/min and an organic oxime solution flow rate of 0.5 μL/min.
4. A syringe containing acetic anhydride vapor dilute to 100 ppb using ambient air is loaded into the second syringe pump, which is set to provide a gas flow rate of 1 mL/min.
5. The open circuit potential of the sensor is monitored to determine when the system has reached a steady-state equilibrium. This potential corresponds to the initial or baseline reading.
6. The test is then started by initiating the flow of analyte vapor. This gas stream is flows through the sensor for 100 seconds and then turned off. The sensor is then allowed to return to its initial potential reading. The liquid syringe pump remains operational and pumping fluid at the designated flow rate during the entire test.
7. The comparison test is conducted by flushing out the system with DI water, and preparing fresh organic oxime and aqueous buffer solution as per step #1.
8. The aqueous buffer will be combined with the organic oxime solution in a 10:1 ratio again, however this time they will be mixed externally by hand.
9. This pre-mixed solution is then loaded into a syringe and the syringe pump is then set to deliver the fluid at a flow rate of 5.5 μL/min.
10. The rest of the comparison test is then carried out by following steps 4 – 6.

Single walled carbon nano-tube (SWNT)-based sensor operation

1. A custom sample pulse injection system was constructed for SWNT-based sensor testing using a 6-port valve (C22-3186EH, Valco Instruments) and dynacalibrator (Model-500, Vici) with permeation tubes containing the various compounds which the sensor could be exposed to.
2. The sensor response is monitored using a nanovoltmeter (Keithley 2182A) while the DC driving current is provided with an AC/DC current source (Keithley 6221).
3. The sensor electronics and pulse injection system are controlled in concert with each other using an in-house program written in LabVIEW (National Instruments, Inc.).
4. The micro-sensor array (contain the SWNT-based sensor being tested) is connected to the 6-port valve using a short length of passivated fused silica capillary.
5. The SWNT-based sensor is then tested using ultra pure helium carrier gas at a flow rate of 1 sccm, and is operated with a drive current of 0.1 mA.
6. Pure helium is allowed to pass over the sensor for 20 seconds while recording the sensor resistance, which established a stable baseline resistance.
7. After 20 seconds, the 6-port valve is switched from sampling mode to injection mode and a 250 μL pulse of dimethyl methyl phosphonate (DMMP) at a concentration of 10 ppm is injected into the carrier gas stream.

8. The resulting resistance change in the SWTN-based sensor is recorded for later analysis and the system is reset for additional test.

Author's Biography

Nicolas Javier Londoño was born in Miami, Florida in 1983. He was homeschooled by his parents until his early teens, at which point he began studying chemistry at Miami-Dade Community College. It was here that his interest in chemical engineering began and in 2002, he completed the Associate in Arts program at MDCC with highest honors and distinctions. He then transferred to the University of California, Berkeley as an ACS scholar to pursue a degree in chemical engineering. While there, he developed an interest in semiconductor processing and micro-fabrication, and performed undergraduate research in surface assembled monolayers. In the fall of 2004, he earned his Bachelor of Science in chemical engineering from U.C. Berkeley, graduating with honors. The following year, he began work as a process engineer at a pharmaceutical manufacturing plant in the Johnson & Johnson network of companies. Here he served as technical support in the production of several transdermal drug delivery products such as NicoDerm® and Scop®. In the summer of 2006 he left this job to begin graduate school at the University of Illinois at Urbana-Champaign. There he worked for Richard I. Masel performing research on liquid based gas sensors. He obtained his Master of Science in chemical engineering in 2010 and has been continuing this research for completion of the Ph.D. program in the same department. Upon graduation, he will join Prof. Bin Chen's group as a postdoctoral researcher at the NASA Ames Research Center in Mountain View, California.